Theoretical AGB and post-AGB Models for Synthetic Population Studies

DISSERTATION

der Fakultät für Physik
der Ludwig-Maximilians-Universität München

vorgelegt von

Agis Kitsikis

aus Ottawa

München, den 19. Dezember 2007

1. Gutachter: Priv. Doz. Dr. A. Weiss
2. Gutachter: Prof. Dr. A. Pauldrach
Tag der mündlichen Prüfung: 29. April 2008

Για *τους ηρωικούς αγωνιστές του Μονάχου* :
“*Hlia rixtw*!”

στὴν μνήμη τοῦ παπποῦ μου Νίκου

Zusammenfassung

Gegen Ende ihrer Entwicklung durchlaufen Sterne im mittleren Massenbereich (zwischen ca. 1 und 8 Sonnenmassen) den *asymptotischen Riesenast* oder AGB (für *asymptotic giant branch*). Der AGB und der Übergang auf die darauf folgende Post-AGB-Phase sind sehr zeitaufwändig zu simulieren (sowohl im Bezug auf Computer- als auch menschliche Ressourcen). Infolgedessen sind die sich aus umfangreichen Rechnungen ergebenden großen Gitter von Modellen rar. Meist sind nur wenige Modelle berechnet. Einige Kataloge von Sternmodellen sind trotzdem in den vergangenen Jahren erstellt worden. Diese sind in der *Populationssynthese* sehr nützlich, die viele verschiedene Modelle benötigt, um die beobachteten Eigenschaften großer Stellarsysteme zu simulieren. Allerdings können solche AGB- und Post-AGB-Gitter nur schwer mit den immer besser werdenden physikalischen Beschreibungen Schritt halten. Die sogenannten synthetischen AGB-Modelle sind eine mögliche Lösung für dieses Problem, weil sie weniger rechenintensiv sind. Jedoch haben sie den Nachteil, dass sie nur grobe Näherungen sind.

In diesem Zusammenhang wurden ausführliche Modelle für Sterne mit Anfangsmassen von 1 bis 6 Sonnenmassen und einem Anteil schwerer Elemente, der zwischen einem Vierzigstel und dem Doppelten des solaren Gehalts liegt, berechnet. Die Rechnungen beginnen auf der Hauptreihe und durchlaufen alle Sternphasen bis zum Weißen Zwerg. Wir konzentrieren uns besonders auf den AGB und Post-AGB.

Unser Parameterraum ist nur mit den neuesten synthetischen Gittern vergleichbar, da keine der früheren Studien vergleichbar große Masse- und Metallizitätsbereiche abdeckt. Außerdem ist die neueste, für AGB und Post-AGB relevante Physik einbezogen. Derartige Verbesserungen sind weder in anderen synthetischen noch in anderen ausführlichen Rechnungen zu finden und stellen den Hauptvorteil dieser Arbeit dar. Es gibt im wesentlichen drei Fortschritte: a) neue, von der chemischen Zusammensetzung abhängige Opazitätsdaten für tiefe Temperaturen, b) modernste, die chemische Zusammensetzung berücksichtigende Beschreibung des Massenverlusts, c) konvektives *Overshooting*. Besonderes Augenmerk wurde auf die konsistente Behandlung der möglichen Anreicherung mit Kohlenstoff in den äußersten Sternschichten gelegt.

Durch Vergleich mit bisherigen Gittern zeigen wir, dass diese Änderungen unerlässlich sind. Zudem sind unsere Modelle, auch ohne vorherige Kalibrierung, in guter Übereinstimmung mit Beobachtungsdaten.

Der neue Katalog enthält 100 AGB- und 60 Post-AGB-Sequenzen. Die AGB-Modelle decken dabei den gesamten Parameterraum ab. Die Post-AGB-Modelle sind auch für den gesamten Metallizitätsbereich verfügbar, allerdings nur, wegen Konvergenzproblemen, für Anfangsmassen zwischen 1 und 2 Sonnenmassen.

Die vorliegende Arbeit bietet der wissenschaftlichen Gemeinschaft die derzeit modernsten und umfangreichsten selbstkonsistenten und sich aus ausführlichen AGB- und Post-AGB-Rechnungen ergebenden Gitter an. Es ist zu erwarten, dass unser Katalog ein wertvolles Instrument für die Populationssynthese wird, und so die über zehn Jahre alten Sequenzen, die momentan in Benutzung sind, ersetzt.

Abstract

Near the end of their evolution, moderate-mass stars (approximatively between 1 and 8 solar masses) go through the *asymptotic giant branch* (AGB) phase. The AGB and the transition to the ensuing post-AGB are very time (both computational and human) consuming to simulate. Hence, large grids of models originating from detailed calculations are rare; only few stars are generally computed. Some stellar libraries have nonetheless been constituted in the past. These are very sought-after by population synthesis modelers, as they try to reproduce observed properties of larger stellar systems by assembling together many individual models. However such AGB and post-AGB grids can rapidly become outdated because of constant input-physics ameliorations. So-called synthetic AGB models are a solution as they are computationally less time demanding: nonetheless their major drawback is that they remain approximations.

In this context, new detailed models for stars of 1 to 6 solar masses, and compositions with a total heavy element content that corresponds to values between a fortieth and a double of the solar one (for two different relative scalings), have been computed. They evolve through all stellar phases from the main sequence to the white dwarf stage; here focus is on the AGB and post-AGB parts.

The parameter space coverage is comparable only with the latest synthetic grids, as none of the previous detailed stellar libraries extend over such wide mass/metallicity intervals. Furthermore, the most recent physics, relevant for the AGB and post-AGB, are included. These updates, at the level of sophistication brought by this work, are present neither in synthetic nor in any detailed computations. Because they are of paramount importance, their inclusion is the major asset of this work. Specifically, three updates have been implemented: a) new chemistry-dependent low-temperature opacities b) up-to-date chemistry-dependent mass-loss prescriptions c) convective overshooting. With overshooting, envelope mixing will be more efficient and dredge-up additional material from deeper layers. The stellar surface will thus be converted from an oxygen- to a carbon-rich one, and changes will directly affect the opacities and in turn the mass-loss rates. While ignored in previous models, these transformations are now taken into account.

We show, how such amendments were a necessity by comparing the results with older grids, and how models are in agreement, without any prior calibration, with observations.

The new stellar library contains 100 AGB and 60 post-AGB sequences. The AGB tracks cover the entire parameter space. Post-AGB models are also available for the full metallicity range but, because of convergence issues, only for star between 1 and 2 solar masses.

To our knowledge this work provides the scientific community with the most up-to-date, self-consistent and extended grid, originating from detailed AGB and post-AGB models. It is expected to be a valuable input-tool for population synthesis work and aims to supersede the more than 10-year old outdated tracks that are currently still being used.

Contents

1. Introduction[1]

The asymptotic giant branch - or AGB - represents one of many stages in stellar evolution. It is a short-lived late episode in the sequence of events moderate-mass stars ($0.8\mathrm{M}_\odot < M < 10\mathrm{M}_\odot$, where $\mathrm{M}_\odot$ is the solar mass) go through during their lifetime[2]. The double nuclear shell-burning of hydrogen and helium around the carbon/oxygen core and the recurrent thermonuclear instability flashes characterize the late AGB. These flashes, also called thermal pulses (TPs), which came about fortuitously in evolutionary calculations of the sixties (Schwarzschild & Härm 1965, Weigert 1966) and initially thought, by Schwarzschild and Härm, to be a numerical error, have become the distinctive mark of the AGB (see Figure 1.1).

Contrarily to the early-AGB (E-AGB) evolution that does not really bear any particular exterior signs, in the AGB's second part, the TPs put forward its unique identity. Extremely short on the evolutionary timescale, the repeated TP occurrences have periods of tens to a few hundreds of thousand years, a time interval too long for direct observation. It is very unlikely to recognize such events dead-on and impossible to observe a full TP-cycle. Aside from theoretical stellar models, their existence can observationally only be inferred in an indirect way. Nevertheless this thermally-pulsating-AGB (TP-AGB) stage receives most of the attention in numerical simulations and is undoubtedly the most influential in the later evolution of the star. As a result, it symbolizes AGB evolution as a whole.

A theoretical study of the TP-AGB amounts to modelling the physical processes occurring in the star during the TP-cycle. Because of the increasing availability of computational resources as well as improvements in numerical methods, TP-AGB evolution can nowadays be routinely followed through most of the TPs, even though it remains a computationally demanding task. But at the end of the TP-AGB, numerical convergence difficulties often impose a premature end of the evolution. In practice a smooth and reliable transition from the last few TPs to the subsequent post-AGB phase is still problematic.

---

[1] In this chapter, when no specific reference is given, I have used *Asymptotic Giant Branch Stars*, edited by Habing & Olofsson (2004), Josef Wagenhuber (1996)'s PhD thesis, *Entwicklung von Sternen verschiedener Massen und Metallizitäten auf dem asymtotischen Riensenast und danach*, Amanda Karakas (2003)'s PhD thesis, *Asymptotic Giant Branch Stars: their influence on binary systems and the interstellar medium* and the review on AGB stars by Herwig (2005a).

[2] Precise mass boundaries are model-dependent. For initial masses higher than about $8\mathrm{M}_\odot$, stars are massive enough to ignite carbon in the core and become super-AGB stars (see Herwig 2005a). These super-AGB stars will become white dwarfs with an oxygen/neon/magnesium core. The focus in this thesis will be on the more classical AGB stars with masses below $8\mathrm{M}_\odot$ and a carbon/oxygen core. The designation "moderate-mass stars" refers, in an equivalent way, to "low- and intermediate-mass stars that will eventually go through the AGB phase".

1.1. AGB stars

Due to their high luminosities, AGB stars are easily detected in the Milky Way but also in the Local Group (within about 10 Mpc) where they have been resolved in many galaxies (e.g. Nowotny et al. 2001, Saviane et al. 2000). They have also been indirectly revealed through their signature in the integrated spectra of stellar systems (e.g. Lançon et al. 1999) when individual stars cannot be resolved.

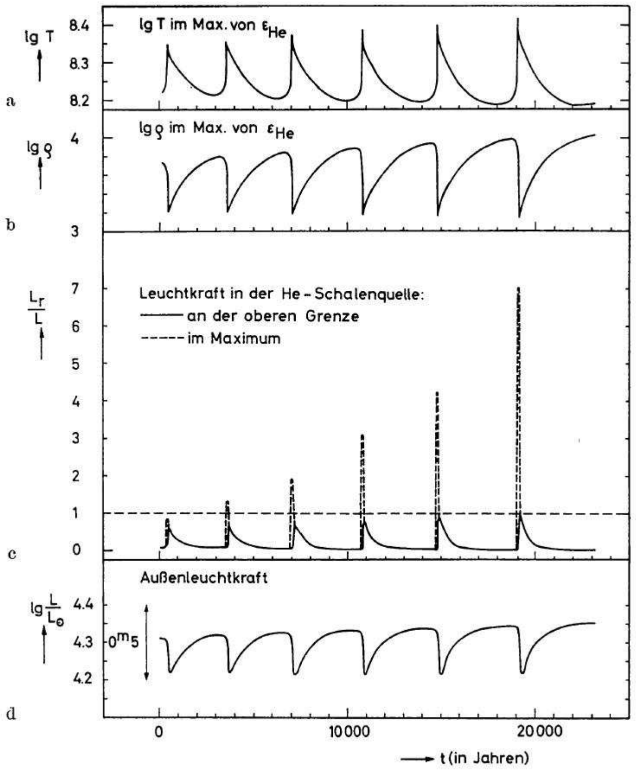

Abb. 7a—d. Die zeitliche Änderung einiger wichtiger Größen im Stern während der thermischen Pulse der He-Schalenquelle

Figure 1.1.: First theoretical evidence for TPs on the AGB. Figure taken from Weigert (1966), where TPs observed in theoretical models were first published and presented in this way. A few months earlier Schwarzschild & Härm (1965) did not show a graphical representation of TPs even though they were also encountered in their calculations and mentioned in the article. The comment here says: "The temporal change of a few important stellar quantities during the thermal pulses of the helium-shell source". Panels show quantities versus time. Panels *a* & *b*: respectively temperature and density in the helium shell at the location of maximum energy production. Panel *c*: helium-burning luminosity. Panel *d*: total luminosity.

Nevertheless, because they are short-lived, AGB stars are rare. A rough estimate (see Habing & Olofsson 2004, p. 19 and p. 411) indicates that, in our galaxy, only about one out of a few tens of thousand stars is a TP-AGB star. Obviously, this infrequency is even more of a handicap in less populated stellar systems like dwarf galaxies.

Many AGB stars are also long-period variables (LPVs). The first LPV was accidently discovered by Fabricius, a clergyman from East Frisia in 1596, while studying Jupiter. Later, the same star was more meticulously observed by the Dutch astronomer Holwarda in 1638. Since then, astronomers have often looked at AGB stars, not always realizing what they were. It is only in the last thirty to forty years that AGB stars have been better studied both observationally and theoretically. They now constitute a field of their own.

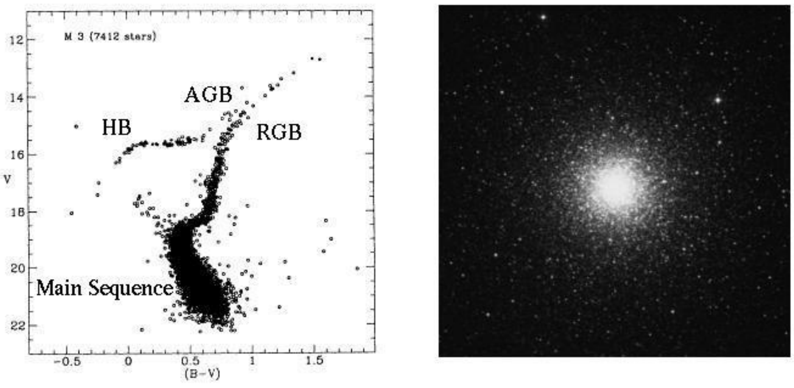

Figure 1.2.: *Left* - HR diagram of the globular cluster M3. Figure taken from Buonanno et al. (1994). The locations of the main sequence, the red giant branch, the horizontal branch and the asymptotic giant branch are approximatively shown. *Right* - Image of M3 taken from *http : //archive.stsci.edu/cgi − bin/dss_form*.

AGB stars are big, luminous and cool. They have radii of a few hundred times the solar radius. They are typically a few thousand to tens of thousand times more luminous than the Sun. They have temperatures at the photosphere (effective temperature) in the range of about half the solar temperature. In fact, low- and intermediate-mass stars reach on the AGB the highest luminosities but also the lowest effective temperatures of their evolution. AGB stars are also old - in the evolutionary sense - as they represent a mature stellar phase.

A star arriving on the AGB will approximately have the same mass as during its earlier evolutionary phases. The AGB is characterized by high mass-loss and is the final stage driven by nuclear burning. Mass-loss on the AGB can reach values up to ten orders of magnitude higher than the pace at which mass is lost on the Sun. Once on the AGB, a star will gradually lose its envelope, leaving behind a bare core with a mass roughly between 0.5 and the theoretical upper limit of 1.4$M_\odot$ (Chandrasekhar 1931). This core, composed of carbon and oxygen, or for the more massive super-AGB stars, oxygen, neon and magnesium, is left to continue its evolution as a post-AGB star, after which it will go through the planetary nebula (PN) phase before finally becoming a white dwarf (WD).

When the effective temperature (or color) and the luminosity (or magnitude) of stars obtained from observations are transposed in a graphic - the Hertzsprung-Russell (HR) or color-magnitude diagram - different groups that share similar evolutionary and physical properties clearly appear (see Figure 1.2). The main sequence (MS), where stars such as the Sun are located, is the most characteristic and well known one. Another one, the red giant branch (RGB), gathers giant stars of a specific evolutionary phase. With advances alternating between observation and theory, physical explanation and understanding was first achieved for the MS and later for the RGB stars. It is only in the early fifties, with the help of better observations, that color-magnitude diagrams of globular clusters showed, what was initially described (see Figure 1.3), since the direction of evolution in the HR diagram was not known then, as "a bifurcation of the red giant branch" (Arp et al. 1953). Later this "bifurcation" became the "asymptotic giant branch" and it was realized that as an evolutionary phase the AGB came after the RGB. During both of these stages stars grow in radius and become giants under similar but not identical conditions.

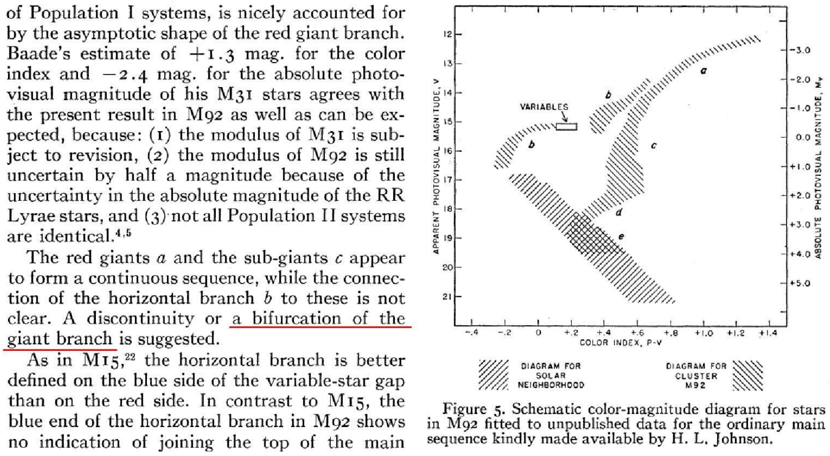

of Population I systems, is nicely accounted for by the asymptotic shape of the red giant branch. Baade's estimate of +1.3 mag. for the color index and −2.4 mag. for the absolute photovisual magnitude of his M31 stars agrees with the present result in M92 as well as can be expected, because: (1) the modulus of M31 is subject to revision, (2) the modulus of M92 is still uncertain by half a magnitude because of the uncertainty in the absolute magnitude of the RR Lyrae stars, and (3) not all Population II systems are identical.[4,5]

The red giants *a* and the sub-giants *c* appear to form a continuous sequence, while the connection of the horizontal branch *b* to these is not clear. A discontinuity or a bifurcation of the giant branch is suggested.

As in M15,[22] the horizontal branch is better defined on the blue side of the variable-star gap than on the red side. In contrast to M15, the blue end of the horizontal branch in M92 shows no indication of joining the top of the main

Figure 5. Schematic color-magnitude diagram for stars in M92 fitted to unpublished data for the ordinary main sequence kindly made available by H. L. Johnson.

Figure 1.3.: First observational evidence of the AGB's existence as a distinct group. This figure is taken from Arp et al. (1953). The AGB stands out as a new regroupment of stars in the M92 globular cluster. In the text, the term "bifurcation of the red giant branch" (underlined) is used. The figure gives a schematic representation of the observational HR diagram obtained by Arp, Baum and Sandage. From the two groups of stars labelled *b*, the "bifurcation" refers to the second one on the right. Only later will "asymptotic giant branch" be widely used and finally establish itself as the standard.

The term AGB was thus originally used to describe a new group of stars in the HR diagram of globular clusters. Today it has come to represent all the moderate-mass stars in a specific phase of evolution that corresponds to the second time they climb into the region of the HR diagram occupied by red giant stars.

An important fraction of stellar objects are of moderate-mass and will therefore go through the AGB phase. Presumably, this is also the case for the Sun. But AGB stars are more than just a state many stellar objects will go through. As a brief - the TP-AGB only lasts a very short time with respect to other phases (Table 1.1) - but important and very rich in physical processes stage, the AGB represents a transition between evolutionary phases where a radical transformation takes places.

Table 1.1.: TP-AGB lifetimes for models with chemical compositions representative of the solar neighborhood and the Large and Small Magellanic Clouds (LMC & SMC). Values are obtained from detailed stellar models with the Garching evolution code. The duration of the TP-AGB is given for comparison with respect to other phase of evolution: MS, RGB, central helium burning (He-b) and the entire AGB.

Model	$t_{\text{TP-AGB}}$	$\frac{t_{\text{TP-AGB}}}{t_{\text{MS}}}$	$\frac{t_{\text{TP-AGB}}}{t_{\text{RGB}}}$	$\frac{t_{\text{TP-AGB}}}{t_{\text{He-b}}}$	$\frac{t_{\text{TP-AGB}}}{t_{\text{AGB}}}$
2.0M$_\odot$ / Solar	$2.58 \cdot 10^6$ yr	0.24%	4.42%	1.46%	14.3%
1.6M$_\odot$ / SMC	$1.06 \cdot 10^6$ yr	0.07%	0.90%	1.02%	10.4%
2.0M$_\odot$ / SMC	$3.61 \cdot 10^6$ yr	0.44%	13.1%	1.81%	23.7%
2.6M$_\odot$ / LMC	$0.99 \cdot 10^6$ yr	0.22%	9.94%	0.93%	14.7%
6.0M$_\odot$ / SMC	$0.09 \cdot 10^6$ yr	0.15%	12.7%	1.19%	21.0%
1.5M$_\odot$ / LMC	$0.79 \cdot 10^6$ yr	0.04%	0.41%	0.80%	7.49%
2.6M$_\odot$ / SMC	$0.47 \cdot 10^6$ yr	0.12%	5.50%	0.58%	10.4%

This turning point will in many ways affect the star itself and its environment. The importance of AGB stars can be considered for the following three major areas of interest.

- First, with respect to stellar evolution, where AGB stars play a crucial role since they are the obligatory passage between two groups of different evolutionary-stage types. From “pre-AGB” phases like the MS, the horizontal branch (HB) and the RGB on one side, to “post-AGB” ones, like the PN and the WD on the other. The transition that takes places is one between the nuclear burning life of a star that started at its formation and the cooling stage after nuclear reactions have totally ceased or are slowly extinguishing. The evolution of moderate-mass stars is often a sequence of long quiescent stages. It can be seen as a succession of hydrostatic equilibrium states. But the TP-AGB - this is also the case for another episode in stellar evolution, the violent He-flash - is not such a long and quiet stage; its development is brief, tumultuous and with a hydrodynamical evolution of the TPs. Furthermore, mixing processes and mass-loss events, that occur on the TP-AGB, are not well understood. For example, the mechanism responsible for these mixing processes is believed to be a combination of convection and rotation in the presence of magnetic fields (Herwig 2005a). But understanding of these workings is still very poor as they represent major unknowns of stellar evolution in general. During the TPs, mixing processes and nucleosynthesis of new elements will give AGB stars a different surface chemical composition than their progenitors and mass-loss will be determinant for their consequent evolution. The chemical signature at the surface will remain and be observable in the post-AGB phases. *In the next section, new updates included in our work, that are associated to three crucial physical processes relevant for the AGB, will be put forward and subsequently presented throughout this thesis.*

Whereas the evolution from the MS until the E-AGB is nowadays quantitatively well calculable, this is not the case for the TP-AGB, where, while sound qualitative interpretation is a fact, theoretical models still need to reach a more satisfying level of accuracy. The AGB represents a challenge in itself as it is a difficult phase to explain with accuracy because of different insufficiently well known physical processes which are brought into play under hydrodynamic conditions.

- Second, with respect to stellar populations. In terms of brightness, AGB stars mainly contribute to the luminosity of intermediate age stellar systems, and therefore are very important for the study of extra-galactic populations (e.g. Battinelli & Demers 2004). As evolved objects, they can give us information on the star formation history in other galaxies. The advantage of AGB stars as tracers of galactic history is that, in many galaxies, if you exclude some rare red supergiants, they are the brightest red stars and have their peak luminosity in the near-infrared, where interstellar extinction is negligible. But descendants of AGB stars, such as PNe, can also be used to probe distant populations. For example, through the use of its luminosity function, in nearby galaxies as far as 20-25 Mpc, the PN phase has been suggested as an excellent standard candle cosmological distance indicator (Ciardullo 2003), and AGB and post-AGB tracks are one of the inputs in synthetic planetary nebula luminosity function simulations (Marigo et al. 2004). Furthermore, the enrichment of the interstellar matter, through the envelopes high mass-loss rates on the AGB, gives us an estimate on the contribution by moderate-mass stars to the chemical evolution of galaxies and globular clusters. The analysis of PN abundances can constrain the AGB models and the environment at the time of the formation of the AGB progenitors.

  AGB stars are an important indicator of distant, galactic or extragalactic, populations. Whether it is simply by observing a large amount of AGB star or by studying the resulting output of combined stellar model grids, AGB stars constitute a tool that serves two purposes: the exploration of galactochemical evolution and the investigation of the collective light emitted by stellar populations.

- Third, with respect to the origin of the elements. The s-process - i.e. the slow, compared to the competing β-decay, neutron capture mechanism which forms neutron-rich isotopes heavier than iron (Clayton 1968) - is responsible for the production of half of all elements with a mass number higher than 90 (Arlandini et al. 1999). The nuclear production site, as agreed both by theory and observations, of the majority of the s-process elements (90 < A < 204), resides in low-mass AGB stars. After their production, elements are mixed to the atmospheres surface by a series of convective

> mixing events regulated by the TPs, and later ejected in the interstellar medium by the high mass-loss.
>
> Studying in detail the nucleosynthesis that goes on in AGB stars is one way to better understand how some nuclei are formed in the Universe. As s-process elements are also found in meteorites, AGB stars play a important role in a field where nuclear physics, astronomical observations, laboratory studies of meteorites, and theoretical stellar evolutionary models all come together.

Because of the high level simulations and quality observations available, the AGB offers an ideal interplay between observation and theory. With data from telescopes and stellar evolution models both being used to tackle different questions, the three areas mentioned earlier can be investigated in a complementary way.

The amount of high quantity and high quality observational data is continuously increasing. For AGB stars in particular, where most of the radiation emitted is in the infrared spectral region, with the IRAS (Infrared Astronomical Satellite) and ISO (Infrared Space Observatory) satellites, the number of observational data has experienced a huge rise because spectrophotometric studies in wavelength regions not accessible from the ground have become feasible. Continuous flux spectra are now easily obtainable for many stars in the range stretching out from the visual to the far infrared. More and more emission or absorption features in spectral lines and bands from silicon monoxide, carbon dioxide, carbon monoxide, water vapor and from other atoms, molecules, dust components as well as polyaromatic hydrocarbons are systematically being studied.

But theoretical understanding is actually behind in this field and progress is necessary if the scientific community wants to be able to keep up and fully take advantage of all the experimental data available (Herwig 2005a). The work presented in this thesis focuses on theoretical models.

It is true, that the general theory on AGB evolution is well understood and that the principal features have been established by many reviews over the last 20 years. Nowadays, one cannot discuss the AGB without the use of words (which will be clarified in the next chapter) like, thermal pulse, mass-loss, third dredge-up, pulse-driven-convective-zone, nucleosynthesis, hot-bottom-burning, s-process, ^{13}C pocket etc. TPs, mass-loss, third dredge-up and the importance of AGB nucleosynthesis were already presented by Iben & Renzini (1983). Later, Lattanzio & Boothroyd (1997) and Blöcker (1999) reviewed the status on hot-bottom-burning and improved the quantitative description of the evolution. Mass-loss and s-process topics have also been separately dealt with in detail by Willson (2000) and Busso et al. (1999).

Nevertheless, major unanswered questions persist and possible improvements in the physics and the numerical description of the models are of considerable importance. One such question is the crucial effect on TP-AGB models of varying surface molecular opacities with different carbon-rich compositions. Marigo (2002) in an effort to address this concern, presented in a simplified approach, new opacity calculations that she applied to synthetic AGB models. While the results of this first attempt confirmed the necessity of such work, more rigorously determined complete opacity tables coupled to detailed evolutionary calculations are still awaited because models require a high degree of complexity which has not yet been reached. More generally, in the latest review on AGB stars, Herwig (2005a) points out major issues that remain unsolved and greatly restrain higher quality modelling. The physics of mixing and the mass-loss prescriptions are two main ones.

Full AGB evolutionary calculations are expensive. The computation of such models requires important computer power as high numerical resolution and considerable computing time is needed. Computational times are even longer when one wants to build grids of models with varying parameters (e.g. initial mass, composition) where hundreds of thousands of models for each sequence are necessary.

For these reasons, what are called synthetic AGB models, have also been produced (Renzini & Voli 1981, Marigo et al. 1996, van den Hoek & Groenewegen 1997). These were more of a necessity in the past when time consuming detailed models could not be carried out. Today they are still useful for many reasons. Synthetic AGB models describe the evolution by analytical formulas fitted to the quantities obtained from detailed stellar tracks. On the contrary, the entire set of stellar structure and nuclear energy generation equations is solved in detailed stellar models, which means they parameterize physical processes. Using synthetic AGB models is a defendable cause for specific goals and under precise conditions, and of course computation rapidity is their big advantage. For instance, because they are well adjustable with observations, synthetic models can reproduce observed quantities better. Put aside the obvious fact that they are by definition approximative, their negative aspect is that synthetic codes cannot be extrapolated to unknown regimes and full evolutionary calculations have to be done before hand. Only later is it possible to match observables in order to calibrate the synthetic models.

The increasing availability of computational resources constantly allow to simulate AGB stars with more and more detailed and realistic calculations. Even though synthetic models are still useful and will remain so, full evolutionary codes are starting to be more widely used. But grids in mass and chemical composition originating from detailed evolutionary models comprise too few cases. The only up-to-date example nowadays is the grid presented by A. Karakas (Karakas et al. 2002, Karakas 2003). It does however not include many recent improvements in the inputs physics.

In addition to the unresolved issues indicated by Herwig (2005a), detailed calculations remain problematic for another reason: the current numerical description of the models.

When TPs occur on the AGB the star goes through a hydrodynamic evolution. As most computer codes use a hydrostatic approximation approach, evolution during this phase is difficult to follow and convergence problems are an important concern independently of each codes different numerical architecture. Going through the last TPs poses complications. Calculations are often forced to stop, before the end of the TP-AGB (Karakas 2003, Herwig 2005b, Kitsikis & Weiss 2007) in the absence of a hydrostatic solution. When the calculations actually go through, the obstacle of convergence is encountered once more shortly after the departure from the AGB and during the post-AGB phase (Miller Bertolami & Althaus 2006): the evolution is stalled again. Imposed artificial modifications in the code (e.g. increasing the value of the mixing length parameter, removing thermal energy in the envelope) are often an inconvenient necessity in order to pursue calculations further until reaching a state where a hydrostatic solution is once more computable. For stars with an initial mass up to approximatively 2-3$M_\odot$, going through the entire AGB and post-AGB phases without any problems is more of an exception rather than the rule; the artificial modifications earlier mentioned often being needed. However, for stars with an initial mass higher than 3$M_\odot$, even with the above interventions, a successful run is very rare (Miller Bertolami & Althaus 2006), and not always trustworthy because it is unclear what the influence of the imposed changes on the evolution is.

1.2. Aim and Structure of the Thesis

In this thesis, as already mentioned, the focus will be on theoretical models. Specifically, detailed - not synthetic - TP-AGB and post-AGB tracks have been computed with the latest version of the Garching stellar evolution code.

From the beginning, the aim was to compute, by including the most recent improvements for the previous two phases of evolution, a large number of stellar tracks in order to produce a grid covering an ample section of the initial mass-composition parameter space.

The motivation of creating such a large grid is to supersede the currently available older ones. At the moment, there are basically two main references for such work in the literature: a) the more than ten-year-old tracks from Vassiliadis & Wood which comprise a TP-AGB (Vassiliadis & Wood 1993) and a post-AGB part (Vassiliadis & Wood 1994), b) the more recent models of Karakas from which only TP-AGB tracks (Karakas et al. 2002, Karakas 2003) are available. There are also other calculations (those of T. Blöcker, F. Herwig, etc), which however do not constitute complete grids; they rather only consist of a few single cases for stars with a specific mass and metallicity value.

The main use of such TP-AGB and post-AGB libraries, is to include them in population synthesis studies. These try to simulate the properties of larger systems by merging together the characteristics of many detailed individual stellar models. The planetary nebula luminosity function code of Marigo et al. (2004) and the population synthesis code for galaxies of Bruzual & Charlot (2003) are two examples. Both still use the tracks of Vassiliadis & Wood but note that their work suffers from serious limitations due to the lack of more up-to-date TP-AGB and post-AGB tracks.

With this work, advancements are brought by incorporating in our code the most recent treatments of, mass-loss, low-temperature molecular opacities and mixing mechanisms at convective boundaries, none of which are present in the two currently available sets. Moreover, our wide initial composition interval is an additional improvement.

It is necessary to note that, the latest published synthetic TP-AGB models by Marigo & Girardi (2007) also form such an extended grid. They are furthermore the only ones that include comparable opacity ameliorations. But our tracks still offer considerable advantages beyond the obvious main one between detailed calculations and approximative ones. For instance, the way P. Marigo approaches the issue of chemically-variable opacities at low-temperatures constitutes a clear limitation. This is because of her adopted simplifications by using analytical fit relations in the opacity prescriptions and including a limited number of molecules. On the contrary, in our work, opacity tables originate from new detailed tables (Ferguson 2006) properly calculated for a large number of species over a large metallicity range.

Only very recently, which further shows the necessity and the increasing interest for such attempts, detailed TP-AGB models by Cristallo et al. (2007) have also been coupled to properly computed low-temperature opacity tables in a similar way to what we will present. However the applicability range of their work is limited since opacity tables solely corresponding to one specific metallicity value and only a single-mass stellar track have been computed.

We thus aspire to propose to the scientific community the most modern, with respect to both detailed and synthetic calculations, TP-AGB and post-AGB grid.

The structure of the thesis is straightforward. In chapters 2 to 5 the necessary background information and the important new input physics of our code are presented. In particular, Chapter 2 introduces the current theoretical understanding on moderate-mass stars, their observational characteristics, and finally the way numerical codes treat stellar evolution. In Chapter 3 the adopted mass-loss and convective overshooting prescriptions are detailed. Our new molecular opacity tables are the subject of Chapter 4. In Chapter 5 we expose the basic components of the Garching stellar evolution code and the input features important for the current calculations.

This first part will prepare the reader for the main undertaking of our work in the last three chapters (6-8), where the results of the calculations, in evolutionary order, “pre-AGB”, AGB and post-AGB phases, are analyzed and discussed.

2. Moderate-mass Stars[1]

2.1. Sketch of Evolution

The stellar formation process favored by observations is the collapse of a homogeneous interstellar gas cloud that becomes gravitationally unstable, into what is called a protostar. The future evolution of this protostar will depend on the mass of the collapsing cloud as, either high enough temperatures for the onset of nuclear reactions will be reached or gravitational collapse will be stopped by degenerate pressure.

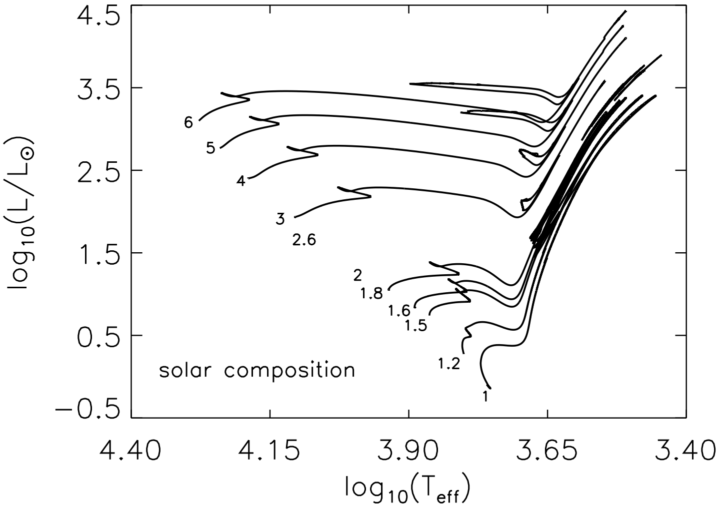

Figure 2.1.: HR diagram. Evolutionary tracks - from the ZAMS up to the E-AGB - for stars of various initial masses, from $1M_\odot$ to $6M_\odot$, with a solar-like chemical composition. Models are obtained with the Garching stellar code. $L_\odot$ is the solar luminosity.

Stars of large mass will go through all nuclear burning stages up to iron and finish their lifes as neutron stars or black holes. For stars of too small initial mass, the free electrons

---

[1] Similarly to the previous introductory chapter, the main references from the literature that have been used for the entire 2nd chapter are Wagenhuber (1996), Karakas (2003), Habing & Olofsson (2004) and Herwig (2005a). Unless particularly relevant, specific references are therefore not given for the most part. In section 2.1, the various scenarios are meant to give a first conceptual understanding in agreement with the accepted stellar evolution theory. The boundaries in $M_\odot$, separating stars that share similar properties, reflect in an approximative way the results of theoretical work. Exact boundaries are model-dependent.

of the ionized interior will stop the contraction through their degenerate pressure before hydrogen-burning temperatures are reached. Protostars of masses less than about $0.08M_\odot$ are forced by degeneracy to cool off to what is called a brown dwarf.

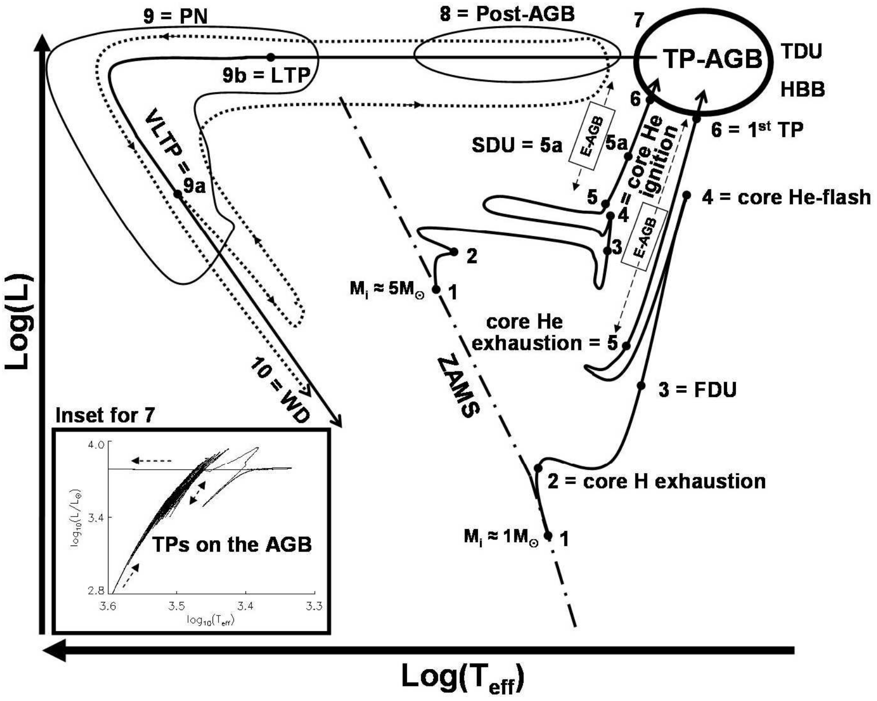

Figure 2.2.: Schematic parallel evolution of a $1M_\odot$ and a $5M_\odot$ star from the ZAMS to the WD stage. The different phases of evolution, as well as the main mixing episodes are indicated. For region 7, details are not shown to avoid overcharging the figure, but a $2M_\odot$ (solar composition) TP-AGB model calculated with the Garching Stellar evolution code is plotted in the inset. TPs are not clearly distinguishable: out of the 20 TPs only the last one is clearly visible. For the born-again scenario cases, the locations of both the LTP and VLTP are shown, but only one track (VLTP case, dotted line) is displayed for simplicity. [The plot is in part based on figures 2.4 and 2.5 from Habing & Olofsson (2004) as well as on figure 1 from Herwig (2005a) and figure 1.1 from Bernard-Salas (2003)]

When high enough temperatures are reached in the center, hydrogen to helium burning sets in and the luminosity of the protostar is no longer due to gravitational contraction but to nuclear energy. At that moment, the newly born star which is considered to be chemically homogeneous and in complete equilibrium (mechanical and thermal) is said to be theoretically located on the zero-age MS (ZAMS). The entire phase, beginning at the ZAMS and ending with central hydrogen exhaustion is referred to as the MS. The majority of a star's life is spent on the MS. Evidence for this statement is that most stars in the observed HR diagram of clusters or galaxies are found on the MS (e.g. Figure 1.2).

Moderate-mass stars are considered to have an initial ZAMS mass approximately between $0.8M_{\odot}$ and $10M_{\odot}$. All of them will begin their nuclear-burning life on the MS and end their lifes as WDs. Depending on their initial mass and composition their in-between evolution will differ. For instance, tracks from the ZAMS to the E-AGB, for stars of various initial masses are shown in Figure 2.1. Moderate-mass stars can be split into two groups: low-mass and intermediate-mass stars. One example from each group, respectively of $1M_{\odot}$ and $5M_{\odot}$, have been chosen here. We will follow their tracks through the HR diagram in order to illustrate the different evolutionary stages (Figure 2.2).

While on the MS (from point 1 to 2 on the tracks), the $1M_{\odot}$ star has a radiative core. The higher temperatures reached in the center of the $5M_{\odot}$ star, combined with the stronger temperature-dependence from the different prevailing hydrogen-burning nuclear reaction, causes a convective core to develop. After the exhaustion of central hydrogen (point 2), both stars leave the MS. They expand, start burning hydrogen in a shell around the inert helium core and move in the HR diagram towards lower effective temperatures and higher luminosities. They become giants for the first time. As they climb the giant branch, their outer layers become convective. The convection extends deeply inwards (in mass) from the surface. The envelope penetrates in the region where partial hydrogen-burning previously took place and material is brought to the surface. This event (point 3) is called the first dredge-up (FDU). As a result of the FDU, an increase in the surface abundances of ^{4}He, ^{13}C and ^{14}N, and a decrease in the ^{12}C abundances takes place. Although the star has so much expanded it can have up to a few hundred times the radius it had on the MS, the majority of its mass is concentrated in a core that represents only a small fraction on the total radius. On the contrary, the highly extended envelope contains a small percentage of the total mass and is not very firmly retained by the core. Parts of the envelope can thus be lost through stellar winds. The more time the star spends as a giant the more envelope mass will be lost. As the stars climbs the RGB, the helium core continues to contract and heat. At some point, core helium-burning starts (point 4). For the $1M_{\odot}$ star this ignition happens off-center in a violent way under degenerate conditions. This violent initial burning is referred to as the He-flash. For the more massive $5M_{\odot}$ case, a tranquil ignition of helium starts in the center, not under degenerate conditions. The mass-boundary between low- and intermediate-mass stars (those that do and those that do not experience the He-flash) is not precisely established by theory and depends on model details (e.g. composition). However, a $2M_{\odot}$ star is an indicative mark.

After the helium ignition, both stars contract and move to hotter and less luminous regions of the HR diagram where, while helium-burning proceeds in the core, hydrogen-burning is being pursued in a surrounding shell. The development and the amplitude of the loop towards higher temperatures in the HR diagram is regulated by the competition between these two energy sources. For the $1M_{\odot}$ representative case, the star is said to be on the HB (for low-metallicity stars with $M \lessapprox 1M_{\odot}$) or the red giant clump (for solar metallicity stars). During the core helium-burning phase, the $5M_{\odot}$ star crosses the well known Cepheid instability strip (this is true for stars with $M \gtrapprox 4M_{\odot}$).

Once central helium has been exhausted (point 5), in an analogous way to the end of central hydrogen-burning, the core contracts, the envelope expands, and the helium-burning location moves outwards into a thin shell surrounding the core. Meanwhile, the already existing hydrogen-burning shell continues its activity. The star ascends in the giant region of the HR diagram for the second time. The structure of the star has now adapted itself to a dual-shell onion-like configuration about the electron degenerate carbon/oxygen nucleus, with the helium-burning shell being the one immediately adjacent to the core. A convective envelope encompasses the whole. For the $5M_{\odot}$ case, the initial expansion of the star and the helium-shell ignition result at first in the extinction of the hydrogen shell. The inner edge of the convective envelope can then penetrate the temporarily inactive shell. Material of complete hydrogen-burning is brought to the surface in a way similar to the FDU. The surface abundances of ^{4}He, ^{12}C and ^{14}N are significantly altered. This event (point 5a) is called the second dredge-up (SDU). Only above a certain critical mass ($\approx$

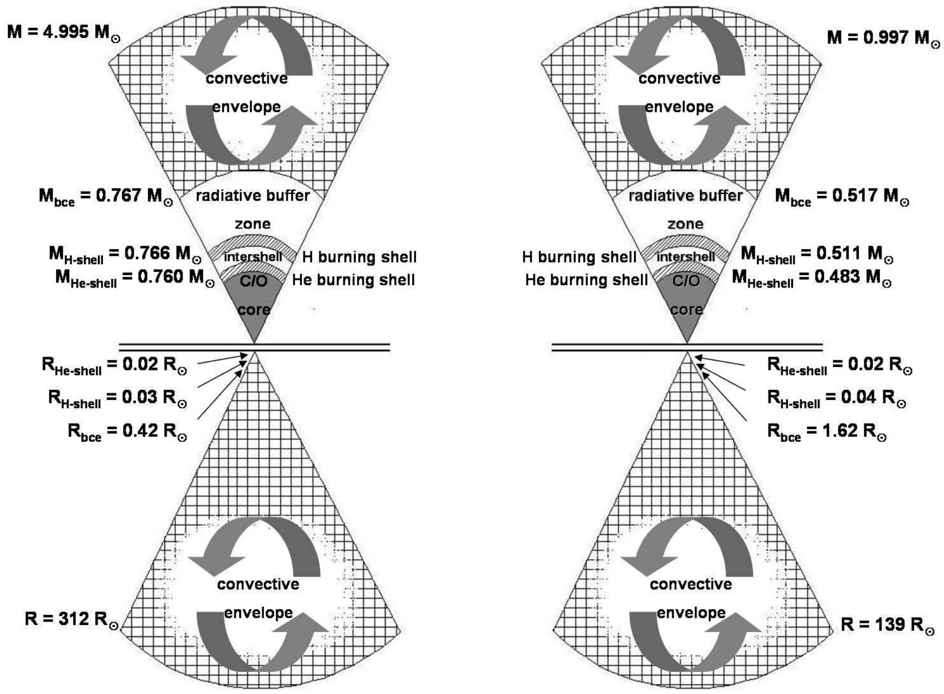

Figure 2.3.: Schematic view of the internal structure for two - $1M_{\odot}$ and $5M_{\odot}$ - AGB models just before the 1st TP. Both are calculated with the Garching stellar evolution code (no mass-loss and overshooting) for a solar-like chemical composition. Upper part: regions plotted against mass fraction. Lower part: regions plotted against radius. M_{bce} and R_{bce} are the mass and the radius at the base of the convective envelope. For the hydrogen- and helium-burning shells, the mass and the radius at the location of maximum energy release are taken. [graphical representation idea partly based on figures 2.6/2.13 from Habing & Olofsson (2004)]

$4M_\odot$) is convection able to penetrate deep enough below the hydrogen shell in order for SDU to occur. The SDU is therefore not present in the $1M_\odot$ where the convective envelope also moves inwards but where the hydrogen burning shell is not extinguished. After the SDU, the hydrogen burning shell is re-ignited and the evolution carried on.

This second ascend into the giant region corresponds to the AGB phase, which is customarily split into two parts, the E-AGB (points 5 to 6) and the TP-AGB (region 7).

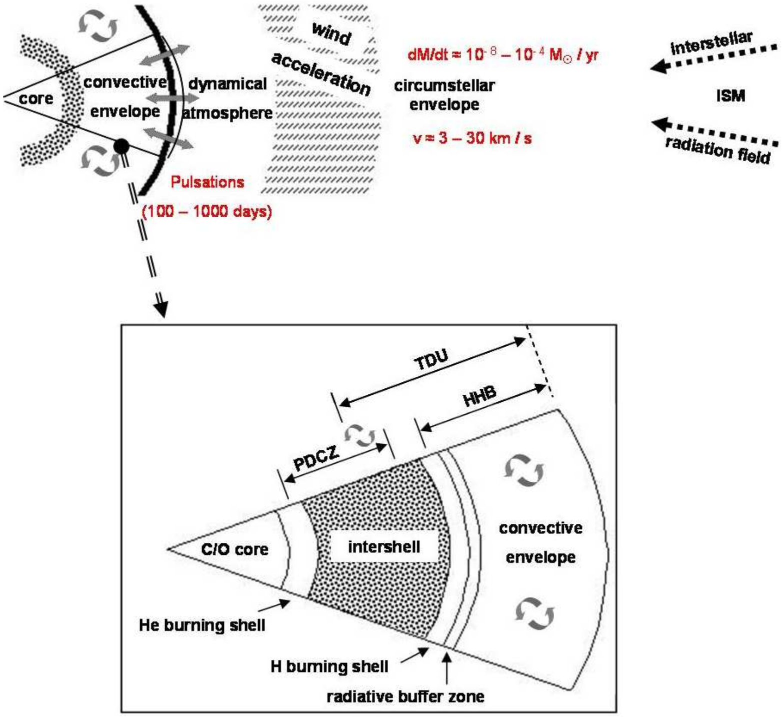

Figure 2.4.: Schematic onion-like shell structure of an AGB star (not drawn to scale). The inset is an enlarged view of the region consisting of the core, the two burning-shells and the envelope. The periodically occurring TDU (third dredge-up), HBB (hot-bottom-burning) and PDCZ (pulse-driven-convective-zone) events are also shown. [Adapted from figure 1.1 from Habing & Olofsson (2004) and figure 1.2 from Karakas (2003)]

Conceptually, the structure of all stars on the AGB is similar. In Figure 2.3 and in the inset of Figure 2.4 the interior configuration of such a star is illustrated. While the region including the core and the two burning shells accounts for an important part of the entire mass (respectively 15% and 52% for the $5M_\odot$ and $1M_\odot$ models in Figure 2.3), its radius extends only over an insignificant fraction of the stars total radius (0.1% and 1%). On the contrary, the convective envelope makes up for more than 99% of the radius. We are in the presence of a small, compact and massive core surrounded by an extremely dispersed envelope. On top of the envelope rests a tenuous and warm atmosphere (Figure

2.4). Further out one finds the more diluted and cold circumstellar envelope (CSE) formed around the star from material removed by the stellar wind. Thus, the main parts of an AGB star, are in order of increasing radius, the core, the envelope and the atmosphere. Each region has very different characteristics. Furthermore, if we add to the previous three components the CSE and consider the entire system as a whole, the physical scales covered are extremely wide. The temperature changes by 7 orders of magnitude, the radius by 10 and the density by 30 (Habing & Olofsson 2004).

On the E-AGB both shells peacefully coexist, with the helium one initially dominating the nuclear production. But as this shell burns outwards in mass, it declines in luminosity because the He intershell layer becomes thinner; on the contrary the hydrogen-burning shell intensifies its activity. At some point the nuclear energy release starts to be dominated by hydrogen-burning. In addition, the helium-shell will not evolve smoothly for long, as it is unstable with respect to small temperature changes. Indeed, thermal instabilities start periodically to arise in this innermost shell. These instabilities result in the so-called flashes or thermal pulses (TPs). When the first TP occurs the star is no longer said to be on the E-AGB but on the TP-AGB.

The TP-AGB evolution will experience many of these short TPs separated by long interpulse phases (Figure 2.5). During the interpulse phase, the helium-shell source (e.g. $L_{\mathrm{He}} \approx 10^2 \mathrm{L}_\odot$ for a $2.6\mathrm{M}_\odot$ star - Figure 2.5) contributes only a little to the surface luminosity, the hydrogen-shell (e.g. $L_{\mathrm{H}} \approx 10^5 \mathrm{L}_\odot$ for a $2.6\mathrm{M}_\odot$ star - Figure 2.5) dominates the energy production, and the star's total luminosity is almost completely supplied by the hydrogen transformed into helium in the outer shell. Consequently the helium intershell grows. Helium is progressively compressed and heated until temperature and density become high enough that strong burning (e.g. $L_{\mathrm{He}} \approx 10^6 \mathrm{L}_\odot$) is triggered in the helium-shell underneath: a TP occurs. The new rapidly produced carbon is then added to the mass of the core. During this short intermission the star goes through a luminosity modulation, while the hydrogen-shell is inactive (e.g. $L_{\mathrm{H}} \approx 10^{-10} \mathrm{L}_\odot$). Between TPs the star burns again hydrogen. The basic physical explanation for a TP is the following.

The helium-shell source reacts to the surplus energy with an initial small temperature increase which immediately results in a thermal runaway. This thermal instability arises because of the coupling of two effects: 1) the high temperature sensitivity of the 3-α reaction, 2) the "thinness" degree of the shell. When temperature rises, both the rate of nuclear energy production as well as the rate of energy loss from the shell increase. For an instability to occur, the energy input has to be greater than the energy loss. The energy generation of the helium-shell is mainly driven by the 3-α reaction for which the production rate per gram is $\propto \rho^2 \mathrm{T}^\nu$ with $\nu \approx 30 - 40$. This large value of ν guarantees a large increase in nuclear energy production for a modest temperature rise. In addition the thin shell is on one hand thick enough so that the energy loss is not very important (because the gradient of the perturbed temperature from the center of the shell to the edge depends on its size: the thinner the shell, the larger the outflow of energy), and on the other thin enough (thickness/radius $\ll 1$) so that the extra added heat, deposited then at constant pressure, leads to a further increase of temperature and rapidly to a thermal runaway.

The above requirements for the instability of the shell hold even for a perfect gas. Electron degeneracy present in the interior regions of AGB stars is not necessary but it enhances the mechanism (Habing & Olofsson 2004). The combination of this well-known thin-shell instability and partial degeneracy is not only present on the AGB, but it is a common feature in nuclear shells around degenerate cores. Other example are accreting WDs (novae), He-core WDs and accreting neutron stars (X-ray bursts).

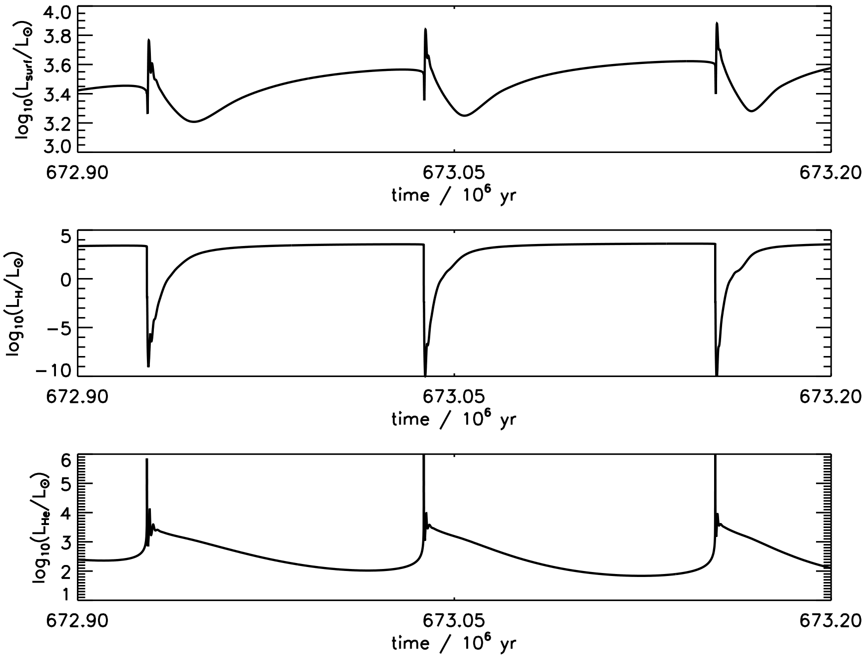

Figure 2.5.: Evolution on the TP-AGB. *From top to bottom* - Plotted against time: total surface luminosity and luminosities of the hydrogen- and helium-burning shells. Three TPs are clearly visible. Data is from a 2.6M$_\odot$ model, with solar-like chemical composition, computed with the Garching stellar evolution code.

Most of the suddenly released energy is used up by the expansion of the layers above. This envelope expansion reduces considerably the temperature in the hydrogen-shell: it cools and L_{H} decreases significantly. The thermal runaway accelerates until reaching a sharp peak. The helium-shell is then widely expanded and therefore no longer thin and unstable. The whole region starts to contract again, the hydrogen-shell is heated up and regains its large energy production. During the interpulse phase the star asymptotically recovers its original overall structure and luminosity. The process starts all over when the helium-shell becomes unstable again.

Like on the RGB, but with a rate orders of magnitude higher, matter from the loosely bound envelope is gradually expelled, through mass-loss events, and a CSE is formed. Towards the end of the TP-AGB, the mass-loss rate is much intensified and the AGB terminates when the entire envelope is ejected from the core.

Mixing episodes similar to the FDU and SDU may occur during the TP-AGB: the so-called third dredge-up (TDU) events (inset of Figure 2.4 and Figure 2.6). The TDU brings the products of partial helium-burning, mostly ^{4}He and ^{12}C, to the stellar surface but also heavier s-process elements. When TDU occurs and the top layers are enriched in carbon, the ratio of the number fraction of carbon to oxygen grows from an initial value below 1. At the moment this ratio reaches and exceeds unity, the AGB star is called a carbon star. The effect of the TDU is closely coupled to another mixing event that occurs deeper inside the star. A convective zone periodically appears in the region found in between the two burning shells. During the TP, when the helium shell starts burning very strongly, the energy deposited cannot be transported by radiation alone, and this pulse-driven-convective-zone (PDCZ) develops immediately above the helium-shell region, and almost reaches the hydrogen-shell at its maximum extent (Figure 2.6). With the decline of helium-shell burning, the PDCZ disappears. During its short existence, the PDCZ, which homogenizes most of the intershell region, will bring material from the helium-burning shell to a region closer to the surface below the hydrogen-burning shell. From there, if later the bottom

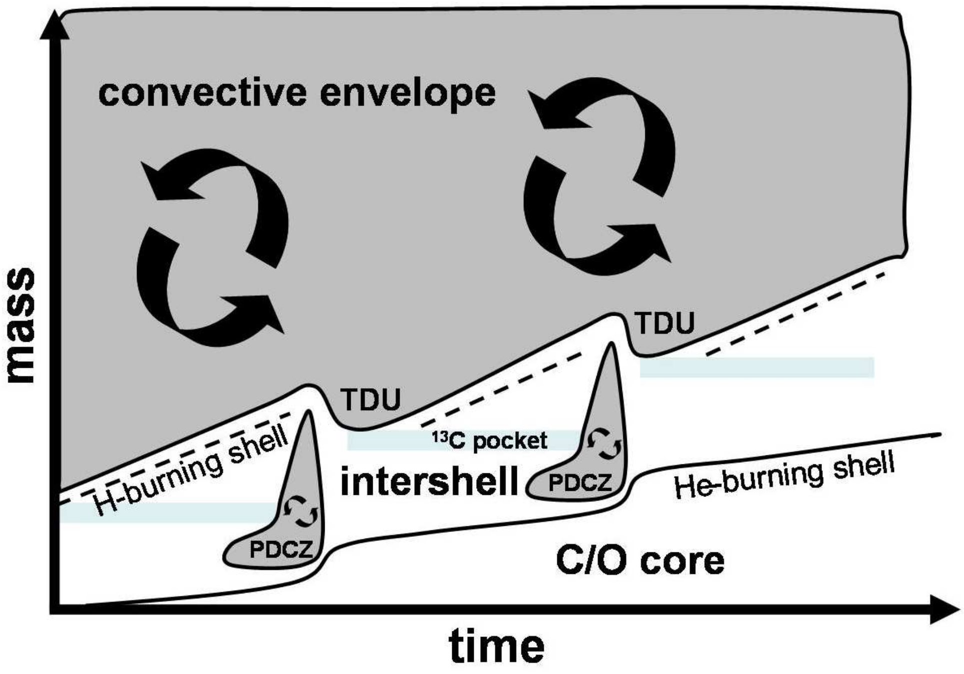

Figure 2.6.: Schematic representation (in mass) of the intershell time-evolution between two TPs. The figure is not to scale. The areas shaded in gray correspond to convective regions. The ^{13}C pocket is produced during the TDU, and provides the neutrons for s-processes to occur. [sketch idea based on many available figures in the literature (e.g. Habing & Olofsson 2004)]

of the envelope is able to reach down during the TDU, material can be dredged-up to the surface. When TDU occurs, in addition to the carbon, s-process elements are mixed-up as well and their presence in the atmosphere of AGB stars is confirmed by observations.

It is the slow neutron capture taking place in AGB stars that produces these so-called s-process elements. This mechanism (slow with respect to the competing β-decay) is responsible for the formation of neutron-rich isotopes heavier than iron (Clayton 1968). In order for s-process to occur in the intershell, neutrons need to be available in sufficient number, and a neutron source is necessary. A good candidate is the ^{13}C(α,n)^{16}O reaction. But an adequate amount of ^{13}C to produce the required number of neutrons is a priori not readily available. A specific mechanism that generates ^{13}C must therefore exist. Currently, the general consensus is that during the TDU, a non-negligible amount of ^{13}C is deposited at the bottom of the envelope, forming a region enriched in ^{13}C, the so-called ^{13}C pocket (Figure 2.6). According to Habing & Olofsson (2004), there seems to be no doubt on the existence of such ^{13}C pockets in real stars, but the responsible mechanism is still uncertain. Nevertheless, the general idea is the following.

Because of the energy released by the TP, the star expands, the outer edge of the PDCZ is pushed outwards to low enough temperatures ($\approx$ 1 million K), the carbon atoms at the top of the intershell begin to recombine (Sackmann 1980, Iben & Renzini 1982b,a), a serious opacity change occurs and finally a small partial mixing layer is formed at the interface between the bottom of the hydrogen-rich envelope and the ^{12}C-rich intershell. The necessary protons and ^{12}C are therefore simultaneously available. This happens during the dredge-up phase when the hydrogen-burning shell is extinguished and the envelope, reaching its lowest mass coordinate, has penetrated into the intershell. The important consequence of this extra mixing is that protons are carried downwards into the intershell. Currently, there are three processes proposed in the literature (Herwig 2005a) that try to explain how this partial mixing takes places: exponential diffusive overshooting (Herwig et al. 1997, Herwig 2000), rotation-induced mixing (Langer et al. 1999) and mixing through internal gravity waves (Denissenkov & Tout 2003). Anyhow, the key point is that, during the subsequent interpulse phase when the star contracts and heats again, the protons captured by ^{12}C temporarily form ^{13}N which is then transformed into ^{13}C by β-decay.

A second important phenomenon, related to envelope convection that can occur during the TP-AGB phase and that is also responsible for changes in surface composition, is given the eye-catching name of hot-bottom-burning (HBB). The convective envelope extends so deep into the interior that it reaches the top of the hydrogen burning shell where temperatures are high enough for nuclear processing. This convective envelope burning occurs during the interpulse phase and becomes important when the temperature at the bottom of the convective envelope exceeds 50 million K. Between the hydrogen-burning shell and the convective envelope, a radiative buffer zone can exist, in which case models do not experience HBB. When this zone disappears for more massive models, HBB occurs. In practice, this happens for stars of masses larger then $\approx 5\mathrm{M}_\odot$. One consequence of HBB is to counteract the effect of the TDU by burning the ^{12}C brought to the surface into ^{13}C and ^{14}N and thus hinder/delay the formation of carbon stars or revert carbon stars back to oxygen-rich ones.

The burning in both hydrogen- and helium-shells, the TDU, the PDCZ, the HBB, the ^{13}C pocket, the s-process element production, can regularly occur and are modulated by the periodicity of the TPs. Understanding the evolution on the TP-AGB amounts to correctly appreciating the interplay between each of the above phenomena.

As the star continues to lose mass, increase its mean luminosity, decrease its average temperature, while regularly going through the TP-cycle variations, it reaches a moment, on the tip of the AGB, when the hydrogen-rich envelope mass surrounding the core is too small to maintain its large radius any longer and the star begins to contract. The AGB phase has effectively come to an end. The star enters the post-AGB evolution (region 8).

From this moment on, the evolution, in the most simple, general and common case, is the following. The two burning-shells surrounding the core continue their activity as in any of the previous interpulse phases on the TP-AGB. The luminosity of the star remains constant but the temperature increases as the mass of the remaining small envelope decreases while layers close to the core become exposed. In the meantime, the ejected envelope cools and expands slowly, revealing the central star. From the low temperatures it had reached, the star horizontally crosses the HR diagram. When the temperature reaches $\approx$ 30 000 K the star enters the PN phase (region 9). The now called central star of the planetary nebula (CSPN) illuminates from beneath the ejected matter which, if it is still dense enough and sufficiently close to the star, shines as a PN. Meanwhile the mass of the remaining envelope is constantly being reduced. There are two reasons for this reduction: mass-loss at the surface and hydrogen nuclear burning from below. At some moment there is not enough mass left in the envelope in order to maintain a temperature high enough for nuclear reactions to occur below. Nuclear processes cannot be sustained any longer. The hydrogen- as well as the helium-burning shells gradually die away and the luminosity decreases. The star finds itself on the upper part of WD cooling track. Depleted of nuclear energy, its temperature and luminosity will continuously decrease, illuminating less and less the increasingly tenuous expanding ejected envelope. All remaining PN phenomena will permanently fade away. The star is on its way to becoming a WD (region 10). As a WD, it will slowly cool off until thermal equilibrium with the external medium is reached and disappear from the visible universe in the form of a cold dark object.

In this first undisturbed evolution, off the AGB, through the PN phase and onto the WD cooling track, the surface abundance of the post-AGB star is a reflection of the stars envelope composition when it leaves the AGB.

Aside from this simple scenario, which is also the most common, other ones have been proposed and encountered in theoretical models. Their occurrence depends on the specific moment during the TP-cycle the star will move off the AGB due to the envelopes reduction.

The fraction of the time span between two subsequent TPs, is the phase of the TP-cycle. The phase at which the star leaves the TP-AGB determines the nuclear burning regime of the post-AGB star. One talks of hydrogen- or helium-burners depending on the predominant source. In all cases both hydrogen- and helium-burning shells coexist but with different relative contributions to the total luminosity. On average, when a star leaves at a phase between 0 and 0.15, it is a helium-burning post-AGB star as it departs just after the TP when the helium-burning luminosity is still very high and hydrogen-burning has not effectively re-ignited yet. If the phase of departure is between 0.15 and 0.3, both shells equally contribute. Finally, for phases between 0.3 and 1 the star is a hydrogen burner with a dominant hydrogen-burning shell.

The TP-cycle phase will also determine the type of post-AGB track in the HR diagram. Indeed, during the post-AGB or PN phases, occasions can occur in which a final TP is experienced. If the TP occurs on the horizontal part of the track in the HR diagram (point 9b), we are in the presence of a *late* TP (LTP). If the star is already on the WD cooling track (point 9a) one talks of a *very late* TP (VLTP). In both cases the envelope rapidly expands again and the star finds itself once more on the AGB, as a *born-again* AGB star. Because a TP occurs, the star is transformed from a hydrogen- to a helium-burning model. A characteristic track of such evolutions is shown in Figure 2.2.

Whether no TP, a LTP or a VLTP occur, depends on the ratio of three time scales that come into play at this point (Herwig 2001a): the TP-time, the H-burning time and the He-burning time. The TP-time is the time, starting from the departure from the AGB, it would take for the next TP to occur in a standard, uninterrupted by mass loss, TP-AGB evolution. The H-burning time is the rate at which the envelope on the post-AGB is reduced due to mass-loss and hydrogen-shell burning. The He-burning time is the time it will take for all nucleosynthesis to stop, including the helium shell burning, on the WD cooling track.

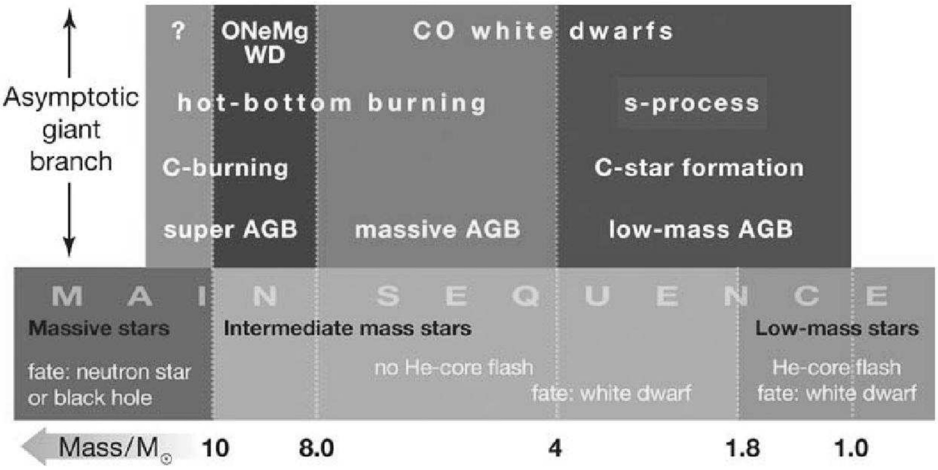

Figure 2.7.: Classification of stars by mass on the MS and on the AGB. This figure is taken from Herwig (2005a) - it corresponds to figure 2 of the paper.

When the stars leaves the AGB at a low cycle phase, the TP-time is by far longer than the He-burning time and the star ceases all nuclear burning on the WD track before the next TP is expected. For higher cycle phases, the TP-time is still larger than the H-burning time but shorter than the He-burning time. In this circumstance a VLTP occurs. Finally for even later phases a LTP occurs on the horizontal part of the HR diagram track. After being on the AGB for the second time, the star evolves in a regular way towards the WD phase.

In the born-again AGB scenario, the hydrogen of the envelope, originally in majoritarian proportions, is burned or mixed with hydrogen poor material from the inner parts. The result is a hydrogen deficient post-AGB star.

The fate of moderate-mass stars with respect to their initial MS mass, has been split, by the recent review of Herwig (2005a), into various categories. This classification is reproduced in Figure 2.7. It summarizes well the current theoretical understanding of AGB evolution.

2.2. Observational Characteristics

2.2.1. AGB Stars

This work focuses on the theoretical study of AGB stars. But it is also necessary to have an idea of their observational characteristics. How do we practically recognize an AGB star through a telescope? How can such a red giant star be distinguished from other neighboring stars found in the same region of the HR diagram?

In the globular cluster example of M3 (Figure 1.2), the differences are small, but one can demarcate some of the AGB stars. This is not always the case as making a clear separation between RGB, supergiant and AGB field stars only through absolute magnitude and color can often be difficult. Nevertheless, one way to recognize them through absolute magnitudes is to use the tip of the RGB. The RGB has a maximum luminosity that is well explained by theory (He-flash). Observationally it can often be well determined, in the Magellanic Clouds (Cioni et al. 2000) for example. Westerlund (1997) gives $M_{bol} \approx -3.9$ or $L \approx 2500 L_{\odot}$. Thus, put aside the very rare supergiants, stars more luminous than the tip of the RGB must be AGB stars. Below the tip, other properties have to be used.

Three features that characterize AGB stars come forward right away: the TPs, the long-period pulsations and the mass-loss rate. The stellar spectrum gives us information on the surface composition and on the mass-loss rate. The surface luminosity variations allow us to study the periodic pulsations.

Let's consider the first feature: the TPs. It is impossible to observe a full TP-cycle, and directly recognizing a TP by catching a star at the beginning of a pulse during the spike of high luminosity is very improbable. Instead, an observable effect related to the TP cycle, the surface composition variation, is used. Often the surface shows overabundances of carbon, s-process elements and nitrogen. These chemical enhancements are a direct consequence of the TDU and HBB.

The goal here, is not to give a detailed discussion of spectroscopic criteria (Jascheck & Jascheck 1987), but to place the AGB stars in the more general context of stellar objects that have unusual surface compositions, and in particular enhanced amounts of carbon and s-process elements. If one takes low resolution optical spectra of luminous cool giants, two main groups appear: the M stars and the C stars. In the spectrum of M stars, the TiO molecule bands prevail, while it is the C_2 and CN bands that dominate in the C star spectrum. This distinction reflects the amount of carbon present at the surface of the stars which results in different values of the C/O number ratio. The M stars' surface has a

C/O ratio less than unity and for the C stars it is higher than 1. The CO molecule is the molecule in the atmosphere of cool stars that has the highest binding energy. Almost all atoms of the least abundant element (C or O) are used to form CO. When C/O<1 there is a surplus of O and when C/O>1 there is a surplus of C. The remaining atoms of the most abundant element are going to form other molecules. If O is the most abundant, TiO molecules will be formed, if C is the most abundant atom, C_2 and CN molecules will be formed. More generally, metallic oxides are present in M stars and carbon compounds in C stars. The M and C case, being respectively the giants stars with the lowest and the highest carbon content, constitute the two extremes in the sequence of the increasing C/O ratio values from below to above unity. Other spectral types with varying degrees of carbon enhancement lie in between. In these intermediate transition cases where C/O≈1, almost all the available carbon and oxygen is locked up in the CO molecule and no material is left to form many carbon compounds or metallic oxides. S stars also have some carbon enhancement (Scalo 1976, Smith & Lambert 1990) but with a C/O value below 1. SC stars have C/O≈1 (Ohnaka & Tsuji 1996). The amount of surface carbon increases along the spectral sequence: M, MS, S, SC, CS, C (Abia et al. 2003). In the general carbon case, not necessarily for AGB stars, alternative spectral classes also exist: the N, R (Dominy 1985, Knapp et al. 2001), J and CH-type stars. The older spectral classifications N and R are nowadays less used as they have been more or less replaced. The N-type giants have a C/O >1 (Keenan & Boeshaar 1980, Ohnaka & Tsuji 1996) and are actually the equivalent of the C stars. The R-type are believed to be tip-RGB or HB stars, they are clearly not on the AGB. The reason for their carbon enhancement is still debated (Fujimoto 1977, McClure 1997). The J-type stars are possibly AGB but they do not have the same spectral signature as the N-type stars (Abia & Isern 2000). The origin of their carbon enhancement is also uncertain.

Low resolution spectra of luminous cool giants can also show enhanced bands of molecules involving s-process elements, the S stars. A well established case is the ZrO molecule which characterizes S stars. Stars with TiO and ZrO bands are MS stars. The N(or C)-type stars also show overabundances of s-process elements (Smith & Lambert 1986, 1990).

The interstellar medium and the atmosphere of *normal* stars have a C/O ratio smaller than 1 and no enhancement of s-process elements. The overabundances in carbon and s-process elements is believed to be the direct result of the TDU, and the M, MS, S, SC and C (or N-type) giants are most likely TP-AGB stars. For the C and S stars mass transfer from a binary might also be the cause of the particular composition, in which case they might not be on the AGB.

Another direct observational evidence for mixing and heavy element nucleosynthesis in AGB stars, was the detection of technitium (Tc) by Merill in 1952. Tc was found in many, predominantly S type, stars. Technitium (Little-Marenin & Little 1979) has no stable isotope. The longest lived isotope is ^{99}Tc which is produced by s-process and is presumed to be the one observed in AGB stars. Since ^{99}Tc has a half-life of about $2{\cdot}10^5$ years its presence at the surface means it has been produced and brought from the nucleosynthesis site to the surface in a relatively short time comparable to the TP-cycle period.

The second criterion, used to recognize AGB stars, is their long-period pulsations.

Stars that have a long period variation of their flux are called long period variables (LPVs). The *General Catalogue of Variable Stars* (Kholopov 1987) classifies the LPVs in 4 classes. The Mira-like (*M*) which have regular variations with a large amplitude in the V-band. The Semiregulars of type a (*SRa*) with relatively regular variations but with a smaller amplitude in the V-band. The Semiregulars of type b (*SRb*) have poor regularity with a small amplitude in the V-band and the Irregulars (*L*), irregular variations at low amplitude. The theory for LPVs is not well developed and mostly based on empirical information. The separation between the different classes is actually based on how the light curves in the optical look like and is far from sharp.

Observations of red giants in the Magellanic Clouds and globular clusters show that Miras have on average a magnitude $M_{\mathrm{bol}} < -3.9$, which corresponds to AGB stars. Semiregulars seem to have luminosities similar to Miras. Actually most AGB stars are believed to be LPVs. The ones that do not pulsate are either entering the E-AGB phase but are still relatively faint or are on their way to the post-AGB phase and are too hot.

The measured high mass-loss rates are the third important characteristic of AGB stars.

As they lose mass, the CSE is formed. If the mass-loss rate is small than the CSE manifests itself as a weak infrared excess on top of the expected stellar flux. When it is heavy, the CSE obscures totally the star which is then almost undetectable at optical wavelengths; its energy is mainly radiated in the infrared. The star appears then as a low-temperature, high luminosity object, resembling a lot to a protostar. Objects with mass-loss rates higher than $10^{-7}\mathrm{M}_{\odot}\ \mathrm{yr}^{-1}$ are AGB stars, supergiants or Luminous Blue Variables (LBVs). The supergiants and LBVs are rare, easily recognized and removed from any sample. It is often automatically assumed that all AGB stars with a rate higher than $10^{-7}\mathrm{M}_{\odot}\ \mathrm{yr}^{-1}$ are TP-AGB stars. As the large majority of such stars are also LPVs, and as we have seen most AGB stars are also LPVs, this interpretation of the data is rightly acceptable.

Objects which are the result of very strong mass-loss are the OH/IR sources. These objects are thought to be M-type stars enshrouded by a thick CSE at the tip of the AGB. This CSE can be detected through its infrared emission - circumstellar grains re-emitting central stellar luminosity - and radio maser (microwave amplification by stimulated emission of radiation) emission from the OH molecules at 1612 MHz or H_2O molecules at 22 GHz. The current picture given by observers is the following. Mira variables are optically visible AGB stars with pulsation periods between 200 and 800 days, and mass-loss rates between 10^{-8} and $10^{-6}\ \mathrm{M}_{\odot} \cdot \mathrm{yr}^{-1}$. The OH/IR stars are closely related to Miras but their range of properties are extended (Deacon et al. 2007, Chapman et al. 1995) as they correspond to a more evolved AGB phase. They have periods between 300 and 3000 days, mass-loss rates between 10^{-7} and $10^{-4}\ \mathrm{M}_{\odot}\cdot\mathrm{yr}^{-1}$ and thicker CSEs. These OH/IR stars have infrared colors and luminosities that are consistent with their classification as AGB stars. When the cloud around the OH/IR source becomes optically thin, the central star, on its way to becoming a post-AGB object has a characteristic spectrum of a F or G giant (Carroll & Ostlie 1996).

Summing up all of the above, as a general rule one can say that stars in the giant region of the HR diagram that show one or more of the following features, have good chances of being AGB stars:

- a luminosity higher than the tip of the RGB
- a mass loss rate higher than $\approx 10^{-7} \mathrm{M}_{\odot} \cdot \mathrm{yr}^{-1}$
- LPV characteristics
- a specific spectral type (mainly M, S or C)
- OH/IR characteristics

2.2.2. Post-AGB Stars and Planetary Nebulae

Observationally it is difficult to classify which objects can be classified as post-AGB stars. In many cases only information about the CSE, which obscures the central star, is available. For low temperature post-AGB stars which are close to the tip of the AGB and have also a thick CSE, the distinction between a post-AGB and a TP-AGB star is often very difficult. Thus, both the circumstellar environment and the stellar properties must be examined when searching for post-AGB stars.

Using the luminosity class and the spectral type of the central star is one way of defining a post-AGB star (Oudmaijer et al. 1995). By comparison to theoretical tracks, stars with spectral types between K and B and with luminosity classes from I to III, should be on the post-AGB. A surface chemical composition baring the signature of TP-AGB evolution (because of TDU and HBB) is also a recognition criterion.

Observing the circumstellar environment is the alternative way. Many post-AGB stars have actually been classified as such from their infrared spectral energy distribution. It is characterized by thermal emission from cool dust, with temperatures around 100 - 200 K. In addition, during the early expansion of the CSE, the line-of-sight optical depth towards the central star is rapidly reduced and an optical counterpart in the spectrum is observed. A typical double-peaked spectral energy distribution is strong evidence for a post-AGB object.

The beginning of the post-AGB occurs when the mass of the envelope is reduced below some critical value and the star begins to cool: at which point the stellar pulsations that took place on the TP-AGB cease. Very early post-AGB objects can be isolated from the late TP-AGB ones by the absence of luminosity variations.

Not all post-AGB stars have a significant observable CSE, as low luminosity stars may take more time to increase their temperature then the CSE needs to dissolve into the interstellar medium. In those cases when a spectral type O is reached, there is no more material around to be illuminated and no PN is formed.

The RV Tau and the R CrB, are two classes of stars that have been classified as post-AGB object, based on their, chemical abundance, pulsation and/or circumstellar material properties.

Detecting post-AGB stars is quite difficult and their detection is influenced by strong selection effects. When using central star characteristics, it is easier to detect more visible objects with a small CSE and thus of smaller mass. If a circumstellar environment criterion is used, object with an enormous amount of material surrounding the star are favored, and these object might be the result of binary mass transfers. Finally, a clear distinction between the tip of the AGB where the still pulsating star is totally obscured by CSE and a star with a small enough envelope mass to have left the AGB and with no more pulsations but still showing characteristics of OH/IR objects for example, is not easy. The 22 GHz maser emission of OH/IR sources is now also being used to detect early post-AGB stars (Deacon et al. 2007).

The brightest PNe have a disk-like appearance, through a telescope they look like planets and reveal a great diversity of shapes. The name *Planetary Nebula* was given by W. Herschel in the 18^{th} century to objects of the Messier Catalogue which resembled Uranus, the planet he had discovered, and that could not be resolved into stars. The spectra of PNe is their more characteristic feature. In particular the optical spectrum greatly differs from the one of stars and other objects. The brightest emission lines in all PNe are the two lines of the doubly ionized oxygen at 5 007 and 4 959 Å (Gurzadyan 1997). PNe have various characteristics and can be divided into different classes according to their shape, the spectrum of the central star, the strength of their emission lines (excitation classes) and their chemical composition. Peimbert (1978) has divided galactic PNe into four types according to their chemical composition. The types I, II, III and IV reflect in this order the decreasing helium and heavy elements abundances. For example, type I PNe are He and N rich.

2.3. Numerical Stellar Evolution Models

Stellar evolution theory requires the solution of a set of partial differential equations. These consist in the basic four stellar structure equations coupled with the ones for the time evolution of the most important isotopes taking part in the nuclear energy production.

For a non-rotating spherically symmetric star with no magnetic fields, Kippenhahn & Weigert (1990) give the following equations in a one dimensional Lagrangian coordinate system:

- the equation of hydrostatic equilibrium,

$$\frac{\partial P}{\partial m} = -\frac{Gm}{4\pi r^4}, \tag{2.1}$$

  where P is the pressure, r the radius and m the mass contained within a spherical shell of radius r. The above equation is a simplification of the more general hydrodynamic equation of motion, $\frac{\partial P}{\partial m} = -\frac{Gm}{4\pi r^4} - \frac{1}{4\pi r^2}\frac{\partial^2 r}{\partial t^2}$. The equation of hydrostatic equilibrium, neglects the term with the second order time derivative and is valid when the evolution of a star is governed by thermal adjustments or nuclear reactions. This is a good estimate for most evolutionary phases but in principle, not for phases during which the star goes through a hydrodynamic evolution. In practice, this simplified equation is nevertheless the one always included as default in stellar codes that use a hydrostatic approximation approach.

- The equation of mass conservation,

  $$\frac{\partial r}{\partial m} = \frac{1}{4\pi r^2 \rho}, \tag{2.2}$$

  where ρ is the density.

- The equation of energy conservation,

  $$\frac{\partial l}{\partial m} = \epsilon_{\mathrm{n}} + \epsilon_{\mathrm{eg}} - \epsilon_{\nu}, \tag{2.3}$$

  where l is the luminosity, and where the entire right hand side, for which the explicit relations are not given here, is the total energy generation. ϵ_{n} represents the nuclear energy generation rate, ϵ_{eg} the energy generation rate from gravothermal sources and ϵ_{ν} the energy loss rate by neutrinos.

- The equation of energy transport,

  $$\frac{\partial lnT}{\partial m} = -\frac{\partial lnP}{\partial m}\nabla, \tag{2.4}$$

  where the specific expression for ∇ - not given here for simplicity - depends on whether the region of the star is radiative or convective.

Finally, if one neglects diffusion effects, and in the simple case of a radiative energy transport, the chemical evolution for I isotopes, each with mass fraction X_i and mass m_i, is only due to nuclear burning and governed by the following equations:

$$\frac{\partial X_i}{\partial t} = \frac{m_i}{\rho}\left(\sum_j r_{ji} - \sum_k r_{ik}\right), \quad i = 1, \cdots I, \tag{2.5}$$

In the above set of I equations, one of them can be replaced by the normalization $\sum_i X_i = 1$. The r symbols refer to nuclear reactions. The r_{ji} are the rates at which isotope j is transformed into isotope i and the r_{ik} the rates at which isotope i is burnt into isotope k.

Chemical composition in the star can also be affected by diffusion. Different types of diffusion exist: concentration diffusion, temperature diffusion and pressure diffusion. Although they are relevant in many cases and can be included in stellar codes, diffusion effects can also often be ignored because they are slow with respect to changes due to nuclear reactions.

The much more important effect of mixing brought by turbulent convective motions has also been discarded in the previous chemical evolution equations. The convective processes occurring in non-radiative regions are very rapid compared to the much slower changes due to nuclear reactions and even more rapid than the extremely slow diffusion processes. It is not discussed here for simplicity purposes, but convection is always considered in stellar evolution codes. Its consequence for the purpose of this work is to homogenize the composition in regions where it takes place. At the boundaries between radiative and convective areas, the physical treatment poses many problems: the *overshooting* phenomenon, important for our models will separately be dealt with in Chapter 3.

The mass m and the time t are the two independent variables of the system presented above (Equations 2.1-2.5). In order to solve this set of partial differential equations it is necessary to specify boundary conditions [at the center ($m = 0$) and at the surface ($m = M$) of the star] and initial conditions [at $t = t_0$] of all the quantities: $r(m, t_0)$, $P(m, t_0)$, $l(m, t_0)$, $T(m, t_0)$ and $X_i(m, t_0)$. While the central conditions are straightforward [$l(0, t_0) = 0$ and $r(0, t_0) = 0$], at the surface [$l(M, t_0)$ and $r(M, t_0)$], determining them is a little more tricky. Because the purpose of this work is not to address these technical details we refer the interested reader to Kippenhahn & Weigert (1990) for more information.

For all $m \in [0, M]$, a solution $r(m)$, $P(m)$, $l(m)$, $T(m)$ and $X_i(m)$ at a given time t is called a stellar model. A set of models for each time t, from t_0 (let's say the ZAMS) until any later evolutionary phase, constitute a stellar track.

As no analytic solutions are possible, a numerical procedure is needed. The one generally adopted for calculating models in hydrostatic equilibrium, is the Henyey method. It is applied on the Lagrangian spatial grid, containing anywhere from a few hundred to a few thousand points. Important terminology terms when dealing with such models are: *timestep*, *iteration* and *convergence*. A timestep is the time between a model at a given time t and a second model at later time $t + \Delta\mathrm{t}$. In order to advance in time, at each new timestep, a new model is produced by performing many consecutive iterations on an initial trial solution until the changes brought to the solution are sufficiently small. When the required degree of accuracy is reached the model is said to have converged and a new $\Delta\mathrm{t}$ is applied to move on to the next model.

Whereas the set of equations and the general solving techniques are often common to all codes, differences may exist in the exact solving method. Moreover, codes do not always use the same input physics. Common differences can be, the treatment of convection, the equation of state, the opacities, the number of elements included in the nuclear network, the nuclear reactions rates, the mass-loss prescriptions, and many more. Thus, many different codes, basically trying to model the same stars, are available in the scientific community.

We will present the relevant, for the work presented in this thesis, characteristics of our evolution code in Chapter 5.

3. Mass-loss and Convective Overshooting

3.1. Mass-loss

3.1.1. Basics

Cool giants, the ones that are found on the RGB and the AGB, are known to lose non-negligible amounts of mass.

For moderate-mass stars, the clearly accepted consensus is that mass-loss on the AGB is both measurable and important. Observations suggest that very little mass is lost before the AGB. Only on the RGB can non-negligible mass-loss occur beforehand. But this is solely true for low-mass stars with low metallicities, for which one to several tenths of solar mass of material can come off. Intermediate-mass stars, that do not experience the He-flash, are hardly affected by mass-loss on the RGB.

Once on the AGB, the mass-loss rate is important enough (e.g. it can reach values up to $10^{-4}\mathrm{M}_{\odot} \cdot \mathrm{yr}^{-1}$) to alter the fate of all moderate-mass stars. It is therefore necessary to include mass-loss in AGB models. More than the mass-loss itself, what is mostly important is to understand, the way mass is lost, and thus to model the temporal variation of the rate during the AGB. The mass-loss rate fluctuations on the AGB influence among others, the number of TPs and therefore the nucleosynthesis connected with them, the TP-cycle phase at which the star will depart from the TP-AGB, the formation of the CSE and the characteristics of the core left behind to evolve as a WD.

Three types of mass-loss mechanisms have received most of the attention (Willson 2000) for cool giants: the solar-type winds in the framework of stationary outflows, stationary outflows involving dust - the so-called dust-driven winds - and pulsation initiated dust-driven winds. Most of the Mira and OH/IR stars are characterized by the third process as they lose mass at a rapid rate due to the combined effect of pulsation and dust formation. There are theoretical and observational reasons (Willson 2000) for considering both of these as a basis for the high AGB (Mira and OH/IR stars are AGB stars - section 2.2) mass-loss. From the theoretical point of view, in order for dust alone to drive the wind through radiation pressure, very extreme conditions would be required. On the other hand, the formation of dust in pulsating stars can greatly enhance the mass-loss rate over what it would be if no dust was present. Furthermore, the dust formation rate is amplified in pulsating stars because of departure from radiative equilibrium. Finally, according to observations all stars with dusty winds also show pulsations (Willson 2000).

It is nowadays clear that the mass-loss phenomenon greatly depends on the interaction of pulsation and dust formation (Wallerstein & Knapp 1998, Bergeat & Chevallier 2005) and this combined effect is believed to be the reason for mass-loss on the AGB. Pulsation-driven shock waves lift the gas to a height of several stellar radii. At such radii solid dust grains form because the temperature is low enough. The radiation pressure accelerates the grains outwards and momentum is transfered to the gas by grain-gas collisions. Although the dust to gas ratio is low (commonly adopted values are $\approx 1/500$, e.g. van Loon et al. 2005), the high opacity of the dust provides a high efficiency. This expelled dust and gas form the expanding CSE.

Another important consideration to take into account is the chemistry of the atmosphere. For example, Sedlmayr and collaborators have directed their attention on chemical reactions in pulsating stars that lead to the formation of grains and their subsequent growth (e.g. Winters et al. 1997). As was seen in the previous chapter, the CO molecule plays an important role because of its strong binding energy that locks together all the available carbon and oxygen. Only then are the remaining nuclei of the most abundant element available to form other compounds. The result is that carbon-rich ($C/O > 1$) atmospheres will form different types of dust than oxygen-rich ($C/O < 1$) atmospheres. The chemistry of dust-formation in oxygen-rich and carbon-rich winds is substantially different (Wachter et al. 2002) and it is necessary, if one wants to be as rigorous as possible, to treat each case separately.

Parametrized mass-loss relations can be empirically determined from observations or derived from theoretical models. Observations are done in the infrared or radio wavelengths. In addition to mass-loss rates, other properties of pulsating stars that should also be determined are the luminosity (L), the radius (R) and the mass (M). Estimating these quantities is very important not only because observational results show a correlation with mass-loss, but also because theoretical work demonstrating a strong dependence of mass-loss rates on stellar parameters (e.g. L, M) has been put forward (Bowen & Willson 1991, Hoefner & Dorfi 1997).

Reimers (1975) was the first to give a empirical relation between the observed mass-loss rates and the three parameters, L, R and M for a group of RGB stars and supergiants. This gave modelers the possibility to use a simple relation in their stellar codes. But his equation either overestimated or underestimated the rates depending on the evolutionary phase. For this reason, in order to allow for a better fitting of the models to observational data, a calibrating parameter η ($1/3 < \eta < 3$ according to Blöcker 1995b) was introduced. To further improve the relation, attempts where made to try various exponents for the parameters or alternatively to use more complicated functional forms (e.g. Willson 2000, for a review on mass-loss).

Reimers relation was originally also used for the AGB, but with time other prescriptions where specifically proposed for this phase.

For example, in addition to the Reimers prescription, Iben & Renzini (1983) include a higher mass-loss rate corresponding specifically to a phase where a *superwind* develops at the end of the AGB. The existence of this superwind, invoked by Renzini (1981), is motivated by the necessity to reproduce observed high AGB mass-loss rates and to have a mechanism powerful enough to produce a PN. This stronger rate is imposed in the models once a certain critical luminosity is reached.

In a different approach, Vassiliadis & Wood (1993) use, instead of the Reimers one, an empirical relation between the pulsation period P and the mass-loss rate $\dot{M}$. In order to account for the superwind phase as well, for $P > 500$ days, $\dot{M}$ is given by another empirically determined relation. Blöcker (1995b), presents yet another period-dependent mass-loss prescription. His equation is based on the theoretical work of Bowen (1988), where the dynamical structure of LPVs is investigated and shock-driven winds in atmospheres of Mira-like stars are calculated. This mass-loss formula appropriate for the AGB evolution is applied for $P > 100$ days.

Both descriptions in these previous works, one been empirical the other theoretical, are nevertheless based on the Bowen-type wind model characteristics as they exhibit a $P - \dot{M}$ relationship. According to Schröder et al. (1999) though, all these earlier dust-driven descriptions used in stellar models (Bowen 1988, Vassiliadis & Wood 1993, Blöcker 1995b), have a drawback. They do not treat the dust formation problem with sufficient detail, as they do not take into account the chemistry of the dust formation which strongly depends on temperature. The pulsations are considered to be responsible for the main energy input, instead of depending on the interaction of the radiation field with the dust grains that have been formed. In order to improve this approach, Schröder et al. (1999) use a mass-loss rate determined by including the detailed description of hydrodynamics, thermodynamics, chemistry, radiative transfer, dust formation and growth (see reviews by Sedlmayr 1994, Sedlmayr & Winters 1997) together with a dynamical wind model for pulsating carbon-rich AGB stars (Fleischer et al. 1992). This work which uses, in AGB models, a mass-loss description proposed by Arndt et al. (1997), is strictly valid for a carbon-rich chemistry and has been further improved by Wachter et al. (2002).

For oxygen-rich winds, the chemistry of dust formation is greatly different and requires its own modelling. Most theoretical works generally deal only with a carbon-rich chemistry because it is very difficult to drive a stellar wind by the action of radiation pressure on grains unless C/O is large and the star is very luminous and very cool (Willson 2000). There were however a few attempts in the past. For example, in his PhD thesis, Wagenhuber (1996) presented a mass-loss relationship, based on older work by (Fleischer 1994), that depends on different surface C/O values and covers therefore the oxygen-rich mixtures as well. This work was actually the first, before the previously mentioned ones, to use a rate based on detailed hydrodynamics, dust formation and chemistry. At the moment there are no up-to-date ready-to-use mass-loss relations theoretically determined for an oxygen-rich mixture. But lately, van Loon et al. (2005), by measuring the mass-loss rates through the modelling of the spectral energy distribution, present an empirically determined relation for oxygen-rich dust-enshrouded AGB stars.

As the star leaves the TP-AGB, after the envelope mass has dropped below a critical value, the period and amplitude of the radial pulsations rapidly decrease. The adaption of pulsation-driven wind calculations are not applicable any longer. Furthermore the temperature increases and the previous strong dependence of $\dot{M}$ on T_{eff} (Wachter et al. 2002, van Loon et al. 2005) is not appropriate. Neither from observations nor from theory is it well known how and at which temperatures the mass-loss rates strongly decrease. Mass-loss is nevertheless also important after the AGB, because it is a factor controlling the timescales during which the star will cross the HR diagram go through the post-AGB and PN phases, and reach the beginning of the WD cooling track. The transition from the AGB to the PN phase involves a change from a slow dense wind, to a fast, rarefied wind (Kwok et al. 1978, Kwok 1982, Kahn 1989). Early calculations (Schoenberner 1983, Wood & Faulkner 1986) that treated very crudely the mass-loss in the late AGB, simply used a Reimers rate or did not even include any mass-loss at all for the post-AGB. Blöcker (1995a) and Vassiliadis & Wood (1994) are the first to include in their calculations a mass-loss prescription for the PN phase based on the values, of the effective temperature and the terminal wind velocity, given by the radiation-driven wind theory of Pauldrach et al. (1988). This descriptions is applicable for temperatures greater than about 20 000K. The transitory post-AGB phase is still not rigorously dealt with.

Current descriptions are unable to predict how mass-loss behaves when the star moves off the AGB. Up to now, no detailed relation has been presented. Preliminary works only give some simple prescriptions to account for the gradual decrease of the mass-loss rate. Schonberner & Steffen (2007), by modelling hydrodynamical dusty-wind envelopes around evolving post-AGB star, and by comparing theoretic and observed spectral energy distributions (SEDs) of post-AGB objects, conclude that in order to form a PN and to have a characteristic double-peaked SED of the post-AGB object, mass-loss with the same strength as on the AGB must continue at least until the star reaches 5 000 to 6 000 K. In their theoretical calculations they impose in a similar way to Blöcker (1995a), a gradual decrease from the strong AGB rate to a Reimers one when the zero-age post-AGB is reached.

The above references on mass-loss descriptions used in AGB models are simply a few we thought necessary to mention. But other works on mass-loss relations have also been published. For both the TP-AGB and post-AGB, the evolution of the mass-loss is far from being well understood and modeled. All prescriptions, empirically or theoretically determined, are used in evolutionary codes with the common understanding that, they reflect only approximatively the way mass is really expelled. These relations are however the best descriptions presently available.

A common approach used to incorporate these mass-loss rates into stellar evolutionary calculations, is to first include one specific relation that depends on stellar parameters. When necessary, the prescription can be adjusted and the calculations redone in order to match observations. It is not the primary goal of this work to match stellar tracks with observations, but instead to use the most up-to-date physics available, including mass-loss prescriptions, in full AGB and post-AGB models. Therefore in a similar way to previous works that presented detailed AGB stellar grids (Karakas 2003, Vassiliadis & Wood 1993), mass-loss prescriptions have been chosen and applied to all models without further intervention.

3.1.2. Adopted Prescription

The widely used Reimers relation gives a quite good description for stars on the RGB and in the stage of central helium burning. But it is in principle not applicable for AGB stars when dust formation becomes important. It is thus always included in stellar codes for the RGB phase and most of the time for the E-AGB evolution as well. In practice, it is only substituted on the TP-AGB after a certain critical luminosity or pulsation period is reached, in order to get higher, and what is though to be more realistic, rates.

Starting from the ZAMS, in the models presented here, mass-loss ($\dot{M}$) has been taken into account in the following way.

- On the RGB, the Reimers relation is used in its following form:

  $$\dot{M}_{\mathrm{R}} = 4 \times 10^{-13} \frac{(L/\mathrm{L}_\odot)(R/\mathrm{R}_\odot)}{(M/\mathrm{M}_\odot)} \eta_{\mathrm{R}}. \tag{3.1}$$

  The variables, L, R and M represent the luminosity, radius and mass of the star. The mass loss rate is given in $\mathrm{M}_\odot \cdot \mathrm{yr}^{-1}$ and η_{R} is the Reimers parameter. In a similar way to what was adopted by Blöcker (1995b) for intermediate-mass stars, η_{R} is set to 1.0 for all stars with initial masses higher than $1.7\mathrm{M}_\odot$. For models with smaller ZAMS masses, the value 0.4 has been chosen in agreement to Karakas (2003). In practice, the previous relation is included in the calculations not only on the RGB but during the entire evolution starting from the ZAMS. Because of its luminosity and radius dependence, equation 3.1 gives a rate that is mostly insignificant in all other phases up to the beginning of the E-AGB. Only for the low-mass stars is the rate on the RGB important - this is the reason why a smaller η value has been chosen.

- Once on the TP-AGB the Reimers rate will continue to be used as the base relation. Already on the E-AGB pulsation periods (see later how these are calculated) start slowly increasing and on the TP-AGB high values of P are periodically reached as the stars evolves through the TP-cycle. When $P > 400$ days, different mass-loss descriptions depending on surface chemistry are used.

  For an oxygen-rich composition (C/O < 1) and for $P > 400$ days, the van Loon et al. (2005) prescription gives:

  $$\log \dot{M}_{AGB} = -5.65 + 1.05 \cdot \log\left(10^{-4}\frac{L}{L_\odot}\right) - 6.3 \cdot \log\left(\frac{T_{\mathrm{eff}}}{3500K}\right). \tag{3.2}$$

  For $P > 400$ days, but for the carbon-rich case (C/O > 1), the Wachter et al. (2002) prescription gives:

  $$\log \dot{M}_{AGB} = -4.52 + 2.47 \cdot \log\left(10^{-4}\frac{L}{L_\odot}\right) - 6.81 \cdot \log\left(\frac{T_{\mathrm{eff}}}{2600K}\right) - 1.95 \cdot \log\left(\frac{M}{M_\odot}\right). \tag{3.3}$$

The 400 day critical period should strictly refer to the oxygen-rich case since according to van Loon et al. (2005), their relation is meant to be used only for dust-enshrouded objects with $P > 400$ days. For the carbon-rich prescription, a period dependency is not separately imposed, because it has directly been substituted in the mass-loss relation through the period-luminosity relation for carbon-rich Miras (Groenewegen & Whitelock 1996). Furthermore, a critical luminosity, below which no superwind occurs and only over which the TP-AGB rate should be used, is given by Wachter et al. (2002). In practice, only their models with initial ZAMS mass below $1.1 M_\odot$ do not reach this limit. Strictly speaking, no critical period but a critical luminosity should thus be necessary for the onset of the carbon-rich rate.

In order to consider the two cases in a consistent way, it has been decided to use the 400 days critical period for both expressions and furthermore not to implement the critical luminosity for the carbon-rich composition. But these simplification with respect to the original recommendations will in practice not influence our use of the relation. Indeed, for the carbon-rich expression to be applicable, the surface composition must have $C/O > 1$ and this means that TDU has already occurred. The rate corresponding to an oxygen-rich mixture will effectively always be used first. When the carbon-rich one is used, this will only occur at least after a few TPs. Therefore the carbon-rich prescription is either not applicable at all or used later in the TP-AGB evolution.

Both of the above equations, one been determined from observations and the other form theoretical modelling are the most up-to-date relations presently available in the literature and for this reason they have been included.

- The beginning of the post-AGB is taken to be the moment, after the departure from the TP-AGB, when the decreasing period of pulsation reaches 100 days. From this post-AGB zero-age, the maximum rate between the Reimers (always with $\eta = 1.0$ or 0.4 depending on initial mass) and the radiation-driven wind for the central star of planetary nebula (CSPN) phase is taken. In practice the Reimers rate is always higher (for the post-AGB and WD stages) and only during the PN phase is the CSPN one used. This CSPN rate, the same used in Blöcker (1995a), depends on the luminosity in the following way:

  $$\dot{M}_{\rm CSPN} = 1.29 \cdot 10^{-15} L^{1.86}. \tag{3.4}$$

  In order to have a smooth transition between the AGB mass loss rate ($\dot{M}_{\rm AGB}$) and the one for the post-AGB, PN and WD phases (Max[$\dot{M}_{\rm CSPN}$,$\dot{M}_{\rm R}$]), a transitory mass-loss prescription is implemented. Starting from the moment the star pulsates with a 150 day period, the rate is gradually decreased until P reaches 100 days. A simple relation gives the mass-loss during this short transition phase:

  $$\dot{M}_{\rm trans} = \dot{M}_{\rm AGB}(t_1) - \Delta\dot{M}(t)\frac{P(t_1) - P(t)}{P(t_1) - P(t_2)}, \tag{3.5}$$

where $\Delta\dot{M}(t) = \dot{M}_{\rm AGB}(t_1) - \dot{M}_{\rm R}(t)$, $P(t_1) = 150$ days and $P(t_2) = 100$ days.

At the end of the TP-AGB, when P is decreasing for the last time from a period above 400 days to the 150 day mark, the $\dot{M}_{\rm AGB}$ rate will keep on being used to maintain a high mass-loss until the post-AGB. We therefore do not switch to the $\dot{M}_{\rm R}$ for $P < 400$ days as is done during the preceding TP-AGB evolution. When $P = 150$ days is finally reached, $\dot{M}_{\rm trans}$ takes over.

Throughout the entire AGB and post-AGB evolution the period of pulsation P is calculated by considering radial pulsations only in the fundamental mode according to Ostlie & Cox (1986), who give $\log P = -1.92 - 0.73 \cdot \log(M/{\rm M}_\odot) + 1.86 \cdot \log(R/{\rm R}_\odot)$. This is in agreement with Blöcker (1995b) who also calculates the pulsation period of his AGB models based on the previous study for Mira variable stars.

In short, for each different evolutionary stage, $\dot{M}$ takes the following values:

- $\dot{M}_{\rm R}$ during the MS, the RGB, core He-burning, the E-AGB, the TP-AGB ($P < 400$ days). $\eta_{\rm R} = 1.0$ or 0.4 depending on $M_{\rm ZAMS}$.
- $\dot{M}_{\rm AGB}$ during the TP-AGB ($P > 400$ days) and at the very end of the TP-AGB ($150 < P < 400$ days). There are two different relations depending on surface C/O value.
- $\dot{M}_{\rm trans}$ at the transition between the TP-AGB and the post-AGB zero-age mark ($100 < P < 150$ days).
- Max[$\dot{M}_{\rm CSPN}$,$\dot{M}_{\rm R}$] during the post-AGB, the PN and the WD phases.

As we finish this section, a few extra remarks are necessary. No detailed comparisons between mass-loss prescriptions have been shown. This is true for all descriptions, whether these are simply mentioned as older examples present in the literature or they are the latest expressions that we have indeed used in our calculations. The specific equations included in our code are given in a straightforward way and, for instance, no analysis on their various parameter dependences was done beforehand. The selection criterion is simple: they are the most recent and updated ones available. We have directly implemented them in our code by following the recommendations given by the authors (e.g. period of pulsation). For phases (*pre-AGB*, post-AGB, PN) for which no updates are available, we include the ones used by the latest relevant work on AGB/post-AGB evolutionary grids (Blöcker 1995a, Karakas 2003).

In order to illustrate our final AGB mass-loss prescription and to show the behavior of the pulsation-period and chemistry dependences, we plot in Figure 3.1 the mass-loss rate on the TP-AGB of one of our models with respect to time. The adopted rate is the thick black line, while the dashed colored ones represent those from the three separate prescriptions: Reimers, oxygen-rich (van Loon et al. 2005) and carbon-rich (Wachter et al. 2002). Initially the Reimers low mass-loss relation is used. As the pulsation period (see Figures 7.1-7.4 in Chapter 7 for the evolution of the P values with respect to time) gradually increases and eventually exceeds the 400 day mark, the oxygen-rich rate takes overs. The

Wachter et al. (2002) rate is adopted only afterwards, when the star, having experienced multiple dredge-up episodes, becomes carbon-rich.

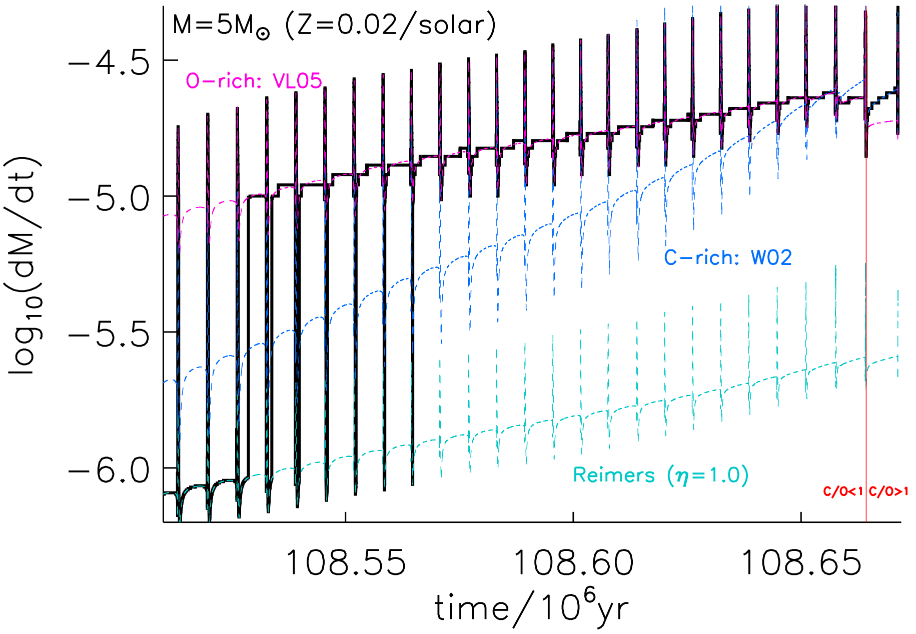

Figure 3.1.: The mass-loss rate (logarithmic units) is shown with respect to time (million years) during the TP-AGB evolution of a 5M$_\odot$ model with solar type composition computed with the Garching stellar evolution code. The actual adopted value is given by the thick black line. The colored dashed lines give the rates from each of the individual prescriptions. Wachter et al. (2002): W02, van Loon et al. (2005): VL05. The vertical red line marks the beginning of the carbon-rich phase.

.

Moreover, one can observe in Figure 3.1 that at the oxygen-rich/carbon-rich transition there is a noticeable drop for all three rates. This effect is due to a temperature increase at the surface of the star because of our new chemistry-dependent opacities (more on this in Chapter 7).

3.2. Convective Overshooting

3.2.1. Basics[1]

Over the years, different versions of the local mixing-length theory (MLT), similar to the one originally proposed by Böhm-Vitense (1958) have been used to model convection in

---

[1] In this section, when no specific reference is given, the general explanatory remarks on convection theory are based on Kippenhahn & Weigert (1990).

stellar calculation codes during the different phases of evolution, including the AGB.

In the MLT, fluid macroscopic mass elements (or "bubbles", "eddies") transport energy and matter inside the convective region. Hot fluid elements move upwards and cooler ones downwards in this dynamically unstable region, defined by the non-fulfillment of the Schwarzschild stability criterion ($\nabla_{\rm rad} < \nabla_{\rm ad}$). The bubbles are accelerated by buoyancy and gain an increasing temperature difference with respect to the surroundings. After having traveled some characteristic distance - the mixing-length - they dissolve and mix with their new environment. In the MLT formalism, an adjustable parameter, $\alpha_{\rm MLT}$, which is the ratio of the mixing-length and the pressure scale height ($\alpha_{\rm MLT} = \Lambda/H_{\rm p}$) is introduced. The value of $\alpha_{\rm MLT}$ is not known but is usually set by requiring that (e.g. Mazzitelli 1979) a solar-type model has the observed solar effective temperature at an age of 4.7 Gyr.

It is well known however, that the MLT has its limitations because it does not take into account basic principle of hydrodynamics. Questionable points include the precise determination of the regions where convective motions occur, and therefore the extent to which the chemical elements are mixed.

Let's consider the situation in the vicinity of the outer boundary of a convective region. The boundary is defined to be at the position of neutral stability ($\nabla_{\rm rad} = \nabla_{\rm ad}$). Elements arriving from inside the convective region, that have been accelerated but have not yet dissolved, reach the inner boundary with a non-zero momentum. Here, the model implies an obvious problem: the fluid elements are supposed to start "braking" only beyond this border, but they are also supposed to actually stop at this same border. The theory does not include additional mixing in the radiative region bordering the convective zone. In practice, what is done in the simplest scenario by producing a sharp transition between mixed and static regions, is to suppose that the elements abruptly stop right at the boundary and mixing does not extend further. Some works smoothly reduce the velocity near the inner boundary (Böhm & Stückl 1967, Bohm & Cassinelli 1971) or use the distance to the boundary as a relevant spatial scale (Canuto & Mazzitelli 1991). But how the physical mechanism, that would decelerate the elements and make them stop exactly at the boundary, quantitatively works is nevertheless uncertain. What is more plausible is that the fluid elements cross the boundary and *overshoot* because of inertia some finite distance into the stable non-convective region, where they will come to rest and dissolve.

In stellar evolution, many studies have dealt with this simple fact. The current issue seems to be, not if overshooting takes place, but how efficient and how far does the mixing overshoot (Herwig 2005a). The question of overshooting is quite open and could be settled only by the use of a better treatment of convection. In the absence of a more sophisticated theory, effort was first made to approach this problem more realisticly while remaining in the MLT formalism. Instantaneous mixing in the convective region has been considered to extend beyond the classical Schwarzschild boundary by some fraction of the pressure scale height ($H_{\rm p}$). The ratio of the overshooting distance and $H_{\rm p}$ is then a free parameter that needs to be calibrated. Several studies have also attacked the problem of overshooting with non-local mixing-length formalisms (e.g. Shaviv & Salpeter 1973). Among others, a review on convective overshooting has been given by Zahn (1991). More recently, approaches based on numerical calculations have presented overshooting as a diffusive process. The important work of Freytag et al. (1996) is one such case. They performed numerical radiation hydrodynamic simulations in two dimensions to study the structure and dynamics of shallow surface convection zones in hot stars (A-type and DA WDs). What is shown is that the descending material is concentrated in fast narrow downdrafts surrounded by broad upflow regions with comparatively low velocities. Accordingly, the MLT picture does not seem appropriate with its rising and falling bubbles. Instead the dynamics should be described in terms of downdrafts which are newly formed in the unstable layers, grow, are horizontally advected, and finally merge. With respect to the mixing beyond the convective boundary, their results show that there doesn't seem to be a finite overshoot distance, like in ballistic approximation of convective overshoot predictions. Instead the velocity field continues with significant convective flux. This reveals, in an independent theoretical way, the actual existence of extra mixing. The velocity declines exponentially with depth of penetration in the radiative region, and the spreading of material in the overshoot region can be described as a diffusion process. In another work, Asida & Arnett (2000) have also found a similar behavior of the decay of the convective velocity field outside the convective zone in their two-dimensional hydrodynamic simulations for the oxygen-burning shell in massive stars.

A simple relation for a depth-dependent diffusion coefficient, appropriate for the overshooting, has been derived by Freytag et al. (1996) from the velocity fields of their models to mimic mixing into the stable layers beyond the convection boundary. Formulated in this way, overshooting can easily be incorporated in stellar models which already have implemented particle diffusion and treat convection as a fast diffusive process, without the direct use of radiation hydrodynamics. In a similar fashion to the instantaneous mixing models, the scale length remains correlated to a free parameter. In general, an essential consequence of all these types of numerical simulations (Freytag et al. 1996, Asida & Arnett 2000, Robinson et al. 2004), is that this scale length, and thus the free overshoot parameter which in practice reflects the efficiency of the extra mixing, depends on particular stellar conditions. Overshooting does not have the same efficiency at all boundary types of stellar convection zones. There is, at the moment, no consensus on a theory that would be applicable in stellar evolution to all convective borders, and each boundary needs to be separately considered.

Therefore, in practice all overshooting prescriptions depend on a free parameter specific for each case. Its value needs to be specified and, similarly to the $\alpha_{\rm MLT}$, is often fixed in some way for each particular convective border type (results will be given in the next section). Schaller et al. (1992) for example, by considering instantaneous overshoot in convective core-mixing, match with their models the observational MS-width for a given value of the extra-mixing distance. With another overshooting description, in stellar tracks of Bressan et al. (1993) and Ventura et al. (1998), different calibrated values of the overshooting parameter on the MS are used for low- and for intermediate-mass stars. Girardi et al. (2000) present a grid of models where distinct overshooting parameters are used for various stellar masses and types of convective regions (e.g. core convection, envelope convection). Finally, the type of diffusive prescription based on the previous hydrodynamical overshoot has been adopted with a given efficiency parameter for envelope convection by

Schlattl & Weiss (1999) and Blöcker et al. (1998) in the solar case. A similar description has also been implemented by Mazzitelli et al. (1999) in AGB models.

In the particular case of AGB stars, convective boundaries where the overshooting phenomenon can be considered, are the bottom of the periodically deepening convective envelope (CE) and the pulse-driven-convective-zone (PDCZ) formed at each TP in the intershell region. What happens at these boundaries plays a major role for the TP-AGB evolution as the effects of both mixing regions *team up* and regulate the TDU efficiency. Herwig and collaborators in a series of papers (Herwig et al. 1997, Herwig 2000, Lugaro et al. 2003, Herwig 2004a,b), have included the exponentially declining overshoot diffusion coefficient following the description of Freytag et al. (1996) at these two convective boundaries. They have shown that this approach of overshooting, when applied to TP-AGB models, is relevant to address some major observational properties. Indeed, their efforts have turned-up to be successful, as models have shown efficient enough TDU to produce surfaces abundances of TP-AGB stars and hydrogen-deficient post-AGB stars that match observations. These effects depend on the value of a certain free overshoot parameter f (next section). Furthermore, a different value of f can be chosen for each BCE and PDCZ convective regions (Herwig 2004a,b).

It is important to note, that, in addition to overshooting, other processes have also been put forward to explain the extra mixing observed at these boundaries in AGB models. These are gravity waves (Denissenkov & Tout 2003) and rotationally-induced mixing (Langer et al. 1999). But, as overshooting based on the exponentially decaying diffusive mixing description, is rather simply implemented in standard stellar codes by a relation depending on a single free parameter, it is currently easier to solely adopt this prescription. It is useful however to re-interpret overshooting as possibly representing the combined effect of more than one physical process acting simultaneously.

3.2.2. Adopted Prescription

In the simple case presented in Chapter 2 it was assumed by equation 2.5 that the chemical evolution varied only because of nuclear burning. If mixing processes are considered, the equation can be rewritten in the following form by describing the whole process as diffusive:

$$\frac{\partial X_i}{\partial t} = \left(\frac{\partial X_i}{\partial t}\right)_{\mathrm{nuc}} + \frac{\partial}{\partial m}\left(D \cdot (4\pi r^2 \rho)^2 \frac{\partial X_i}{\partial m}\right). \tag{3.6}$$

The first term on the right hand side represents the change in abundances due to nuclear burning exactly corresponding to equation 2.5. D is the diffusion coefficient and depends on the assumed mixing model. Three possibilities are considered, D_{rad}, D_{c} and D_{os}. When the region dealt with is radiative, $\mathrm{D}_{rad} = 0$ and the original equation 2.5 is recovered. If convection is considered, the diffusion coefficient D_{c} is given by a standard relation not specified here for simplicity. In the radiative regions which are right at the border of a convectively unstable area a depth-dependent coefficient, D_{os} (Freytag et al. 1996, Herwig et al. 1997) is given by the following relation:

$$D_{\rm os} = v_0 \cdot H_{\rm p} e^{\frac{-2z}{f \cdot H_{\rm p}}} \tag{3.7}$$

where z is the distance from the boundary in the outer radiative region, $H_{\rm p}$ is the pressure scale height and v_0 the typical velocity of the convective elements (obtained from the MLT in the inner regions just before the Schwarzschild border). f is the free overshooting parameter. It represents a measure of the efficiency of the extra mixing. The larger f is, the further the extra mixing extends outside the convective region.

The above relation is based on the hydrodynamical simulations of Freytag et al. (1996) which are done for conditions representative of shallow stellar surface convection zones in hot stars. From simulations of overadiabatic convective envelopes of A-stars and DA WDs, they find that $f \approx 0.25$ and 1.0 respectively. Hydrodynamical simulations for deep envelope or core convection are not yet available and a calibration of the efficiency parameter is thus necessary for cases where a direct value from simulations is lacking. The values of f can be expected to be considerably smaller with increasing depth, as the deceleration of the matter is likely to be more severe, in the deep interiors, under adiabatic conditions. By including this descriptions of overshooting, a number of studies have constrained f to different values at various boundary.

Blöcker et al. (1998) and Schlattl & Weiss (1999) determine the best f value to be 0.07 for solar deep envelope convection in order to solve the lithium problem. Herwig et al. (1997) match the width of the MS by applying overshooting during core convection. The obtained value of 0.016 corresponds to the same MS width as the one determined by Schaller et al. (1992) who applied an instantaneous overshoot description with a mixing distance given by $d_{\rm os}/H_{\rm p} = 0.2$. This same 0.016 value of f is further also assumed (Herwig et al. 1997) to hold for the deep envelope convection zones of AGB stars. According to Herwig (2000), the value of f on the AGB is also independently constrained between 0.01 and 0.03 by comparing surface oxygen abundances of hydrogen-deficient post-AGB star models with observations. Moreover, Weiss & Porcherot (2007) match color-magnitude diagrams of open clusters, with the same Garching evolution code used to compute the results presented in this thesis, by setting f to a 0.018 value.

In accordance to work from Bressan et al. (1993) and Ventura et al. (1998) that use a different overshooting description, Herwig et al. (2000) in their grid of evolutionary models apply on the MS a reduced overshoot efficiency of 0.008 for stars with initial ZAMS mass $\leqslant 1.5{\rm M}_\odot$. This is also in qualitative agreement with the approach of Girardi et al. (2000) who again with another overshooting description, consider an increasingly efficient extra-mixing on the MS for core convection, making the value of the overshooting distance across the border of convection gradually increase from 0 at $M_{\rm ZAMS} = 1{\rm M}_\odot$ to its maximum value at $M_{\rm ZAMS} = 1.5{\rm M}_\odot$. In addition, depending once more on initial mass, they apply different extra-mixing distances for envelope convection.

On the AGB, instead of applying his 0.016 standard f value at all convective boundaries, Herwig (2004a) investigates cases where different values for $f_{\rm CE}$ and $f_{\rm PDCZ}$ are used. His benchmark case, which represents a minimum overshooting situation, is: $f_{\rm PDCZ} = 0.002$, $f_{\rm CE} = 0.016$. In a paper studying the s-process nucleosynthesis in AGB stars, Lugaro et al. (2003) on one hand conclude that f_{PDCZ} = 0.016 may be too large, and on the other assume a much higher f_{CE} = 0.128 in order to obtain s-element abundances close to what is observed. Nevertheless, such a high efficiency at the bottom of the CE leads to a much too important TDU, especially for low metallicities, according to Herwig (2004b). They therefore apply f_{PDCZ} = 0.008 and f_{CE}=0.016 for the two different convective zones, in AGB models of extremely metal-poor intermediate-mass stars.

In this work, having as a goal to present a grid of models for moderate-mass stars, as large as possible in mass and metallicity space, with the most up-to-date prescriptions but without an overly big set of free parameters, we have decided to use the following overshooting description.

The evolution code has already particle diffusion implemented and treats convection as a diffusive process. The above 3.7 relation for the D_{os} can thus easily be applied. This has already been done with the same code by Schlattl & Weiss (1999) for solar envelope convection.

Overshooting is considered during all phases of evolution starting from the ZAMS and at all convective boundaries. The value of the f parameter varies in the following way. The standard value is taken to be 0.016. On the MS this value is used for stars with $M_{\mathrm{ZAMS}} \geqslant 1.5\mathrm{M}_{\odot}$. For $1.0 \leqslant M/\mathrm{M}_{\odot} < 1.5$ the overshooting efficiency is gradually increased: starting from a value of 0 for $M_{\mathrm{ZAMS}} = 1.0\mathrm{M}_{\odot}$ it reaches 0.016 at $M_{\mathrm{ZAMS}} = 1.5\mathrm{M}_{\odot}$. The intermediate values are given by the following relation $f = 0.032 \cdot (M/\mathrm{M}_{\odot}$ - 1.0). After the MS, f is kept constant at 0.016 in all cases. On the TP-AGB particularly, we have taken f_{CE} = f_{PDCZ} = 0.016.

4. Low-Temperature Molecular Opacities

4.1. Opacity Tables in Stellar Evolution Codes

One of the ingredients in the input physics of stellar evolution codes, alongside the equation of state data and the nuclear reaction rates, is the opacity information.

Directly calculating opacities for a given frequency, temperature and density in stellar evolution programs is a computationally very costly task and currently not feasible. What is rather done, is to calculate mean - not frequency-dependent - opacities and to store them in tables. These pre-tabulated files, where opacities are basically stored by temperature and density are used afterwards during the evolutionary computations to estimate interpolated values for a specific temperature-density combination.

The frequency-independent mean opacity values can be determined in different ways. For the modelling of the radiation transfer through optically thick regions - the interior and the envelope of stars - the diffusion approximation is a good description of the physical condition of the gas, and the Rosseland mean opacity is expected to then be the best estimate. When the material is optically thin, it is not a valid approximation any longer, and the Planck mean opacity can be used. For envelopes of AGB stars the diffusion approximation is valid and the Rosseland mean opacity is used.

Furthermore, opacities also depend on the composition of the environment, and tables for different chemical arrangements need to be computed.

As a difficult and time-demanding task, the production of such opacity tables has developed into a specialized branch and different groups are active in this field.

The most recent grids of AGB models (e.g. Karakas 2003) use the tabulated OPAL opacities from Iglesias & Rogers (1996) (OPAL96) which are available for a wide range of metallicities at high temperatures. But these OPAL96 tables have to be complemented with other ones for lower temperatures. This was done in the past with the molecular opacities from Alexander & Ferguson (1994) that consider the regime of molecular contributions. Recently, a new version of updated molecular opacities from Ferguson et al. (2005) has been made available. In all of these tables though, the base mixture corresponds to a solar-scaled abundance distribution. This means that all elements heavier than hydrogen and helium - the metals - always have the same relative abundances (similar to the solar ones) with respect to each other, for all mixtures. Each different metallicity table has thus a solar-scaled distribution.

But because of TDU events, the surface chemical composition of AGB stars can be altered during the TP-evolution. More importantly, the dredged-up material modifies the relative metal distribution at the surface and can often turn an oxygen-rich star (C/O $<$ 1) into a carbon-rich (C/O $>$ 1) one. In these situations, the scaling of the heavy elements is not the solar one anymore since, while the abundance of most metals remains the same, the content of some (mainly carbon) is enhanced. For the OPAL96 opacities is is not a problem because tables can be produced for specific carbon and oxygen enrichment in variable proportions.

This is not the case for the Alexander & Ferguson (1994) or Ferguson et al. (2005) tables in the low-temperature regime where molecular contributions to the opacity is actually more important. These tables have been pre-calculated for specific mixtures and do not allow for any other abundance changes. All extensive AGB grids (e.g. Vassiliadis & Wood 1993, Karakas 2003) have used up to now opacity tables for solar-scaled distributions of the metals (with C/O $\approx$ 0.48) to compute their models even when TDU turns the envelope mixture into a carbon rich one (C/O $>$ 1). As each element differently contributes to the total absorption, the change in individual metal abundances should be taken into consideration for elaborate opacity tables. Until recently, this drawback had mostly been neglected in AGB models.

4.2. TP-AGB Evolution with Carbon-Enhancement

Depending on which element - oxygen or carbon - is most abundant, different molecular absorption bands in the visual and infrared (e.g. Lançon & Wood 2000) dominate the spectrum of M- and C-type stars. Molecular equilibrium calculations given by Russell (1934), were the first quantitative explanation of the important differences in the spectrum of oxygen- and carbon-rich stars. The strong binding energy of the CO compound regulates the molecular abundances for different C/O ratios. While strong TiO, VO and H_2O bands are present for C/O $<$ 1, the C/O $>$ 1 case shows C_2, CN and SiC absorption features. Furthermore, this carbon-enhancement also affects the chemical composition of the dust grains as amorphous silicates and amorphous carbon grains are respectively present for each case (e.g. Ivezic & Elitzur 1995, Habing 1996). Observationally, these spectral differences appear as a sharp discontinuity in near- and far-infrared colors between M and C-type stars. Data is being released in huge amounts (e.g. the DENIS and 2MASS projects) and theory should account for these observations.

Tsuji (1966) had already shown the importance of different molecular opacity sources and was the first to include the effects of absorbers such as H_2O, CO and OH in opacity calculations. But in stellar evolution codes low-temperature molecular opacities are still incompletely treated since the adopted descriptions (Alexander & Ferguson 1994, Ferguson et al. 2005) correspond to gas mixtures for a single value of the C/O ratio. Only few works have proposed molecular opacity tables for variable C/O ratios (Alexander et al. 1983, Lucy et al. 1986) and some (Bessell et al. 1989, 1991) have presented analytical fits, as a function of carbon and oxygen abundances, to some already existing tables (Alexander et al. 1983). But even fewer works have coupled such opacities to evolutionary calculations (Scalo & Ulrich 1975).

With an important publication (Marigo 2002) on the effects of molecular opacities for varying surface C/O ratios, P. Marigo is the one that has most recently presented work in which synthetic AGB models are connected to an appropriate opacity description at low temperatures. The adopted procedure to compute the molecular opacities, through analytical fit relations, closely resembles that of Scalo & Ulrich (1975) and is incorporated in the P. Marigo synthetic code for TP-AGB evolution. The possibility to consistently compute the opacities for any chemical composition, during the evolutionary calculations is a huge advantage of this approach and the effects detected in the models help account for a number of observational properties of carbon stars.

The molecular opacity routine shows an abrupt change in the dominant opacity sources at the transition (C/O = 1) from oxygen- to carbon-rich envelopes. The most significant consequence of this effect is the sudden cooling of the stellar models (see section 7.3). This is important because, as the mass-loss descriptions depends on the effective temperature, the decrease in temperature leads to a increase in mass-loss when the star becomes a carbon star. The low temperatures and high mass-loss rates have many direct implications on AGB evolution. They can alter the expected number of C with respect to M and S stars, the total number of TPs, the number of TPs during the carbon-rich phase, the nucleosynthesis, the maximum C/O ratio obtained etc. For example, because mass-loss is higher during the carbon-rich phase, TP-AGB evolution is shorter, fewer TPs occur and therefore less nucleosynthesis.

Nevertheless the adopted simplifications in the Marigo approach, constitute a clear limitation of the opacity calculations (in section 7.3.3 we will show how these opacities are coupled to our AGB models). The total Rosseland mean opacity is simply taken to be the sum of the Rosseland mean opacity of each individual molecule. This is supposed to hold under most physical conditions met in AGB envelopes, even if it is not generally correct. Furthermore, by neglecting TiO and VO molecules for oxygen-rich compositions as well as HCN and C_2H_2 for carbon-rich ones, only a limited number of molecular species - they are however among the most relevant opacity sources in AGB stars - are included. Finally, the AGB models to which these opacities were coupled are synthetic, and therefore simply represent an approximation to detailed stellar evolution calculations.

On one hand, multidimensional interpolations between pre-tabulated values of detailed opacity calculations - like the ones of Iglesias & Rogers (1996), Alexander & Ferguson (1994) and Ferguson et al. (2005) - would be a more accurate alternative. In that case, the parameters that should at least be taken into account are density, temperature, total metal content and hydrogen, carbon, oxygen and nitrogen abundances. On the other hand, there is a necessity to couple these opacities to a stellar code which actually solves the entire set of stellar structure and nuclear generation equations in order to get a fully consistent model directly parameterizing the occurring physical processes.

A large enough grid of tables, to adequately cover the abundance changes found in AGB envelopes, with accurate molecular opacities was not available until now.

In this context, J. Ferguson from the Wichita State University (WSU) low-temperature opacity group, produced detailed opacity tables (Ferguson 2006) for different C/O ratio compositions, tailored to the specific needs of TP-AGB models produced by the Garching detailed stellar evolution code.

4.3. New Low-Temperature Opacities for Variable Chemical Compositions

In our code, opacity tables are generally created by merging data from different sources. They are constructed beforehand, all in the same way, and subsequently included in the stellar computations. This is also the case for the new tables we present.

The new low-temperature opacities calculated by Ferguson (2006) (WSU06) include molecular absorption processes. We have combined them with high-temperature tables for completely identical set of mixtures from Iglesias & Rogers (1996) (OPAL96). In order to easily merge the new WSU06 opacities with the OPAL96 ones and incorporate them in the evolutionary code, the values have been tabulated in an identical way as the standard OPAL96 tables: the chemical mixtures specific for each OPAL96 table are labeled by mass fraction values of hydrogen (X) and metals (Z) and accordingly sets of tables for the same X and Z combinations have also been chosen to catalog the new opacity sets.

The two-dimensional opacity tables are given for various, temperature - density combinations. Actually, opacity groups have decided not to directly use density as a variable to tabulate opacity values [cm^2/g] but rather a parameter R defined as ρ/T_6^3, where ρ is the density [g/cm^3] and temperature is given in millions of degrees by T_6 (this is simply a convention and the decision was originally based on the fact that some massive MS stars are nearly polytropically structured along constant R values). Consequently, the tabulated logarithm of the Rosseland mean opacity is given as a function of $\log R$ and of the logarithm of the temperature, $\log T$.

For the standard OPAL96 tables (created directly from the OPAL web-tool interface), values of $\log T$ are taken in the interval [3.75, 8.70] and those of $\log R$ in the interval [-8.0, 1.0]. The new low-temperature WSU06 opacities are given for the same $\log R$ range, but cover the $\log T$ space of [3, 4.10]. In order to produce single tables covering the entire temperature range, we have merged both sets in the following way. The WSU06 opacities for $3.00 < \log T < 3.70$ and the OPAL96 ones for $4.10 < \log T < 8.70$ are directly taken. When $3.70 < \log T < 4.10$, a linear interpolation in $\log T$ between both opacity values was done in order to smoothly match both regimes for which the values are actually in excellent agreement. The resulting tables are further extended in the high density regime with the Itoh et al. (1983) electron conduction opacity results. These results, corresponding to dense matter in the liquid metal phase, are not relevant for our AGB envelope opacities but rather appropriate to white dwarfs. They are simply included in order to obtain tables of similar temperature - density coverage as the ones previously used in our evolution code. Within this $\log R - \log T$ grid, the interpolation during the evolution is done by a two-dimensional, bi-rational spline algorithm (Spaeth 1973).

Because these mean Rosseland opacities have to be pre-calculated and then stored into tables, it is necessary to consider beforehand the chemical composition of the mixtures. A mixture is first characterized by the unit mass fractions of hydrogen (X) and helium (Y).

The remaining fraction (Z = 1 - X - Y) corresponds to the metals. The total metallicity of a mixture is given by the value of Z. Not taking into account the small, with respect to hydrogen and helium, abundances of each metal element, a specific composition can be defined by only two of the three X, Y, Z parameters. In our case, each two-dimensional $\log R - \log T$ table is given for a specific X - Z combination. Values of X vary from 0 to 1, taking the values: 0.0, 0.1, 0.2, 0.35, 0.5, 0.7, 0.8, 0.9, 0.95. For Z, the following values range from 0 to 0.1: 0.0, 0.0001, 0.0003, 0.001, 0.002, 0.004, 0.01, 0.02, 0.03, 0.04, 0.06, 0.08, 0.1. All X - Z combinations are valid, except for the X = 0.95 which can obviously not be matched with Z = 0.06, 0.08 and 0.1. In addition, a table for the combination, X = 1.0, Z = 0.0, Y = 0.0, is calculated. Finally 11 additional mixtures for which Y = 0.0, are considered. These are, for (X, Z) combinations, the following: (0.9999, 0.0001), (0.9997, 0.0003), (0.999, 0.001), (0.998, 0.002), (0.996, 0.004), (0.99, 0.01), (0.98, 0.02), (0.97, 0,03), (0.96, 0.04), (0.94, 0.06), (0.92, 0.08).

Table 4.1.: Chemical abundances of the metals for different C/O ratio values used for the computations of the opacity tables. Abundance values are scaled logarithmically. Set 1 corresponds to the base solar-scaled distribution from Seaton et al. (1992). Sets 2-6 have been enriched by different amounts (see text) in carbon, oxygen and nitrogen with respect to the base composition and have the indicated C/O ratio values (in number fractions).

el.	Set 1 (solar) C/O = 0.48	Set 2 C/O = 0.9	Set 3 C/O = 1.0	Set 4 C/O = 1.1	Set 5 C/O = 3.0	Set 6 C/O = 20.0
C	8.55	8.90	8.97	9.03	9.48	10.47
N	7.97	8.14	8.18	8.22	8.56	8.91
O	8.87	8.95	8.97	8.99	9.00	9.17
Ne	8.07	8.07	8.07	8.07	8.07	8.07
Na	6.33	6.33	6.33	6.33	6.33	6.33
Mg	7.58	7.58	7.58	7.58	7.58	7.58
Al	6.47	6.47	6.47	6.47	6.47	6.47
Si	7.55	7.55	7.55	7.55	7.55	7.55
P	5.45	5.45	5.45	5.45	5.45	5.45
S	7.21	7.21	7.21	7.21	7.21	7.21
Cl	5.50	5.50	5.50	5.50	5.50	5.50
Ar	6.52	6.52	6.52	6.52	6.52	6.52
K	5.12	5.12	5.12	5.12	5.12	5.12
Ca	6.36	6.36	6.36	6.36	6.36	6.36
Ti	5.02	5.02	5.02	5.02	5.02	5.02
Cr	5.67	5.67	5.67	5.67	5.67	5.67
Mn	5.39	5.39	5.39	5.39	5.39	5.39
Fe	7.51	7.51	7.51	7.51	7.51	7.51
Ni	6.25	6.25	6.25	6.25	6.25	6.25

There are accordingly a total of 126 different-mixture opacity tables in two dimensions ($\log R - \log T$). During the evolution, the interpolation in mixture is done within the different tables with parabolic polynomials, first in X between the three tables closest to the model value, and then in $\log Z$.

To this new set of 126 tables, where opacities are given as a function of $\log R$, $\log T$, X and Z, an extra dimension is added if the relative abundances, for a given Z, of heavy elements is considered (see Table.4.1).

At first, as a base distribution, heavy elements with nearly solar abundances are considered. Usually, abundances for each element are given in a logarithmic scale (the hydrogen abundance is 12.00 in this scale) by $\log N_{el}/N_H + 12$ where the N_i are abundances by number. The adopted scaling is the one from Seaton et al. (1992) (Set 1), which is almost identical to Grevesse & Noels (1993). This initial elemental distribution is the one used in the stellar code starting from the ZAMS and during all evolutionary stages. In order to account for the variations, due to TDU, in envelope composition on the TP-AGB, 5 additional mixtures where considered (Sets 2-6). The sets are characterized by different values of the C/O ratio (in number). Besides the solar-scaled mixture, sets of tables for C/O values of 0.9, 1.0, 1.1, 3.0 and 20.0 are calculated. While carbon is the element that experiences major enhancement in our evolution code, the abundances of oxygen and nitrogen rise as well. To get a first approximative idea of the relative level of enrichment for each of the three elements and accordingly evaluate the necessary mixtures for the opacity sets, in order to mimic as accurately as possible the model variations, preliminary trial calculations were carried out. The evolution of carbon, oxygen and nitrogen was monitored at each inter-pulse phase after the occurrence of TDU. Having followed many TPs in some test cases (with the overshooting prescription presented in section 3.2.2 and with different mass-loss prescriptions) for $2M_\odot$ / $Z_{ZAMS} = 0.02$ models, approximate values for the envelope enhancement in these three elements were determined.

The different mixtures were then obtained by adding different average amounts (in number fractions), dX_C, dX_O and dX_N, of carbon, oxygen and nitrogen. Starting from the initial solar distribution, the C/O = 0.9, 1.0 and 1.1 mixtures where obtained for $dX_O = 1/3 dX_C$ and $dX_N = 1/10 dX_C$, the C/O = 3.0 for $dX_O = dX_N = 1/10\ dX_C$, and the C/O = 20.0 for $dX_O = dX_N = 1/40\ dX_C$.

In Table 4.1, each sets composition is given in logarithmic scale. After interpolation has been done in X and log Z for three tables with C/O values closest to the model one, a final parabolic polynomial interpolation in C/O is done. As the most abrupt opacity changes occur at the C/O = 1 transition, the 0.9 and 1.1 values have been chosen on each side of this critical point in order to better sample the region. Sets for C/O = 3.0 and 20.0 were considered to be appropriate for interpolations of any higher value.

As an example we plot in Figure 4.1 the behavior of our new opacity values with respect to temperature for different C/O mixtures. As can be seen the opacity profile changes significantly, passing by a minimum at C/O = 1, as C/O increases from 0.48 (the solar value) to 20.0. The big advantage of our approach is precisely that we are able to account for these opacity changes instead of only considering the C/O = 0.48 curve independently of the actual C and O relative abundances in the models. This variable-opacity issue in association with AGB models will be discussed in section 7.3.3.

Alternative sets of tables for a different - not solar-scaled - base composition were also constructed (Table 4.2). The reason for this, is that two main types of metal mixtures for stellar chemical compositions is nowadays distinguished: a solar-scaled one (Set 1) and another one, in which contrarily to most other metals, the α-elements are enriched. These heavy elements (O, Ne, Mg, Ca, Si, Ti) are produced on relatively short times scales ($\sim 10^7$ yr instead of a few 10^9 yr for iron which is mainly produced by Type Ia Supernova - Coelho et al.2007) in Supernova II explosions, when oxygen captures an α-particle. The enhancement of the α-elements with respect to their relative solar number fractions is of the order of 0.2 to 0.5 dex. It is still not very clear how these different metal scalings are related to stellar populations, but galactic Pop I and Pop II stars have traditionally been characterized by solar and α-enhancement distributions respectively. Furthermore, elliptical galaxies and the galactic bulge seem to be particularly rich in α-elements. It is therefore widely accepted that in addition to the solar one, stellar models need at least one more base metallicity mixture. Different compositions for opacity tables have been

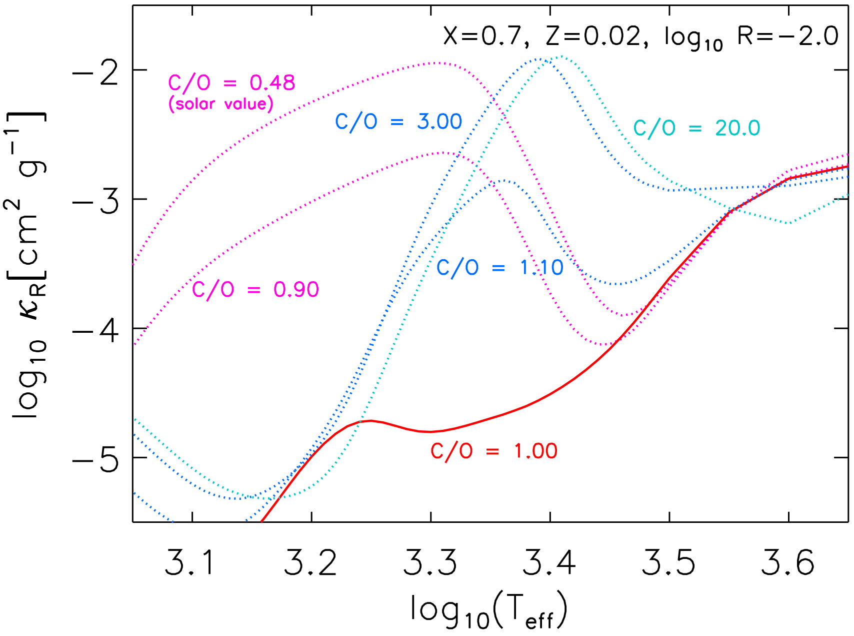

Figure 4.1.: Opacity profiles for different C/O ratios. Opacity values versus temperature (both in logarithmic units). Colored curves are representative of different C/O values as indicated on the figure. The important transition value C/O is indicated by a solid red curve. The data corresponds to the sets in Table 4.1 for a mixture specified by the given X, Z and R values.

.

implemented and not always with the same type of α-enhancement. In general, opacity table mixtures with, both varying or fixed enrichment factors for all α-elements have been used (e.g. Weiss et al. 2006, Coelho et al. 2007). In this work, Set 7 is obtained from Set 1 by adding a fixed 0.4 dex of abundance to O, Ne, Mg, Ca, Si and Ti. The effects of α-enhanced opacity tables in stellar evolution calculations was lately investigated by Weiss et al. (2006), but not the influence of a variable C/O chemistry on TP-AGB models. Thus, in order, once more, to consider TDU related surface changes, five additional tables (Set 8-12) for the same as previously C/O ratio values have been constructed.

Before finishing this section we quickly recapitulate on the work that has been done in order to generate our band-new opacity data.

J. Ferguson provided us with 12 newly calculated sets of 126 tables (WSU06) for the low-temperature regime. We obtained from the OPAL web-tool 12 corresponding sets for the high-temperature regime and subsequently merged them with the WSU96 ones. In our final sets, the tables cover the following temperature interval: $\log T$ = [3.00, 8.70]. The 12 sets actually consist of two groups of 6 sets presented in Tables 4.1 and 4.2 which are based on two different types of initial compositions (solar-scaled and α-enhanced). In each group, a set corresponds to a chemical mixture for a given value of the C/O ratio; these vary from the initial value (0.48 or 0.19) to 20.0 (intermediate values are 0.9, 1.0, 1.1 and 3.0). The mixtures with different C/O ratios have been obtained by increasing, with respect to the initial value, the amount of C, O and N in order to mimic the enhancements

Table 4.2.: Same as Table 4.1 but for a fixed α-enhanced distribution. Set 7 is obtained by adding 0.4 dex to the abundances of the α-elements (marked by an asterisk) of Set 1 (Table 4.1). Based on Set 7, the composition of Sets 8-12 have been calculated in a similar way to the solar-scaled sets for the indicated C/O ratios.

	Set 7 (α-enh.)	Set 8	Set 9	Set 10	Set 11	Set 12
el.	C/O = 0.19	C/O = 0.9	C/O = 1.0	C/O = 1.1	C/O = 3.0	C/O = 20.0
C	8.55	9.35	9.42	9.48	9.89	10.87
N	7.97	8.45	8.50	8.56	8.92	9.29
*O	9.27	9.40	9.42	9.44	9.42	9.57
*Ne	8.47	8.47	8.47	8.47	8.47	8.47
Na	6.33	6.33	6.33	6.33	6.33	6.33
*Mg	7.98	7.98	7.98	7.98	7.98	7.98
Al	6.47	6.47	6.47	6.47	6.47	6.47
*Si	7.95	7.95	7.95	7.95	7.95	7.95
P	5.45	5.45	5.45	5.45	5.45	5.45
*S	7.61	7.61	7.61	7.61	7.61	7.61
Cl	5.50	5.50	5.50	5.50	5.50	5.50
Ar	6.52	6.52	6.52	6.52	6.52	6.52
K	5.12	5.12	5.12	5.12	5.12	5.12
*Ca	6.76	6.76	6.76	6.76	6.76	6.76
*Ti	5.42	5.42	5.42	5.42	5.42	5.42
Cr	5.67	5.67	5.67	5.67	5.67	5.67
Mn	5.39	5.39	5.39	5.39	5.39	5.39
Fe	7.51	7.51	7.51	7.51	7.51	7.51
Ni	6.25	6.25	6.25	6.25	6.25	6.25

connected to dredge-up events on the AGB. Finally, in each set, the 126 tables correspond to different X-Z value combinations.

As a result, tracks of any arbitrary initial metallicity Z, for two separate base metal distributions can be evolved. These tracks are coupled to our opacity data. Once on the TP-AGB, where TDU events start modifying the surface composition, appropriate opacity tables are used in order to interpolate to any value of the C/O ratio.

5. Stellar Evolution code and Model Characteristics

The models presented in this thesis are produced with the Garching stellar evolution code, which will simply be referred to as the evolution code from now on. It is a descendant of the original Kippenhahn-code (Kippenhahn et al. 1967) and has been constantly updated over the years. The code has been partly described and its improvements successively reported by Weiss (1987, 1989), Wagenhuber & Weiss (1994), Weiss & Schlattl (2000) and Weiss et al. (2005). Finally, an up-to-date description of the code has recently been published in order to specifically introduce its main features and latest improvements. We therefore refer the reader to Weiss & Schlattl (2007) for more details. In this chapter we simply give some information on the relevant, for our work, characteristics.

In order to solve the set of partial differential equations of stellar evolution (Section 2.3), the numerical procedure adopted is the Henyey method. It is applied on the Lagrangian spatial grid (in relative mass coordinates $M_{\rm r}/M_{\rm star}$), which contains - in the present models - anywhere from about 1400 to 4500 points (e.g. during TPs) and adapts itself to structure changes. An algorithm controlling the grid resolution, guarantees that the equations are solved with a given accuracy. Because of the numerical improvements that have been implemented in the code over the years, in order to control the choice of the time-steps and the grid resolution (Wagenhuber & Weiss 1994), the He-flash but also many TPs on the AGB can be followed without convergence problems and intervention. There are two types of time-steps. The main evolutionary time-steps and the smaller nuclear time-steps. The nuclear time-steps which are subdivisions of one evolutionary time-step, adapt themselves to composition changes and are followed until the whole evolutionary time-step is covered.

Nuclear burning and particle transport are simultaneously computed in a single iterative scheme (implemented by H. Schlattl). For this work, we do not take into account particle diffusion nor semi-convection. Therefore, convection alone affects the transport of particles. It is treated in the most simple way, according to standard MLT with the Schwarzschild criterion for stability. The $\alpha_{\rm MLT}$ parameter was not calibrated but given a value of 1.75 for all models. This value is nevertheless very close to the one (1.71) calibrated to the solar model using the same code but with diffusion (Meissner & Weiss 2006). $\alpha_{\rm MLT}$ = 1.75 is also used in the grid of AGB models by Karakas (2003). As particle diffusion can be implemented in our code and convection is treated as fast diffusive process, convective overshooting as presented in Chapter 3 is easily included by specifying the appropriate diffusion coefficient. In particular we use a value of 0.016 for the overshooting parameter f at all convective boundaries during the entire evolution. Only on the MS for stars with an initial mass below $1.5M_{\odot}$ do we gradually increase the value of f from 0 (for $1.0M_{\odot}$) to the standard 0.016 value (for $1.5M_{\odot}$).

The nuclear network follows the evolution of the 9 species (^{1}H, ^{3}He, ^{4}He, ^{12}C, ^{13}C, ^{14}N, ^{15}N, ^{16}O, ^{17}O) that take part in the main energy production. Reaction rates are taken from different sources. For hydrogen burning, they are mostly from Adelberger et al. (1998). Helium burning reaction rates are by Caughlan et al. (1985) (CF85) and Caughlan & Fowler (1988) (CF88). All these rates have been updated when necessary. In particular two changes lately added in our code have been discussed by Weiss et al. (2005): the S-factor for the ^{14}N(p,γ)^{15}O bottleneck reaction of the CNO-cycle from the recent result by the LUNA collaboration (Formicola et al. 2004), and the 3-α rate from Fynbo et al. (2005) have been revised. Finally the rate of the very important ^{12}C(α,γ)^{16}O reaction was also updated with the Kunz et al. (2002) one.

The code incorporates the Irwin (see Cassisi et al. 2003) equation of state (EOS), based on the Eggleton et al. (1973) EOS, which is calibrated to the OPAL one (Rogers et al. 1996). The used opacity tables have been presented in Chapter 4 and mainly consist of a merger between two sources, the OPAL96 high-temperature tables (Iglesias & Rogers 1996) and the WSU06 low-temperature ones from Ferguson (2006). Mass-loss is considered throughout the entire evolution as exposed in Chapter 3.

Table 5.1.: The ten initial compositions used for the stellar models.

total metallicity type	super solar		solar		LMC		SMC		metal poor	
Z	0.04		0.02		0.008		0.004		0.0005	
X	0.635		0.695		0.731		0.743		0.7535	
Y	0.325		0.285		0.261		0.253		0.2460	
met. scaling	sol.	α-enh.	sol.	α-enh.	sol.	α-enh.	sol.	α-enh.	sol.	α-enh.
mixture	I	II	III	IV	V	VI	VII	VIII	IX	X

The initial helium mass fraction has been chosen according to $Y = Y_{p} + Z \cdot \Delta Y/\Delta Z$, where the Y_{p} is the primordial big bang nucleosynthesis helium abundance and $\Delta Y/\Delta Z$ the rate of fresh helium production supplied to the interstellar medium by stars with respect to their metallicity.

Values of $Y_{p} = 0.245$ and $\Delta Y/\Delta Z = 2.0$ have been chosen in our case. These are in agreement with many observational constraints. In particular, the latest publication on the 3rd year WMAP results give $Y_{p} = 0.24819$ (Spergel et al. 2007). This results is based on the analytical formula of Kneller & Steigman (2004) fitted on the new ΛCDM WMAP results. Other recent results in the literature are: $Y_{p} = 0.2384$ (Peimbert et al. 2002), $\Delta Y/\Delta Z = 2.5$ (Pagel & Portinari 1998), $\Delta Y/\Delta Z = 2.2$ (Casagrande et al. 2007), $\Delta Y/\Delta Z = 1.6$ (Balser 2006), $2.8 < \Delta Y/\Delta Z < 3.6$ (for $Y_{p} = 0.23$) and $2.0 < \Delta Y/\Delta Z < 2.8$ (for $Y_{p} = 0.24$) (Maciel 2001) and $\Delta Y/\Delta Z = 1.1$ (for $Y_{p} = 0.250$) (Fukugita & Kawasaki 2006).

For each initial helium content, five Z values are selected to specify the total metallicity mass fractions. These are Z = 0.04, Z = 0.02, Z = 0.008, Z = 0.004 and Z = 0.0005. They are chosen to approximatively represent super-solar, solar, LMC (Large Magellanic Cloud), SMC (Small Magellanic Cloud) and metal-poor type metallicities. Five (X, Y, Z) combinations have thus been used to determine the initial composition of the stellar models. Additionally, for each Z value, two separate distributions for the heavy elements have also been adopted: a solar-scaled and an α-enhanced one (see Section 4.3). Table 5.1 shows the ten final initial mixtures that are used and Table 5.2 the metal distributions for the solar and α-enhanced scaling types.

Table 5.2.: The two sets of metal distribution types chosen to initially set the composition of the models. Values are scaled logarithmically. The solar distribution is taken from Seaton et al. (1992) - it is almost identical to Grevesse & Noels (1993). For the α-enhanced one, 0.4 dex has been added to the abundance of the elements marked with an asterisk (the α-elements).

el.	solar	α-enhanced
C	8.55	8.55
N	7.97	7.97
*O	8.87	9.27
*Ne	8.07	8.47
Na	6.33	6.33
*Mg	7.58	7.98
Al	6.47	6.47
*Si	7.55	7.95
P	5.45	5.45
*S	7.21	7.61
Cl	5.50	5.50
Ar	6.52	6.52
K	5.12	5.12
*Ca	6.36	6.76
*Ti	5.02	5.42
Cr	5.67	5.67
Mn	5.39	5.39
Fe	7.51	7.51
Ni	6.25	6.25

With initial mass values ranging from $1M_\odot$ to $6M_\odot$, 11 models (1.0 / 1.2 / 1.5 / 1.6 / 1.8 / 2.0 / 2.6 / 3.0 / 4.0 / 5.0 / $6.0M_\odot$) have been computed for each of the ten compositions of Table 5.1. In principle, evolutions start on the ZAMS and end on the WD cooling track if no major numerical convergence problem are encountered. When difficulties occur, the models *crash* during, the AGB, or the last TPs of the TP-AGB, or an extra TP (LTP or VLTP) on the post-AGB or the born-again AGB phase after a LTP/VLTP has occurred.

From the total 110 initial models that reach the E-AGB, 100 of them evolve through the entire or a satisfactory part of the TP-AGB (for details see Chapter 7), while only 60 of them have a post-AGB evolution (see Chapter 8). We will now present and discuss our grid in the next three chapters.

6. From the ZAMS to the E-AGB

Although the study of AGB and post-AGB evolution is the main motivation of our calculations, for completeness, we look at some properties of the stellar models before reaching the TP-AGB. At the moment, we thus only focus on the preceding evolution. The TP-cycle study will be treated in the next Chapter.

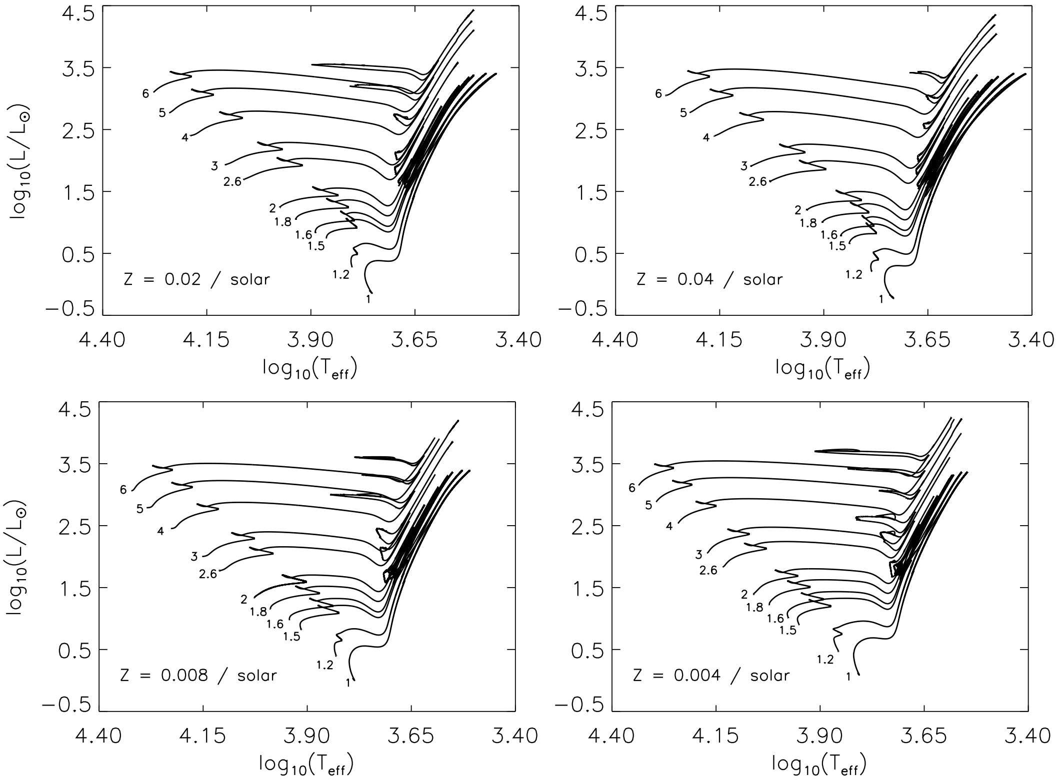

Figure 6.1.: HR diagrams for the Z = 0.04, 0.02, 0.008 and 0.004 solar-scaled mixtures. Initial ZAMS masses (in $M_{\odot}$) are given for each case. Tracks evolve until the 1st TP of the AGB.

The evolution prior to the TP-AGB is important for us because the history of each track affects the structure and the composition of the models that reach the 1st TP, at the beginning of the TP-cycle. In addition to presenting our models, we will compare them to other existing evolutionary computations, for which TP-AGB tracks are also available. The characteristics of the models that will mainly interest us, are the stellar lifetimes, the surface $^{12}C/^{13}C$ isotopic carbon ratio, and the core masses at the beginning of the TP-AGB. We also briefly comment on the He-flash of low-mass stars.

In Figure 6.1, the HR diagrams from the ZAMS to the E-AGB, for the four Z = 0.04, 0.02, 0.008 and 0.004 solar-scaled mixtures are presented. Similarly, in Figure 6.2, the tracks for the other four complementary mixtures with an α-enhanced scaling of the metals, are plotted. The models of both metal scalings for Z = 0.0005 are finally given in Figure 6.3.

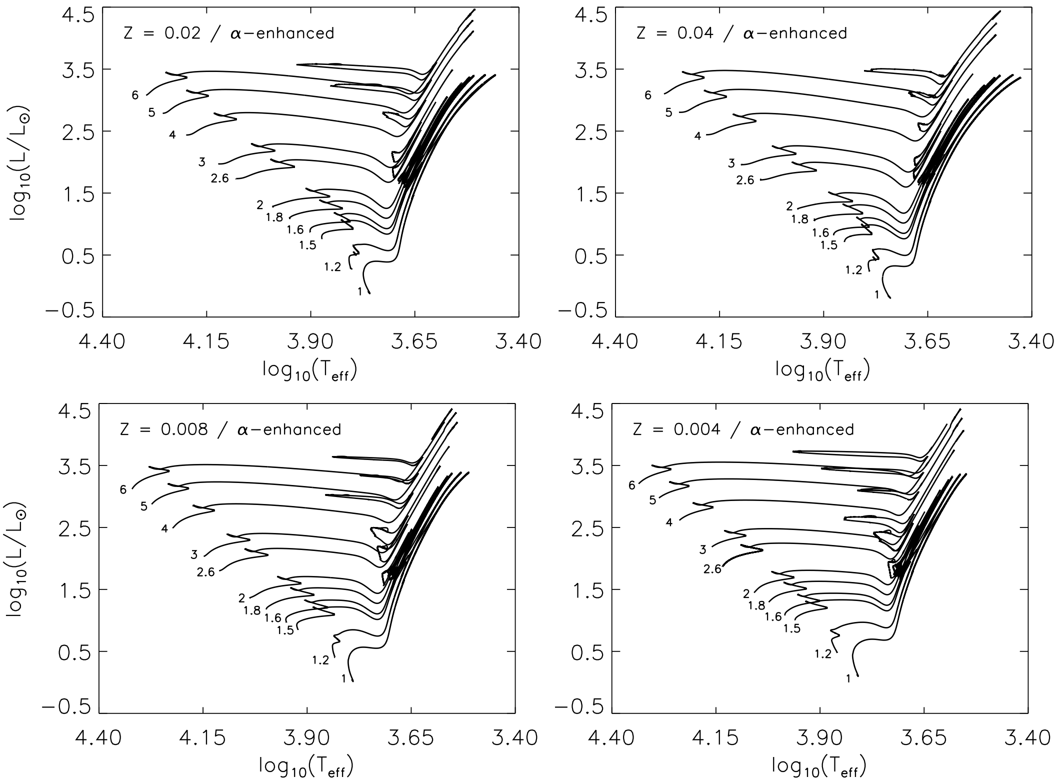

Figure 6.2.: Same as Figure 6.1 but for the four α-enhanced mixtures.

6.1. Lifetimes

The stellar lifetimes corresponding to the evolutionary tracks of Figures 6.1 - 6.3, are tabulated in Tables 6.1 - 6.3. The first column gives - in solar units - the initial ZAMS mass of the models. In the next four columns, values correspond to the times - in millions of years - in the following phases: MS (main sequence), RGB (red giant branch), helium core-burning, E-AGB. The two last columns give the total mass and the core mass at the beginning of the TP-AGB (1^{st} TP).

The end of the MS is taken to be the moment when the central hydrogen abundance drops below 0.01 in the calculations. At the moment a track reaches the tip of the RGB (highest luminosity - lowest temperature), the RGB phase is considered over. The end of core helium-burning is defined, similarly to core hydrogen-burning, by the first model for which the helium core abundance decreases to lower than 0.01 values. From there, the star is considered to be on the E-AGB until the 1^{st} TP is reached (the model with the highest helium-burning luminosity).

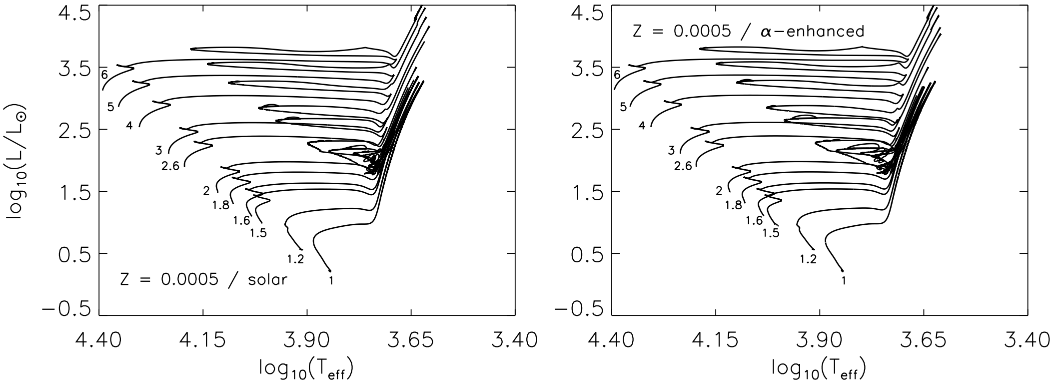

Figure 6.3.: HR diagrams similar to Figures 6.1 and 6.2 for both the solar-scaled and α-enhanced Z = 0.0005 models.

Lifetimes are affected by the included physics, mainly: convection, opacity tables, initial composition and reactions rates. In Chapter 3 the issue of convective overshooting was discussed and our prescription described. Overshooting will be specifically important during the TP-AGB phase, but here we first look at its prior influence on lifetimes.

Convective mixing in stellar interiors is an important source of uncertainty affecting stellar lifetimes, and the amount of overshooting that needs to be included is a debated topic. One effect of overshooting on evolutionary models is to prolong their lifetime. Overshooting increases the mixing efficiency. As a result, more fresh fuel is available during convective core-burning phases and the times spent on the MS and during He-core burning is longer.

Sets of TP-AGB tracks from two different studies which also provide the evolution and the lifetimes of the different phases before the AGB are those of Vassiliadis & Wood (1993) [VW93] and Karakas (2003) [K03].

The older VW93 models are evolved with nuclear rates from Harris et al. (1983) and Fowler et al. (1975) for hydrogen-burning. For helium-burning and beyond they have adopted the Caughlan & Fowler (1988) ones. Opacities used are those of Huebner et al. (1977). They do not have core overshooting, but do include semi-convection during core helium-burning. Convection is treated with $\alpha_{\rm MLT}$ = 1.6.

Z = 0.02 / solar							Z = 0.008 / solar						
$M_{\rm ZAMS}$	$t_{\rm MS}$	$t_{\rm RGB}$	$t_{\rm He\text{-}b}$	$t_{\rm EAGB}$	$M_{\rm tot}(1)$	$M_{\rm c}(1)$	$M_{\rm ZAMS}$	$t_{\rm MS}$	$t_{\rm RGB}$	$t_{\rm He\text{-}b}$	$t_{\rm EAGB}$	$M_{\rm tot}(1)$	$M_{\rm c}(1)$
1.0	8616.2	3350.1	110.17	12.971	0.709	0.501	1.0	6751.9	2521.0	104.48	10.369	0.742	0.513
1.2	4473.9	1555.6	106.47	12.368	0.981	0.509	1.2	3600.5	1182.0	97.963	10.474	0.999	0.521
1.5	2560.8	242.28	108.73	11.645	1.353	0.511	1.5	2097.9	193.39	99.367	9.8133	1.366	0.521
1.6	2091.5	172.58	110.80	12.243	1.476	0.508	1.6	1725.1	137.98	100.87	11.363	1.490	0.516
1.8	1465.8	99.847	130.85	13.305	1.595	0.496	1.8	1223.8	78.851	128.10	11.802	1.637	0.497
2.0	1075.0	58.364	177.34	15.417	1.895	0.478	2.0	900.54	32.110	236.41	14.571	1.941	0.464
2.6	510.25	12.302	140.08	10.175	2.530	0.518	2.6	448.03	9.9558	106.62	6.7430	2.506	0.569
3.0	344.35	7.1561	83.500	5.7529	2.900	0.596	3.0	309.24	5.9283	60.199	3.7127	2.863	0.672
4.0	161.46	2.7018	28.711	1.8755	3.821	0.765	4.0	152.27	2.3324	23.405	1.2466	3.812	0.801
5.0	92.624	1.3843	13.577	0.9122	4.800	0.830	5.0	90.826	1.2398	12.184	0.6929	4.776	0.868
6.0	60.471	0.8147	8.1598	0.4890	5.767	0.928	6.0	60.976	0.7491	7.7504	0.4100	5.711	0.991

Z = 0.04 / solar							Z = 0.004 / solar						
$M_{\rm ZAMS}$	$t_{\rm MS}$	$t_{\rm RGB}$	$t_{\rm He\text{-}b}$	$t_{\rm EAGB}$	$M_{\rm tot}(1)$	$M_{\rm c}(1)$	$M_{\rm ZAMS}$	$t_{\rm MS}$	$t_{\rm RGB}$	$t_{\rm He\text{-}b}$	$t_{\rm EAGB}$	$M_{\rm tot}(1)$	$M_{\rm c}(1)$
1.0	8648.4	3974.3	119.31	14.213	0.682	0.504	1.0	5771.4	2050.5	92.852	10.965	0.776	0.517
1.2	4788.6	1527.4	119.81	12.305	0.963	0.513	1.2	3141.2	966.74	94.451	9.3231	1.026	0.525
1.5	2697.1	231.58	122.80	12.425	1.349	0.513	1.5	1847.2	164.02	94.336	9.2462	1.383	0.527
1.6	2196.0	167.42	124.74	14.042	1.476	0.510	1.6	1525.1	117.01	103.22	9.0807	1.505	0.521
1.8	1527.7	96.664	158.38	13.966	1.611	0.496	1.8	1088.4	65.247	131.73	11.283	1.672	0.499
2.0	1108.6	54.286	226.81	17.353	1.903	0.481	2.0	812.67	27.464	199.22	11.361	1.935	0.488
2.6	509.95	13.146	140.91	10.013	2.518	0.528	2.6	410.03	8.5853	82.059	4.0737	2.472	0.639
3.0	337.90	7.6362	83.253	6.2347	2.893	0.596	3.0	286.74	5.2255	50.584	2.3417	2.834	0.744
4.0	151.95	2.8971	29.886	2.1740	3.826	0.750	4.0	145.00	2.1178	20.483	1.1477	3.801	0.809
5.0	84.428	1.4122	13.929	1.0935	4.791	0.810	5.0	88.228	1.1468	11.488	0.5852	4.775	0.894
6.0	53.949	0.8091	7.9334	0.5929	5.651	0.893	6.0	60.070	0.7068	7.5367	0.3372	5.700	1.060

Table 6.1.: Solar-scaled metallicity models. Evolutionary timescales from the ZAMS until the 1st TP. Time is given in 10^6 yrs. In addition to the initial ZAMS mass, $M_{\rm ZAMS}$, the total mass, $M_{\rm tot}(1)$, and the mass of the core, $M_{\rm c}(1)$, at the 1st TP are also given (in solar units).

Z = 0.02 / α-enhanced

$M_{\rm ZAMS}$	$t_{\rm MS}$	$t_{\rm RGB}$	$t_{\rm He\text{-}b}$	$t_{\rm EAGB}$	$M_{\rm tot}(1)$	$M_{\rm c}(1)$
1.0	8442.0	3065.5	112.02	10.614	0.713	0.502
1.2	4153.6	1607.1	105.88	10.772	0.985	0.508
1.5	2287.8	304.00	99.117	11.415	1.346	0.514
1.6	1865.5	212.48	109.24	9.9499	1.468	0.513
1.8	1465.8	99.847	130.85	13.305	1.569	0.501
2.0	1075.0	58.364	177.34	15.423	1.867	0.488
2.6	510.25	12.297	140.08	10.175	2.529	0.513
3.0	344.35	7.1561	83.500	5.7529	2.909	0.585
4.0	146.84	2.7657	28.801	1.9129	3.823	0.766
5.0	85.371	1.3850	14.328	0.8164	4.802	0.846
6.0	56.370	0.7959	8.3754	0.4509	5.715	0.946

Z = 0.008 / α-enhanced

$M_{\rm ZAMS}$	$t_{\rm MS}$	$t_{\rm RGB}$	$t_{\rm He\text{-}b}$	$t_{\rm EAGB}$	$M_{\rm tot}(1)$	$M_{\rm c}(1)$
1.0	6633.4	2419.4	98.966	10.164	0.755	0.508
1.2	3441.4	1194.1	98.397	9.2639	1.011	0.517
1.5	1971.4	218.60	97.908	8.8516	1.360	0.526
1.6	1619.9	154.04	100.92	9.3640	1.483	0.522
1.8	1147.0	86.083	118.83	11.511	1.616	0.505
2.0	850.65	35.418	238.79	15.050	1.939	0.464
2.6	421.73	10.360	111.36	5.6708	2.503	0.578
3.0	292.00	6.0452	62.486	3.2070	2.857	0.684
4.0	144.93	2.3134	22.858	1.3036	3.811	0.799
5.0	87.124	1.2145	121.36	0.6650	4.771	0.875
6.0	58.838	0.7307	7.5395	0.4267	5.713	0.996

Z = 0.04 / α-enhanced

$M_{\rm ZAMS}$	$t_{\rm MS}$	$t_{\rm RGB}$	$t_{\rm He\text{-}b}$	$t_{\rm EAGB}$	$M_{\rm tot}(1)$	$M_{\rm c}(1)$
1.0	8445.6	3482.5	111.90	13.314	0.678	0.505
1.2	4181.9	1728.5	107.84	12.716	0.964	0.512
1.5	2293.0	315.64	108.53	11.806	1.333	0.518
1.6	1861.1	222.36	109.39	12.835	1.462	0.514
1.8	1291.9	125.72	131.82	12.497	1.562	0.504
2.0	1108.6	54.286	226.81	17.853	1.855	0.494
2.6	509.95	13.146	140.91	10.013	2.520	0.515
3.0	337.90	7.6362	83.252	6.2347	2.908	0.574
4.0	132.12	3.0023	32.044	2.3654	3.804	0.749
5.0	74.606	1.4437	15.476	0.9332	4.753	0.830
6.0	48.420	0.8106	8.8116	0.4817	5.397	0.935

Z = 0.004 / α-enhanced

$M_{\rm ZAMS}$	$t_{\rm MS}$	$t_{\rm RGB}$	$t_{\rm He\text{-}b}$	$t_{\rm EAGB}$	$M_{\rm tot}(1)$	$M_{\rm c}(1)$
1.0	5696.1	2004.1	94.355	9.5685	0.784	0.515
1.2	3053.4	974.38	93.588	8.6953	1.032	0.523
1.5	1781.6	173.96	93.097	8.6722	1.379	0.531
1.6	1468.9	124.17	99.306	8.6461	1.498	0.529
1.8	1047.6	67.684	126.58	10.905	1.662	0.506
2.0	782.24	28.666	197.48	10.426	1.933	0.494
2.6	392.18	8.6687	79.021	3.9082	2.469	0.648
3.0	277.07	5.2243	48.452	2.5145	2.833	0.744
4.0	140.83	2.0926	21.321	0.9967	3.801	0.827
5.0	86.130	1.1276	11.536	0.5443	4.786	0.908
6.0	58.868	0.6937	7.1015	0.3700	5.740	1.050

Table 6.2.: Same as for Table 6.1 but for the α-enhanced metallicity models.

Z = 0.0005 / solar							Z = 0.0005 / α-enhanced						
$M_{\rm ZAMS}$	$t_{\rm MS}$	$t_{\rm RGB}$	$t_{\rm He\text{-}b}$	$t_{\rm EAGB}$	$M_{\rm tot}(1)$	$M_{\rm c}(1)$	$M_{\rm ZAMS}$	$t_{\rm MS}$	$t_{\rm RGB}$	$t_{\rm He\text{-}b}$	$t_{\rm EAGB}$	$M_{\rm tot}(1)$	$M_{\rm c}(1)$
1.0	5041.2	1262.2	83.219	9.4308	0.847	0.523	1.0	5034.3	1246.6	82.220	9.1452	0.843	0.527
1.2	2662.3	727.55	86.164	7.4351	1.078	0.537	1.2	2650.9	725.59	80.412	8.3182	1.077	0.538
1.5	1560.7	158.70	73.039	6.7829	1.351	0.570	1.5	1536.4	142.67	87.219	6.1783	1.409	0.559
1.6	1278.6	104.02	87.687	6.7574	1.521	0.561	1.6	1268.5	104.90	91.057	5.9047	1.523	0.562
1.8	912.34	46.277	147.74	6.5325	1.701	0.551	1.8	904.79	47.096	144.84	6.4154	1.700	0.554
2.0	682.51	22.101	127.21	5.6236	1.906	0.584	2.0	676.61	22.188	126.53	5.4208	1.903	0.588
2.6	351.50	7.1310	59.160	2.4622	2.464	0.732	2.6	348.59	7.1208	59.499	2.3104	2.467	0.737
3.0	250.82	4.4426	39.685	1.6650	2.857	0.780	3.0	249.01	4.4098	38.353	1.7691	2.859	0.777
4.0	132.50	1.8581	17.728	0.8079	3.867	0.848	4.0	131.74	1.8480	17.972	0.7419	3.871	0.862
5.0	83.085	1.0331	9.9502	0.4567	4.875	0.937	5.0	82.733	1.0312	9.8540	0.4491	4.878	0.943
6.0	57.746	0.6695	6.3498	0.4317	4.208	1.128	6.0	57.554	0.6858	6.2844	-	-	

Table 6.3.: Same as for Tables 6.1 and 6.2 but for both the α-enhanced and solar-scaled Z = 0.0005 models.

K03 uses nuclear burning rates from Caughlan & Fowler (1988) with the exception of ^{1}H(p,$\epsilon + \nu$)^{2}H that is from Harris et al. (1983). Opacity values are taken from a variety of sources, but are basically the OPAL96 opacities at high temperatures combined with the Huebner et al. (1977) and Cox & Stewart (1970b,a) at lower temperatures. She does not include overshooting nor semiconvection, and uses a $\alpha_{\rm MLT}$ = 1.75 for convection.

Both K03 and VW93 present three sets of different metallicities that correspond to solar, LMC and SMC compositions. K03 does calculations with the following (Y, Z) initial mixtures: (0.2928, 0.02), (0.2551, 0.008) and (0.2476, 0.004). The three sets of VW93 correspond to (0.25, 0.016), (0.25, 0.008) and (0.25, 0.004), where the He content is kept constant.

Our corresponding tracks are the ones with the following mixtures: (0.285, 0.02), (0.261, 0.008) and (0.253, 0.004).

The first remark is that our MS lifetimes lie somewhere in between the K03 and VW93 ones. As the left side of Figure 6.4 shows, the general trend is well matched. Our ages are longer than the K03 ones but shorter than the VW93. As total metallicity decreases - from top to bottom - the different results agree better and better. But the lifetimes in the plots are given in logarithmic units, in absolute values they correspond to differences of the order of 10%.

In more detail, for the solar-type metallicity case, we get lifetimes on average higher by 12% with respect to K03 and 17% lower than the VW93 results. For both cases combined, the biggest difference is the lower age by 30% (2.6 billion years) for our 1M$_\odot$ model in comparison to the VW93 one, and the smallest is between our 5M$_\odot$ and the older by 3 million years model of VW93 (the difference is ≈3%).

For the Z = 0.008 tracks, average differences are 10% and -12% respectively for K03 and VW93. They are even smaller for the Z = 0.004 case, where they only differ by 6% and -7%.

One reason for the differences encountered with the VW93 models are the initial compositions considered as also pointed by Karakas (2003). VW93 use the same helium abundances (0.25) for each of the three metallicity cases. While this value is close to our 0.253 one for the Z = 0.004 models - which also give the best agreement -, the Y values are increasingly different for the other two metallicity types (for the solar-type metallicity, ΔY = 0.032). For the same metallicities we therefore have more helium. A higher Y means a lower X value. As the MS lifetime depends on the amount of hydrogen available our models have shorter lifetimes. They can however not be as short, for the solar metallicity case, as those from K03 since she has an even higher Y value of 0.2928. We have not run models with a lower initial helium content in order to estimate the differences brought in our models by these chemical composition differences, but we suppose the outcome is similar than for K03 who find that their disagreement with VW93, which is larger than ours, drops to less than 10% for similar initial composition. For the Z = 0.008 and Z = 0.004 models, where our initial compositions are closer, lifetime differences are indeed less than 10%.

The fact that our values agree well with the K03 ones and that the discrepancies observed for both with VW93 are mainly due to initial composition is further asserted if we compare some test models (solar metallicity) that we ran (black triangles in Figure 6.4) without

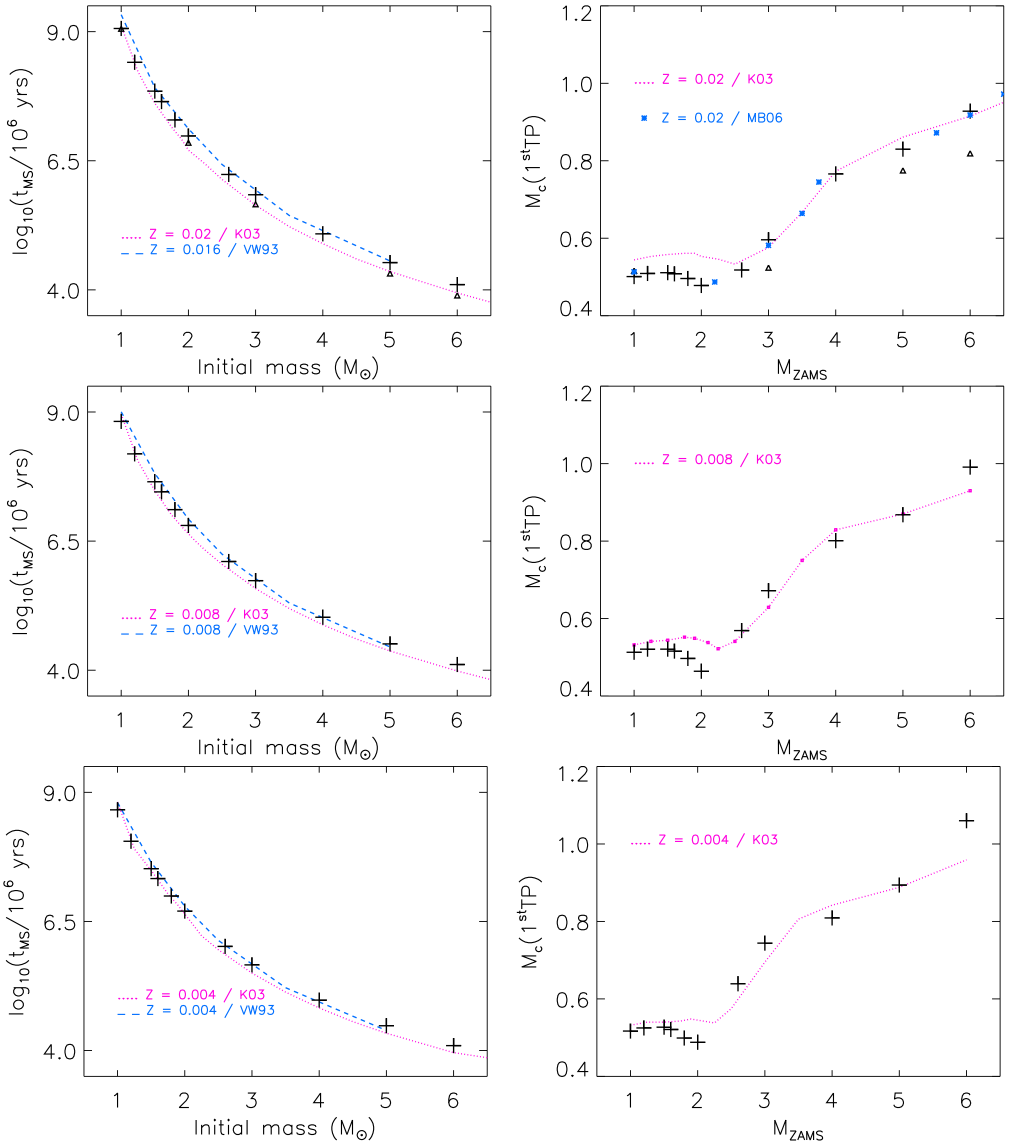

Figure 6.4.: The black crosses indicate our values. The black triangles in the uppermost two panels are models with no overshooting. The dashed blue lines correspond to results from VW93, and the red dotted lines to the models of K03. The blue diamonds are values obtained by Miller Bertolami (2006) [MB06]. *Left* - MS lifetimes with respect to initial ZAMS mass. *Right* - core masses at the end of the E-AGB with respect to initial ZAMS mass (in $M_\odot$).

the inclusion of overshooting. The 4 models seen in the top left panel for the 2, 3, 5 and

$6M_\odot$ cases have been computed with identical code parameters except for overshooting which has been switched off. It is obvious that the agreement with the K03 results (who also do not use overshooting) is very good. For the actual differences in years, they are only of the order of a few percent. As an example, for the $3M_\odot$ track, our MS lifetime is only 5 million years higher (this corresponds to about 2%). Therefore we can conclude that the main difference between our models and the ones from K03 - which originate from two distinct codes but use the same, high-temperature opacities, reaction rates and α_{MLT} - are mainly due to core overshooting which increases the central hydrogen-burning time.

We do not show any graphical representation but simply note that the general trend for the MS lifetimes of our models is decreasing for decreasing initial metallicities. This is expected because lower metallicities produce lower opacities and thus higher luminosities and effective temperatures, which finally render shorter lifetimes. The shorter MS durations are thus given by the Z = 0.0005 models, and the longer ones for Z = 0.04. The biggest difference is between the $1.2M_\odot$ models of these two metallicity cases where the difference reaches 44% (2.1 billion years). For higher mass models the differences between the highest and lowest metallicity cases are smaller (they drop to $\approx$ 1.6% for the $5M_\odot$ case). These trends agree with the results of K03, VW93 and also of other stellar model grids (e.g. Girardi et al. 2000). Finally the effect of the metal scaling in our models brings a slight decrease in age for the α-enhanced calculations for each metallicity type of the order of a few percent.

For $M_{\mathrm{ZAMS}} < 2M_\odot$, our core He-burning lifetimes are in good agreement, irrespective of metallicity, with the older results, as they either match the K03 lifetimes very well (2 to 3%), or lie in between the VW93 and K03 values. But for higher masses, our results are significantly different than those of both VW93 and K03. They are actually much lower for all three comparison compositions. The lifetimes of K03 were already below the ones of VW93, ours are even shorter. According to K03, their discrepancies with respect to VW93 are mainly due to a different treatment of semi-convective mixing (Castellani et al. 1985), the suppression of core-breathing pulses in the VW93 models and opacities. We use, like K03, the OPAL96 opacities and no semi-convection, but we include core overshooting, whereas K03 does not. As an example, our $3M_\odot$ model for Z = 0.008 is 37.2 million years younger the the same K03 evolution. This age deviation corresponds to to a 62% difference. The deviation is even larger when compared to the VW93, where ages are older. If we neglect overshooting in our models this difference is amplified. Another example is for a $5M_\odot$ evolution with solar metallicity, VW93 obtain a core He-burning lifetime of 23.53 million years, K03 gets 19.885 and our models give 13.577.

One additional update in our calculations with respect to both VW93 and K03, is the very important $^{12}C(\alpha,\gamma)^{16}O$ reaction. We use the latest rate from Kunz et al. (2002). Instead, K03 and VW93 both incorporate the reaction rate given by Caughlan & Fowler (1988) [CF88]. This rate is important because the core helium-burning time depends on it. The general trend is that faster rates for this reaction lead to longer lifetimes. This was presented by Bono et al. (2000) who compare the effect of three rates: the Caughlan et al. (1985) [CF85] (it is $\approx$ 2.35 times faster than the CF88), the CF88 and another one 1.7 times the CF88 rate. The biggest difference is found between the slowest CF88 and the fastest CF85 rates with core helium-burning lifetimes of about 10% longer for CF85.

We have ran 3 extra test calculations (2, 3 and 5$M_\odot$ with solar metallicity) with the old rate to analyze the differences. Our default new rate (Kunz et al. 2002) and the old one (CF85) used in our code, are both higher than the CF88 by about a factor of 2 at helium-burning temperatures. The CF85 rate is nevertheless still faster than the Kunz et al. (2002) one. Therefore, a small decrease is observed in our models since the new rate (Kunz et al. 2002) produces shorter lifetimes by 4.9, 1.4, and 4.4% respectively.

These comparisons within are own code and the work by Bono et al. (2000) show that the new $^{12}C(\alpha,\gamma)^{16}O$ rate can not explain the large discrepancies found with the core helium-burning lifetimes of both VW93 and K03 - which in any case also do not agree between themselves. These two studies use the slowest CF88 rate. Any of the other older or more recent rates are faster. Therefore, lifetimes with the CF88 rate represent the case of shortest possible lifetime with respect to this reaction. Longer lifetimes for VW93 and K03 would render a even more significant difference with our calculations.

We have also compared our results with core He-burning lifetimes from the Padova Stellar Database given by Girardi et al. (2000). These authors use a rate for the above reaction that is 1.7 times the CF88 one, therefore close to the one that is incorporated in our models. They also include helium core overshooting (with a different prescription than ours). The agreement with our helium core-burning lifetimes is, if not that good, at least better than with the K03 ones. For the 5$M_\odot$ models we get higher ages by 12% and 14% for solar and LMC metallicities. The fact that our values are higher is agreement with our faster rate which is 2 times as fast (instead of 1.7) as the CF88. On the contrary the values of K03 which are higher than ours have differences approaching 100% with those of the Padova Database. For the 3$M_\odot$ models of the same metallicities the differences between our models and the Padova ones are more significant but again less important than with the K03 ones. In the following order, K03, Padova Database and our results, the values are: a) for solar metallicity, 115.4, 98.6 and 83.5 million years, b) for LMC metallicity, 97.4, 79.0 and 60.2 million years. We do not have an explanation for these disagreements, but note that our differences deviate by an extent similar to the one already found between these previous studies.

6.2. The $^{12}C/^{13}C$ surface ratio at the FDU

As noted in Chapter 5, we only follow the evolution of a limited number of relevant species involved in the major energy-producing reactions. We do not have a full nucleosynthesis code containing a big number of species. Detailed surface abundances are therefore not our primary concern.

Nevertheless we do follow the surface abundance variations for the most important elements, for example carbon, oxygen and nitrogen which will be of paramount importance on the TP-AGB because of the influence of TDU and HBB phenomena on the evolution. For this reason, overshooting was included in the stellar code in order to obtain efficient TDU on the TP-AGB. But it has also been considered during the other phases of evolution. VW93 and K03 do not use overshooting at all on the TP-AGB or during the previous evolution. On the contrary, F. Herwig and collaborators (Herwig et al. 1997, Herwig 2000, Lugaro et al. 2003, Herwig 2004a,b), who include overshooting on the TP-AGB, also use it during the entire evolution at all convective boundaries. As seen in Chapter 2, mixing events from a deepening convective envelope can also occur on the RGB, the FDU episodes. Having already adapted a first time the overshooting efficiency for low-mass stars (between $1M_\odot$ and $1.5M_\odot$) during core hydrogen-burning phases in order not to obtain any unrealistic effects (perpetuation of an inexistent convective core because of the inclusion of overshooting), it is with the same concern that we investigate the consequence of overshooting with our prescription on the RGB. In particular, we look at the ^{12}C/^{13}C surface ratio.

This carbon isotopic abundance ratio has been used to trace the FDU mixing event. ^{12}C is present in the photospheres of MS stars, but ^{13}C is only present after products of the CN cycle of nuclear reactions reach the surface via convective mixing. The presumed primordial value (i.e. solar value) is about 90, but a decrease to values of 20-40 is expected due to the FDU. There seems to be an agreement between theoretical models and observations on the values of this ratios for intermediate-mass stars (e.g. Boothroyd & Sackmann 1999) but not for low-mass stars (e.g. Charbonnel et al. 1998). Furthermore, values as low as 3-4, which is the nuclear CN-cycle equilibrium value, have also been measured by other groups (e.g. Smith et al. 2002, Pilachowski et al. 2003). Standard models of RGB stars do not predict such low ratios after the FDU but rather values that only go as low as ≈ 20. In order to explain these differences, an “excess” mixing mechanism that would penetrate deeper into the star has been invoked as a necessity to explain the data. One theory proposed for this extra mixing at the base of the convective envelope is the meridional circulation caused by rotation on the RGB. More recently Eggleton and collaborators advance the following explanation: a molecular weight inversion created by the ^{3}He(^{3}He, 2p)^{4}He reaction is responsible for the extra mixing (Eggleton et al. 2006, 2007); they attribute it to the Rayleigh-Taylor instability. Finally, Charbonnel & Zahn (2007) argue that the non-canonical mixing process is instead due to a double diffusive instability called thermohaline convection.

The top graphic in Figure 6.5 shows the maximum extend of the base of the convective envelope during the FDU episode with respect to initial mass for the five different solar-scaled metallicities. Deepest FDU occurs for the Z = 0.04 case and the shallowest for the Z = 0.0005. This trend of increasing FDU with metallicity is compatible with previous works (Karakas 2003, Boothroyd & Sackmann 1999). For stars with masses below $2M_\odot$ the differences are not so important. Only for higher mass stars is the metallicity effect considerable. Our graphic can be compared to figures 3.5 and 2 respectively in K03 and Boothroyd & Sackmann (1999). A similar behavior of the deepening convective envelope is observed in all cases and the values are very close. The higher metallicity case (Z = 0.04), not present in both of these previous calculations, has almost identical values than the Z = 0.02 one in our case. This seems to suggest that the inwards extent of the envelope reaches a maximum plateau for high enough values of Z instead of increasing like for less metal rich models. On the other hand, the depth increase (up to $\approx 0.3M_{\rm star}$) from Z =

0.0005 to Z = 0.004 is considerable for intermediate-mass models.

The bottom panel of Figure 6.5 shows the $^{12}C/^{13}C$ ratio as a function of initial mass for the same five metallicities. It can be compared to figures 3.7, 3.8 and 3.9 in K03 and figures 3 and 4 in Boothroyd & Sackmann (1999). For the low-mass models values are very close for all Z, but for the intermediate-mass stars, numbers decrease with diminishing metallicities. This trend is also obtained by K03 and Boothroyd & Sackmann (1999). Our values range in the interval [23, 35], having an initial ratio - before FDU - of about 92 for all five solar-scaled metallicities. The expected main decrease is therefore obtained, but ratios never reach lower equilibrium values around 3 to 4. The ratios obtained with the K03 code are very close for the Z = 0.02 case but differ a little more for the LMC and SMC metallicities. This is to be expected since K03 uses an initial abundance spread scaled to the solar composition only for Z = 0.02 but not for Z = 0.008 and Z = 0.004. While she has an initial ratio value of about 90 for Z = 0.02, it is of 36.4 (Z = 0.008) and 34.8 (Z = 0.004) for the other two cases. Our five compositions in Figure 6.5 on the other hand, always have solar-scaled distribution. For a given Z, the lowest $^{12}C/^{13}C$ ratios are obtained for the higher mass stars: if we take the $6M_\odot$ cases (except for the Z = 0.0005 model), our values in order of decreasing metallicity are, 25.2, 24.9, 24.3 and 23.7 (Z = 0.04, 0.02, 0.008, 0.004). This is in agreement with the number presented by K03 which

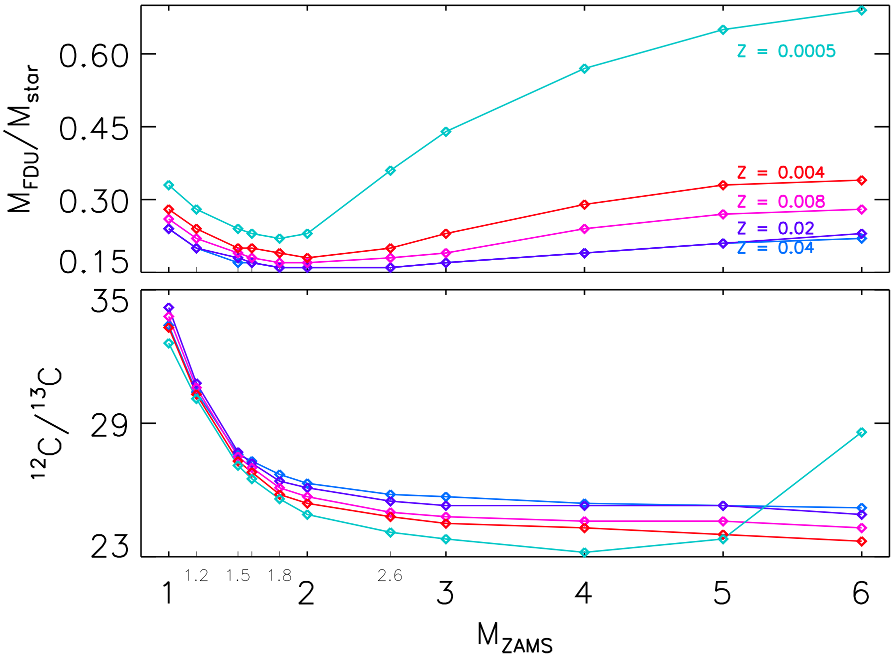

Figure 6.5.: As a function of initial stellar mass: *top panel* - maximum depth (in relative mass coordinates) reached by the bottom of the convective envelope during the FDU on the RGB, *bottom panel* - surface number abundance ratio of $^{12}C/^{13}C$ after the FDU occurrence.

are nevertheless a little lower. For the 0.02, 0.008 and 0.004 metallicities, K03 obtains for the same mass star, ratios of about 22.8, 16.9 and 16.4 respectively - these correspond to differences of 9, 30 and 31%. For the solar metallicity case, for which initial metallicity abundances are similar we see that the agreement is better than 10%.

We thus recognize that our overshooting prescription, necessary for the TP-AGB, gives our models $^{12}C/^{13}C$ surface abundances during the FDU that are in accordance with other codes which do not include convective overshooting.

6.3. The Core He-Flash

Low- and intermediate-mass stars are separated by the occurrence or absence of the He-flash on the first giant branch. As the inactive core, after the exhaustion of central hydrogen, contracts and heats up, while ascending in the giant region, helium burning will start when the required temperature is reached ($\approx$ 100 million K). Low-mass stars need to contract much more in order to approach those temperatures; in the meantime the electron-degeneracy develops. While more massive stars ignite helium peacefully in the center, low-mass stars perform this initial burning explosively at a location that is off-centered by a couple of tenths of mass coordinate.

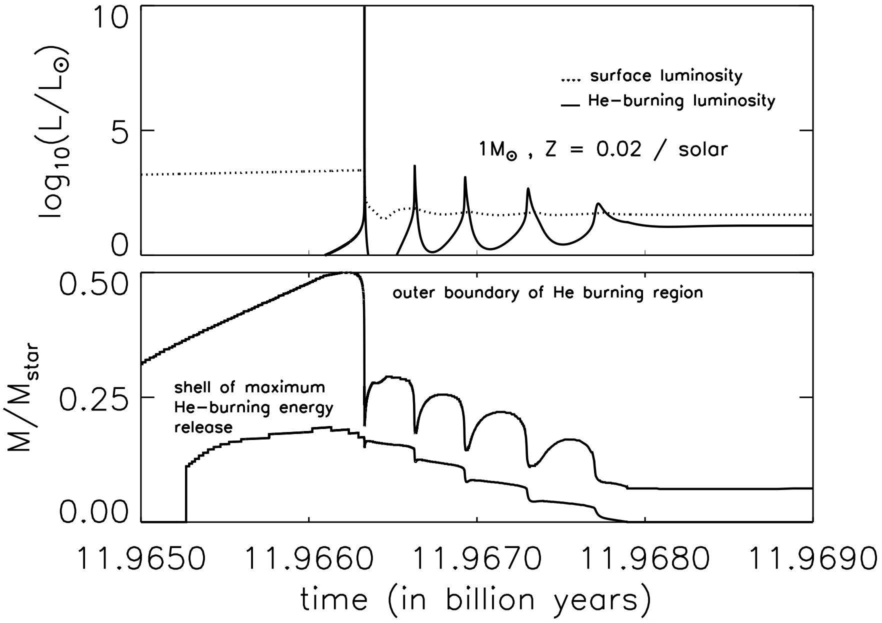

Figure 6.6.: Model experiencing a He-flash. *Top panel* - total and helium-burning luminosities vs time. *Bottom panel* - time evolution of two helium-burning region mass shells: the location of maximum energy release and the outermost boundary with helium-burning.

Whether helium ignition happens peacefully in the core of intermediate-mass stars or through the He-flash for low-mass stars, the total surface luminosity does not vary by considerable amounts in both cases. But during a He-flash the helium-burning luminosity increases by many orders of magnitude. It can reach up to $10^{10} L_\odot$ (for a few hundred thousand years) which is much more than the few hundred or thousand times the solar luminosity for the more massive stars.

In Figure 6.6 two graphics present the evolution during a He-flash for a $1 M_\odot$ star with solar composition. The small variation of the radiated surface luminosity is plotted together with the big luminosity jump of the helium-shell. After the flash, which reaches 10^{10} times the solar luminosity, a few small oscillations occur before peaceful burning settles in. In the bottom panel, we show the location of the helium-burning shell of maximum energy release during the flash. We see how the first ignition happens at a mass coordinate of about 0.12 and reaches almost 0.2 during the highest helium-burning luminosity. The outer boundary of the helium-burning region is also plotted, and the oscillations are once more present.

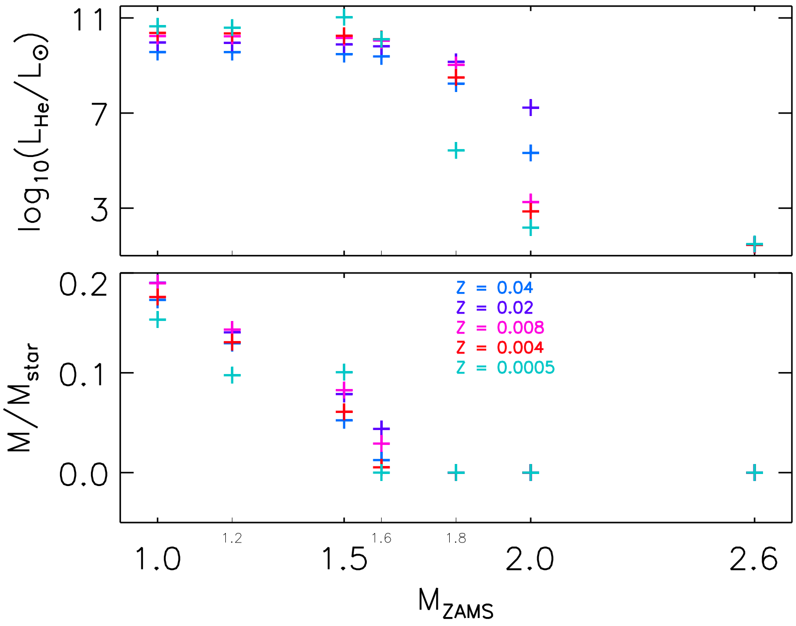

Figure 6.7.: Evolution on the tip of the RGB for stars with initial masses from $1 M_\odot$ to $2.6 M_\odot$. *top panel* - maximum helium-burning luminosity after central helium ignition. *bottom panel* - maximum extent of helium-burning shell with highest energy release. [values are superposed for masses where only one metallicity seems to be plotted]

The separation between intermediate- and low-mass stars is not clear, since it depends on metallicity and in general model details. For example, models with and without core overshooting behave differently in this respect: when convective overshooting is not included, a He-flash tends to occur for stars of higher mass.

Figure 6.7 presents the highest helium-burning luminosity reached on the RGB during central helium ignition for all our models (here only the ones below $2.6M_\odot$ are shown) with solar-scaled metallicities. The maximum extent of the shell of highest energy release is also plotted in the bottom panel. We see that the trend is similar independent of metallicity and that no models above $2M_\odot$ go through the He-flash. While the severity of the flash increases - higher helium-burning luminosities and core temperatures because of stronger degeneracy - for lower Z values at masses from $1M_\odot$ to $1.6M_\odot$, higher metallicity models seem to continue having moderately high helium luminosities for higher initial mass. Indeed for $2M_\odot$ stars, the strongest energy release happens at the center for all values of Z, but the two higher metallicity models reach 10^5 and $10^7L_\odot$, which is much higher than the two lower Z ones. Actually for all stars with initial masses higher than $1.8M_\odot$, helium is ignited at the center. In our models, which include overshooting, the boundary between low- and intermediate-mass stars is thus between $1.8M_\odot$ and $2M_\odot$. Only the two higher metallicity $2M_\odot$ models experience “mild” (10^5 and $10^7L_\odot$) flashes for a short time. In comparison, models of K03 give a maximum initial mass for a He-flash to occur at about $2.25M_\odot$. This value is higher than ours but she does not include overshooting. Models with core overshooting obtain lower values: Bertelli et al. (1986) get about $1.6M_\odot$ and Herwig (2005a) sets according to his models the low-mass star boundary at $1.8M_\odot$. This agrees well with our value (for further discussion on the metallicity dependent low/intermediate-mass star boundary in section 7.3).

6.4. Core Mass at the 1^{st} TP

After helium core exhaustion, the star is said to be on the E-AGB and starts to climb once more in the giant region of the HR diagram. As it reaches the end of the E-AGB, before the onset of the instability flashes, one property characterizing the structure of the star, that will play an important role in the subsequent evolution, is the mass of the core. The interest on the size of the core comes from the fact that at the end of the TP-AGB the remaining bare core will become the future WD.

During the TP-AGB, on the one hand the piled-up nuclear burning ashes increase the size of the central inert core, but on the other the mass lost by the envelope reduces the available fuel and ultimately stops the growth of the central region. It is thus the competition between these two phenomena that mainly regulate the final outcome and the end of the TP-AGB. As nuclear burning is more or less constant, it is the rate at which the envelope material is lost that becomes important. A weak mass-loss rate will give the core time to grow and a strong one should result in a post-AGB object of smaller size. Parameters indirectly influencing the mass-loss rate are, temperature, luminosity, composition, mass of the star, TDU, HBB, opacities etc. But some of these quantities can also directly influence the size of the core. For example, as part of the material is dredged-up at each TDU episode and mixed into the envelope, if the TDU is efficient enough - compared to the growth of the central part after the last deep penetration of the envelope - the size of the core can be reduced.

When studying the TP-AGB evolution the question is therefore to see if, with respect to its mass at the beginning of the TP-cycle, the size of the core will actually grow, remain the same or decrease. For this reason it is necessary to know the size of the core we start off with at the end of the E-AGB phase. Additionally, the time spent on the TP-AGB also depends on the initial remaining envelope mass that needs to be ejected between the 1st TP and the beginning of the post-AGB evolution when the star moves to higher temperatures.

The total mass of the star and the core mass at the 1st TP are given in the last two columns of Tables 6.1 - 6.3. Low-mass stars have already lost a considerable amount of their envelope (up to 32% of the total mass for the $1M_{\odot}$, $Z = 0.04$ / α-enhanced model) during the previous evolution - mainly on the RGB. But the more massive intermediate-mass models remain almost as massive as on the MS - they lose on average only a few percent of their total mass - because they spend less time as giants.

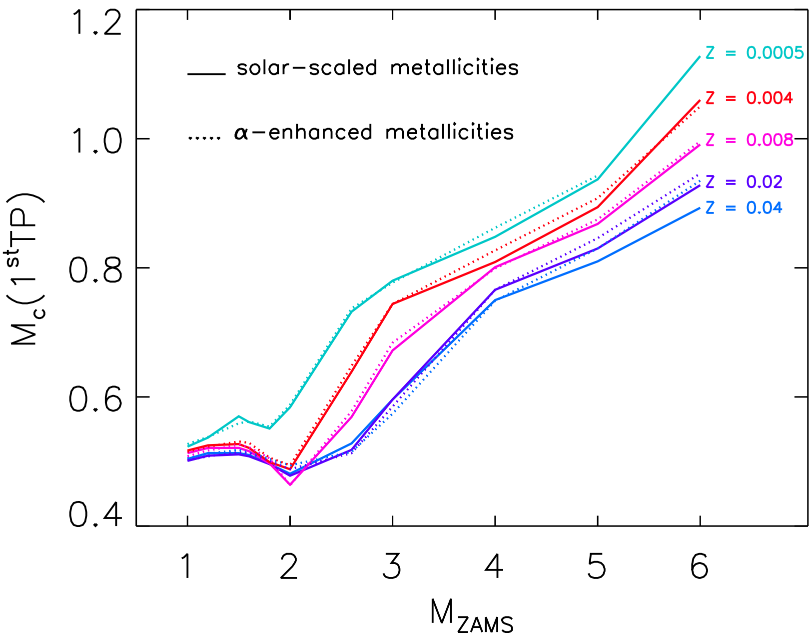

Figure 6.8.: Mass (in $M_{\odot}$) of the core at the 1st TP with respect to initial ZAMS mass (in $M_{\odot}$).

This is the reason why, as presented in Chapter 3, we have chosen a different Reimers mass-loss parameter η_R for the two cases. All our models up to $1.6M_{\odot}$ have $\eta_R = 0.4$ and the ones starting at $1.8M_{\odot}$ are calculated with $\eta_R = 1.0$. This is similar to the prescription adopted by Blöcker (1995b) for calculations leading to TP-AGB models. He uses 0.5 for the 1 $M_{\odot}$ case and 1.0 for 3 $M_{\odot}$ on the RGB. K03 uses only a 0.4 Reimers parameter for all stars. On the other hand VW93 does not include mass-loss before the AGB for $M_{\rm ZAMS} > 1{\rm M}_\odot$. Finally, Herwig et al. (2000) also use an almost identical prescription to ours with a 0.5 value for $M \leqq 1.7{\rm M}_\odot$ and 1.0 for all higher mass. Therefore, our choice corresponds well to what has been previously used, especially in the most recent calculations, and for the pre-AGB evolution was mainly made for compatibility with the early evolution of existing TP-AGB grids.

In Figure 6.8 we present the core mass at the $1^{\rm st}$ TP with respect to the initial ZAMS mass of the models. The colored curves represent the five different metallicities. Solid lines are for the solar-scaled compositions and the dashed ones for the α-enhanced mixtures.

For masses between $1{\rm M}_\odot$ and $2{\rm M}_\odot$, core sizes are very similar for all compositions. After a drop in core mass for stars with $M_{\rm ZAMS} = 2{\rm M}_\odot$, a metallicity dependence is clearly visible: lower metallicity models render higher mass cores. But the increasing behavior is the same for all Z. Small differences exist between the solar-scaled and the α-enhanced models, the later ones having cores slightly larger for the most part. The largest spread observed between models of different Z values is for the $3{\rm M}_\odot$ and the $6{\rm M}_\odot$ cases. In order of increasing metallicity for the five solar type mixtures, the sizes (in ${\rm M}_\odot$) are 0.780, 0.744, 0.672, 0.596 and 0.596 in the $3{\rm M}_\odot$ case, and 1.128, 1.060, 0.991, 0.928 and 0.893 in the $6{\rm M}_\odot$. These correspond to spreads respectively of 24 and 21%.

We have also compared our core masses with existing sets of models in the left side of Figure 6.4. From top to bottom, the red dotted curves represents results given by K03 for the 0.02, 0.008 and 0.004 metallicities. For all three cases our values match the trend and the values between $2.6{\rm M}_\odot$ and $5{\rm M}_\odot$ very well. For the low-mass stars, agreement is increasingly better as we decrease the initial mass. The biggest discrepancies for all three metallicities arise for the $2{\rm M}_\odot$ model. As an example, for the solar mixture case our result is 0.478 compared to 0.553 from K03, thus a value lower by 14%. The $6{\rm M}_\odot$ tracks for LMC and SMC metallicities also do not agree very well with the K03 values.

For the solar composition case, the models of Miller Bertolami (2006) (blue diamonds in the top right panel of Figure 6.4), who use a similar code, include the same overshooting prescriptions and RGB mass-loss as we do, agree even better then the K03 ones. In addition, the Miller Bertolami (2006) results also match very well the core of our low-mass stars ($1{\rm M}_\odot$ and $2.2{\rm M}_\odot$).

We also plot the core masses for some models calculated with no overshooting and no mass-loss until the $1^{\rm st}$ TP. These are the black triangles in Figure 6.4. The change is significant as the mass of the core drops in all three cases by 12, 6.5 and 5% for the 3, 5 and $6{\rm M}_\odot$ cases. Our masses when overshooting is included, agree therefore better with the K03 ones even if this treatment for the mixing at the convective boundaries is ignored in her models.

When our tracks reach the $1^{\rm st}$ TP on the AGB, their core masses and lifetimes (due to the dominance of the MS) agree well with previous works that use different evolution codes. This is true even for calculations that do not include overshooting from the ZAMS up to the TP-AGB. Our surface carbon isotopic ^{12}C/^{13}C ratios, modified due to the FDU of the convective envelope, are also coherent with models that do not include overshooting.

No convergence problems were encountered during the entire evolution until the 1st TP was reached. The average timestep used during these pre TP-AGB phases is around 10 000 yrs and the number of models needed to reach the TP-AGB range anywhere from 3000 to 25 000 (depending on the initial stellar masses). The number of iterations for a model to converge is typically 3. The timestep and the number of iterations can vary during the different evolutionary phases. The best example is the He-flash, where it may take up to a few hundred iterations for models to reach convergence and the timesteps can be as low as 10^{-4} years; this however occurs without any numerical problems.

7. On the TP-AGB

In the previous chapters the basics on moderate-mass star evolution were introduced. Details, relevant for the purpose of this work, of our models up to the E-AGB were also presented. We now focus on the TP-AGB models before turning to the post-AGB tracks in the next chapter.

The beginning of the TP-AGB is considered to occur at the first major TP. By *first major TP* we mean the first TP with a He-burning luminosity - $\log_{10}(L_{\mathrm{He}}/\mathrm{L}_{\odot})$ - higher then 4. We designate the end of the TP-cycle by either one of the following two possibilities: a) the moment when, as it is departing the AGB, the pulsation period of a model drops below 100 days (see mass-loss chapter) if calculations reach the post-AGB phase uninterrupted, b) the last model before computations stop due to convergence problems.

The characteristics and important phenomena (TPs, burning shells, TDU, HBB, convection, etc) occuring during the pulsating phase of the AGB, which have already been explained, will be used to discuss our models and the effect of the main up-to-date features (mass-loss & overshooting prescriptions, molecular opacities, initial mass and composition parameter space).

7.1. A First Glance at the Models

Figures 7.1 to 7.4 display the temporal evolution of some important quantities during the TP-cycle for models of different masses but all with a solar-like composition. From top to bottom the five graphics give: i) total surface luminosity (in solar units) and effective temperature, ii) luminosity of the hydrogen- (solid) and helium-burning (dotted) shells, iii) total and core masses, iv) period of pulsation and mass-loss rate, v) carbon over oxygen number fraction ratio and mass fractions of carbon, oxygen and nitrogen at the surface of the star.

Following are some general remarks on the behavior on the models.

The only star at this composition to go through the full TP-AGB and into the post-AGB phase is the $2\mathrm{M}_{\odot}$ one. This can be seen on the plots of Figure 7.3 at the end of the last TP by the increase of the effective temperature, the decrease of the surface luminosity and the total ejection of the envelope. All other computations experienced a crash beforehand.

The total TP-AGB lifetimes vary from a maximum of about 2.6 Myr for the $2\mathrm{M}_{\odot}$ model to as little as an estimated (see discussion below) 170 Kyr for the $6\mathrm{M}_{\odot}$ case. As for the TP-cycle period, its upper and lower approximate limits are 160 ($1\mathrm{M}_{\odot}$) and 3 Kyr ($6\mathrm{M}_{\odot}$).

When the computed evolution does not cover the entire TP-AGB, the mass of the remaining envelope depends on how massive the models initially are. For higher-mass stars, the envelope that has not yet been ejected can be as much as 2.241M$_\odot$ (M_{ZAMS} = 6M$_\odot$), but for the 1M$_\odot$ model, it consists only of a negligible 0.039M$_\odot$. Effectively the lower-mass models ($\lessapprox$ 2.6 - 3M$_\odot$) have gone through all TPs and crash only during the last shell-flash. As models become more massive, the number of TPs increases (from 2 to 34). Mass-loss rates, always higher than 10^{-8} M$_\odot \cdot$ yr^{-1}, can reach values of up to 10^{-4} M$_\odot \cdot$ yr^{-1}.

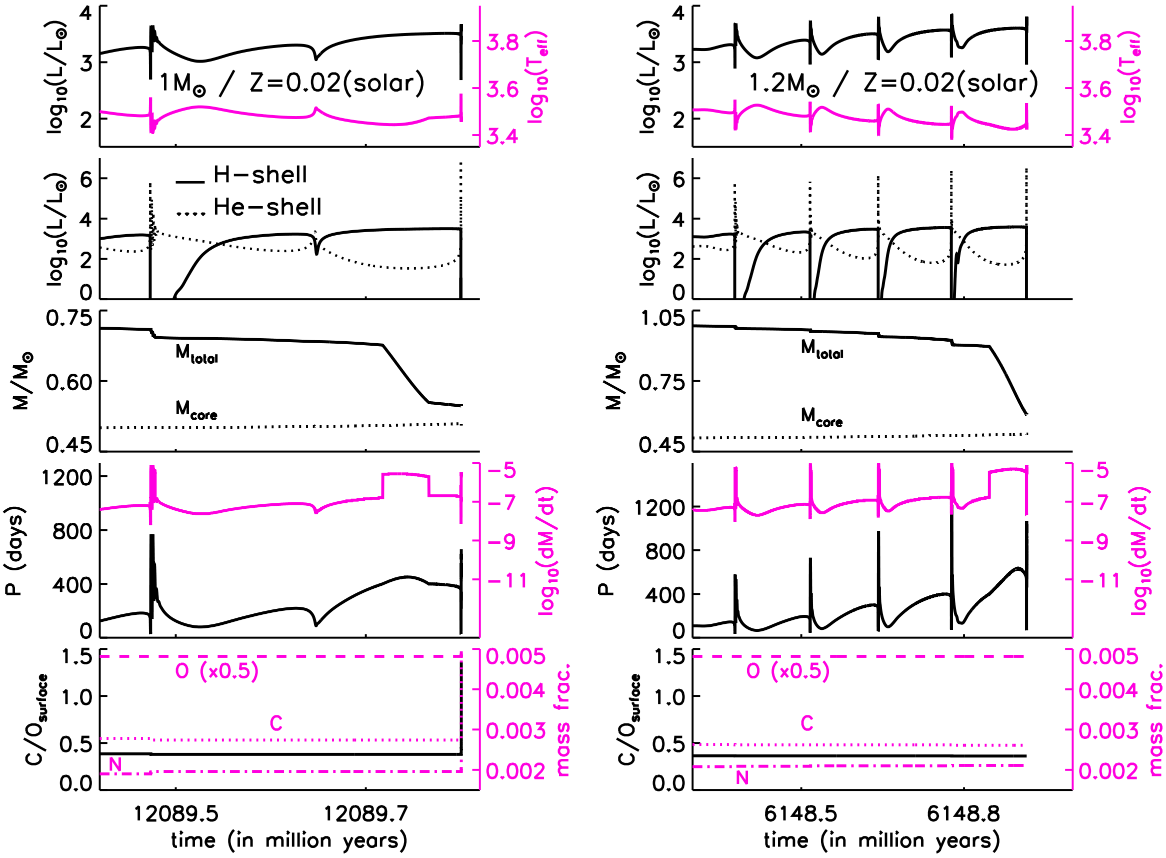

Figure 7.1.: TP-AGB evolution of 1M$_\odot$ and 1.2M$_\odot$ models with a Z = 0.02 solar-scaled composition (see text for details).

The 1M$_\odot$ and 1.2M$_\odot$ models do not experience dredge-up at all throughout their TP-AGB evolution - but one TDU episode occurs for the 1M$_\odot$ case during the last shell-flash as the star is ready to depart the TP-AGB only to be stopped by convergence problems. TDU is first observed during the last 3 TPs for stars of 1.5M$_\odot$ and 1.6$_\odot$. The surface mass fraction of carbon almost doubles in both cases, and the amount of oxygen and nitrogen is also increased. The C/O number ratio nevertheless remains below unity as it respectively reaches values of 0.724 and 0.753. The 2M$_\odot$ and 2.6M$_\odot$ models experience more TDU episodes and become C-stars with final C/O ratios of 1.204 and 1.426. The 6M$_\odot$ star is the only one at this metallicity to experience HBB. This is clearly visible in the right bottom plot of Figure 7.4: between TPs 3 and 29, because of HBB at each interpulse, the carbon content globally decreases despite the repeated TDU episodes and the nitrogen mass fraction doubles.

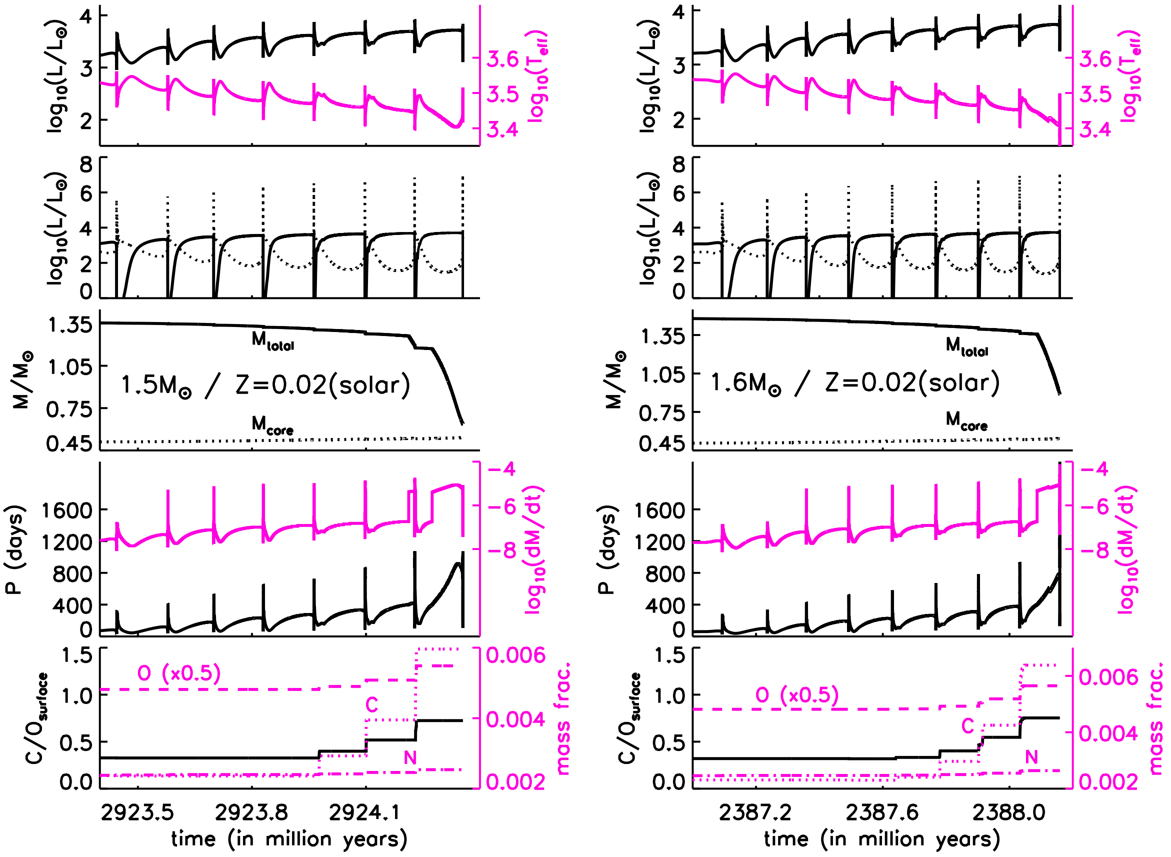

Figure 7.2.: Same as Figure 7.1 for 1.5M$_\odot$ and 1.6M$_\odot$ models.

The third row of graphics shows that, for most models, the major part of the envelopes mass is abruptly lost at the end of the TP-AGB during the last or last-few TPs. Until then, the mass of the star decreases smoothly and gradually. This is because the adopted prescriptions (van Loon et al. 2005, Wachter et al. 2002), which give rise to intensive mass-loss, are only used for pulsation periods higher than 400 days. Even though such periods are reached at each shell-flash, the time is too short in order to eject a considerable amount of mass. It is only when the pulsation periods are high enough for a longer time, during an interpulse, that mass-loss has a more radical impact on the models. The 5M$_\odot$ and 6M$_\odot$ stars go through more TPs and reach this critical period during many interpulses; the mass decrease before the last TPs are attained is therefore steeper. For all models the period of radial pulsations varies between about 100 and 2500 days, the highest values being reached by the more massive stars.

In general, the behavior shown in these graphics for the various initial masses is also typical of the behavior of stars at the other chemical compositions in our grid.

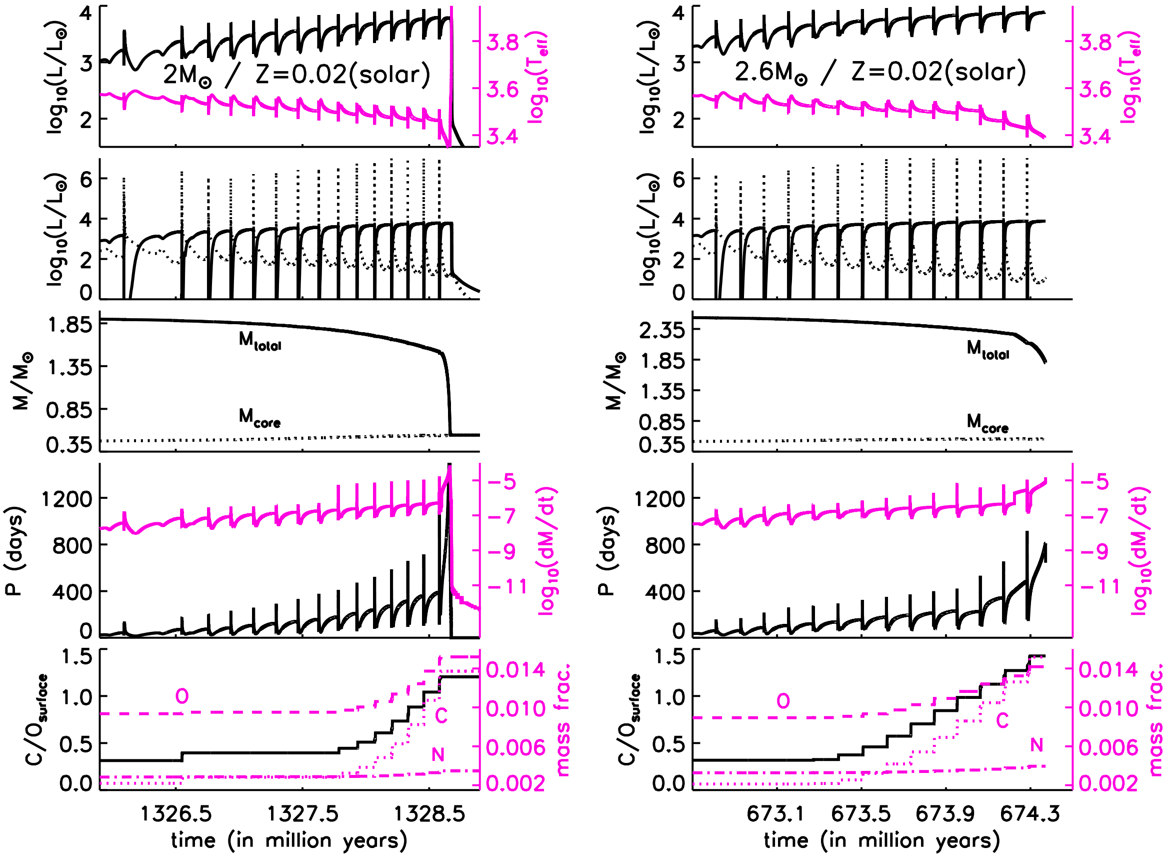

Figure 7.3.: Same as Figure 7.1 for 2M$_\odot$ and 2.6M$_\odot$ models.

But total metallicity does affect model characteristics, and theoretical AGB evolution is actually known to depend on both Z and M_{ZAMS} in a complex way. On the contrary the effect of different metal scalings for a same Z value, included in this work, has not been investigated up to now.

Here are some typical trends found in our models. Stronger TDU is obtained at lower metallicities and higher masses. It is well known from previous works that the efficiency of dredge-up increases with core mass, envelope mass, and decreasing metallicity (e.g. Herwig 2005a). This is consistently found in both detailed models (e.g. Karakas 2003) or synthetic ones (e.g. Marigo 2001). Our calculations confirm this trend for the commonly used metallicities (solar, LMC and SMC); but they also extend it to higher (Z = 0.04) and lower (Z = 0.0005) values of Z.

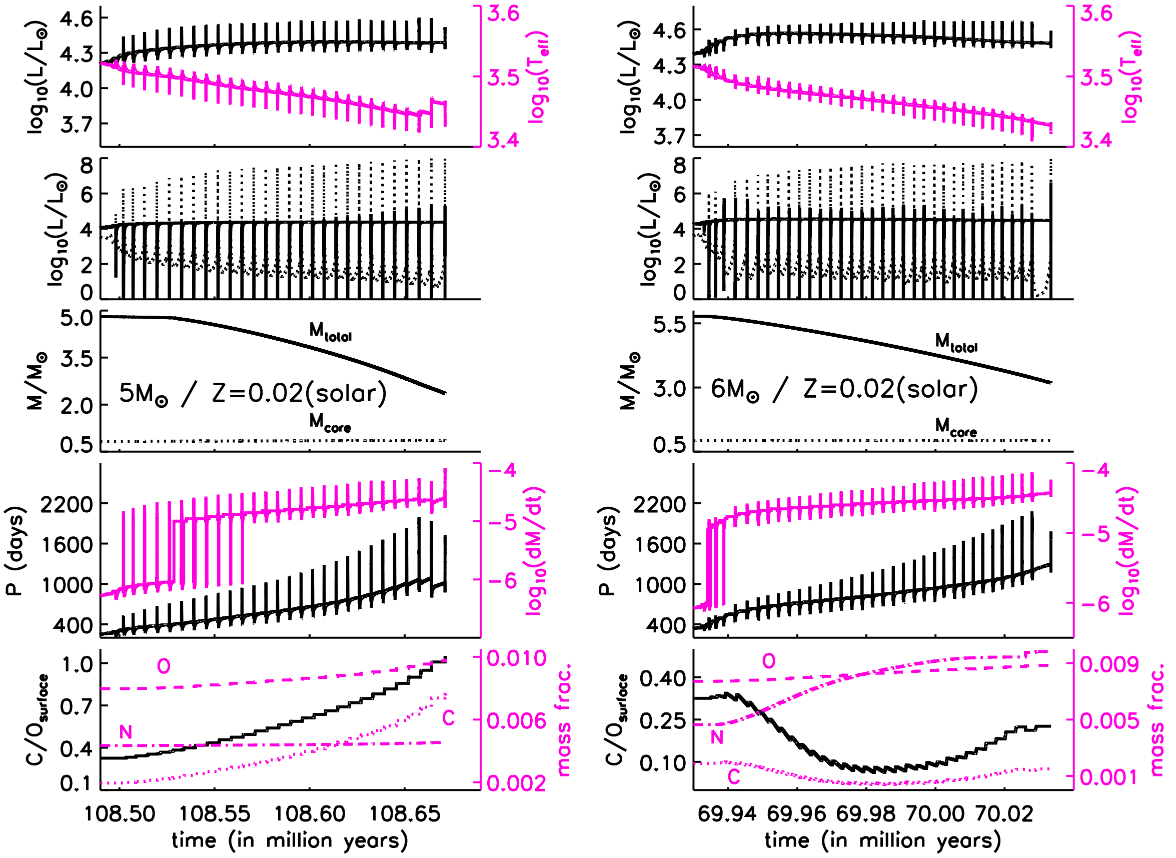

Figure 7.4.: Same as Figure 7.1 for 5M$_\odot$ and 6M$_\odot$ models.

For the Z = 0.04 case (both solar and α-enhanced metal distributions), the first stellar track to experience TDU is the 2.6M$_\odot$ one: this happens after the 10th TP. On the contrary, all solar-scaled and α-enhanced models with Z = 0.0005 already experience TDU at the 1st or 2nd TP. The highest values ($\approx$ 5 - 6) for the final surface C/O ratio, which is a direct consequence of strong and repeated TDU, are also reached by these lowest metallicity models. Our C/O ratios do not attain final values as high as those obtained in the latest set of detailed AGB models by Karakas (2003), where models with a Z = 0.004 metallicity feature values of more than 20 (the 2.5M$_\odot$ has C/O$_f$ = 21.371). For the same metallicity our model with the most C-enhancement (1.2M$_\odot$) has C/O = 4.305 at the AGB's end. We thus generally obtain C-stars with less carbon content.

It is important to note that the inclusion of overshooting in our code is the reason why many of our models experience TDU. Without this treatment, no TDU would be seen in any mass models with Z = 0.04 and 0.02, but only in lower metallicity ones. Similarly, most codes have to treat convective boundaries in a more elaborate way than with the simple Schwarzschild criterion. While some use this same overshooting approach (Herwig 2005a, and references therein), others do not include it in the usual sense (e.g. Karakas 2003, Frost & Lattanzio 1996), but recognize for example the discontinuity in the ratio of the radiative to adiabatic temperature gradients at the extremities of convective zones. In order to get TDU, they essentially extend convection until a neutral border is found. In effect, all these are very similar methods that increase the amount of material mixed from the lower layers to the surface.

Another typical tendency recovered by our results, is the fact that HBB is more efficient at, higher masses and lower Z. Irrespective of composition, all $6M_\odot$ stars experience HBB. HBB also occurs in the $5M_\odot$ models but only for $Z \leqslant 0.008$. No other models below this mass show signs of HBB. This critical $5M_\odot$ mass only above which HBB occurs in our models is rather high, as HBB is found for metal-poor chemistries at masses as low as $3.5M_\odot$ in recent calculations (e.g. Karakas 2003, Herwig 2004a). Our results are more in agreement with older computations which found HBB only above $5M_\odot$ even at low Z (Vassiliadis & Wood 1993).

As expected, the number of TPs increase with initial ZAMS mass. With our mass-loss prescription low-mass stars experience as few as 2 TPs ($1M_\odot$ / solar-scaled, Z = 0.04), while more massive ones can have up to 70 TPs ($6M_\odot$ / α-enhanced, Z = 0.004). The number of TPs roughly seems to increase with decreasing metallicity, especially for the higher mass models (as do the Karakas models). However this behavior is not pronounced enough to lead to any real dependence on Z. Furthermore, the very metal poor (Z = 0.0005) results do not follow this trend and have fewer TPs.

In contrast to the $M_{\rm ZAMS}$ and Z dependences, no substantial differences are globally encountered as a consequence of the two metallicity scalings. This parameter does not significantly influence the number of TPs or the occurrence of TDU and HBB. Models with an α-element enhancement simply follow a similar behavior to the same metallicity models with a solar-scaled distribution. As a general rule, differences only of the order of 1 to 2 TPs are present, and all models with a given $M_{\rm ZAMS}$ and Z that show HBB, do so for both heavy element distributions. The same is true for TDU with one exception: the $1.2M_\odot$ / Z = 0.02 models. The solar-scaled composition star does not experience TDU during a 5-TP-evolution, while its α-enhanced counterpart shows one dredge-up episode at the $4^{\rm th}$ TP (out of a total of also 5).

Since oxygen is an α-element but not carbon, the initial C/O ratio on the Main Sequence and therefore on the AGB before TDU occurs will not be identical for the two distributions. The solar ratio has a value of 0.48 and our α-enhanced composition gives C/O = 0.19. Once TDU starts, if it occurs at each TP, since the amount of dredged-up carbon and oxygen is equivalent for both cases, on one hand it will simply take more TPs for a non-solar composition to reach a particular C/O value, and on the other, both surface carbon contents will gradually converge provided that the TP-AGB evolution is long enough. In that case, comparable surface carbon and oxygen compositions will simply be offset by a few TPs.

M_{ZAMS}	No TPs	$M_{\mathrm{c}}(1)$	$M_{\mathrm{c}}(\mathrm{TDU})$	No $\mathrm{TP}_{\mathrm{TDU}}(\mathrm{i})$	$\mathrm{C/O_f}$	$M(\mathrm{f})$	$M_{\mathrm{c}}(\mathrm{f})$	No $\mathrm{TP}_{\mathrm{HBB}}(\mathrm{i})$	No $\mathrm{TP}_{\mathrm{HBB}}(\mathrm{f})$	TP-AGB lifetime (10^3 yrs)		
										t_{mod}	$\approx t_{\mathrm{extra}}$	t_{total}
					Z = 0.04 / solar							
1.0	2	0.504	-	-	0.381	0.514	0.510	-	-	244.754	-	244.754
1.2	4	0.513	-	-	0.356	0.524	0.521	-	-	311.523	-	311.523
1.5	6	0.513	-	-	0.331	0.533	0.531	-	-	523.002	-	523.002
1.6	7	0.510	-	-	2.128	0.544	0.536	-	-	705.362	0.5 (0)	706
1.8	10	0.496	-	-	2.371	0.539	0.537	-	-	1 107.536	-	1 107.536
2.0	13	0.481	-	-	0.322	0.552	0.552	-	-	1 876.474	-	1 876.474
2.6	15	0.528	0.566	10	0.449	1.037	0.587	-	-	999.657	28 (0)	1 028
3.0	10	0.596	0.605	4	0.507	0.976	0.628	-	-	402.750	14 (0)	417
4.0	8	0.750	0.751	2	0.583	1.988	0.751	-	-	86.755	31 (2)	118
5.0	16	0.810	0.812	2	0.444	2.573	0.829	-	-	94.703	44 (5)	139
6.0	26	0.893	0.893	1	0.455	3.333	0.908	6	17	74.350	48 (12)	86
					Z = 0.04 / α-enhanced							
1.0	2	0.505	-	-	0.163	0.516	0.510	-	-	235.332	-	235.332
1.2	3	0.512	-	-	0.154	0.523	0.520	-	-	333.567	-	333.567
1.5	5	0.518	-	-	0.139	0.539	0.535	-	-	466.447	-	466.447
1.6	6	0.514	-	-	0.150	0.698	0.536	-	-	576.262	16 (0)	592
1.8	8	0.504	-	-	0.134	0.538	0.536	-	-	856.256	-	856.256
2.0	13	0.494	-	-	0.135	0.590	0.552	-	-	1 394.989	4 (0)	1 399
2.6	16	0.515	0.558	10	0.432	0.745	0.580	-	-	1 288.965	5 (0)	1 294
3.0	13	0.574	0.587	5	0.442	0.912	0.613	-	-	617.336	9 (0)	626
4.0	8	0.750	0.749	1	0.234	1.795	0.763	-	-	96.381	26 (1)	122
5.0	15	0.830	0.830	1	0.225	2.919	0.845	-	-	77.211	52 (8)	129
6.0	25	0.935	0.935	1	0.219	3.351	0.946	4	18	54.590	48 (12)	103

Table 7.1.: Selected properties for the Z = 0.04 models (see text for details).

M_{ZAMS}	No TPs	$M_{\mathrm{c}}(1)$	$M_{\mathrm{c}}(\mathrm{TDU})$	No $\mathrm{TP}_{\mathrm{TDU}}(\mathrm{i})$	$\mathrm{C/O}_{\mathrm{f}}$	$M(\mathrm{f})$	$M_{\mathrm{c}}(\mathrm{f})$	No $\mathrm{TP}_{\mathrm{HBB}}(\mathrm{i})$	No $\mathrm{TP}_{\mathrm{HBB}}(\mathrm{f})$	TP-AGB lifetime (10^3 yrs)		
										t_{mod}	$\approx t_{\mathrm{extra}}$ (TPs)	t_{total}
					Z = 0.02 / solar							
1.0	2	0.501	-	-	1.357	0.547	0.508	-	-	327.675	36 (0)	364
1.2	5	0.509	-	-	0.361	0.608	0.524	-	-	537.625	25 (0)	563
1.5	8	0.511	0.526	5	0.724	0.637	0.539	-	-	911.274	15 (0)	926
1.6	9	0.508	0.522	5	0.753	0.888	0.538	-	-	1 066.336	69 (0)	1 135
1.8	8	0.496	0.503	2	1.252	1.031	0.524	-	-	1 372.882	159 (1)	1 532
2.0	15	0.478	0.484	2	1.204	0.543	0.543	-	-	2 581.483	-	2 581.483
2.6	14	0.518	0.533	5	1.426	1.802	0.560	-	-	1 560.967	311 (2)	1 872
3.0	12	0.596	0.596	1	1.407	2.029	0.617	-	-	693.755	141 (2)	835
4.0	14	0.765	0.766	2	0.711	2.137	0.783	-	-	156.353	54 (3)	210
5.0	29	0.830	0.831	2	1.051	2.354	0.850	-	-	169.289	60 (7)	229
6.0	34	0.928	0.928	1	0.226	3.178	0.937	3	29	98.985	71 (23)	170
					Z = 0.02 / α-enhanced							
1.0	2	0.502	-	-	0.164	0.551	0.505	-	-	319.945	43 (0)	363
1.2	5	0.508	0.518	4	0.384	0.561	0.521	-	-	529.722	12 (0)	542
1.5	8	0.514	0.530	5	1.834	0.542	0.540	-	-	929.208	-	929.208
1.6	9	0.513	0.523	4	0.859	0.545	0.544	-	-	1 018.272	-	1 018.272
1.8	11	0.501	0.509	4	1.240	0.551	0.540	-	-	1 412.476	2 (0)	1 414
2.0	14	0.488	0.494	2	1.248	0.629	0.537	-	-	2 196.938	9 (0)	2 206
2.6	15	0.513	0.527	5	1.453	1.853	0.547	-	-	1 821.007	412 (3)	2 233
3.0	14	0.585	0.588	2	1.332	1.922	0.612	-	-	907.181	207 (2)	1 114
4.0	13	0.766	0.766	1	0.681	1.958	0.774	-	-	158.834	37 (2)	196
5.0	21	0.846	0.846	2	0.541	3.215	0.860	-	-	117.461	94 (15)	211
6.0	37	0.946	0.946	1	0.252	3.260	0.954	1	32	91.610	58 (19)	150

Table 7.2.: Same as Table 7.1 but for Z = 0.02.

$M_{\rm ZAMS}$	No TPs	$M_{\rm c}(1)$	$M_{\rm c}$(TDU)	No $TP_{\rm TDU}$(i)	C/O$_{\rm f}$	M(f)	$M_{\rm c}$(f)	No $TP_{\rm HBB}$(i)	No $TP_{\rm HBB}$(f)	TP-AGB lifetime (10^3 yrs)		
										$t_{\rm mod}$	$\approx t_{\rm extra}$	$t_{\rm total}$
					Z = 0.008 / solar							
1.0	5	0.513	0.513	1	1.170	0.619	0.531	-	-	698.898	85 (0)	784
1.2	4	0.521	0.521	1	1.309	0.663	0.531	-	-	482.655	41 (0)	524
1.5	5	0.521	0.524	2	2.204	0.538	0.537	-	-	794.177	-	794.177
1.6	7	0.516	0.520	2	2.570	0.555	0.537	-	-	1 029.957	4 (0)	1 034
1.8	9	0.497	0.499	2	2.004	1.164	0.526	-	-	1 556.110	201 (1)	1 757
2.0	16	0.464	0.464	1	1.732	1.354	0.528	-	-	4 081.799	260 (1)	4 342
2.6	10	0.569	0.569	1	2.860	0.758	0.576	-	-	984.120	6 (0)	990
3.0	11	0.672	0.672	1	1.699	2.133	0.686	-	-	352.172	144 (3)	496
4.0	19	0.801	0.801	1	1.358	3.348	0.816	-	-	178.647	253 (25)	432
5.0	38	0.868	0.868	1	1.062	2.443	0.879	9	24	188.148	62 (12)	250
6.0	46	0.991	0.991	1	0.281	3.498	0.993	1	46	97.485	79 (39)	176
					Z = 0.008 / α-enhanced							
1.0	5	0.508	0.515	3	2.354	0.550	0.523	-	-	667.889	24 (0)	692
1.2	5	0.517	0.520	2	2.434	0.554	0.531	-	-	641.089	6 (0)	647
1.5	4	0.527	0.527	1	1.787	1.034	0.537	-	-	634.407	50 (0)	684
1.6	5	0.522	0.522	1	1.999	1.173	0.536	-	-	830.354	63 (0)	893
1.8	5	0.505	0.505	1	2.365	0.524	0.522	-	-	1 446.966	-	1 446.966
2.0	12	0.464	0.472	2	1.916	1.513	0.498	-	-	3 458.889	320 (1)	3 779
2.6	10	0.578	0.578	1	2.530	0.772	0.592	-	-	921.296	6 (0)	927
3.0	12	0.684	0.684	1	1.526	2.074	0.698	-	-	367.321	87 (2)	454
5.0	32	0.875	0.875	1	0.563	1.824	0.887	9	25	195.952	37 (6)	233
6.0	44	0.996	0.996	2	0.508	3.089	0.988	1	42	108.084	66 (22)	174

Table 7.3.: Same as Table 7.1 but for Z = 0.008.

M_{ZAMS}	No TPs	$M_{\mathrm{c}}(1)$	$M_{\mathrm{c}}(\mathrm{TDU})$	No $\mathrm{TP}_{\mathrm{TDU}}(\mathrm{i})$	$\mathrm{C/O_f}$	$M(\mathrm{f})$	$M_{\mathrm{c}}(\mathrm{f})$	No $\mathrm{TP}_{\mathrm{HBB}}(\mathrm{i})$	No $\mathrm{TP}_{\mathrm{HBB}}(\mathrm{f})$	TP-AGB lifetime (10^3 yrs)		
										t_{mod}	$\approx t_{\mathrm{extra}}$	t_{total}
Z = 0.004 / solar												
1.0	4	0.517	0.522	2	4.279	0.537	0.531	-	-	590.409	3 (0)	593
1.2	4	0.525	0.529	2	4.305	0.555	0.536	-	-	530.145	5 (0)	535
1.5	5	0.527	0.531	2	3.581	0.731	0.537	-	-	691.108	19 (0)	710
1.6	7	0.521	0.525	2	3.156	0.537	0.536	-	-	1 056.562	-	1 056.562
1.8	5	0.499	0.505	2	3.318	0.598	0.493	-	-	1 686.695	33 (0)	1 720
2.0	14	0.488	0.495	2	3.035	0.529	0.528	-	-	3 609.374	-	3 609.374
2.6	9	0.639	0.639	1	2.868	0.914	0.653	-	-	463.827	8 (0)	472
3.0	11	0.744	0.744	1	2.235	1.381	0.746	-	-	200.714	16 (0)	217
4.0	26	0.809	0.809	1	2.442	1.655	0.818	-	-	259.943	2 (0)	263
5.0	35	0.894	0.894	1	1.036	2.787	0.898	6	31	164.360	75 (15)	239
6.0	62	1.060	1.060	1	0.707	3.461	1.047	1	62	88.046	2 (30)	90
Z = 0.004 / α-enhanced												
1.0	5	0.515	0.515	1	3.175	0.554	0.532	-	-	682.685	19 (0)	702
1.2	5	0.523	0.523	1	4.177	0.538	0.533	-	-	674.829	0.6 (0)	675
1.5	5	0.531	0.531	1	3.365	0.550	0.543	-	-	783.520	-	783.520
1.6	3	0.529	0.529	1	2.752	0.521	0.519	-	-	894.331	-	894.331
1.8	8	0.506	0.506	1	3.123	0.529	0.526	-	-	1 529.455	-	1 529.455
2.0	10	0.498	0.498	2	3.449	0.519	0.512	-	-	2 199.189	0.2 (0)	2 200
2.6	10	0.647	0.647	1	2.522	1.632	0.665	-	-	443.615	61 (1)	505
5.0	38	0.908	0.908	1	0.772	2.642	0.912	4	32	159.533	69 (13)	229
6.0	70	1.050	1.050	1	0.372	3.366	1.048	1	70	100.072	73 (36)	173

Table 7.4.: Same as Table 7.1 but for Z = 0.004.

M_{ZAMS}	No TPs	$M_{\mathrm{c}}(1)$	$M_{\mathrm{c}}(\mathrm{TDU})$	No $\mathrm{TP}_{\mathrm{TDU}}(\mathrm{i})$	$\mathrm{C/O}_{\mathrm{max}}$	$M(\mathrm{f})$	$M_{\mathrm{c}}(\mathrm{f})$	No $\mathrm{TP}_{\mathrm{HBB}}(\mathrm{i})$	No $\mathrm{TP}_{\mathrm{HBB}}(\mathrm{f})$	TP-AGB lifetime (10^3 yrs)		
										t_{mod}	$\approx t_{\mathrm{extra}}$	t_{total}
Z = 0.0005 / solar												
1.0	4	0.523	0.527	2	5.184	0.539	0.537	-	-	600.331	-	600.331
1.2	4	0.537	0.548	3	4.125	0.551	0.550	-	-	518.908	-	518.908
1.5	4	0.570	0.582	3	4.219	0.579	0.578	-	-	553.484	-	553.484
1.6	5	0.561	0.566	2	4.462	0.579	0.578	-	-	619.811	-	619.811
1.8	5	0.551	0.551	1	4.205	0.565	0.564	-	-	733.834	-	733.834
2.0	6	0.584	0.588	2	4.180	0.600	0.599	-	-	603.197	-	603.197
2.6	9	0.733	0.733	1	3.560	1.019	0.734	-	-	211.692	3 (0)	215
3.0	10	0.780	0.780	1	3.776	1.277	0.772	-	-	162.996	25 (1)	188
4.0	20	0.848	0.848	2	1.861	2.397	0.829	-	-	178.286	31 (3)	209
Z = 0.0005 / α-enhanced												
1.0	3	0.528	0.528	1	6.183	0.535	0.533	-	-	446.329	-	446.329
1.2	3	0.538	0.538	1	6.590	0.547	0.545	-	-	483.113	-	483.113
1.5	4	0.560	0.560	1	5.602	0.568	0.567	-	-	510.437	-	510.437
1.6	3	0.564	0.564	1	2.568	0.559	0.558	-	-	456.902	-	456.902
1.8	6	0.555	0.555	1	4.588	0.561	0.561	-	-	752.815	-	752.815
2.0	6	0.588	0.588	1	4.716	0.599	0.598	-	-	577.109	-	577.109

Table 7.5.: Same as Table 7.1 but for Z = 0.0005.

This small deviation can further be reduced when the C/O value in the solar-scaled model first reaches unity. This is because the stronger mass-loss (Wachter et al. prescription for a C-rich star) imposes a relatively shorter C-star phase with less remaining TPs and dredge-up episodes. This allows the α-enhanced model to *catch-up* until it also reaches the C-star phase. As a consequence, for a given mass and total metallicity, both types of models at the end of the AGB roughly have a similar surface value, the α-enhanced models having sometimes a few more TPs.

We take as an example the two $2.6\mathrm{M}_\odot$ / Z = 0.02 models. Both experience TDU at the 5th TP, their final C/O ratios are 1.426 and 1.453 (solar and α-enhanced) and they have a total of 14 and 15 thermal pulses. At the 4th dredge-up episode the solar model has C/O = 0.574, but one has to wait until the 7th TDU occurrence in order for the α-enhanced one to have a similar value (0.596). As the models evolve, this 3-TP shift is reduced to 2: the C/O ratios exceed unity for the first time at the 8th and the 10th dredge-up episodes respectively. At the end of the computations both models for a similar remaining mass almost have the same surface C/O value with only 1 more TP for the α-enhanced case.

The points presented and discussed above are some of the general features found in our models, an inventory of which is made in Tables 7.1 - 7.5 for the following metallicities: Z = 0.04, 0.02, 0.008, 0.004 and 0.0005 with both metal distributions. There are 13 columns in each table. In the first column the initial zero-age Main Sequence mass, M_{ZAMS}, is given. The second column contains the total number of TPs experienced by the model. The next two columns give the mass of the core, at the 1st TP - $M_{\mathrm{c}}(1)$ (the same values as in Tables 6.1 - 6.5) - and at the 1st TP at which TDU occurs - $M_{\mathrm{c}}(\mathrm{TDU})$. No $\mathrm{TP}_{\mathrm{TDU}}(\mathrm{i})$, is the pulse number of the first dredge-up episode. In column 6, $\mathrm{C/O}_{\mathrm{f}}$ is the final surface ratio value of the carbon over oxygen number fractions. M(f) and $M_{\mathrm{c}}(\mathrm{f})$ are respectively the final, total and core, masses. Columns 9 and 10 give the pulse number at which the HBB starts - No $\mathrm{TP}_{\mathrm{HBB}}(\mathrm{i})$ - and ends - No $\mathrm{TP}_{\mathrm{HBB}}(\mathrm{f})$. In the last three columns, the lifetime of the TP-AGB in thousands of years is tabulated. t_{mod} is the time the actual computed model evolved through the TP-cycle; it is given up to the third decimal place which corresponds to a year. If the model evolved through the entire TP-AGB, this time is the final TP-AGB lifetime, t_{total}. For models with a premature end, an additional time, t_{extra}, that would be needed to eject the remaining envelope is estimated. t_{total} is then the sum of t_{mod} and t_{extra}. In parenthesis beside t_{extra}, we also give an approximative number of TPs that would still occur before the end of the AGB.

Both the time and the number of TPs left are very rough estimates. Their purpose is simply to allow us to better appreciate how far in the evolution have our models progressed and how close they are to the post-AGB. In order to determine these quantities the following four assumptions were made: a) the mass of the core of the last model will effectively not change before the departure from the AGB, b) by comparison to models which have evolved uninterrupted, we decide that a star will begin its post-AGB evolution when the envelope mass represents only 0.5% of the total mass, both the c) interpulse period of the last TP and the d) estimated average mass-loss rate from the last interpulse, are taken to be constant during the remaining evolution. We then directly compute the remaining time and the number of additional TPs.

Both the extra time and number of TPs can be taken to actually be upper limits to what would have normally been computed. One reason for this is the fact that the mean mass-loss rate, that depends on the gradually decreasing effective temperature and increasing luminosity, should become larger and larger during the remaining evolution. The purpose of these numbers only remains qualitative and we therefore do not give the mean $\dot{M}$ values and the last interpulse periods $t_{\rm ip}$ used for the estimates.

As can be seen in the tables, models with $M_{\rm ZAMS} \leqslant 3{\rm M}_{\odot}$ have almost reached the end and only a couple will go through more than 1 TP. Even the most massive $6{\rm M}_{\odot}$ stars have gone through at least 50% of their TP-cycle both in terms of time and number of TPs. For the Z = 0.004 (α-enhanced) and Z = 0.005 (both metal distributions) low metallicity cases, some of the higher mass tracks are not available because very early convergence problems did not allow us to present useful models.

7.2. Other AGB Codes and Available Grids

Only a handful of detailed stellar codes have been developed and specifically applied to AGB (and post-AGB) evolution of late. The most known ones, some updated more then others over the years, are the following:

- the FRANEC (Frascati Raphson-Newton Evolutionary Code) code (e.g. Straniero et al. 1997, Cristallo et al. 2007),
- the MSSSP (Mount Stromlo Stellar Structure Program) code (e.g. Wood & Zarro 1981, Frost & Lattanzio 1996),
- The EVOL code (e.g. Blöcker 1995b, Herwig 2000, 2004b),
- The LPCODE (e.g. Althaus et al. 2005),
- The STARS code (e.g. Eggleton 1971, Stancliffe et al. 2004),
- our Garching Stellar Evolution code.

All of them have produced AGB tracks and articles on different topics have been published. Generally, few stellar models are computed. Grids in mass and metallicity are available but they are often of limited extent as they cover a small range of $M_{\rm ZAMS}$ and Z values. It is more common to find large grids that derive from synthetic models. One example is the latest set of Marigo & Girardi (2007).

From the few extended grids consisting of detailed models, the ones most widely referred to are, to our knowledge, those of Vassiliadis & Wood (1993) [VW93] and Karakas (2003) [K03]. Both are computed with different versions of the same MSSSP program. In the last chapter we presented the code details and compared their tracks to ours for the interval covering the evolution from the ZAMS until the E-AGB.

The VW93 tracks are given for the following 4 metallicities: Z = 0.016, 0.008, 0.004 and 0.001. For each composition there are 7 initial mass values in the range $0.89{\rm M}_{\odot} \leqslant M \leqslant$

5.0M$_\odot$. K03 computes models for Z = 0.02, 0.008 and 0.004 with 1.0M$_\odot$ $\leqslant M \leqslant$ 6.0M$_\odot$ (14 different initial masses).

In addition to the important updates included in our evolution program (low-temperature molecular opacities, mass-loss prescriptions, overshooting) that are absent in the VW93 and K03 codes, our models cover, for a similar initial mass range (1.0M$_\odot$ - 6.0M$_\odot$), a much wider metallicity interval (Z = 0.04 to Z = 0.0005) and have an extra degree of freedom in composition with the two different metal distributions for each value of Z. The 10 compositions for which we computed tracks have been given in Table 5.1.

7.3. Main Properties and Basic Predictions of the Models

7.3.1. Lifetimes and Thermal Pulses

In Figure 7.5 the duration of the TP-AGB phase as well as the number of TPs experienced during the entire TP-cycle are given with respect to initial ZAMS mass. We give our results as well as those of VW93[1] and K03 for the metallicities common to the three sets (for the representative solar case, VW93 use Z = 0.016 instead of the Z = 0.02 value in our models and the ones of K03).

The same general behavior is found at all values of Z for the three different sets. There is always a peak at masses between about 2M$_\odot$ and 2.5M$_\odot$ for both the duration and the number of TPs. Our results correspond better to those of VW93 as the K03 ones are noticeably higher, especially for the low metallicities. The solar-Z case gives the best agreement between the three sets. The following are representative examples for Z = 0.02. Our 1.8M$_\odot$ star has a 13% longer duration time than the 1.75M$_\odot$ K03 one (1.372 and 1.190 Myr). The 5M$_\odot$ models give: 0.262 (VW93), 0.180 (K03) and 0.169 Myr. This corresponds roughly to a 6% offset of our model from the K03 one.

In all three sets, models with a solar Z have the shortest evolutionary times, whereas those with Z = 0.008 have the longest. But there does not seem to be a decreasing or increasing trend for the duration of this phase with metallicity.

A determinant factor that should influence the TP-cycle lifetime is the mass-loss prescription. Both VW93 and K03 use the same description for $\dot{M}$. But the K03 lifetimes are systematically longer then the ones by VW93 especially for the low-mass and the two lower-metallicity cases. As an example, the biggest difference is found for the 2.5M$_\odot$ / Z = 0.004 model where, VW93 give $t_{\text{TP-AGB}}$ = 1.248 Myr and K03, 2.790. This difference corresponds to about 55%. Smaller differences are seen between the two older sets for the solar-metallicity case where the two 4M$_\odot$ tracks nevertheless still differ by 17% (0.315 and 0.262 Myr). The lower lifetimes of VW93 are at least consistent with the fact that for a Z = 0.008 composition they also obtain less TPs then K03. One argument to explain these unexpected time differences could be the lack of, or the reduced, mass-loss prior to the AGB in the VW93 calculations. But this seems insufficient as RGB mass-loss mainly

---

[1] In the Table 1 of Vassiliadis & Wood (1993), what we believe to be a misprint was corrected: the TP-AGB lifetime for the 1.5M$_\odot$ / Z = 0.008 model has been changed from $9.385 \cdot 10^5$ to $9.385 \cdot 10^6$ yr.

affects stars that go through the He-flash and discrepancies are seen in higher mass models as well. K03 herself does not give a satisfying answer for this problem. It is somewhat intriguing that our updated models produce lifetime values that recover the results obtained, not by K03, but by an older version (VW93) of the same code, which has less common physics (e.g. opacities, reaction rates, mixing-length parameter) with ours, even though both VW93 and K03 use the same mass-loss prescription. We do not have the data in order to compare, but another argument to explain these discrepancies would be the possibly lower VW93 core masses (with respect to K03) for low-mass stars at the beginning of the TP-AGB.

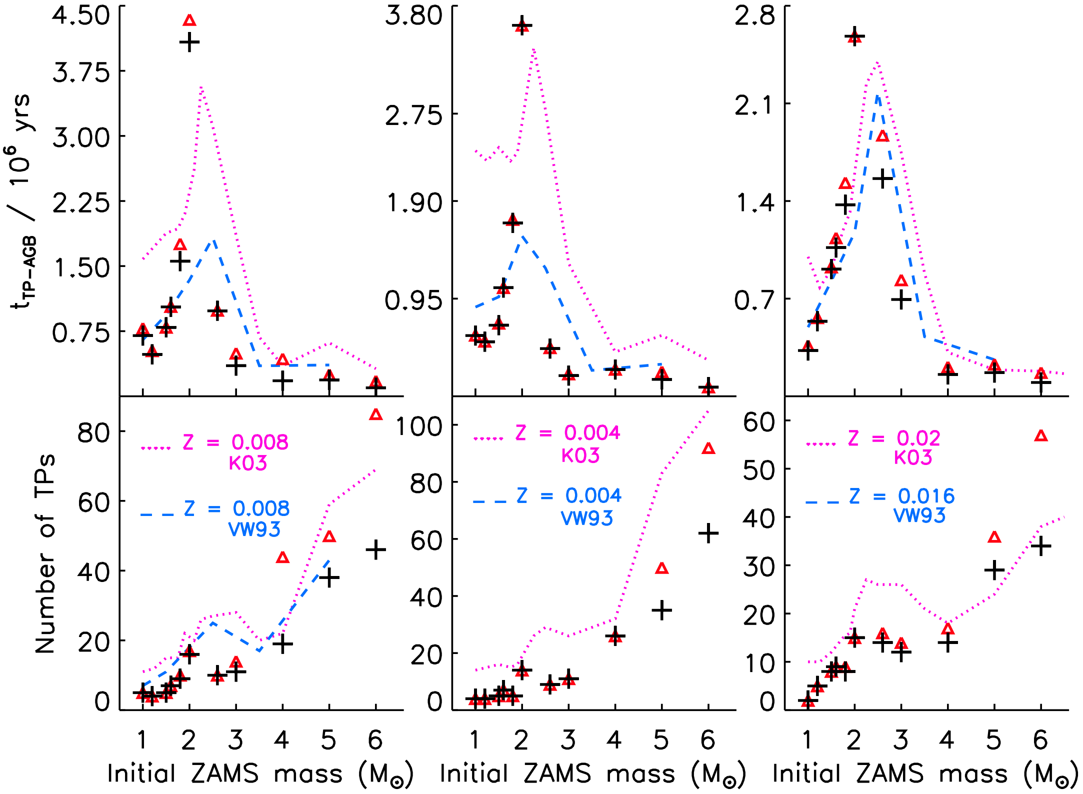

Figure 7.5.: TP-AGB lifetimes and number of TPs versus M_{ZAMS} for metallicities representative (left to right) of the Large (LMC) and Small (SMC) Magellanic Clouds and the Sun. Black crosses: models results. Red dotted lines: Karakas (2003) (K03). Blue dashed lines: Vassiliadis & Wood (1993) (VW93) - for Z = 0.004 and Z = 0.02, the number of TPs is not available. Red triangles: model results + estimated remaining evolution (see section 7.1 for details.)

.

To the contrary, our models do run with different mass-loss relations. First we include mass-loss on the RGB with a higher Reimers η parameter (0.5 or 1.0 instead of: 0.4 / K03 and 0.3 or 0.0 / VW93): thus our models are for the most part less massive already at the

1^{st} TP on the AGB. This is true especially for the lower mass stars that go through the He-flash and lose a higher amount of mass. Moreover, both our O- and C-rich formulas (respectively van Loon et al. 2005, Wachter et al. 2002)) produce higher values of $\dot{M}$ than the VW93 mass-loss prescription during most of the TP-cycle. It is therefore expected to find fewer TPs and shorter lifetimes than the VW93 and K03 results. This is indeed the case as is shown in Figure 7.5. Put aside the $2M_{\odot}$ stars, all other masses give lifetimes lower than the K03 ones and most of the time of VW93 as well. We simply get a more peaked distribution than the two previous sets because of our $2M_{\odot}$ models. The number of TPs experienced by our models is always lower than in both the other studies. Even for the $2M_{\odot}$ stars for which the K03 tracks are on average shorter by 39%, the number of TPs vary between 14 and 16 for our models but 16 and 22 for the K03 ones.

Two other complementary reasons for our shorter lifetimes that are also connected to mass-loss, are the inclusion of convective overshooting and C-rich molecular opacities. Our mass-loss relations depend on the chemistry of the envelope which is modified by mixing events like TDU in turn influenced by overshooting. The extra mixing prescription activates TDU at lower core masses and make it more efficient. As a result, models become C-rich earlier in their evolution and the strong C-rich mass-loss rates are promptly used. In addition, the use of appropriate molecular opacities (section 7.3.3) will cause a notable cooling of the models when C/O > 1. This decrease of T_{eff} will precipitate even more the rise of the mass-loss rate because of the temperature dependence. The succession of events is therefore straightforward: overshooting induces efficient TDU, the star becomes a C-star and C-rich molecular opacities cool the stellar surface, strong C-rich mass-loss rates come into play, the lifetime on the star is further reduced.

TP-AGB models with a different mass-loss description are those of Blöcker (1995b). They are available for a Z = 0.021 composition and lifetimes are given only for stars of initial masses of $3M_{\odot}$, $4M_{\odot}$ and $5M_{\odot}$. A single mass-loss description is not used in this work; different versions of the Blöcker mass-loss are rather tested to produce various AGB models with more or less TPs. In all cases, their average lifetimes are also higher than ours. For $3M_{\odot}$, models with a total number of TPs between 17 and 86 give a average TP-AGB lifetime of 2.483 Myr. This is much higher than our value ($693.755 \cdot 10^{-3}$ Myr) even if we add the estimated extra time which gives a total TP-AGB time of about 0.835 Myr. For the $4M_{\odot}$ models, their 454 000 years are once more higher than our 156 353. Finally, two of their $5M_{\odot}$ models produce lifetimes (0.029 and 0.058 Myr) sensibly lower than ours ($169.289 \cdot 10^{-3}$ Myr) and a third one gives a higher value, 0.283 Myr. The Blöcker (1995b) lifetimes are even higher than the K03 ones which give 1.746, 0.315 and 0.190 Myr respectively for the three masses.

The characteristic peaked distribution of the TP-AGB lifetimes in Figure 7.5 is a consequence of total stellar mass, remaining envelope and core mass mass at the first TP. On the TP-AGB, like in all phases of nuclear-burning evolution, low-mass stars basically live longer than more massive ones because, even though they possess less fuel, they reach lower temperatures and thus reduced burning rates in their interior. During the TP-AGB phase this translates into longer quiescent interpulse times for smaller stars. In addition low-mass stars also have less envelope mass and weak mass-loss rates while intermediate-mass ones have larger envelopes and strong mass-loss. Accordingly at the lower and upper initial-mass extremities defining moderate-mass stars, one has either prolonged lifetimes and few TPs or many TPs with shorter evolutions. Most moderate-mass stars at the beginning of the TP-AGB, have a total mass roughly identical to their initial mass, except those that undergo the He-flash. They can lose as much as 30% (see Tables 6.1 - 6.3) of their initial mass before they reach the first TP; an even smaller envelope is then left to continue the evolution. Our 2M$_\odot$ models are at the boundary between low- and intermediate-mass stars. With increasing initial mass, they are the first stars to reach the TP-AGB with a total mass that is almost identical to their ZAMS mass. This is because they experience a mild He-flash and lose only very little of their envelope on the RGB. The $M_{\rm tot}(1)$ columns in Tables 6.1 - 6.3 show how, for all compositions, only about 0.1M$_\odot$ (5% of $M_{\rm ZAMS}$) has been lost in these models. Our most long-lived models are thus massive enough not to have gone through an intensive He-flash and still have their entire envelope, but they also have a mass sufficiently low in order to evolve a long time on the TP-AGB. This He-flash transition is also responsible for the size of the core which is an even more important factor to take into consideration. While Figure 6.3 shows an augmenting core size trend at the first TP with increasing ZAMS mass, there is a clear dip for all metallicities at about 2M$_\odot$. This dip is mainly responsible for the lifetime peak seen on the TP-AGB.

In fact, one should not compare our long-lived 2M$_\odot$ models to the equivalent mass ones of K03 but rather to the star with the longest TP-AGB lifetimes, or smallest core mass. This is because the shift of the peak between different sets of models corresponds to the maximum $M_{\rm ZAMS}$ at which a He-flash, however mild, still occurs.

We saw in section 6.3 that, because of the inclusion of convective overshooting, the boundary between low- and intermediate-mass stars is, for our models, in the range 1.8 to 2.0M$_\odot$, while it is about 2.25M$_\odot$ for K03. This displacement seen in Figure 6.3, where the lowest K03 core mass is shifted to larger ZAMS masses with respect to our values, is indeed recovered in Figure 7.5 in which the longest TP-AGB lifetimes from the K03 models are obtained for stars of 2.25M$_\odot$ (Z = 0.004 / $3.39 \cdot 10^6$ yr, 0.008 / $3.57 \cdot 10^6$ yr) and 2.5M$_\odot$ (Z = 0.02 / $2.40 \cdot 10^6$ yr). At these three metallicities we get maximum lifetimes (all for 2M$_\odot$ stars) higher by only 6, 13 and 7 % respectively, instead of the, on average, 39% shorter K03 evolution specifically for her 2M$_\odot$ models. The fact that, for the solar metallicity case, K03 finds the longest lifetimes in a higher mass star than for LMC and SMC chemistries is also in agreement with our results. From Figure 6.6 we see that, while for the low metallicities the last model to show a strong luminosity peak at the tip of the RGB is the 1.8M$_\odot$ one, for the Z = 0.02 case it is the 2M$_\odot$ model. The stars showing a mild flash-peak ignite helium at the center while all previous ones had ignited their fuel off-center. In addition to the location of helium ignition, a smaller helium core (which will eventually burn to become the carbon-oxygen core of the AGB star) and the presence of a central convective zone extending, at the flash, up to the hydrogen burning shell are linked to this transition. Low-mass models which experience strong flashes, initially ignite helium off-center because neutrino cooling reduces central temperatures and do not show a convective zone at the center during the flash-peak. On the contrary the last models to show a *decently* strong flash ignite their fuel in the center of a small core which is rapidly surrounded by a convective zone. For instance, in our solar composition models the mass of the helium core at the flash decreases from 0.473M$_\odot$ (1M$_\odot$ model) to 0.391M$_\odot$ (2.0M$_\odot$ model) and then starts increasing again after degeneracy no longer plays a role in helium ignition.

Before the He-flash, evolutionary times decrease with both total and, of course, core mass. After this event, the size of the core does not monotonically increase with total mass anymore but shows this degeneracy induced dip. Lifetimes will therefore reflect this change because they depend on burning temperatures and thus nuclear rates. The longest lived stars will be those with the smallest cores. This will be true for central He-burning and the AGB. On the TP-AGB in particular, the interpulse period (section 7.3.6) and the luminosity (section 7.3.5) can be parametrized as a function of the core mass; and smaller cores lead to larger interpulse periods, lower luminosities, higher effective temperatures and lower mass-loss rates.

Having the smallest core size and a still large enough envelope, the models at the boundary between low- and intermediate-mass stars will have the longest TP-AGB lifetimes. Any star more or less massive than these will always evolve on shorter timescales.

As for our stars in the range 1M$_\odot$ - 2M$_\odot$, their core masses are lower with respect to K03 (Figure 6.3) and therefore responsible for longer interpulse periods. But we have higher mass-loss rates and smaller envelopes (because of our RGB mass-loss). As a results our models have less TPs and overall shorter lifetimes.

In Figure 7.5 we also plot (red triangles) the lifetimes and number of TPs when the extra estimates given in columns 12 and 13 of Tables 7.1 - 7.5 are added. Put aside the 5M$_\odot$ and 6M$_\odot$ models, the difference is negligible both for the lifetimes and TPs. The general trends as well as the differences found with respect to previous models are therefore not affected by the early convergence problems encountered.

The TP-AGB lifetimes of all our models for the five Z values and the two metal scalings are given in Figure 7.6. The lifetime behavior of models with different metallicity scalings is very similar and the peak is once again found at each metallicity in both cases. However, it is much less pronounced for the Z = 0.0005 case and corresponds to a lower ZAMS mass. The mildness of the peak and its shift to lower masses are understandable from Figure 6.7. On one hand the dip at the low-/intermediate-mass star boundary for the lowest Z case is clearly at 1.8 instead of 2M$_\odot$, and on the other the relative mass decrease at that point is less important than for the other metallicities. From Figure 6.6, it is evident that this transition happens at lower masses for lower metallicities. In Table 6.3, the 1.8M$_\odot$ one is the first of our models at this metallicity to reach the TP-AGB with a mere 5% of mass in default.

In all earlier evolutionary phases, including the E-AGB (we do not show a graphical representation), lifetimes decrease with decreasing metallicity. This is because low Z values induce low opacities thus high luminosities and temperature. The same should be true on the TP-AGB were the higher core masses (Figure 6.7) at low metallicities also correspond to shorter interpulse times and a dredge-up efficiency which increases with decreasing Z, thus accelerating the onset of the high C-rich mass-loss rates. But the complex interplay between the various phenomena makes this dependence difficult to estimate. From Figure

7.6 it is not clearly understandable how TP-AGB duration varies with metallicity and no specific trend is seen.

We also compare the relative contribution of the TP-AGB phase to the total AGB lifetime (rightmost graphic in Figure 7.6) for our solar-scaled models and the K03 ones. Put aside the Z = 0.0005 case, it is clear that with increasing Z, the time spent on the TP-AGB with respect to the total AGB lifetime decreases. While the Z = 0.04 tracks live at most 10% of their life in the TP-cycle, the Z = 0.004 models can have a TP-AGB phase that accounts for as much as more than 20% of the total AGB one. The lowest metallicity case does have the larger $t_{\mathrm{TP\text{-}AGB}}/t_{\mathrm{AGB}}$ ratio at low masses and matches the Z = 0.004 tracks at the higher ones. The absence of the peak is seen again. It could be due to the lack of mass-resolution at the He-flash transition. If it were present it could very well be higher than the Z = 0.004 models, thus following the general Z dependence. Our results differ from those of K03 once more by the location of the peak, which is shifted to higher masses but also wider. In addition, K03 finds for the 5M$_\odot$ and 6M$_\odot$ models a ratio of up to 0.4 for Z = 0.004, a value

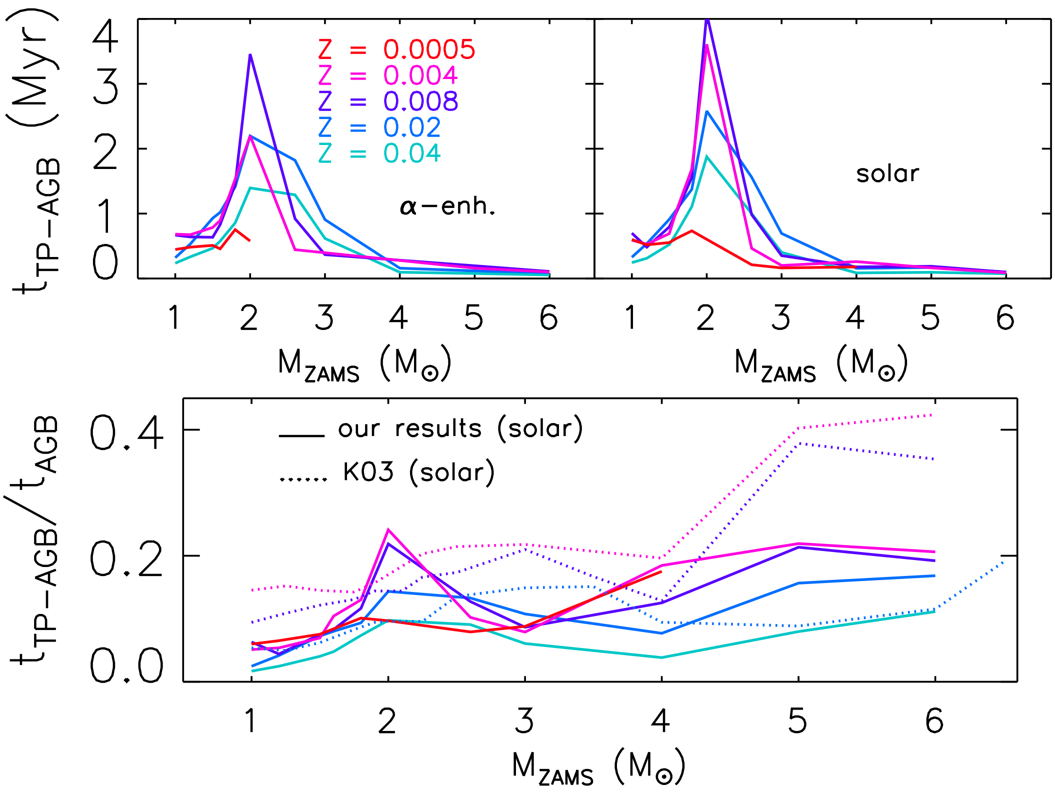

Figure 7.6.: *Top* - TP-AGB lifetimes versus initial mass for our 10 different compositions. *Bottom* - TP-AGB duration with respect to the entire AGB (E-AGB+TP-AGB) for our solar-scaled compositions and the K03 solar-scaled models.

much higher than any of our results. This is because our 5M$_\odot$ and 6M$_\odot$ models experience early convergence problems and stop prematurely their TP-AGB evolution.

In short one can say that total AGB lifetimes increase with increasing metallicity mainly because of the E-AGB duration. For a population of moderate-mass stars, there is always a maximum lifetime which occurs for the model with the smallest core when it reaches the TP-AGB. This models corresponds to the last model to experience a mild He-flash at the transition from low- to intermediate-mass stars. The location of the peak with respect to initial mass ($\approx$ 2M$_\odot$) depends on metallicity, higher Z values rendering higher transition masses. Furthermore, the transition mass depends on the inclusion or not of overshooting: models that do not consider it (e.g. VW93, K03) obtain the transition at higher masses. If our grid had a finer mass-resolution around this point it is likely that we would find different masses for each Z value. Instead our longest-lived AGB models occur at $M_{\rm ZAMS}$ = 2M$_\odot$ for all compositions except the Z = 0.0005 case where it is at 1.8M$_\odot$. The time proportion that our stars spent in the TP-cycle phase with respect to the total AGB roughly does not exceed 20% with an increasing proportion as metallicity decreases.

7.3.2. Initial-Final Mass Relation

We have already looked (Figure 6.7) at the characteristics of the core mass at the beginning of the TP-AGB. We find a good agreement of our values with those of Miller Bertolami (2006) for Z = 0.02, and with those of K03 for intermediate-mass stars at Z = 0.02, 0.08 and 0.004. For the low-mass stars our core masses are smaller than the K03 ones.

During the TP-AGB the mass of the carbon/oxygen core will grow because the ashes of nuclear burning, but it will decrease because of TDU events that remove the upper parts of the core and mix it to the surface.

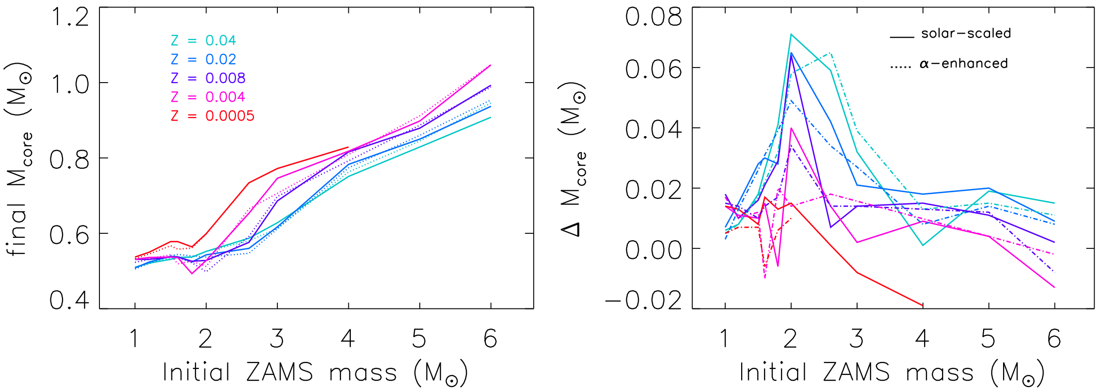

Figure 7.7.: *Left panel:* Final core mass as a function of initial ZAMS mass and composition. *Right panel:* Core mass evolution from the beginning to the end of the TP-AGB.

The left panel of Figure 7.7 gives the final core mass at the end of the AGB. The behavior is, as expected, similar to the one in Figure 6.7: core mass increases with ZAMS mass and decreasing metallicity, the dip at the ≈ 2M$_\odot$ transition is present. The right panel gives the amount by which the core has grown between the 1st TP and the end of the TP-AGB. Most stars experience a increase of their core of about 0.02M$_\odot$. But the He-flash transition stars can grow by as much as 0.07M$_\odot$. There are also some stars that see their cores decrease in mass because of very efficient TDU: the 4M$_\odot$ / Z = 0.0005 model has a core at the end of the TP-AGB that is 0.02M$_\odot$ less massive.

The peak for the 2M$_\odot$ models agrees well with the fact that these stars experience mild TDU (with respect to higher mass stars) and have the longest TP-AGB lifetime: their cores have therefore more time to grow and are not reduced by too strong TDU episodes.

Core growth also increases with metallicity, because TDU is less efficient at high Z. For the Z = 0.04 models, the core mass increase of 0.071M$_\odot$ (2M$_\odot$) and 0.065M$_\odot$ (2.6M$_\odot$) is the biggest for both solar and α-enhanced distributions. On the other hand the low-Z (0.004, 0.0005) models which already experience efficient TDU episodes early in their evolution are the only ones to see their core mass decrease.

In Figure 7.8 we compare our final core results with those of VW93 and K03. Our values are systematically lower. This originates from the combined effect of the initially lower cores at the 1st TP, as well as our strong mass-loss rates and efficient TDU on the TP-AGB. The difference between our results and the two previous ones is even more evident for the lower mass stars below 2M$_\odot$, where deviations were already present before the TP-AGB phase.

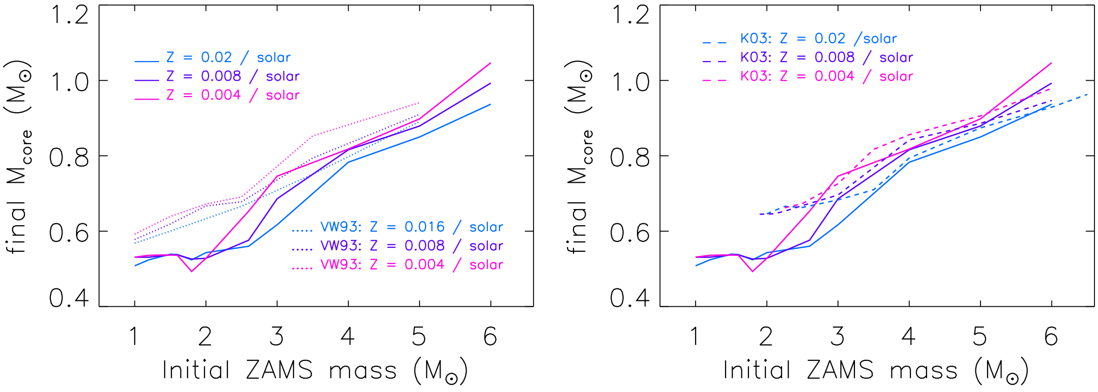

Figure 7.8.: Final core mass as a function of initial ZAMS mass and composition. *Left panel:* comparison with the Vassiliadis & Wood (1993) models. *Right panel:* comparison with the Karakas (2003) models.

As for the TP-AGB lifetimes, the initial-final mass relation (IFMR) depends in a complex way on all the phenomena occuring during the TP-cycle and it is not easy to predict it through simple logical deductions. In Figure 7.9 we show the predicted IFMR of two (Z = 0.02, 0.008) of our solar-scaled metallicity models, the Weidemann (2000) relation (values from his Table 3), as well as observational results from white dwarf masses in binary systems and open clusters. We take data for: M37 (Kalirai et al. 2005), NGC 2516 (Ferrario et al. 2005), Praesepe (Claver et al. 2001, Ferrario et al. 2005, Dobbie et al. 2006),

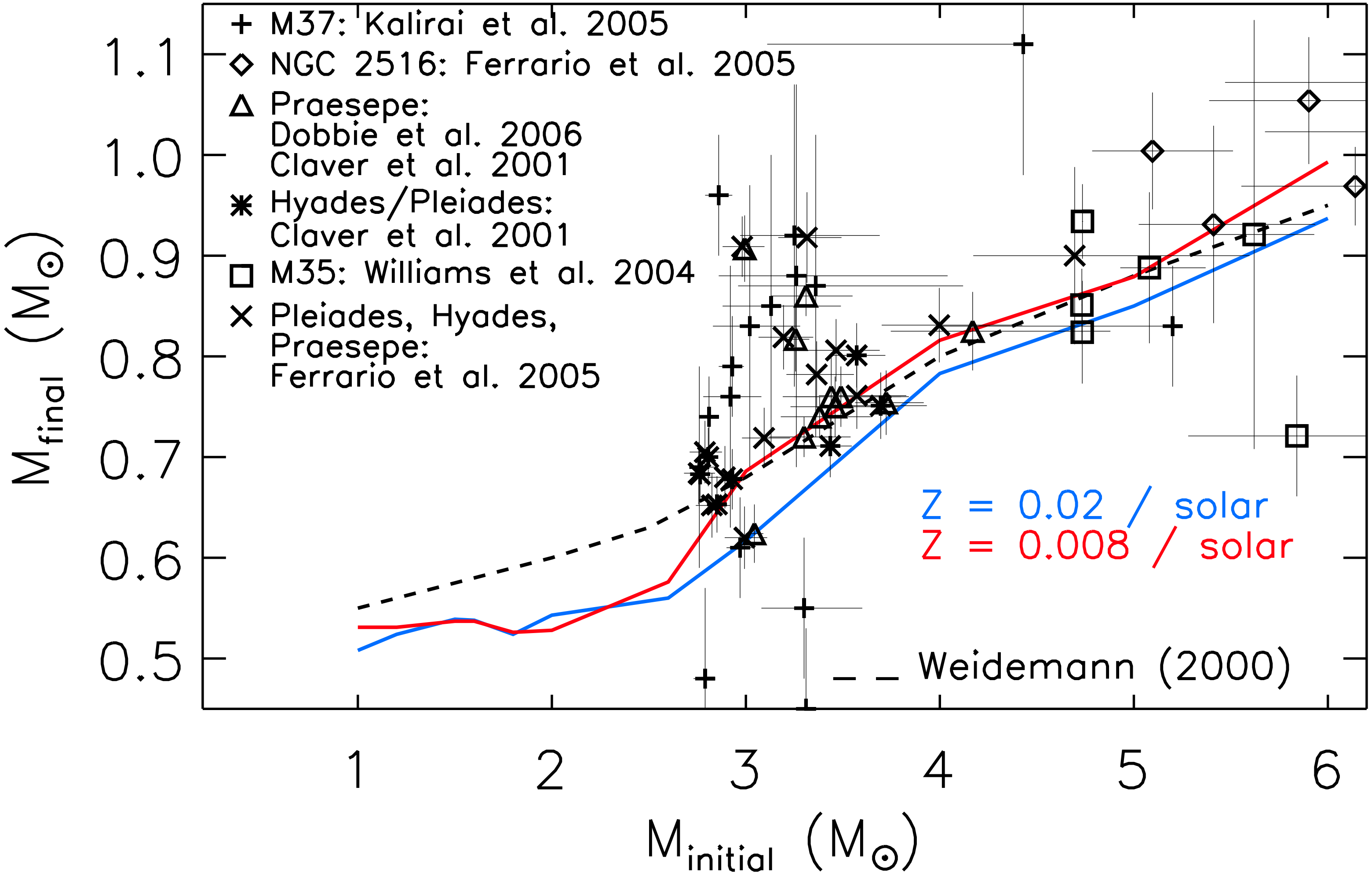

Figure 7.9.: The initial-final mass relation from our models (colored lines) for two solar-scaled metallicity compositions. The Weidemann (2000) relation (dashed line) as well empirical data for white dwarfs in open clusters and binary systems are also given (see text for details).

M35 (Williams et al. 2004), Hyades and Pleiades (Claver et al. 2001, Ferrario et al. 2005). These observations do not cover the low-mass star range but we have found no good-quality data in the literature corresponding to this region.

The Weidemann (2000) relation lies between our two IFMRs. It is only higher for the lower masses. The empirical data does not allow us to clearly test our results as the points are too scattered especially around the $3M_\odot$ region. These data points are mainly those of M37 from Kalirai et al. (2005). With respect to these M37 measurements, Marigo & Girardi (2007) invoke the argument of Dobbie et al. (2006): because the initial metallicity of M37 is not well known, the mass determination of its white dwarfs may still greatly vary. If we exclude the M37 data points form figure 7.9 the agreement with our results is quite good.

Finally, we note that our Figure 7.9 is very similar (some extra observational data has been added) to figure 26 of Marigo & Girardi (2007), where the IFMR of their TP-AGB synthetic models is plotted for 7 different metallicity values ranging from 0.03 to 0.00001. If we consider all our metallicity-dependent IFMRs, as plotted in Figure 7.7, their results manifestly agree well in a qualitative way with ours throughout the entire initial mass-range. This is important because there are no other IFMR originating either from detailed or from synthetic grids that cover such a wide metallicity interval.

7.3.3. Effects of the New Opacity Prescription

One of the main new features of our TP-AGB models is the use of low-temperature molecular opacities for varying surface C/O ratios. In Chapter 4, we have presented these new Ferguson (2006) (F06) opacity tables included in our code.

As was already shown for both low-mass (Marigo 2002) (M02) and massive (Marigo 2007) AGB stars, the most remarkable consequence of such C-rich opacities in our work is the sudden cooling of the stellar tracks after C/O reaches unity. The synthetic TP-AGB tracks of P. Marigo (e.g. Marigo & Girardi 2007), coupled to her routine estimating opacities in an approximative way but for any composition, have become the reference as the only extended synthetic grid taking into account this phenomenon.

Only very recently, detailed TP-AGB models by Cristallo et al. (2007) (C07), calculated with the FRANEC code, have been coupled to other properly computed C-rich opacity tables. However, results solely for one single model ($2M_\odot$ / Z=0.0001) were presented.

In Figures 7.10 and 7.12, we look at the effect of our new opacity tables on the temperature profile of our own models.

The first example is a $2M_\odot$ star with an initial solar composition (Figure 7.10). We deliberately use a very small mass-loss rate in order to follow the evolution longer and decouple the effect of decreasing temperature from the mass-loss. For comparison, models with (solid lines) and without (dotted lines) C-rich variable opacities have been computed. Two different sets have been used: the blue lines correspond to the new F06 tables and the black lines to the M02 opacities.

The M02 opacity-routine results were initially used in our code as a simple first attempt to better model the low-temperature molecular opacities before the F06 tables were created. Here we present the differences between both, but the F06 tables are the ones that are used in all of the models that constitute our grid. The 3-dimensional interpolation (in X, log Z and C/O) used in our code between the F06 opacity tables has already been presented. The M02 opacities were implemented in a similar but simplified way.

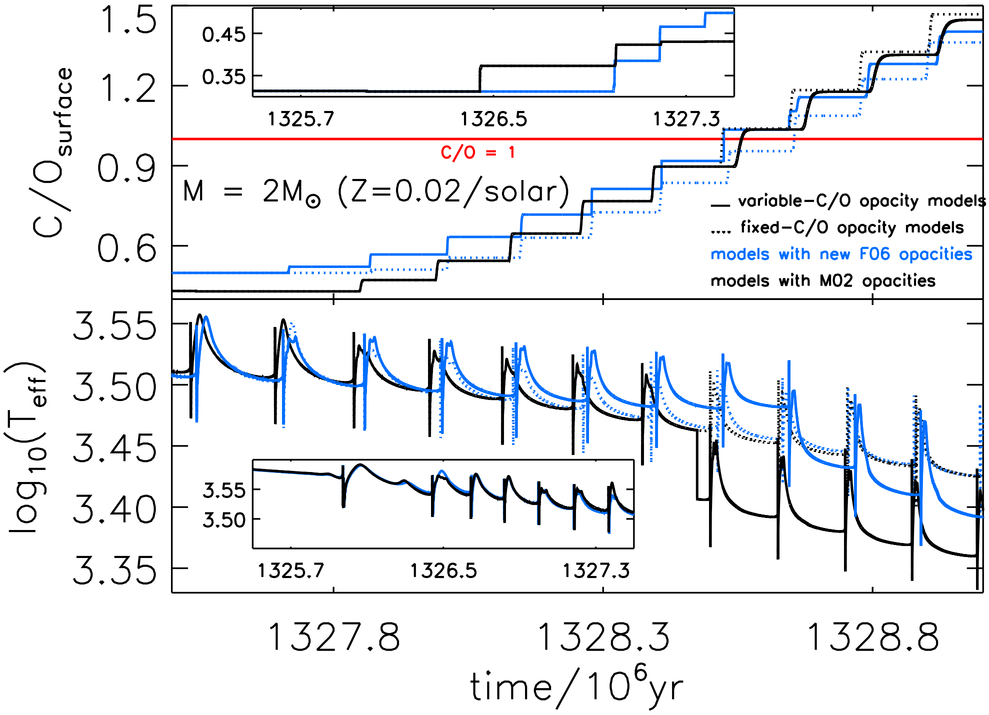

Figure 7.10.: Influence of the new Ferguson (2006) (F06) molecular opacities on a 2M$_\odot$ model with a Z = 0.02 / solar-scaled composition. The two insets correspond to the previous evolution starting at the 1st TP. The models with the Marigo (2002) (M02) opacities are shifted by -0.072 Myr with respect to the other models. Mass-loss rates weaker than the ones produced by our standard prescription are used (further explanations are given in the text).

We use a detailed stellar evolution program and on-the-fly calculations are not feasible. Instead of computing the opacities for each composition during the evolution like in the M02 synthetic code, we interpolate between pre-calculated tables of different compositions provided to us by P. Marigo (priv. communication). The interpolation is not done in three dimensions like for the F06 case, but rather in two dimensions (X and log Z). In order to account for the C-enhancement we use the following approximative method. When no C-rich opacities are considered, the interpolation in log Z is normally done between table sets calculated for different values of Z (0.02, 0.03, 0.04, 0.07 and 0.1) with the same solar-scaled distribution of the heavy elements. For C-rich opacities we substitute all the solar-scaled tables of Z values above 0.02 with tables corresponding to the same total metallicity, but where the heavy element increase is solely due to carbon. The mixture for the Z = 0.03 case is computed for a Z = 0.02 solar-scaled base composition plus an additional 0.01 fraction of carbon. Similarly, the Z = 0.04 tables result from a 0.02 carbon increase, the Z = 0.7 ones from a 0.05 carbon increase, etc. Instead of all being 0.48, the C/O ratios of the different metallicity sets are thus 0.48, 1.86, 3.24, 7.38 and 11.52.

For the model in figure 7.10, when the total surface metallicity reaches 0.03, the C/O ratio is below unity at a value of about 0.9. Thus, the composition of our Z=0.03 tables with the M02 opacities overestimates by a factor of two (the Z=0.03 tables have C/O = 1.86) this ratio. Furthermore the effect of the C-rich opacities was initially shown by M02 to have a sudden effect mainly at the C/O = 1 boundary and not earlier. We thus decided to keep on using the solar-scaled opacity set as long as C/O < 1 or $Z_{\rm surf} \approx 0.03$. Only afterwards do we substitute the C-enhanced Z = 0.03, 0.04, 0.07 and 0.1 sets. The temperature drop in Figure 7.10 for the M02 model is very sudden because of this switch to the different opacity set. As this was a test case before implementing the F06 tables and the opacity interpolation scheme was anyhow crude, we did not worry about this abrupt change that does not appear in other model quantities (total luminosity, shell-burning luminosities, dredge-up, etc) because of the small enough timesteps. Finally, while the set of tables with the M02 calculations was combined with older high-temperature opacities obtained from the OPAL web site in 1995, the F06 ones were extended by 2006 OPAL opacities. As a result, models with F06 (blue) and M02 (black) opacities are offset on the TP-AGB, because of the previous evolution on which low-temperature molecular opacities have no effect, by 72 Kyr. In the figure, the black models have accordingly been shifted backwards in time for clarity.

The temperature of the variable-C/O M02-opacity model (solid black line) decreases, around the 1328.5 Myr mark, by 0.05 dex with respect to the dotted black line (fixed-C/O opacities). This difference continues to increase to 0.07 dex in the next 4 TPs. The C/O increase, associated with TDU episodes, is not really affected by the M02 opacities as it continues to regularly occur and by the same amount in both cases; the TP occurrences are only slightly shifted between the two models.

As expected, the F06 (solid blue line) models also show a temperature decrease after the C/O = 1 boundary has been crossed. The drop is much smoother because of the continuous interpolation between a same set of tables and a direct coupling to the actual surface C/O value, but it is also less pronounced; the temperature reduction reaches gradually only 0.3 dex at the end of the plotted evolution. The model with the variable-C/O opacities has a slightly higher surface C/O ratio. This is because at the 4th and 5th dredge-up episodes, the C-enhancement was not as strong as in the chemically-fixed (dotted blue line) opacity model. After the 5th TP, the C/O increase is regular and with the same strength in both models.

The temperature drop when the star becomes C-rich is amplified in the case of our Z interpolation of the M02 opacity tables. This is because the mass fractions of the CNO elements are only approximatively taken into account by the higher metallicity opacity tables obtained solely through C-enhancement, and the value of the C/O ratio is overestimated. As a result, opacities are higher.

We also observe a further particularity of the F06 C-rich opacity track. As the C/O ratio approaches unity, the effective temperature initially increases, by about 0.025 dex, before it decreases again. This increase is not observed in the fixed-C/O opacity case and in the M02-opacity model. Such a behavior is in fact perfectly explainable from the opacity profiles of the F06 tables at different C/O ratio values in Figure 7.11.

We plot for 6 different values of the C/O ratio, the Rosseland mean opacity as a function of effective temperature. The temperature, density and chemical composition reproduce an environment similar to the one present in the outer envelope of the models of Figure 7.10 around the 1328.4 Myr mark ($\log_{10} R = -1.0$ corresponds to $\log_{10} T_{\rm eff} = 3.5$ and $\log_{10} \rho = -8.50$). If one follows the progression of the curves with increasing C/O ratio (0.48, 0.90, 1.00, 1.10, 3.00, 20.00), it is clear that, for our temperature region of interest, the opacity first decreases until the C/O = 1 boundary is reached and then increases again up to opacity values higher than the initial solar one. The opacity for O-rich compositions is mainly due to the TiO and H_2O molecules. As carbon content increases, these molecules dissociate, more CO molecules are formed and the total opacity goes down. Once C/O > 1, very few O atoms able to form more CO molecules remain and C-bearing molecules (e.g. CN, C_2, C_3), that dominate the opacity, accumulate. The opacity fluctuations at temperatures lower than about 3.47, in both increasing and decreasing directions, are more sudden around the

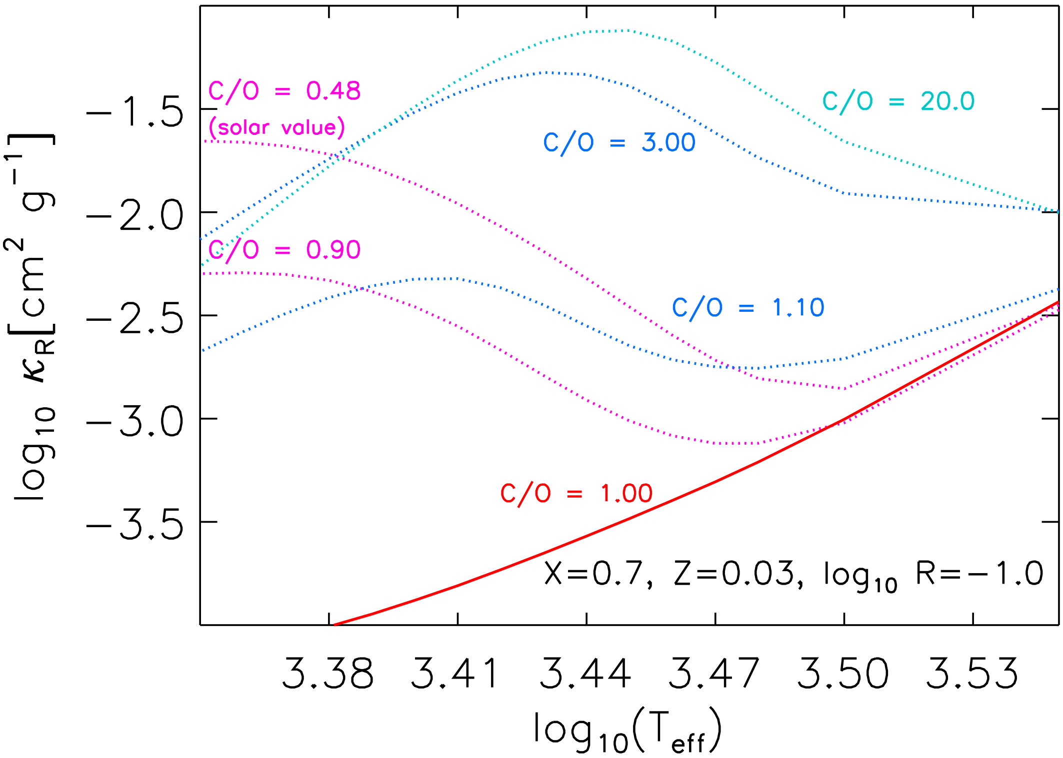

Figure 7.11.: Rosseland mean opacity as a function of effective temperature from the new F06 tables for different C/O ratio values.

C/O = 1 transition (0.9 < C/O < 1.1). As higher opacities in stellar envelopes correspond to larger radii, hence lower effective temperatures, this opacity change is directly reflected in the temperature profile where the temperature goes up before dropping again.

Figure 7.12 displays the temperature and surface C/O evolution of another model at lower metallicity for which we do not show the effect of the M02 opacities, but only those of the F06 ones. In the left panels, we follow the evolution with almost no mass-loss, like in the previous example, but for many more TPs. In the right panels the same models are computed, this time with our standard mass-loss description.

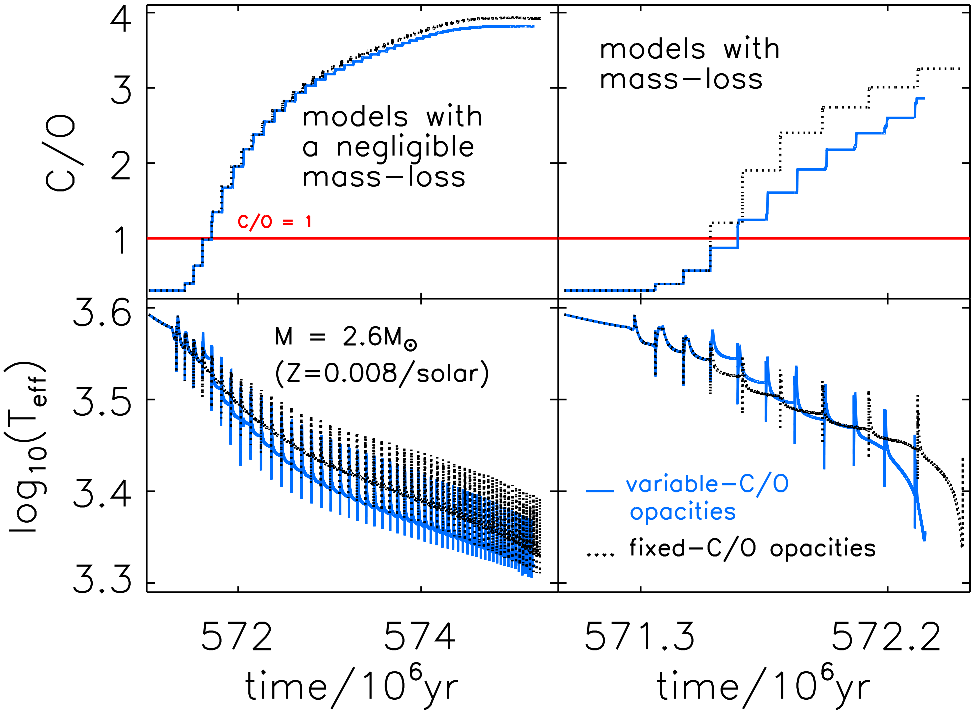

Figure 7.12.: *Left Panels* - same as Figure 7.10 for a 2.6M$_\odot$ / Z=0.008-solar model. Only tracks with/without the F06 opacities are presented. *Right Panels* - similar models as in the left panels but with the inclusion of our standard mass-loss prescription.

Once more we see the same opacity-dependent temperature behavior. That is, an initial increase as the C/O ratio approaches unity, followed by a gradual drop when C/O > 1. The temperature difference in the left panel between the variable- and fixed-C/O opacity models increases and reaches a maximum ($\approx$ 0.03 dex) after about 15 TPs. This originates form the fact that the most noticeable opacity change occurs around the C/O = 1 transition, but as the ratio value increases, the opacity values saturate and do not increase much. For a considerable jump of the C/O ratio - from 3 to 20 - the corresponding opacity increase is relatively small ($\approx$ 0.25 dex). The C/O increase is stronger during the first TPs. Its efficiency decreases after a while, then almost drops to zero and the C/O surface ratio reaches a constant plateau a little under a value of 4. Both models follow each other closely for many TPs, but the fixed-opacity track experience slightly more efficient TDU episodes and towards the end reaches a surface chemistry with a little additional carbon.

The evolution is evidently much shorter (right panels) when mass-loss is included. Temperature drops much more rapidly in both cases because of the mass-loss, but in the variable-C/O opacity model it is more pronounced due to the higher C-rich mass-loss rates, coupled to T_{eff} by a stronger dependence. The temperature difference between both models actually reaches 0.1 dex at the end of the evolution. This is much higher than the 0.03 dex for the models with no mass-loss. The combined effect of the F06 opacity sets, and the inclusion of mass-loss affect the TDU events. The fixed opacity model experience deeper dredge-up which efficiently brings more carbon to the surface.

Our F06 set extends over a large range in Z for two base compositions (solar-scaled and α-enhanced) and additionally take into account H and C/O variations. To the C/O parameter we link (Chapter 4) specific variations of C, N and O. The interpolation in metallicity is continuously performed during the evolution: when the total Z value increases because of the dredged-up elements, opacities corresponding to an overall enhanced-metal distribution are considered. It is true that this approximation of the TDU effect by higher metallicity opacities may be more or less adequate in different situations. While in the metal-rich models, which already have large opacity values, the difference might not be of importance, in the metal-poor calculations the overall mass of dredged-up carbon can be much greater than all the other heavy elements, such as iron, which basically remain unchanged to their initial very low value. In that case, a global metallicity interpolation would overestimate the iron abundance and its atomic contribution to opacity. In our case, it does however not underestimate, like it would in any simple overall Z interpolation scheme, the carbon atomic and molecular contributions because we do consider different C/O compositions. It is actually difficult to assess, solely by simple argumentation, the opacity contribution of extra heavy element sources which operate in different layers of the star. But the iron overestimated contribution should mainly have a gradual effect, spread over the entire TP-AGB evolution, rendering globally higher opacities and cooler models. The most relevant opacity dependency, which has a sudden and more noticeable effect for TP-AGB models is the C/O one, which we take into account.

Opacity tables with variable carbon content for the Z = 0.0001 case, have been created and coupled to AGB models by C07. Like we did in our comparison between the fixed-, the M02- and F06-opacity tracks in Figure 7.10, they also show the temperature dependence of their tracks on opacity sets that treat surface chemistry in different ways. Their figure 4 (upper left panel of our Figure 7.13) shows the surface temperature evolution on the TP-AGB for a $2\mathrm{M}_{\odot}$ model. Three different opacity sets are tested: a) Z-fixed, one in which only hydrogen variations are considered but total metallicity is fixed, b) Z-int, another one with both hydrogen and total metal content variations taken into consideration, and c) CN-int, a third one with variations in hydrogen, carbon and nitrogen accounted for.

Their Z-fixed model is obviously a most crude approximation. Their Z-int case is our previous standard procedure that had been used in our code for a while. The CN-int case is similar to our F06 opacity treatment in that it accounts for H, C and N enhancements, but does on the contrary not scale all other heavy elements to the increasing total metallicity like it is done in our (as well as in their Z-int) interpolation.

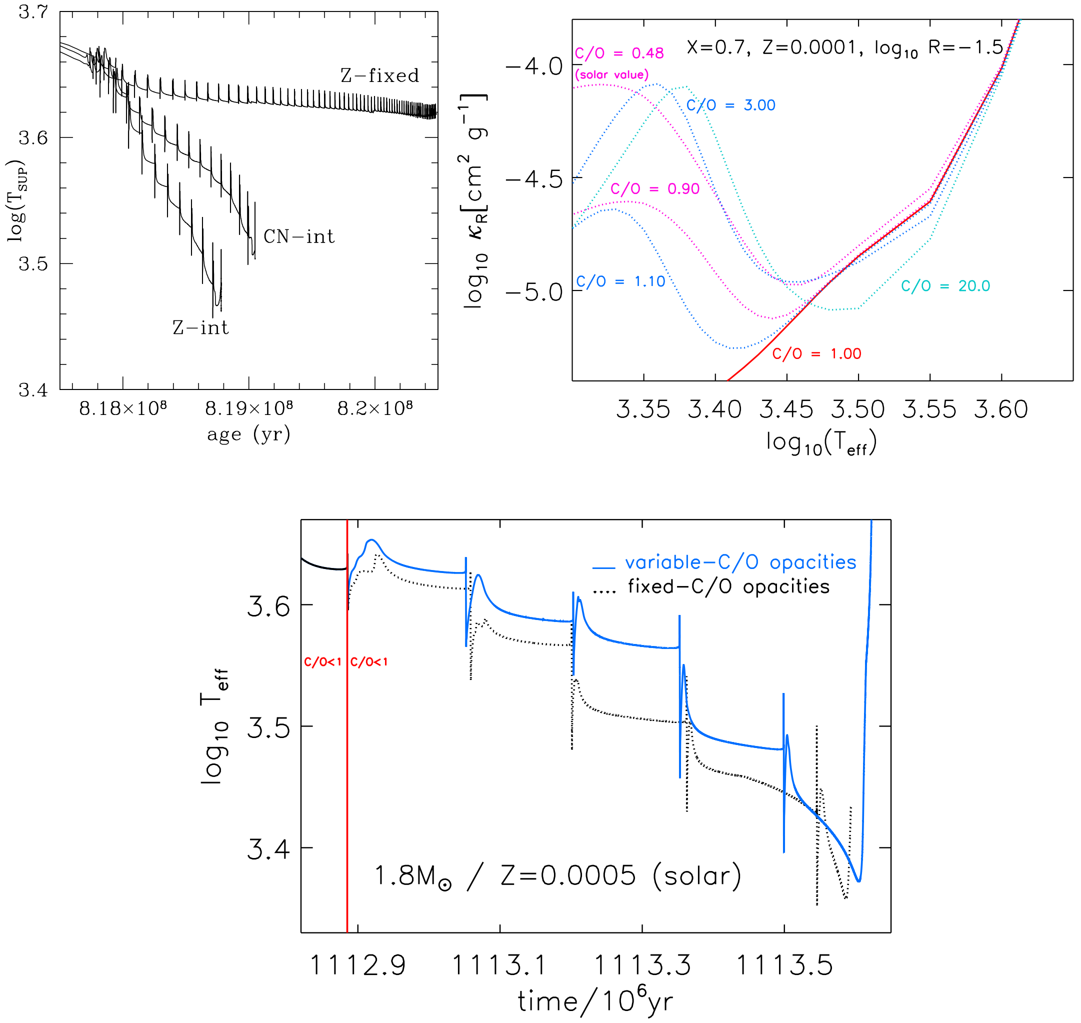

Figure 7.13.: *Upper left panel* - Figure 4 of Cristallo et al. (2007) (C07). Surface temperature as a function of time for their $2M_\odot$, Z = 0.0001 model. The three cases are discussed in the text. *Upper right panel* - Rosseland mean opacity profile from the new F06 tables with respect to $T_{\rm eff}$ for different C/O ratio values at Z = 0.0001. *Lower panel* - $T_{\rm eff}$ as a function of time for our $1.8M_\odot$ / Z=0.0005 (solar) model with/without variable-C/O opacities.

For their opacity tables, C07 use solar-scaled initial composition values given by Anders & Grevesse (1989) with some small more recent updates. Our base composition from Seaton et al. (1992) is very similar to theirs. Based on the molecular data of their table 1, the C07 opacity grid was computed with the COMA code of Aringer (2000)'s PhD thesis. Our new F06 opacities have been computed in a similar way as explained in Ferguson et al. (2005) - the latest updated and expanded published version of the widely used low-temperature tables from Alexander & Ferguson. C07 properly compute the molecular opacities for 3.2 < log T < 4.05, and F06 provides us with tables in the following range, 3.0 < log T < 3.70. Both sets extend the tables to higher metallicities with the OPAL Web tool. It is beyond the scope of this work to discuss the conception of these two tables. We simply compare their effect on TP-AGB models.

The C07 CN-int set considers varying carbon and nitrogen independent enhancements taking into account all the possible combinations. While the C07 tables have, in the more general case, a better independent coverage of both C- and N-parameter spaces, they do not treat O-enhancement. Our approach, in the specific case of TP-AGB evolution, deals with the nitrogen and oxygen variations by coupling them to the increase of the most important element, carbon, and parameterizes the chemical changes with respect to the C/O ratio. In low-metallicity stars, the Z = 0.0001 case for instance, TDU is more efficient. Along with carbon, oxygen can also be dredged-up.

Because of our overshooting prescriptions we do find O-enhancement in our models. Our lower metallicity stars (Z = 0.0005) show final surface C/O ratios that reach values of up to about 5 (see Table 7.5). As an example we take the $1.8M_\odot$ model. At the end of the AGB, the C/O ratio is 4.205: during the TP-cycle the oxygen abundance increases from $0.239{\cdot}10^{-3}$ to $4.09{\cdot}10^{-3}$ while the carbon goes from $0.0451{\cdot}10^{-3}$ to $12.90{\cdot}10^{-3}$. If only the carbon increase is taken into account, and the oxygen is left to its initial abundance, the final C/O value would be 7.227. Considering opacity tables solely with C-enhancement, as C07 do, would imply in this case an overestimation of the C/O value.

Two important remarks, regarding O-enrichment, should be done at this point. Firstly, TDU is less efficient in low Z stars and more efficient in high Z ones. But the amount of dredged-up oxygen and carbon does not necessarily follow a strict correlation. In all our opacity tables the oxygen (and nitrogen) increase is coupled to the carbon one as reflected in solar metallicity computations. For the metal-rich models where C/O will never cross the unity barrier, this has little effect. But for the low-metallicity cases, oxygen increase for a given C/O value might still be, even if it is to a lesser extend than if no oxygen increase were considered, underestimated and as a consequence the C/O ratio overestimated. Nevertheless, regarding the C/O ratio as our main parameter, with carbon, oxygen and nitrogen variations couple to it, even if this is done in an identical way for all Z, is from our point of view the most profiting parameterization in terms both of accuracy and computing time.

The second remark is that the oxygen increase depends on the prescription implemented for convection. Detailed AGB models which do not include overshooting at convective boundaries (e.g. Karakas 2003) do not find surface oxygen enrichment. Others (e.g. Herwig 2000) like ours that do, find higher oxygen contents. This oxygen abundance is actually one of the arguments of Herwig (2000) to support the inclusion of overshooting in TP-AGB models. Indeed, the surface composition of [WC]-type central stars of planetary nebulae (e.g. De Marco et al. 1998, Koesterke & Hamann 1997) and PG 1159 stars (Dreizler & Heber 1998, Werner et al. 1999) can be explained from the abundances found in progenitors AGB stars. These H-deficient post-AGB stars show surface abundances that are very C- but also O-rich. Models without overshoot never show more than a very small oxygen increase if they do at all.

In any case the CN-int C07 opacities should globally be similar to ours. The interesting feature to notice in Figure 7.13, is the actual temperature increase, and not decrease, of the CN-int track with respect to the Z-int case. C07 correctly point out the cooling of the their tracks with the inclusion of the C-rich opacities, but this is only valid if one takes the Z-fixed track as a reference. The Z-int interpolation approach of C07 is similar to our dotted lines and the CN-int to our solid ones.

The main focus in the literature has been the increase of the Rosseland mean for higher contents of carbon and therefore lower surface temperatures. Here we observe a temperature increase, which implies a opacity decrease. This is indeed the case if we look once more at the opacity profile (upper right panel of Figure 7.13). The metallicity of the environment is different than in Figure 7.11: we have a much lower Z at 0.0001. From the y-axis, it is obvious that the overall opacity values are much smaller than for the metal-richer case of Figure 7.11. What is more interesting is the fact that the curves, with larger than unity C/O ratios, have been horizontally *shifted* towards lower temperatures. The consequence of this translation is twofold. First the C-rich opacities are no longer higher than the O-rich ones in the temperature range roughly between 3.4 and 3.6. Second the opacity dip for the high C/O (20) cases, also shifted to lower temperatures, is below $\log_{10} T_{\rm eff} = 3.55$, a range in which the models lie.

In their paper, C07 do not give their models C/O surface values. It is nevertheless known that TDU efficiency increases with decreasing metallicity. Our $2M_\odot$ lowest metallicity model (Z = 0.0005) experiences TDU at the 2nd TP and has a surface carbon over oxygen ratio of 4.180 after 6 TPs. The $1.9M_\odot$ lowest metallicity model of K03 (Z = 0.004) show a final C/O value after 16 TPs of 8.1795. The C07 models, of even lower metallicity, experience between 12 and 16 TPs. It is most probable that the C/O ratio is very large (especially if no O-enhancement is present) and high enough as to produce low opacities at temperatures between 3.45 and 3.60.

This temperature increase for chemistries with C/O values higher than 1, is furthermore found in our own low-metallicity models. To show this we plot, in the bottom panel of figure 7.13, the temperature evolution of our $1.8M_\odot$ / Z = 0.0005 (solar) star with and without the inclusion of variable-C/O opacities. After the critical C/O = 1 transition, the blue line is systematically above the black dotted one. The temperature difference between the two cases increases up to a maximum of 0.06 dex before decreasing again. At the end of the evolution, both models see their effective temperature drop down to similar values, with the fixed-opacity model reaching the lowest ones. In the habitual simple scenario, C-star models with C-rich opacities live less because they reach low temperatures earlier, and promptly lose their envelope due to high mass-loss rates. Here we witness the opposite effect for a low-metallicity C-star: the more accurate C-rich opacities prolong the TP-AGB lifetime by about 0.02 Myr.

The stellar surface of a star sees its metallicity increase during the TP-cycle. This implies an opacity and in turn a temperature change. The dependence of the evolution on the

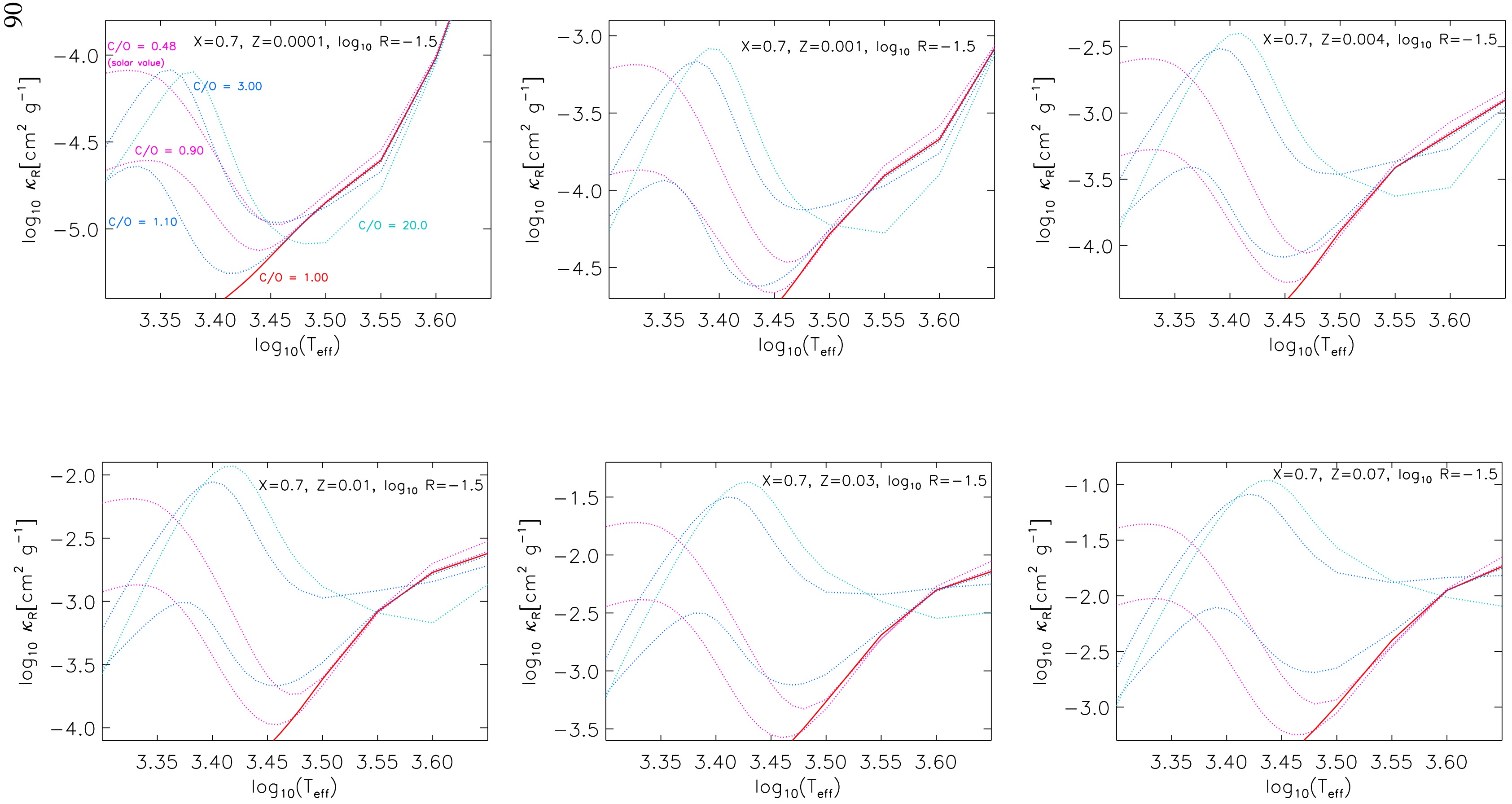

Figure 7.14.: Opacity profiles for varying C/O ratio values with respect to temperature. From left to right and top to bottom, panels show in sequence the behavior of these profiles as metallicity increases from Z = 0.0001 to Z = 0.07.

C/O ratio with respect to the O- and C-rich regimes has already been shown (e.g. Marigo 2002, 2007, Cristallo et al. 2007). But the magnitude and the direction of this dependence with varying metallicity has not yet been investigated in detail. It is therefore important to study the sensitivity of these TDU-related fluctuations on Z. We saw that the total surface metallicity of an AGB star - which depends on $M_{\rm ZAMS}$ and $Z_{\rm ZAMS}$ - in connection to the C/O value, further influences the temperature-opacity interplay. As for most others factors regulating TP-AGB evolution in a complex and interconnected way, it is difficult to describe such dependencies by simple means.

Put aside the general opacity increase with increasing metallicity, a first step is noticing the aforementioned shift of the C-rich opacity curves to lower temperatures as Z increases. This is shown with more clarity in Figure 7.14 where a set of opacity profiles in the same temperature range ($3.30 < \log T < 3.65$) for different C/O values is plotted at different metallicities. The transition, in terms of opacity changes from an O-rich to C-rich composition, is less and less pronounced at decreasing metallicity. As suggested by the previous works of P. Marigo (Marigo 2002, Marigo & Girardi 2007), the effect of this transition can almost become negligible in AGB population of very low metallicity since the formation of molecules becomes less efficient at lower Z because of higher temperatures and lower abundances of involved isotopes. But for high values of the C/O ratio, we observe a noteworthy opacity decrease at the higher temperature end. As this dip also follows the general drift to lower temperatures, its influence can become important in metal-poor C-rich cases when the O-rich/C-rich transition does not play a role anymore.

In summary, we note that, while the sudden cooling, at the C/O = 1 transition, of the TP-AGB tracks affecting the evolution is recovered with our new F06 opacities, we also put forward the opacity decrease and thus temperature increase that can occur in two different scenarios: a) metal-rich AGB stars that experience TDU as the C/O ratio goes from its initial low value to the critical transition one, b) metal-poor AGB stars that have already become C-rich because of very efficient TDU when the surface C/O ratio reaches higher values. Both of these cases can either result in an overall reduction of the expected strong cooling effect or in an actual increase of the surface temperature, thus moving the tracks towards *bluer* temperatures and prolonging the TP-AGB evolution. The necessity to couple variable-C/O opacity tables and TP-AGB computations is therefore further asserted as these opacities can influence the evolution in two opposite directions.

7.3.4. C-star lifetimes

In section 7.3.1 we compared the TP-AGB lifetimes of our models with previous theoretical tracks. Now we look at our results with respect to observational work from AGB stars in the Magellanic Clouds (LMC, SMC). We specifically compare theoretical values of our C-rich models to C-star lifetimes in the LMC and SMC.

The duration of the C-rich TP-AGB phase from our models is first plotted against initial mass in Figure 7.15. For the Z = 0.04 case only results are unavailable because at these high metallicities no models attain a surface C/O value higher than unity.

As expected, the models with the lower lifetimes are those with the highest metallicity

(Z = 0.02) because the TDU is less efficient in those stars. One should also expect to find longer lifetimes as metallicity decreases because the efficiency of the dredge-up episodes increases with decreasing Z. As in the total TP-AGB lifetime case (Figure 7.6) this is not what we find. The peak duration of the 2M$_\odot$ model is higher at Z = 0.008 (solar) than at Z = 0.004. Furthermore all Z = 0.0005 models have, put aside the solar metallicity case, the lowest lifetimes. This is once more related to the dependence on the core mass at the 1st TP. The Z = 0.0005 models in Figure 6.7 show the smallest relative dip at the He-flash transition mass. As a result, the AGB maximum lifetime is not much higher at the peak then the other different mass models.

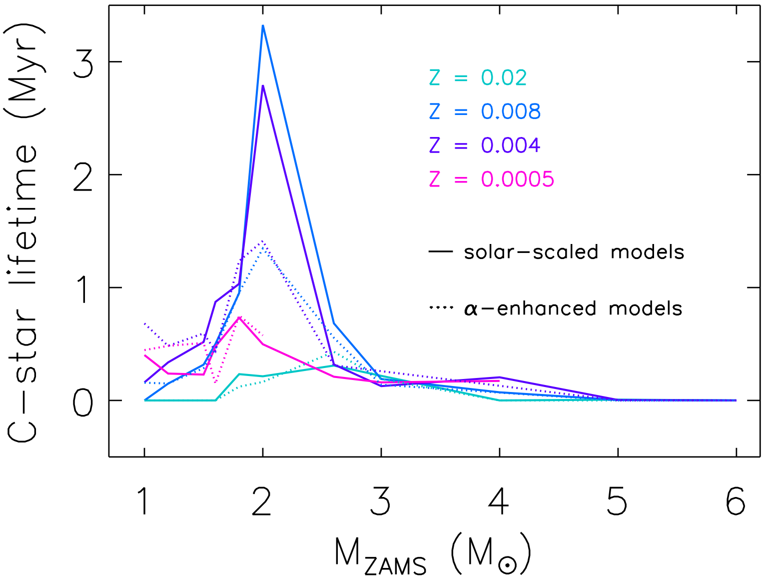

Figure 7.15.: Lifetimes of models during their C-rich TP-AGB phase.

Again, the metallicity dependence on the location of the peak is evident. The Z = 0.0005 models lifetimes, reach their maximum at an initial mass of 1.8M$_\odot$, while the Z = 0.008 and 0.004 case do so at 2.0M$_\odot$. For the solar metallicity case there is no clear maximum lifetime point. But a rather elongated bump, shifted towards higher masses, is seen.

The O- and C-rich TP-AGB models, observationally correspond to M- and C-stars. Girardi & Marigo (2007) by using M- and C-star counts in the Magellanic Cloud clusters, have derived limits to the lifetimes for the corresponding phases. For the M-stars, SMC lifetimes are poorly constrained by the data and LMC ones have maximum values of about 4 Myr but do not show any clear behavior.

The duration of the C-star phase has a clear peak reaching up to 2-3 Myr for stars with turn-off masses between 1.5M$_\odot$ to 2.8M$_\odot$. Moreover they find a shift towards lower masses of the lifetime peak as one moves from LMC to SMC metallicities. In their figure 3 (upper left panel of our Figure 7.16), they compare the observational results of LMC C-stars to C-rich TP-AGB models found in the literature that have already been used in population synthesis of galaxies. All model lifetimes - put aside the P. Marigo ones - are significantly shorter than the observed values. As discussed in Girardi & Marigo (2007), synthetic

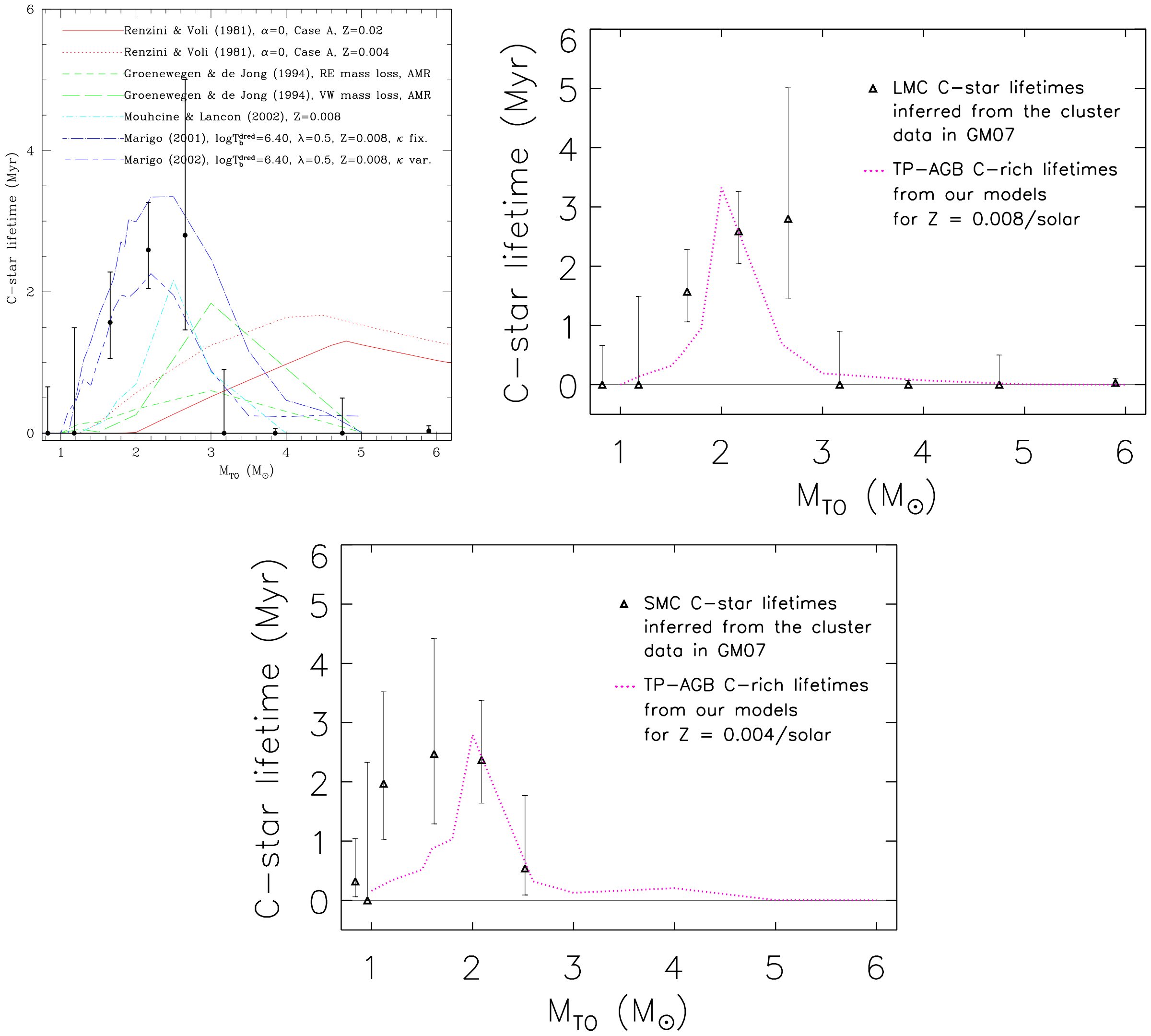

Figure 7.16.: C-star phase lifetimes (Myr) as a function of turn-off mass. The black dots (with error bars) are results (Girardi & Marigo 2007, GM07) obtained from observational data of the Magellanic Cloud Clusters. *Upper left panel* - Figure 3 from GM07. Observational data corresponds to the LMC. Model details, indicated on the figure, are from, Renzini & Voli (1981), Groenewegen & de Jong (1994), Mouhcine & Lançon (2002), Marigo (2001, 2002). *Upper right panel* - Observational results are from the LMC. Our TP-AGB models (dotted red line) correspond to a Z = 0.008 / solar-scaled metallicity. *Lower panel* - Observational results from the SMC. We plot our TP-AGB models (dotted red line) for a Z = 0.004 / solar-scaled metallicity.

TP-AGB models prior to Groenewegen & de Jong (1993) fail to reproduce the C-star Luminosity Function (CSLF) observed in the Magellanic clouds. These produce C-star lifetimes that are too short with respect to the observations and display a bump that is shifted towards higher masses. The synthetic models of Groenewegen & de Jong (1993) were the first calibrated to the CSLF. All subsequent calibrated models are better behaved and centered around lower-mass values. They still however do not exhibit high enough lifetimes. Finally the P. Marigo synthetic models, which are also calibrated to the CSLF, give the best agreement between models and observations. They over- or underestimate the times depending on the inclusion of fixed- or variable-chemistry molecular opacities.

Our detailed TP-AGB models have not been calibrated to the CSLF. We plot in the upper left and lower panels of Figure 7.16 our C-star lifetimes for the two solar-scaled metallicities ($Z = 0.008$ / $Z = 0.l04$) that correspond to LMC and SMC compositions, and compare them to the results inferred from the observational cluster data by Girardi & Marigo (2007).

For the LMC, like it is also the case of the P. Marigo models, our results fit the data well in comparison to all the other sets of synthetic models. Actually, our lifetimes are very similar to the ones of M02 also with variable-C/O opacities. Our profile has its peak slightly displaced to lower metallicities and a little narrower than the observed and M02 ones. For the SMC C-star case as well, our $Z = 0.004$ models reach the maximum observed lifetimes. The, broader and shifted to lower masses (≈ 1.2-$1.8\mathrm{M}_{\odot}$) in comparison the LMC, observational peak is less well recovered by out results.

This metallicity shift of the peak towards lower masses with decreasing Z is very similar to the core-mass dependence observed on AGB lifetimes in section 7.3.1. However, the observational shift is much more important than ours: for a metallicity decrease from LMC to SMC composition, the maximum C-star lifetime moves from $2.66\mathrm{M}_{\odot}$ to $1.62\mathrm{M}_{\odot}$. Between our $Z = 0.008$ and $Z = 0.004$ sets of models, the peak remains at $2\mathrm{M}_{\odot}$. Even if more mass resolution was available around the critical point, the difference would certainly not be as large as the observed one.

Notwithstanding these divergences, the important result of this section is that our models, without any specific calibration to observed C-stars, agree better with Magellanic Cloud cluster data than previous synthetic TP-AGB grids that have already been used in evolutionary population synthesis.

7.3.5. The Core-mass - Luminosity Relationship

Many analytical relations describing the evolution on the TP-AGB by linking together characteristic stellar parameters are available. The $M_{\mathrm{c}} - L$ relationship, between the maximum quiescent surface luminosity L at each interpulse and the core mass M_{c}, is one of them. Over the years, this parameterization has evolved from initially simple linear relations (e.g. Paczyński 1970, Iben 1977) depending only on M_{c}, to more complex non-linear forms (e.g. Wagenhuber & Groenewegen 1998, Izzard et al. 2004) through which the luminosity of a TP-AGB star depends on more than just the core mass.

M_{c} - L linear expressions, with a simple dependence only on M_{c}, imply that there exists a maximum luminosity a TP-AGB star can have; one corresponding to the Chandrasekhar limit at $\approx 1.4\mathrm{M}_\odot$. But it has been shown that, for stars massive enough to experience HBB (e.g. Blöcker 1995b, Wagenhuber & Groenewegen 1998) and for low-mass stars experiencing strong TDU but not HBB (e.g. Herwig et al. 1998, Marigo et al. 1999), deviations from these simple linear relationships occur and violate the predictions.

The core-mass - luminosity relationship (CMLR) during the TP-cycle is also an important input of synthetic TP-AGB modelling since it governs many essential properties of the evolution. While early synthetic codes (e.g. Groenewegen & de Jong 1993, Marigo et al. 1996) neglected any departure due to HBB and strong TDU, the latest synthetic evolution codes (Marigo & Girardi 2007) use the more complex CMLRs. We do not fit our results with any updated analytical relation, but rather compare them to existing CMLRs found in the literature. In fact, Karakas (2003) which had presented the latest grid of detailed models, compared her results with three different types of fits. Because of the lack of any new published parameterization since then, we choose the same ones to do our comparison.

The first expression, used by Marigo et al. (1996) in synthetic calculations, is a combined version from the work of Boothroyd & Sackmann (1988a) and Groenewegen & de Jong (1993). For stars with a core mass in the range $0.5 \lesssim M_\mathrm{c}/M_\odot \lesssim 0.66$, Boothroyd & Sackmann (1988a) give the following relation:

$$L/L_\odot = 238000 \cdot \mu^3 \cdot Z_\mathrm{CNO}^{0.04} \cdot (M_\mathrm{c}^2 - 0.0305 \cdot M_\mathrm{c} - 0.1802). \tag{7.1}$$

For stars that have $M_\mathrm{c}/M_\odot \geqq 0.95$ (Groenewegen & de Jong 1993), the equation below gives the interpulse peak luminosity:

$$L/L_\odot = 122585 \cdot \mu^2 \cdot (M_\mathrm{c} - 0.46) \cdot M^{0.19}. \tag{7.2}$$

When $0.66 \lesssim M_\mathrm{c}/M_\odot \lesssim 0.95$, a linear interpolation between the two is adopted. In the previous formulas, M is the total mass of the star (all masses are given in solar units), $\mathrm{Z_{CNO}}$ the total abundance in mass fraction of C, N and O elements, and $\mu = 4/(5\mathrm{X} + 3 - \mathrm{Z})$ the mean molecular weight of a fully ionized gas; both $\mathrm{Z_{CNO}}$ and μ variables refer to values in the envelope of the star.

The second CMLR, is one presented by Wagenhuber & Groenewegen (1998). They fit the maximum pre-pulse luminosity by a linear relation with respect to core-mass, and add a correction for HBB. Their equation is:

$$\begin{aligned} L/L_\odot = {} & (18160 + 3980 \cdot Z) \cdot (M_\mathrm{c} - 0.4468) \\ & + 10^{(2.705+1.649 \cdot M_\mathrm{c})} \\ & \cdot 10^{(0.0237 \cdot (\alpha-1.447) \cdot M_\mathrm{c}(1)^2 \cdot M_\mathrm{env}^2 \cdot [1-exp\{-\Delta M_\mathrm{c}/0.01\}])} \\ & - 10^{(3.529-(M_\mathrm{c}(1)-0.4468) \cdot \Delta M_\mathrm{c}/0.01)}. \end{aligned} \tag{7.3}$$

α is the mixing length parameter, Z the total metallicity, $M_\mathrm{c}(1)$ the mass of the core at the 1st TP, M_env the envelope mass, and ΔM_c the difference between the core mass at the first and the current TP. We note that contrarily to other works with no overshooting (e.g.

K03) our ΔM_c values do not always grow during the AGB evolution (see right panel of Figure 7.7). They can remain constant or even decrease for high metallicities (Z = 0.0005) because of very efficient TDU.

The third relation is one taken from Izzard et al. (2004). They fit the peak luminosity as a sum of the CMLR and a term due to HBB (L_env) by:

$$L/L_\odot = f_\mathrm{d} \cdot (f_\mathrm{t} \cdot L_\mathrm{CMLR} + L_\mathrm{env}). \tag{7.4}$$

Two different equations are used for L_CMLR. For $M_\mathrm{c}(1) > 0.58\mathrm{M}_\odot$,

$$\begin{aligned} L_\mathrm{CMLR} = {} & 3.7311 \cdot 10^4 \\ & \cdot max\Big[(M_\mathrm{c} - 0.52629) \cdot (2.7812 - M_\mathrm{c}), \\ & 1.2 \cdot (M_\mathrm{c} - 0.48)\Big]. \end{aligned} \tag{7.5}$$

But when the core mass at the 1st TP is lower than 0.58,

$$L_\mathrm{CMLR} = max\Big[10, 4 \cdot (18160 + 3980 \cdot Z) \cdot (M_\mathrm{c} - 0.4468) - 4000\Big]. \tag{7.6}$$

The correcting luminosity due to envelope burning, L_env, is given by:

$$\begin{aligned} L_\mathrm{env} = {} & 1.50 \cdot 10^4 \cdot M_\mathrm{env}^2 \cdot [1 + 0.75 \cdot (1 - Z/0.02)] \\ & \cdot max\Big[0, (M_\mathrm{c}/M_\odot + 0.5 \cdot \Delta M_\mathrm{c,noTDU}/M_\odot - 0.75)^2\Big]. \end{aligned} \tag{7.7}$$

Finally, the relations for both f_t and f_d factors respectively are:

$$f_\mathrm{t} = min\Big[1, \Big(\frac{\Delta M_\mathrm{c,\,noTDU}}{0.04}\Big)^{0.2}\Big], \tag{7.8}$$

and

$$f_\mathrm{d} = 1 - 0.21807 \cdot min\Big[1, exp\{-11.613 \cdot (M_\mathrm{c} - 0.56189)\}\Big], \tag{7.9}$$

where $\Delta M_\mathrm{c,\,noTDU}$ is the core-mass change between the first and current TP without the occurrence of dredge-up.

We plot in Figure 7.17 the peak interpulse-luminosity (solid colored lines) with respect to the core mass of all our Z = 0.02 (solar-scaled) models. The fits used by Marigo et al. (1996) (M96) and those of Wagenhuber & Groenewegen (1998) (WG98) and Izzard et al. (2004) (I04) are also shown by colored symbols. The general trend is, as expected, qualitatively recovered.

First we look at the lower mass stars. Put aside the $1.8\mathrm{M}_\odot$ and $2.0\mathrm{M}_\odot$ models, for core masses below $0.7\mathrm{M}_\odot$, the agreement with the older M96 fits is very good after the initial luminosity increase of the first few TPs. At these low core masses the K03 results (their figure 4.11) also match the M96 fit well after a few TPs. On the other hand the WG98 and I04 give luminosities that are systematically lower then our results. Similarly, the K03 luminosities are higher (their figures 4.13 and 4.15) than the fitted ones of WG98 and I04, but they do not deviated as much as ours do from the parametrized relations.

The 1.8M$_\odot$ and 2.0M$_\odot$ models particularly give high values of L; they are even higher than the ones from the M96 relation. This is related to the fact the first TDU episodes occur early at the beginning of the TP-AGB. In the [1.0M$_\odot$, 2.6M$_\odot$] mass range (see Table 7.2), out of the models that do experience TDU, the 1.8M$_\odot$ and 2M$_\odot$ are the only ones where this happens so early: already at the 2nd TP instead of the 5th as it is the case for all other masses (for which luminosities agree very well with the M96 fit).

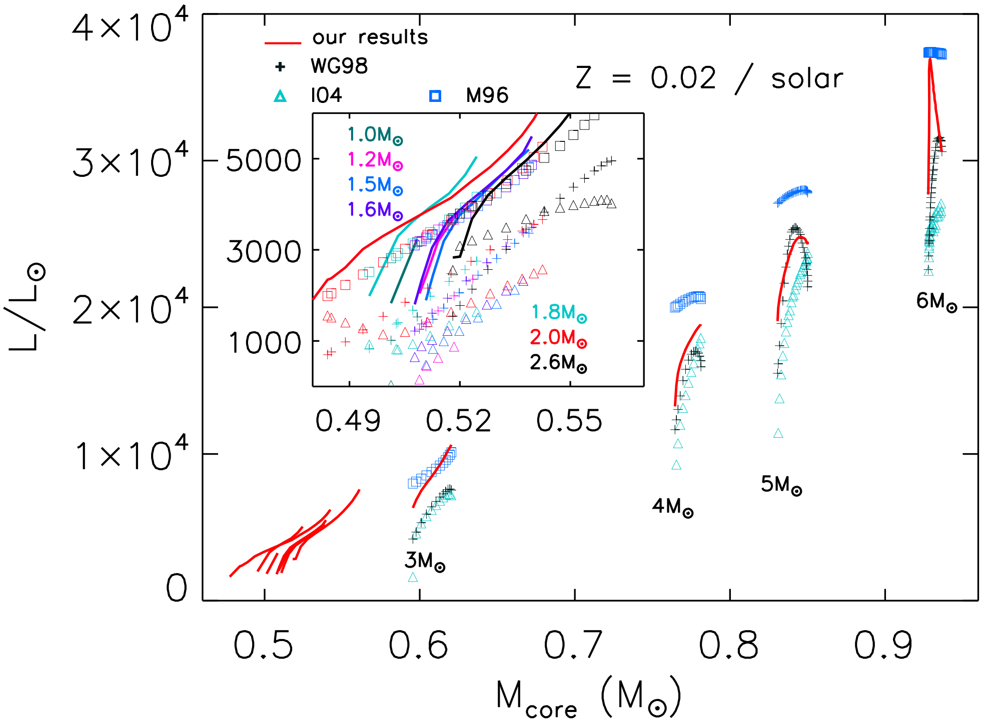

Figure 7.17.: Maximum pre-pulse luminosity (in solar units) for Z = 0.02 / solar-scaled models as a function of the core mass (in solar units). Our results are given by the solid colored lines. Open symbols represent three different fits: Marigo et al. (1996)[(M96), squares], Izzard et al. (2004) [(I04), triangles], Wagenhuber & Groenewegen (1998) [(WG98), crosses]. The inset is an enlarged view of the lower mass models for clarity.

During what WG98 call the *turn-on phase* strong TDU in low-mass stars can affect the CMLR fits. This turn-on phase, which comprises the first few TPs of the TP-AGB evolution, is the time needed for all global quantities (L, $T_{\rm eff}$, etc) to reach their asymptotic behavior during the interpulse. For $M_{\rm c} \lesssim 0.7$M$_\odot$, the effect of this turn-on phase on the CMLR is quite important if deep dredge is present for a substantial amount of time. This is why our two 1.8M$_\odot$ and 2M$_\odot$ models render higher L values than the M96 fit which does not account for this effect. In equation 7.3, WG98 account for it by the final term of the last line. I04's f_t factor (equation 7.8) has a similar purpose.

But despite these more correct fits during the turn-on phase of lower mass stars, both WG98 and I04 relations give lower luminosities than ours. We explain this discrepancy in the following way. The relation of WG98 was obtained by fitting models calculated by an older version of our evolution code, while the I04 fit comes from the K03 models. Our treatment of convection and subsequently that of TDU is responsible for the higher luminosities we obtain. Overshooting, which increases the TDU efficiency, was not included both by WG98 and I04. Moreover, while we use a $\alpha_{\rm MLT}$ parameter of 1.75 (K03 do as well), WG98 take 1.5 and it is known that lower $\alpha_{\rm MLT}$ values render reduced TDU strengths. In fact, for Z = 0.02, models produced with the Garching code (ours and those of WG98) experience TDU events only when overshooting is included. Furthermore, the Z = 0.02 K03 models first experience TDU for a star of 2.25M$_\odot$ and only after 20 TPs. In figure 4.11 of K03 we see that the agreement of her results with the M96 fit for the low-mass star is globally as good as ours. But while we get slightly higher luminosities than the fit because of our stronger TDU she obtains slightly lower ones.

We look now at the higher mass stars ($M_c > 0.7$M$_\odot$). The agreement between our results and the M96 fit is worse than for the low-mass models. The M96 luminosities are always higher than ours. The differences with respect to WG98 and I04 have however been reduced for the 4M$_\odot$ and 5M$_\odot$. In we compare our end-luminosities for the 5M$_\odot$ and 6M$_\odot$ models with those of K03 (in their figure 4.11) we get lower values. The K03 luminosities, similarly to ours, are lower then the M96 fit during the first TPs, but as the star evolves, they reach and exceed (for the 6M$_\odot$ and 6.5M$_\odot$) the parametrized ones. Our 4M$_\odot$, 5M$_\odot$ and 6M$_\odot$ models terminate early due to convergence problems (they stop with total remaining masses of 2.137M$_\odot$, 2.354M$_\odot$ and 3.178M$_\odot$). For the 4M$_\odot$ one, luminosity differences are relatively small with respect to the M96 parameterization at the last TPs; it is probable that further evolution would render higher luminosities and better agreement with the fit. The 5M$_\odot$ in contradiction to the same mass K03 models, does not experience HBB and therefore has much lower luminosities. For our 6M$_\odot$ model, it reaches up to the M96 fit but afterwards follows the expected decreasing luminosity-trend after HBB stops. In this case it is not the early convergence problems that are responsible for the low luminosities since the star has already reached the peak luminosity in its evolution and HBB is extinguished.

The I04 fit matches reasonably well our result for the 4M$_\odot$ and also shows a good agreement for the 5M$_\odot$ model. For the 6M$_\odot$ star, WG98 and I04 fail to reproduce the luminosity increase of our models due to HBB. This is also what K03 notices (her figures 4.13 and 4.15) with her results. The term - that depends on $\alpha_{\rm MLT}$ - in the third line of equation 7.3 (WG98) corrects for HBB higher luminosities. If the value of the mixing length parameter is increased, the relation renders higher luminosities and can better fit results. In order to get a much better agreement for the 4M$_\odot$, 5M$_\odot$ and 6M$_\odot$ stars, we increase $\alpha_{\rm MLT}$ to 3.00. Likewise, to fit the VW93 and K03 models respectively, WG98 change the mixing length parameter from 1.5 to 2.25 and K03 from 1.75 to 2.5. Thus, as was also commented by both WG98 and K03, augmenting the $\alpha_{\rm MLT}$ permits, in addition to accounting for the luminosity increase caused by HBB (6M$_\odot$), to match the luminosity of models with deep

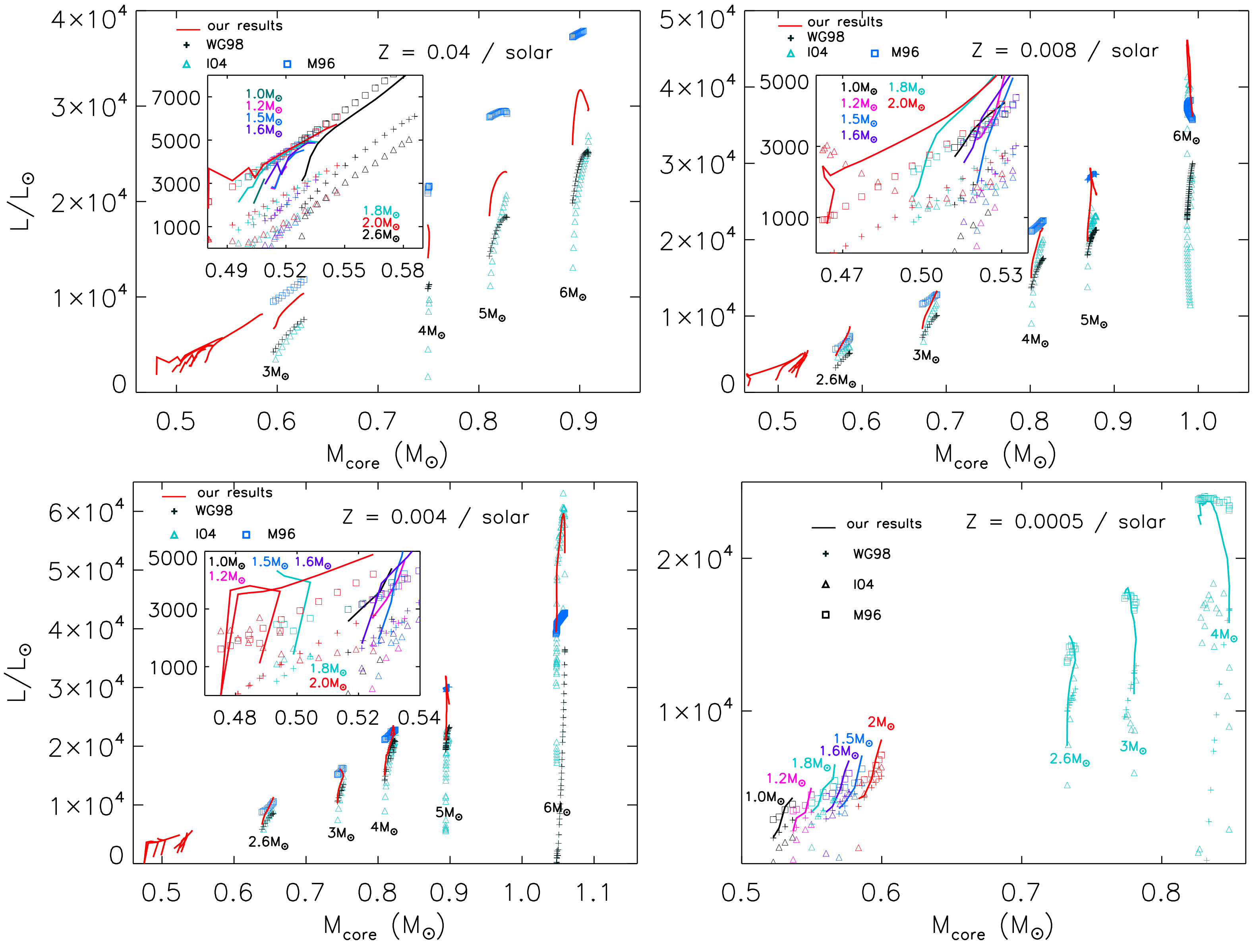

Figure 7.18.: Same as Figure 7.17 but for the other four solar-scaled metallicities, Z = 0.04, Z = 0.008, Z = 0.004, Z = 0.0005, of our grid.

TDU ($4M_\odot$, $5M_\odot$) and no HBB.

Figure 7.18 is similar to the 7.17 one but the four additional solar-scaled metallicity results (Z = 0.04, 0.008, 0.004 and 0.0005) are plotted. For the most metal-rich case, the behavior, agreement and discrepancies between models and fitting relations is globally similar to the Z = 0.02 case. One difference is that there are no low-mass models experiencing TDU: as a consequence our luminosities never exceed (like for the $1.8M_\odot$ and $2M_\odot$, Z = 0.02 cases) the M96 fits. Also the $3M_\odot$ evolution, because TDU occurs only after 4 TPs - instead of the 1st one (Z = 0.02 case) - and is much less efficient, does not have L values that match the M96 fit.

For the other three metal poorer cases, the luminosity spread throughout the evolution for different-mass models is larger. From the 1st TP until the end of the TP-AGB, luminosities can increase by as much as $3 \cdot 10^4$ $L_\odot$. Often our results match the lower WG98 / I04 luminosities during the first TPs and later reach the higher M96 values.

The lower mass ($1M_\odot$-$2M_\odot$) Z = 0.004 and 0.008 models give results that systematically reach higher values than all three fits. This is once more due to our stronger TDU: dredge-up is present already during the 1st or 2nd TP in the evolution of stars that will go through a total of 5 to 15 TPs. On the contrary, for the Z = 0.0005 low-mass case, TDU begins only at the 2nd or 3rd TP for evolutions that last only 4 to 6 TPs. The disagreement between our results and the fits is therefore not present and our models with $M_c < 0.7M_\odot$ at Z = 0.0005 give the best agreement from all other metallicities. The I04 fit still gives too low luminosities at the first TPs, but ultimately matches our curves.

For the masses above $2.6M_\odot$ (put aside the $6M_\odot$) the agreement for Z = 0.008, 0.004 and 0.0005 is much better than at higher metallicities; the luminosity spread given by the fits is simply larger. Our models start the TP-AGB evolution at higher L values but reach the same end-luminosities as the parametrized relations. The $5M_\odot$ and $6M_\odot$ models, that experience HBB, see their luminosities exceed those of the M96 fit which do not account for this deviation from the simple CMLR. Once again the low WG98 luminosities can be increased by adjusting the mixing length parameter (in equation 7.3) to higher values in order to match our results. But needed α_{MLT} corrections are less significant than in the Z = 0.02 models as, at these lower metallicities, TDU is already more efficient.

From the three fits presented here, the K03 models have the best agreement with the I04 parameterization (their figure 4.15). This is expected since I04 derived their relation based on the K03 results. Nevertheless the K03 luminosities are still higher than the predicted I04, and in order to get a good agreement, at Z = 0.02 and Z = 0.004, with the WG98 relations, K03 need to increase the value of α_{MLT}.

One additional argument to explain, for the intermediate-mass models that become carbon-rich ($\approx 2M_\odot$-$5M_\odot$), our higher luminosities with respect to the more recent WG98 and I04 fits, is the inclusion of new variable-C/O opacities from Ferguson (2006). In the right panel of Figure 7.12 we saw how the effect of the variable opacities, in addition to the lower surface temperature, is to reduced the strength of the TDU episodes. In the next section (Figure 7.21) we look at the differences brought by this opacity change on the interpulse period, the He-burning luminosity and the surface luminosity of the $2.6M_\odot$ / Z = 0.008 (solar-scaled) model in Figure 7.12. The strength of the shell-flash is reduced and the total surface luminosity during the interpulse phase increased with respect to a fixed opacity evolution. In Figure 7.21, the luminosity increase reaches ≈ 0.1 dex, that is from $\log_{10}(L/\mathrm{L}_\odot) = 3.85$ to 3.95. This corresponds to a luminosity increase from $7.08 \cdot 10^3$ $\mathrm{L}_\odot$ to $8.91 \cdot 10^3$ $\mathrm{L}_\odot$, namely $0.183 \cdot 10^4$ $\mathrm{L}_\odot$. This essentially matches the difference between our models luminosity (red line) and the WG98 and I04 fits (black crosses and green triangles) at the end of the evolution in the top right panel of Figure 7.18. For higher mass carbon-rich stars (i.e. not the $6\mathrm{M}_\odot$ for which the surface C/O ratio is always < 1) this effect is amplified.

To summarize, we mention that the available core-mass - luminosity relations agree reasonably well with our results. At low core masses ($\lesssim 0.7\mathrm{M}_\odot$) the best agreement is given by the M96 fit. Nevertheless, the effect of strong TDU early in the evolution is not accounted for and luminosities are sometimes underestimated. For the higher core masses, the fits that best match our results are those of I04 but we systematically get higher luminosities. In general, discrepancies are mainly due to our inclusion in the models of overshooting and variable molecular opacities. Both affect the TDU and in turn the luminosity. From our range of Z values, the best agreement with the older fits (derived from models with no overshooting and fixed C/O-opacities) is found for the low metallicities because TDU is already important even without convective overshooting. As far as α-enhanced compositions go, the models do not show any particularly interesting features different from the solar-scaled ones; we therefore do not plot any results.

In order to take into account the resulting new behavior of the models, a project aiming to fit our tracks with updated parameterized relations and supersede those of WG98 and I04 is currently underway. This enterprise is nevertheless to be taken with a grain of salt as one is compelled to retain the following.

On average, the luminosity differences between the previous fits and our results throughout the entire core-mass range and distinct metallicity values correspond to about 10 to 20% in solar luminosity units. Such disparities, often in opposite directions and with various amplitudes but within this order of magnitude, are also present among other older studies: the M96, WG98 and I04 fits, the K03 results, etc. The M96 relations were already elaborate enough to mimic the general luminosity behavior of AGB models, but they are a cruder approximation (as can be seen from Figures 7.17-7.18 and equations 7.1-7.9) than the WG98 and I04 ones. These depend on more parameters, are much more complex and deliver a higher degree of fitting flexibility and accuracy in accounting for model details. The level of precision reached by these fits is satisfying and we advocate that, for the moment, trying to reach a higher one is not a necessity. The reason is that models depend too much on poorly known physics and much improvable numerics.

The very important opacity ameliorations brought by our work, are indeed a real progress because they improve the complexity of a known phenomenon shown to be relevant for AGB evolution. This update depends only on computational and human effort since it uses more detailed physics formulated within a theoretically sound context. On the other hand the mass-loss and convective overshooting prescriptions are physical processes that, lack such understanding, for which no solid theory is available, and which are themselves parameterized. The effects brought on the models by these two updates are therefore much more subject to uncertainty. In addition, the numerical description of the AGB and post-AGB phases that can greatly influence the output of the calculations (as we will see in Chapter 8 for example) is in great need of furtherance.

At the moment, the ambiguity brought by the inadequate treatment of physics and numerics, is likely greater than other improvements. The parameterized mass-loss, convection, and numerical descriptions can very well be responsible for the divergence between most results from different codes. Other effects brought by important improvements like detailed opacity updates could then be masked. The differences observed between tracks at the current level of sophistication should be meaningful only if the above aspects are considered, and any updates brought to the models, and therefore to the fits, are thus limited by them.

It is nevertheless commonly accepted to continue reproducing the latest models (ours at present) with new relations, merely because they are the most modern ones. The changes brought by our results are important enough for new functions to be necessary. One has only to keep in mind that such analytical functions will most likely correspond solely to a specific grid and have little predictive power. In making these new fits, because of their already high level of complexity, it would moreover be of little use to increase the number of free parameters.

As it was the case for the CMLR in this section, a similar comparison of our results with another parameterized relation is presented next.

7.3.6. The Core-mass - Interpulse-Period Relationship

A second very important quantity, for synthetic AGB models, describing the evolution on the AGB, is the core-mass - interpulse-period relationship. We compare once again our results, with the relations obtained by Boothroyd & Sackmann (1988b) (BS88b), WG98 and I04.

The first parameterization of BS88b for the interpulse-period ($\tau_{\rm ip}$) is presented for two different metallicity values:

$$\log(\tau_{ip}/years) = \begin{cases} 4.50 \cdot (1.689 - M_c) & Z = 0.02 \\ 4.95 \cdot (1.644 - M_c) & Z = 0.001 \end{cases} \tag{7.10}$$

The second relation of WG98, with dependences, in addition to M_c, on Z and $\alpha_{\rm MLT}$, is the following [ζ = log(Z / 0.02)]:

$$\begin{aligned} \log(\tau_{\rm ip}/years) = & \, (-3.628 + 0.1337 \cdot \zeta) \cdot (M_{\rm c} - 1.9454) \\ & - 10^{-2.080-0.353\cdot\zeta+0.2\cdot(M_{\rm env}+\alpha_{\rm MLT}-1.5)} \quad . \\ & - 10^{-0.626-70.30\cdot(M_{\rm c}(1)-\zeta)\cdot\Delta M_{\rm c}} \end{aligned} \tag{7.11}$$

The third relation of I04 modifies the previous WG98 one by including a dependency on the TDU efficiency-parameter λ. This parameterization, which is based on the K03 models gives:

$$\begin{aligned}\log(\tau_{\rm ip}/years) &= a_{\rm s}\cdot(M_{\rm c}-b_{\rm s})\\ &- 10^{-2.080-0.353\cdot\zeta+0.2\cdot(M_{\rm env}+\alpha-1.5)}\\ &- 10^{-0.626-70.30\cdot(M_{\rm c}(1)-\zeta)\cdot\Delta M_{\rm c}}\\ &+ 0.15\cdot\lambda^2.\end{aligned} \tag{7.12}$$

The values for the a_s and b_s constants at different metallicities are given in Table 7.6.

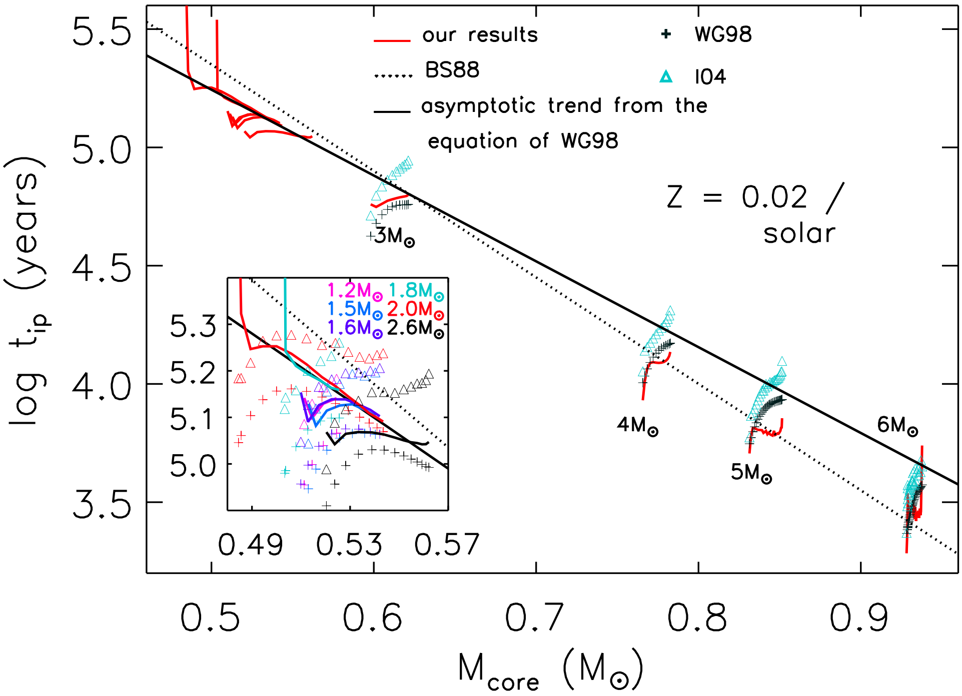

Figure 7.19.: Interpulse period (in log scale) for Z = 0.02/solar-scaled models as a function of the core mass (in solar units). Our results are given by the solid colored lines. Fits obtained by different authors have also been plotted: asymptotic trend of the equation from Wagenhuber & Groenewegen (1998) [(WG98), solid black line], Boothroyd & Sackmann (1988b) [(BS88b), dashed black line], Izzard et al. (2004) [(I04), triangles], WG98 [crosses]. The inset is an enlarged view of the lower mass models for clarity.

In Figure 7.19, $\tau_{\rm ip}$ is plotted against $M_{\rm c}$ for our Z = 0.02 (solar-scaled) models (solid colored lines). The black dotted line corresponds to equation 7.10 for Z = 0.02, the black solid one to the first term of equation 7.11. The symbols correspond to the WG98 and I04 fits.

Globally our low-mass results follow very well the WG98 asymptotic behavior while our higher-mass ones agree better with the BS88b relation. Out of the two most recent fits, the WG98 one is in best agreement with our models. The evidently higher interpulse periods for the 1.8M$_\odot$ and 2M$_\odot$ models at the beginning of the evolution are to be ignored. They come from the fact that, often during the first few TPs, some He-shell flashes are too mild or suppressed: the peak He-luminosity does not exceed values of 3-4 in logarithmic solar units and the H-burning shell is not completely extinguished (see the 2$^{\text{nd}}$ TPs in the left sides of Figures 7.1 and 7.3). The specific flash is thus not counted as a TP and the interpulse-time is considered to continue until the next He-shell flash event: consequently τ_{ip} is doubled.

Z	0.02	0.008	0.004	0.0001
a_s	-3.821	-4.189	-4.255	-4.5
b_s	1.8926	1.8187	1.8141	1.79

Table 7.6.: Numerical values for the a_{s} and b_{s} constants of equation 7.12

For all models, interpulse times increase until they reach an asymptotic value and eventually slightly increase once more at the end.

The fit of I04 systematically gives higher τ_{ip} values than our results. The WG98 relation shows a much better agreement throughout the entire mass range: a) for low-mass cores, interpulse times are a little lower but asymptotically reach our values towards the end of the evolution, b) for higher mass stars, they meet our values at the beginning and overestimate them as the models evolve in time (or core mass).

For the more massive models K03 obtain larger τ_{ip} values than those obtained by the WG98 fit. They attribute this larger τ_{ip} increase to deep dredge-up. The subsequent I04-relation improved the WG98 one by fitting the K03 models to include a TDU λ-dependency. This overall increase is not so clear in our models: the interpulse-period values that we obtain for the more massive stars are some times higher (3M$_\odot$) and other times (4M$_\odot$-5M$_\odot$) lower with respect to the WG98 ones. What is certain is that the WG98 fit is based on models which experience much less efficient TDU episodes because no overshooting is used. In order to try and explain these results, in addition to the TDU we invoke the opacity effects. The consequence of including variable-C/O opacity tables in our code is to decrease the τ_{ip} values. This is more evident when we also look at the other metallicities (Figure 7.20).

The BS88b and I04 relations are not always available at all composition for the exact Z values of the models. For this reason, in the plots of Figure 7.20, we use the metallicity values that are closer to ours for the comparison.

The worst agreement is obtained for the very low metallicity case (Z = 0.0005). Our periods have values much lower than all three fits. At the high Z = 0.04 metallicity the respective behavior of our results and the parameterized relations is very similar to the previous Z = 0.02 case. For the two intermediate metallicities, Z = 0.008 and 0.004, the WG98 fit agrees reasonably well with our values but the I04 ones still gives values that are too high.

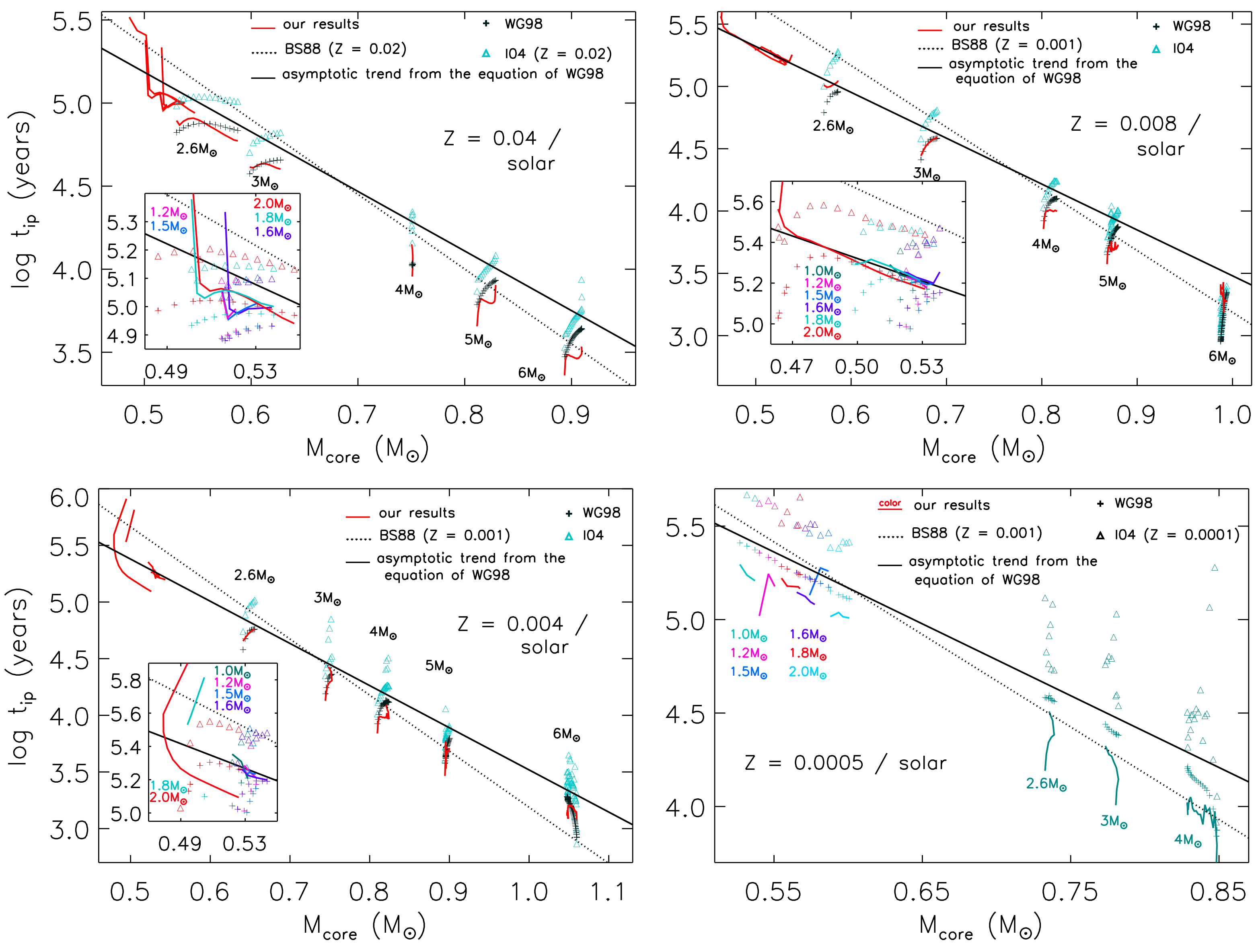

Figure 7.20.: Same as Figure 7.19 but for the other four solar-scaled metallicities, Z = 0.04, Z = 0.008, Z = 0.004, Z = 0.0005 of our grid. When the different fits are not available for the exact metallicity of our models, the fit with the closest Z value is plotted and indicated in parenthesis beside the reference.

We have already seen, earlier in this chapter, how the Ferguson (2006) variable-C/O opacities affect the effective temperature of the models and the surface luminosity. But they also play a role with respect to $\tau_{\rm ip}$. The interpulse period is dependent on the strength of the shell-flash; models with stronger shell-flashes have larger interpulse times while models with weaker flashes shorter $\tau_{\rm ip}$. It seems that the new variable-C/O opacities render milder shell-flashes. Their effect is clearly visible in Figure 7.21. At the last TPs of the plotted evolution the fixed-opacity model gives $\tau_{\rm ip} = 0.18$ Myr and the variable opacity one 0.12 Myr. These values correspond to 5.26 and 5.08 on the $M_{\rm core}$ - $\log_{10} \tau_{\rm ip}$ plot, which is a difference of 0.18 dex. In the top right panel of Figure 7.20 the largest difference for the $2.6 M_\odot$ star between our result (red line) and the I04 fit (green triangles), based on models with fixed-C/O opacities, is ≈ 0.25 dex. As the I04 relation was fitted on the K03 models we conclude that if the K03 models were computed with variable-C/O opacities, their interpulse periods would most probably be lower and the agreement of the I04 fit with our results much better.

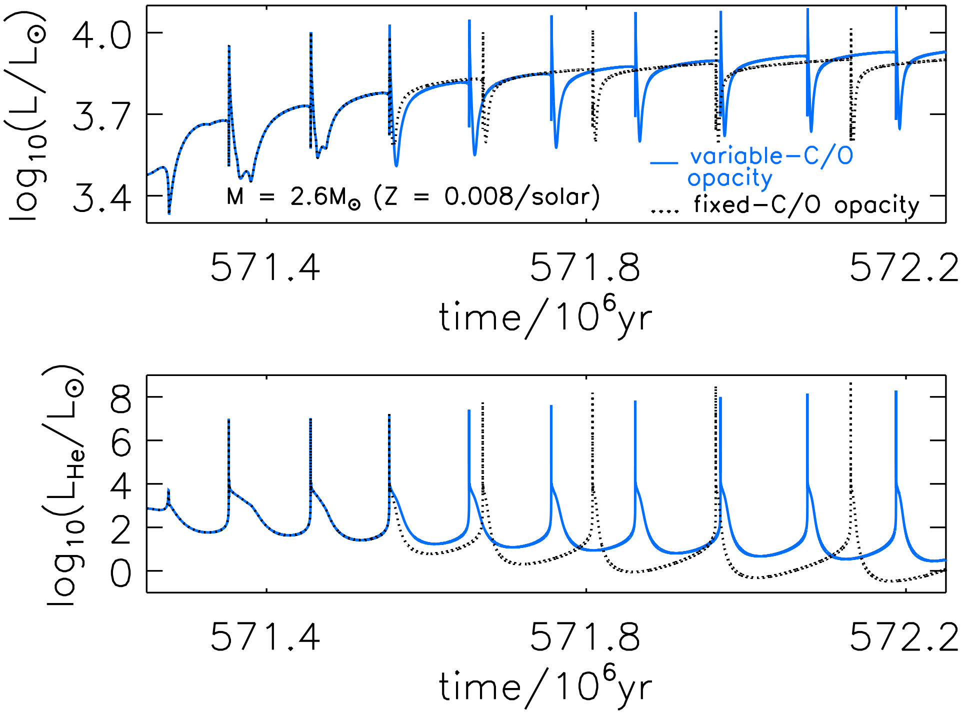

Figure 7.21.: Effect of the new low-temperature molecular opacities on the surface and He-burning luminosities for a $2.6 M_\odot$ (Z = 0.008/solar) star (same model as in the right panel of Figure 7.12).

The same effect of reduced interpulse times is also seen for the lowest metallicity models. As an example we give the $1.8 M_\odot$ / Z = 0.0005 (solar-scaled) model which we already discussed in section 7.3.3. Figure 7.22 shows the $\tau_{\rm ip}$ reduction as a consequence of the inclusion of the new opacities. The ≈ 0.08 dex decrease is enough to explain the offset (bottom right panel of Figure 7.20) for this specific model between our results and the WG98 fit, but only partly sufficient for the I04 case which give even higher values. We remember that in this case (Figure 7.13), contrarily to the 2.6M$_\odot$ / Z = 0.008 model, the effect of the C-rich opacities was to increase $T_{\rm eff}$.

In view off all this, it is difficult, like for most global quantities of TP-AGB stars, to clearly explain the individual influence of the various input physics and therefore the small discrepancies with the previous fits. The new opacities are not sufficient to explain by themselves the overall low interpulse times obtained for most of our models. But it nevertheless seems that, whether the variable-C/O molecular opacities induce higher or lower effective temperatures, the interpulse periods are always affected. Models which include them give lower values of $\tau_{\rm ip}$.

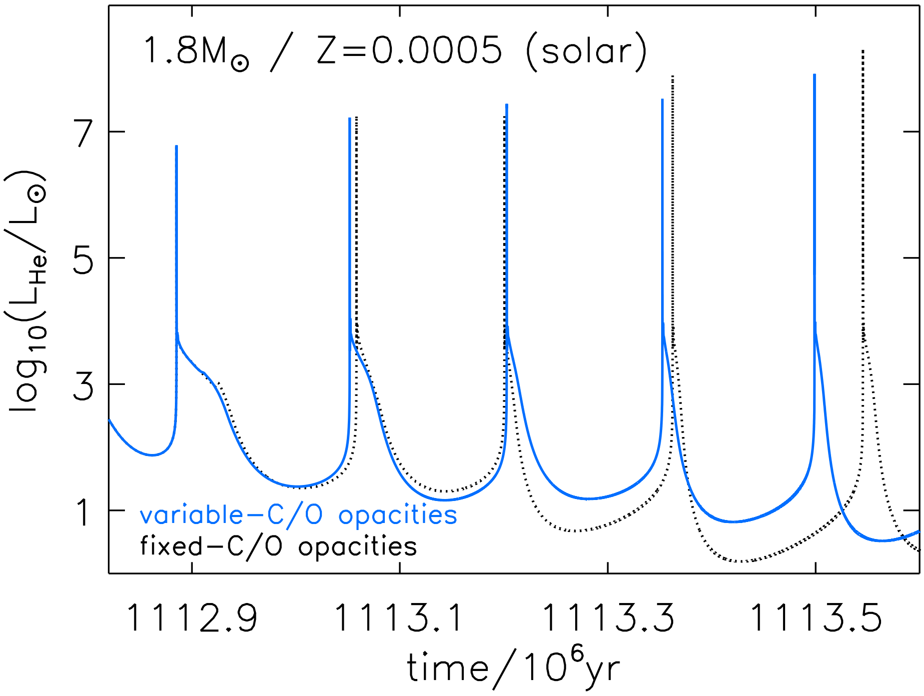

Figure 7.22.: Effect of the new low-temperature molecular opacities on the He-burning luminosity and interpulse period for a 1.8M$_\odot$ (Z = 0.0005/solar) star (same model as in the bottom panel of Figure 7.13).

In summary, the WG98 $\tau_{\rm ip}$ parameterization fits our results best. This is not surprising since their relation was based on detailed models created with an older version of our code. The simple explanation for the lower interpulses periods of our models is the interplay between the various updated physics in our code. The inclusion of molecular opacities is only one of the inputs that reduces the interpulse times for C-rich models.

7.4. Summary and future Work

In the present chapter we presented the main features of our TP-AGB models, compared them to other models and to some observational data.

The tracks are consistent with the ones available in the scientific community, and in particular with the two most recent extended grids from Vassiliadis & Wood (1993) and Karakas (2003). Discrepancies with respect to these older calculations are due to new input updates during both the pre-AGB evolution and the TP-AGB evolution.

Our higher mass-loss rates on the RGB and E-AGB, as well as the inclusion of convective overshooting before the AGB phase give models, that have not experienced beforehand the He-flash ($M_{\rm ZAMS} \lesssim 2{\rm M}_\odot$), lower core and envelope masses when they reach the TP-AGB. The small envelope masses will reduce the TP-AGB lifetimes and the initial low values of the core masses will be reflected in the final TP-AGB core sizes. For the higher mass stars ($M_{\rm ZAMS} \gtrsim 2{\rm M}_\odot$), the size of our cores at the $1^{\rm st}$ TP on the AGB are in good agreement with older results.

On the TP-AGB, the convective overshooting, mass-loss prescriptions and variable low-temperature molecular opacities mainly render more efficient dredge-up, less core-growth, higher surface luminosities, lower interpulse periods, less thermal pulses, lower temperatures for C-rich models, lower final C/O ratios, shorter evolutions for most stars but higher values for the longest lived ones (at the He-flash transition mass).

Particular attention is given to this transition mass ($M \approx 2{\rm M}_\odot$) between low- and intermediate-mass stars; the mass that separates stars that do and those that do not experience the He-flash. A noticeable dip in the initial-final mass relation, which is less evident in previous grids, is seen for these stars. This turning point is shifted to lower masses (from $2.25{\rm M}_\odot$ to $2{\rm M}_\odot$) with respect to Karakas (2003) because of the inclusion of convective overshooting.

While they are mostly lower over the entire mass range, the TP-AGB lifetimes of our He-flash transition models are a little higher but still in relative agreement (on average $\approx$ 8% depending on metallicity) with the Karakas (2003) ones.

Our large initial composition range confirms and extends the dependence of TDU and HBB on metallicity. Furthermore we also note the metallicity dependence of the He-flash transition point, with lower Z values producing lower masses. This mass translation is also reflected in the lifetime peak. We also give different metallicity dependent initial-final mass relations which are similar to the results from the latest synthetic AGB grids (Marigo & Girardi 2007).

The predicted, by synthetic models, cooling of the tracks, when appropriate low-temperature molecular opacities for variable surface chemistries are used, is confirmed by our detailed calculations. In addition we put forward the eventual warming up of the models with the inclusion of such opacities. This increase of the surface temperature can occur in two different scenarios: a) in metal-rich AGB stars that experience TDU, as the C/O ratio goes from its initial low value to the critical transition one (C/O = 1), b) in metal-poor AGB stars that have already become C-rich because of very efficient TDU, when the surface C/O ratio reaches higher values.

We also compared the core-mass - luminosity and core-mass - interpulse-period relationships available in the literature with our results. For the first relation, the best fits are those of Marigo et al. (1996) ($M_c \lesssim 0.7$M$_\odot$) and Izzard et al. (2004) ($M_c \gtrsim 0.7$M$_\odot$). Our results give overall higher luminosity values. The Wagenhuber & Groenewegen (1998) parameterization gives the better agreement with the interpulse periods for which we obtain lower values.

We compare our AGB models to two sets data originating from observational results. The IFMR and the C-star lifetimes. Our IFMRs are in good agreement with the observed white dwarf data from open clusters and binary systems for intermediate-mass stars. No good quality data for low-mass stars was available to do the comparison. We also compare our final masses to the Weidemann (2000) IFMR. For intermediate-mass stars the agreement is good but for low-mass stars our masses are always lower.

The compatibility with the C-star lifetime data, derived from observational C-star counts in the LMC and SMC, is very good in comparison to previous available grids. Only Girardi & Marigo (2007) match the results as well as ours, but their values are produced by the P. Marigo synthetic models which have previously been calibrated to the observed carbon star luminosity function.

7.4.1. Outlook

In the 7.3.5 and 7.3.6 subsections, we presented the core-mass - luminosity and the core-mass - interpulse-period relations from our models. With our extended grid in mass and metallicity, these results offer the possibility to derive new parameterizations based on updated models. This is important because such parameterizations are used in synthetic TP-AGB codes. Wagenhuber & Groenewegen (1998) fitted full models produced by an older version of our code. Izzard et al. (2004) parametrized the Karakas (2003) grid results. A similar project to fit our new results is underway by M. Groenewegen.

Recently, with the synthetic population models they developed, Marigo et al. (2004) have tried to theoretically understand the Planetary Nebula Luminosity Function (PNLF) and reproduce its bright cut-off invariance property. Older AGB (Marigo et al. 1999, Marigo 2001) and post-AGB (Vassiliadis & Wood 1994, see next chapter) tracks are used as input for these models. Producing new models that could be incorporated in the Marigo et al. code was one of the main scientific motivations of this work in order to further continue the investigation of the population effects on the bright PNLF cut-off. For example as central stars of planetary nebulae in the mass range 0.70 - 0.75M$_\odot$ seem to be responsible for the cut-off luminosity, our obtained lower masses could make this parameter correspond to higher progenitor masses - now thought to peak at ≈ 2.5M$_\odot$ - and thus to shorter evolutions. A younger age of last star formation burst in a given galaxy would then be required.

Finally, the most important application of this work is to include our detailed TP-AGB tracks in galaxy models and replace the current commonly used synthetic TP-AGB grids. The integrated luminosity of galaxies reflects their star formation history. In order to interpret their emitted light, one tries to reproduce observed integrated spectra first by summing individual models of stars into a simple stellar population.

According to Bruzual & Charlot (2003), modern population synthesis of galaxies still suffers from limitations. One of the essential uncertainties is the lack of detailed grids for the TP-AGB phase; these stars are very bright and have a decisive impact on the integrated light properties.

In particular, the luminosities, colors, lifetimes and relative number of M- and C-type stars in a sample are important for the construction of galaxy models. As the transition from M- to C-type depends on the details of TP-AGB evolution, any updates influencing the behavior of the stellar tracks (e.g. variable-C/O opacities, mass-loss prescriptions, convective boundary treatment) are expected to be reflected in the galaxy models. The Bruzual & Charlot (2003) models adopt the effective temperatures, bolometric luminosities and lifetimes of TP-AGB stars from the models of Vassiliadis & Wood (1993). With higher lifetime values for the longest lived stars ($\approx 2\mathrm{M}_\odot$) but shorter ones at other masses, lower effective temperatures, higher luminosities and different distribution of M- and C-type stars, our tracks will certainly influence the galaxy models.

8. Post-AGB Evolution

In the last chapter of this thesis we conclude the presentation of our work and deal with the post-AGB tracks.

To be accurate, on should consider the post-AGB phase to fill in the gap between extreme AGB stars (end of the TP-AGB cycle) and the beginning of the PN stage when the central star is hot enough to ionize the circumstellar material (see sketch in Figure 2.2) [1]. But it is customary, by generalization, to refer to the entire modeled evolution after the departure from the AGB as a post-AGB track. This loose statement is even more permissible since a model, after leaving the true post-AGB region in the HR diagram and evolving through the PN phase, will often experience a LTP or VLTP, become a born-again AGB star, and cross the post-AGB phase a second time.

We therefore define our tracks in the following way. The moment, at the end of the TP-AGB, when the decreasing radial pulsation period of the star drops below 100 days is the zero age of our post-AGB evolutions. The models end, either when they do reach the WD cooling track, or at whichever point convergence problems occur beforehand (in most cases when a LTP or a VLTP is present, models crash during their second trip on the AGB).

From the initial 110 models of our mass-metallicity grid (Chapter 6), 100 were evolved with no computational complications through a satisfactory portion of the AGB pulse-cycle (Chapter 7). Out of these 100 TP-AGB models, we have corresponding post-AGB tracks for 60 of them in the [$1M_\odot$, $2M_\odot$] mass range. All higher mass model calculations stopped before the end of the TP-AGB phase and could not be followed further.

Moreover, half of the 60 progenitor models also experience convergence problems during their last TP. 30 tracks uninterruptedly evolved through the TP-AGB - post-AGB transition without any complications. For the other 30 cases, in order to bypass the phases of no-convergence during the last TP, models were frozen in time, the small remaining mass was removed, and only then were they let to normally continue their post-AGB evolution.

8.1. The tracks in the HR diagram

According to the most recent works on the planetary nebulae luminosity function (e.g. Schönberner et al. 2007, Marigo et al. 2004), the only available set of post-AGB tracks

---

[1] Post-AGB stars - especially when the central star is resolved - are also designated by the term Protoplanetary Nebulae (PPNe). We will however use the more generic name *post-AGB star*.

for different masses and metallicities is, until today, the one of Vassiliadis & Wood (1994) (VW94). These tracks originate from the VW93 TP-AGB models. VW94 define a transition time, $t_{\rm tr}$ (see also Renzini 1989, Schoenberner 1990), between the moment the star leaves the TP-AGB and the point where $\log_{10} T_{\rm eff} = 4$. In their synthetic planetary nebula luminosity code, Marigo et al. (2004) take this 10 000 K point to be the beginning of the post-AGB tracks.

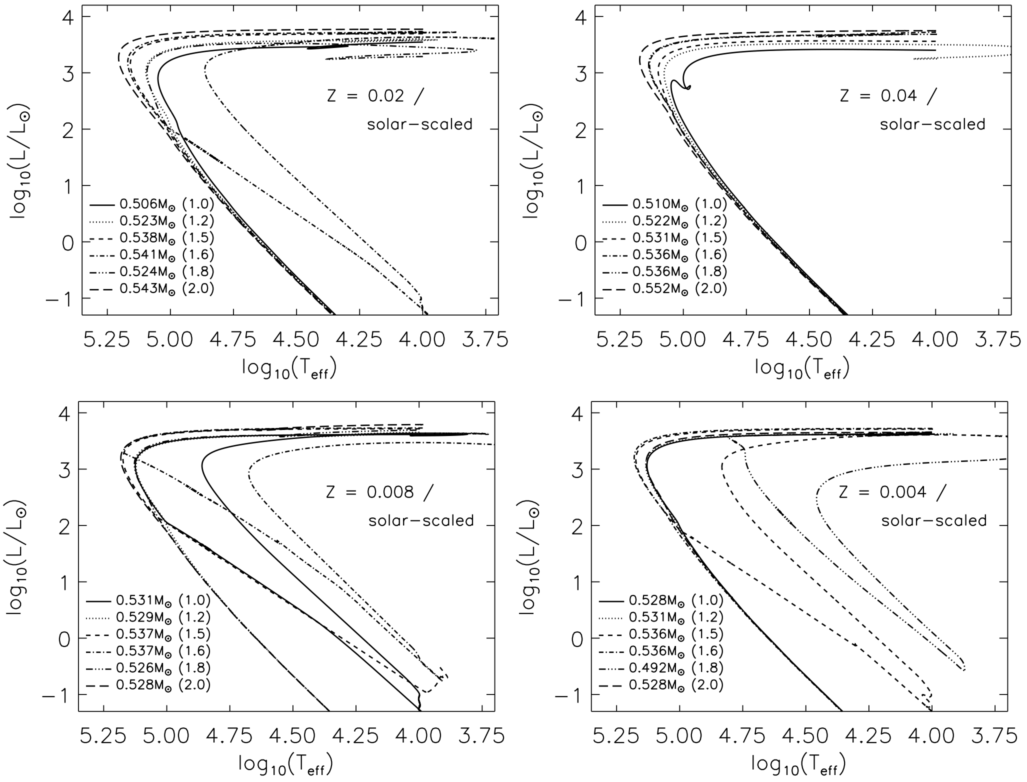

Figure 8.1.: Post-AGB HR diagrams for the four indicated solar-scaled mixtures. Stellar masses (in $M_\odot$) at the beginning of the post-AGB tracks as well as initial ZAMS masses (in parentheses) are given for each case.

Not all of our 60 post-AGB tracks directly result from smooth calculations from TP-AGB models. Post-AGB models that needed some sort of intervention during their transition phase, mostly start after the 100 days period position. We therefore designate another zero-age starting point, in agreement with previous work, at 10 000 K. Accordingly, all our tracks in Figures 8.1-8.3 begin at this second post-AGB zero-age.

Furthermore, we also define a transition time between the beginning of our post-AGB tracks and the $\log_{10} T_{\rm eff} = 4$ point. When available, the moment the pulsation period drops below 100 days is taking as the initial starting point.

Analogously to Figures 6.1 and 6.2 for earlier phases, Figures 8.1 and 8.2 give the post-AGB evolution of the solar-scaled and α-enhanced models with Z = 0.04, 0.02, 0.008 and 0.004. In Figure 8.3 we plot our models for both Z = 0.0005 metallicity scalings. The mass of the star at the beginning of the post-AGB evolution is indicated in solar units for each case on the graphic (in parenthesis the initial ZAMS mass is also given).

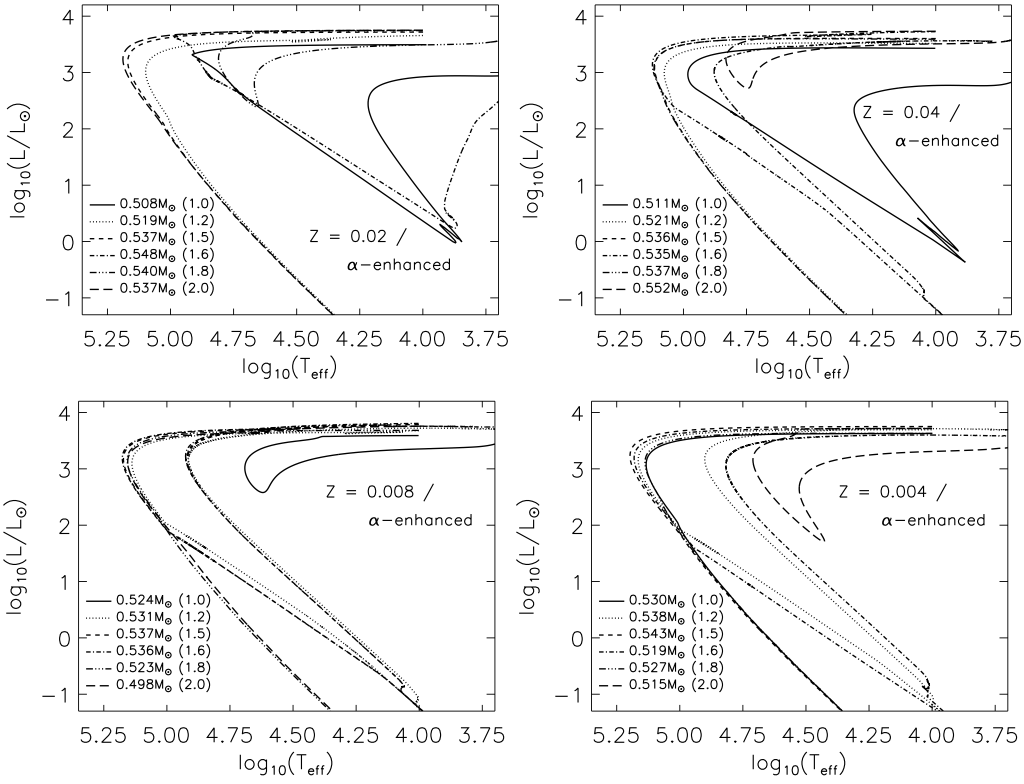

Figure 8.2.: Same as Figure 8.1 for the α-enhanced mixtures.

Most models do not experience a TP during their post-AGB evolution: they unaffectedly evolve through the PN phase and onto the WD cooling track. But one third of our tracks do experience a LTP or a VLTP. These are shown by the long excursions to lower temperatures and luminosities in the HR diagram. When they arrive on the AGB, calculations stop and the tracks do not continue for a second time through the PN phase; they thus never reach the WD cooling track.

Another necessary remark on the beginning of the tracks should be done. Sometimes a very small loop in the HR diagram is seen. It correspond to the secondary pulse that occurs after a main TP. When a TP happens to take place close to the end of the TP-AGB, a secondary pulse is seen on the post-AGB track. This small pulse can occur after the star has increased its temperature over $\log_{10} T_{\mathrm{eff}}$ = 4, or before. When it occurs around this 10

000 K mark, the track can go past this point more than once. We take as the second post-AGB zero-age the first time the 10 000 K temperature mark is reached. As a consequence, in Figures 8.1-8.3, some stars are seen to cool down to lower temperatures from initially higher than 10 000 K temperatures, before continuing on the post-AGB horizontal track.

In Tables 8.1 and 8.2 we give a selection of results for all post-AGB tracks plotted in the previous sets of figures. Results for all solar-scaled models are tabulated in Table 8.1, and those for α-enhanced ones in Table 8.2.

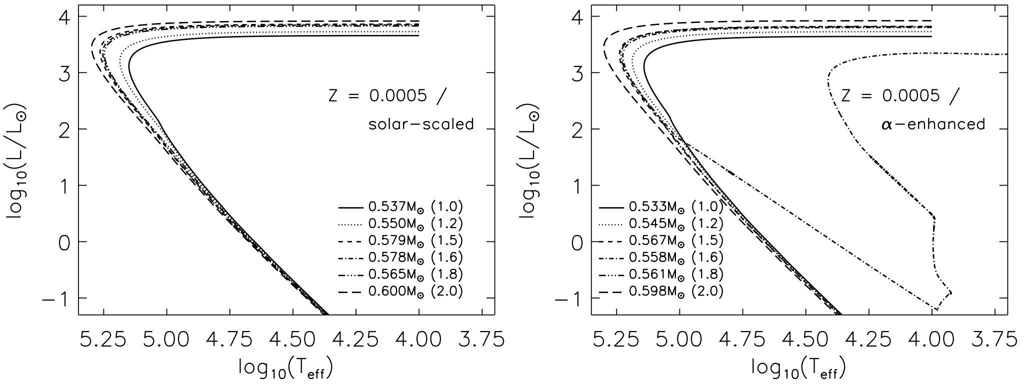

Figure 8.3.: Same as Figure 8.1 for the two different scalings of the Z = 0.0005 metallicity models.

In each case, the first columns give the initial MS mass, M_{ZAMS}. The second column the effective temperature at the beginning of the post-AGB models, $T_{\mathrm{eff,i}}$. When an asterisk is printed beside the value of the temperature, it indicates that the value does not coincide with the P = 100 days transition point. Instead it corresponds to the moment we continue our calculations after bypassing the difficult convergence phase for models which experienced problems at the end of the TP-AGB. For these models the pulsation period is already lower than 100 days and part of the initial post-AGB evolution is not available: temperatures are higher as the star has already moved towards the blue. As a consequence, the transition times, t_{tr} (third columns), are shorter then what they would be. The fourth column gives the mass of the star at the 10 000 K zero-age point. We indicate whether the post-AGB track is a H- or a He-burner in the fifth column. As explained in section 2.1, this depends on which of the two shell-sources is predominant. Most models mainly burn hydrogen and only 4 are He-burners when they leave the TP-AGB. In addition those tracks that experience a extra TP and return on the AGB also become He-burners. Whether this is the case and which type of post-AGB TP is experienced is indicated in column 6. Unfortunately, like we already pointed out, lack of convergence stops our models during their second passage on the TP-AGB and these secondary He-burning tracks are not available. Finally the last column indicates if our models have reached the WD phase or if they crashed earlier during their second return on the AGB.

Z = 0.0005 / solar

M_{ZAMS}	$T_{\mathrm{eff,i}}$	t_{tr}	M_{T4}	?-burner	TP	End
1.0	3.68	4.274	0.537	H	no	WD
1.2	3.69	2.403	0.550	H	no	WD
1.5	3.72	0.905	0.579	H	no	WD
1.6	3.72	1.076	0.578	H	no	WD
1.8	3.71	0.545	0.565	H	no	WD
2.0	3.73	0.335	0.600	H	no	WD

Z = 0.008 / solar

M_{ZAMS}	$T_{\mathrm{eff,i}}$	t_{tr}	M_{T4}	?-burner	TP	End
1.0	3.70*	0.577	0.531	H/He	VLTP	2nd AGB
1.2	3.71*	0.027	0.529	H	no	WD
1.5	3.69	1.840	0.537	H/He	VLTP	during VLTP
1.6	3.72*	0.192	0.537	H/He	VLTP	2nd AGB
1.8	3.72*	0.021	0.526	H	no	WD
2.0	3.73*	0.013	0.528	H	no	WD

Z = 0.004 / solar

M_{ZAMS}	$T_{\mathrm{eff,i}}$	t_{tr}	M_{T4}	?-burner	TP	End
1.0	3.71*	0.030	0.528	H	no	WD
1.2	3.71*	0.032	0.531	H	no	WD
1.5	3.71*	0.276	0.536	H/He	VLTP	2nd AGB
1.6	3.69	1.605	0.536	H	no	WD
1.8	3.71*	0.020	0.492	H/He	LTP	2nd AGB
2.0	3.68	1.325	0.528	H	no	WD

Z = 0.04 / solar

M_{ZAMS}	$T_{\mathrm{eff,i}}$	t_{tr}	M_{T4}	?-burner	TP	End
1.0	3.57	49.717	0.510	He	no	WD
1.2	3.60	4.042	0.522	He	no	WD
1.5	3.64	7.858	0.531	H	no	WD
1.6	3.71*	0.021	0.536	H	no	WD
1.8	3.70*	0.783	0.536	H	no	WD
2.0	3.70	0.628	0.552	H	no	WD

Z = 0.02 / solar

M_{ZAMS}	$T_{\mathrm{eff,i}}$	t_{tr}	M_{T4}	?-burner	TP	End
1.0	3.71*	0.037	0.506	H	no	WD
1.2	3.70*	0.033	0.523	H	no	WD
1.5	3.70*	0.445	0.538	H	no	WD
1.6	3.72*	0.020	0.541	H/He	VLTP	2nd AGB
1.8	3.73*	0.667	0.524	H	no	WD
2.0	3.70	0.528	0.543	H	no	WD

Table 8.1.: Selection of results for post-AGB models with a solar-scaled metal distribution. See text for details.

Z = 0.0005 / α-enhanced

M_{ZAMS}	T_{eff}	t_{tr}	M_{T4}	?-burner	TP	End
1.0	3.67	4.880	0.533	H	no	WD
1.2	3.69	2.742	0.545	H	no	WD
1.5	3.71	1.341	0.567	H	no	WD
1.6	3.71	1.248	0.558	H/He	VLTP	2^{nd} AGB
1.8	3.71	0.575	0.561	H	no	WD
2.0	3.73	0.332	0.598	H	no	WD

Z = 0.008 / α-enhanced

M_{ZAMS}	T_{eff}	t_{tr}	M_{T4}	?-burner	TP	End
1.0	3.71*	2.572	0.524	H/He	LTP	2^{nd} AGB
1.2	3.72*	0.027	0.531	H/He	VLTP	2^{nd} AGB
1.5	3.73*	0.016	0.537	H/He	VLTP	2^{nd} AGB
1.6	3.74*	0.013	0.536	H/He	VLTP	2^{nd} AGB
1.8	3.68	1.039	0.523	H	no	WD
2.0	3.73*	0.012	0.498	H	no	WD

Z = 0.004 / α-enhanced

M_{ZAMS}	T_{eff}	t_{tr}	M_{T4}	?-burner	TP	End
1.0	3.71*	3.169	0.530	H	no	WD
1.2	3.72*	1.985	0.538	H/He	VLTP	2^{nd} AGB
1.5	3.70	1.725	0.543	H	no	WD
1.6	3.69	1.636	0.519	H/He	VLTP	2^{nd} AGB
1.8	3.67	1.756	0.527	H	no	WD
2.0	3.73	0.510	0.515	H/He	LTP	2^{nd} AGB

Z = 0.04 / α-enhanced

M_{ZAMS}	T_{eff}	t_{tr}	M_{T4}	?-burner	TP	End
1.0	3.58	51.989	0.511	He/He	LTP	2^{nd} AGB
1.2	3.63	10.657	0.521	H	no	WD
1.5	3.60	23.111	0.536	He	no	WD
1.6	3.72*	0.021	0.535	H/He	VLTP	2^{nd} AGB
1.8	3.66	2.417	0.537	H	no	WD
2.0	3.73*	0.539	0.552	H/He	LTP	2^{nd} AGB

Z = 0.02 / α-enhanced

M_{ZAMS}	T_{eff}	t_{tr}	M_{T4}	?-burner	TP	End
1.0	3.71*	0.046	0.508	H/He	LTP	2^{nd} AGB
1.2	3.72*	0.026	0.519	H	no	WD
1.5	3.71*	1.498	0.537	H	no	WD
1.6	3.70	1.368	0.548	H/He	LTP	2^{nd} AGB
1.8	3.73*	0.495	0.540	H/He	LTP	2^{nd} AGB
2.0	3.71*	0.113	0.537	H	no	WD

Table 8.2.: Same as Table 8.1 for α-enhanced metallicity models.

8.2. Convergence issues

Before further continuing with the post-AGB evolution, an important parenthesis is here necessary. In the introduction and many times throughout this thesis, we have mentioned the existence of convergence problems during the computations. These complications arise very often in advanced stages of the TP-AGB when the star has lost an appreciable amount of mass, and in born-again AGB models when an extra TP occurs on the post-AGB track.

In the literature, this issue has already been mentioned, but seems to recurrently *appear* and *disappear*. Over the last twenty years, similar convergence difficulties in different codes (MSSSP, EVOL, LPCODE, our Garching code - see section 7.2) have been recognized by the groups interested in detail modelling of the TP-AGB and post-AGB phases (e.g. Wood & Faulkner 1986, Herwig 2005a, Miller Bertolami & Althaus 2006, Karakas & Lattanzio 2007, Kitsikis & Weiss 2007). But at other times, with the same codes, computational problems are either not found or barely mentioned (Vassiliadis & Wood 1993, 1994, Blöcker 1995a,b). Vassiliadis & Wood (1993) manage, although strenuously, to go through the entire TP-AGB and post-AGB evolution for stars with final masses up to $0.94\mathrm{M}_{\odot}$, while Wood & Faulkner (1986), also with the MSSSP code, do not. No comment on convergence problems in the EVOL code is made by Blöcker (1995a,b) but Herwig (2005a) mentions numerical convergence difficulties already at $M_{\mathrm{ZAMS}} = 2\mathrm{M}_{\odot}$.

In the most recent calculations, problems already appear for low-mass stars. In fact, only evolutions for MS initial mass stars up to $1\mathrm{M}_{\odot}$ seem to be easily calculable. Miller Bertolami & Althaus (2006) are confronted with convergence problems shortly after the departure from the AGB for all models except for the $1\mathrm{M}_{\odot}$ case. Similarly, for Karakas (2003) and Karakas & Lattanzio (2007) the only model to leave the AGB is the $1\mathrm{M}_{\odot}$ / Z = 0.02 one; in all other cases calculations cease before the end of the TP-AGB phase.

The other computationally challenging phase of moderate-mass stars, the He-flash at the tip of the RGB, being nowadays routinely followed by evolutionary codes (e.g. the Garching code), this convergence issue at the end of the TP-AGB is very important. It is the missing link in the modelization of the evolution from the MS to the WD phase for moderate-mass stars.

In order to circumvent these complications, various artifices have been used. Stripping-off the remaining envelope (e.g. Wood & Faulkner 1986) when a crash occurs and letting the resulting model evolve from the beginning of the post-AGB to the WD phase, increasing the value of α_{MLT}, the mixing length parameter, during the difficult phases (Herwig 2005b, Miller Bertolami & Althaus 2006, Miller Bertolami 2006, Kitsikis & Weiss 2007) or imposing artificial boundary conditions in the envelope integration for born-again AGB models (Miller Bertolami & Althaus 2006) are only some of them. Even with these artifices, success in bypassing the difficult stages is not guaranteed and supposes a skillful intervention of the person doing the calculation. This is also one of the reasons not many large TP-AGB/post-AGB grids originating from detailed models are available: the human-interaction necessary, essential for all models in oder to make them converge, is time consuming.

From the list of papers commenting on this issue, Wood & Faulkner (1986) are the only ones to treat it most extensively. Their interpretation has been cited by later works (e.g. Miller Bertolami & Althaus 2006) to explain the computational problems, however without pushing the investigation further. They attribute the code failure of their hydrostatic evolutionary calculations to the radiation pressure being so large, at the base of the convective envelope, that it supplies all the pressure support required by the model and hence forces the gas pressure to zero. Karakas & Lattanzio (2007) admit having no satisfactory explanation; however they note that these problems do not seem to be associated to the high radiation pressure because earlier TDU episodes with similar low values of β are easily computed.

In general, observed model symptoms are similar in most codes (e.g. Miller Bertolami & Althaus 2006, Karakas & Lattanzio 2007, Kitsikis & Weiss 2007). For the low-mass stars ($M_{\rm ZAMS} < 2{\rm M}_{\odot}$) the evolution either continues uninterrupted through the TP-AGB - post-AGB transition, or stops on the TP-AGB when stars have practically lost their entire envelope. For the more massive stars, the remaining envelope can be large enough so that one or more TPs would occur. Convergence difficulties, whether on the TP-AGB or in the born-again AGB phase, mostly happen during the start of the TDU events, after the He-luminosity peak.

The goal of this thesis was not to specifically treat this important and interesting issue. From the moment it was recognized, focus was on finding a simple acceptable approach to go through this difficult phase. Increasing the mixing length parameter was the initial recipe; with it, models only up to $M_{\rm ZAMS} = 3{\rm M}_{\odot}$ (Kitsikis & Weiss 2007) where evolved all the way to the WD phase. For the $3{\rm M}_{\odot}$ case in particular, the value of $\alpha_{\rm MLT}$ at the end of the TP-AGB had to be increased from 1.75 to almost 15! Higher values of $\alpha_{\rm MLT}$ render more efficient convection. As a result, the star becomes compact, the importance of the radiation pressure is reduced and better convergence is reached. Herwig (2005b) and Miller Bertolami & Althaus (2006) also increase $\alpha_{\rm MLT}$, but up to values of 2.5-3.0 and 5.0-6.0 (Miller Bertolami 2006) respectively.

According to Herwig (2005a), $\alpha_{\rm MLT}$ on the AGB could have higher values by as much as 15% and is uncertain by at least ±20% (Ludwig et al. 1999). A small increase could therefore have a physically defensible justification. But values even up to only 4-5 are far too important. Besides, more efficient convection during the TDU - where problems usually occur - entail more dredged-up material, a modified surface abundance, and in our case a direct influence on the evolution through the chemistry dependent opacity and mass-loss prescriptions.

The increased mixing length approach was therefore abandoned, and we decided on the following method. After a models final crash at the end of the TP-AGB, we *freeze* the calculations in time by switching off nuclear burning, mixing processes and gravothermal energy. Mass-loss, the only process kept active, is intensified in order to strip-off the remaining envelope. Afterwards, all processes are once more smoothly activated, when the star is about to leave the TP-AGB with an effective temperature of approximatively 3.7 (in logarithmic units), and the post-AGB evolution is left to normally continue with the appropriate mass-loss prescription. Like mentioned earlier in section 8.1, by bypassing this difficult stage, the post-AGB tracks often begin with pulsation periods below 100 days and thus after the zero-age as it was defined by the mass-loss relations. This recipe was unfortunately successful only for low-mass models ($M_{\rm ZAMS} \leqq 2\rm M_{\odot}$) that experienced convergence problems. For higher masses, we were not able to make the *trick* work. Finally, during their return on the AGB, tracks experiencing a LTP or VLTP also did not converge properly and were compelled to stop on the born-again AGB phase.

The ratio of gas to total pressure ($P_{\rm gas}/P$) in the star is given by β. At the very base of the envelope on the AGB, convection carries only a small fraction of the energy. The region underneath the envelope and above the H-burning shell is fully radiative. Energy transportation by radiation alone should thus be considered in these boundary regions. In advanced stages of the TP-AGB, when computational problems start to develop, our models show values of $\beta \ll 1$ at the bottom of the convective envelope. Similar values are also found during the post-AGB evolution in the region between the envelope and the core. This causes the density to drop almost to zero and convergence to fail.

For these regions between the upper part of the H-burning shell (i.e. core), and the bottom part of the convective envelope for a AGB star or the entire envelope for a post-AGB star, Wood & Faulkner (1986), starting from the equations of hydrostatic equilibrium and radiative transfer, link (their equation 2) the value of β to the mean opacity $\langle\kappa\rangle$, the luminosity L and the core mass $M_{\rm c}$ by the following relation

$$\frac{P_{\rm rad}}{P} = 1 - \beta \approx \frac{\langle\kappa\rangle\, L}{4\pi c G M_{\rm c}}, \tag{8.1}$$

with $\langle\kappa\rangle = P^{-1}\int_0^P \kappa dP$ being the integrated value of the opacity over a few pressure scale heights in this region of negligible convection. As the luminosity L approaches the local Eddington limit, $L_{\rm Ed} = 4\pi c G M_{\rm c}/\langle\kappa\rangle$ ($\beta = 0$), the expansion of the stars envelope must be occuring hydrodynamically, and no solution is found in our hydrostatic calculations. At this point the dependence on opacity can be one of the reasons why convergence problems occur. Wood & Faulkner (1986) mention for example that an analytical fit for opacity values rather than tabulated ones is used in order to ensure smoothness in critical limiting cases. Similarly for Miller Bertolami & Althaus (2006), problems are more noticeable when the newer OPAL opacities are used in their code. According also to Karakas & Lattanzio (2007), opacities may be related to the problem. We have not systematically compared our results with different opacity tables. Nevertheless, we notice that C-rich models, that use our new low-temperature molecular opacity tables crash earlier than O-rich models, experiencing no TDU, calculated with the older opacity tables for fixed compositions. A different spline interpolation scheme through the new tabulated values could for example smoothen the opacity variations.

These are simply a few hints for future investigations. Before any premature discussion, further work needs to be done in order to identify the problem, and successfully follow the complete AGB and the transition to the post-AGB in a satisfactory way. These convergence difficulties are an important issue that needs to be addressed, as they are seemingly present in all current codes.

8.3. The Models

Like previously noted, the most up-to-date and wide-ranging post-AGB grid is currently the one of VW94. In agreement with its progenitor AGB grid (VW93), the total 27 models of VW94 are available for the Z = 0.016, 0.008, 0.004 and 0.001 metallicities, in the mass interval from 0.558$M_\odot$ to 0.943$M_\odot$. A smaller set of tracks, originating from the Blöcker (1995b) AGB models, are those from Blöcker (1995a) [B95]. These are only calculated for one specific composition with a solar-like metallicity (Z = 0.021) and comprise 6 models in the mass range [0.524$M_\odot$, 0.940$M_\odot$].

Unfortunately, because of the converge problems encountered, the post-AGB tracks presented here correspond to stars not more massive than 0.6$M_\odot$: they range from 0.492$M_\odot$ to 0.600$M_\odot$. The positive side is however that our grid comprises 60 models through 10 different initial compositions and a much denser mass resolution with respect to the previous grids.

8.3.1. Hydrogen- and Helium-Burning Models

If the star leaves the TP-AGB at a phase cycle (section 2.1) between 0 and 0.15, it becomes a He-burning post-AGB star as it departs just after the TP when the He-burning luminosity is still very high and H-burning has not effectively re-ignited yet. For higher cycle phases it emerges as a H-burning post-AGB star. The big majority of our models are H-burners, and only 4 of our tracks leave the TP-AGB as He-burners. These are the 1$M_\odot$ / 1.2$M_\odot$ Z = 0.04 (solar-scaled) and the 1$M_\odot$ / 1.5$M_\odot$ Z = 0.04 (α-enhanced) models. All tracks experiencing an extra TP on the post-AGB will eventually also be converted into He-burners but as our calculations do not continue past the born-again AGB phase, these additional He-burning tracks are not available. For these statistics, we can thus not consider the 30 tracks for which an intervention at the end of the TP-AGB was necessary to bypass the convergence difficulties because we have interfered with the evolution. Indeed computations were purposely let to continue their post-AGB evolution during stages of easy convergence which were mainly during quiescent H-burning phases: all these models are therefore H-burners. With respect to the other 30 models we thus have about 15% of He-burning post-AGB tracks.

Such a low number-ratio between He-burning and H-burning post-AGB stars is very similar to the one found in the VW94 and B95 models. Most of the He-burning models of VW94 originate from born-again AGB stars that had originally left the AGB as H-burners. As for B95, no direct (before a born-again AGB) He-burning tracks are available.

This ratio would most likely be lower if more massive models were also available. This is because of the interaction of the mass-loss prescription on the TP-AGB and the cycle phase. Graphics 7.1-7.4 show how, for lower mass stars, the higher mass-loss rates (over periods of 400 days) are only adopted during the end of the TP-cycle. In general, as the probability of the envelope being completely ejected is higher during periods of strong mass-loss, it is expected that a non negligible number of these stars will leave the TP-AGB close to a He-flash.

On the contrary, for the more massive stars, the mass-loss rate remains high for a larger fraction of the interpulse: the phase numbers at which stars will leave the TP-AGB will therefore correspond to a much wider range and relatively less tracks will be He-burners.

Regardless of the initial mass of the models, in both low- and high-mass cases, the strong mass-loss rates always come into play during the more advanced cycle phases. In that sense, considering the entire [$1M_\odot$, $6M_\odot$] mass-range, our mass-loss prescription favors post-AGB models with high cycle phases and therefore H-burning tracks which are more subject to experience a LTP or a VLTP. In order to get more models to depart form the TP-AGB close to shell-flash, mass-loss rate would need to be extremely well adjusted with cycle phase, something which is very unlikely.

8.3.2. Transition Times

The transition times, $t_{\rm tr}$, have already been defined earlier in this chapter. Between models from different studies, the $t_{\rm tr}$ values will greatly depend on the moment the high mass-loss is switched off and an end to the TP-AGB is assigned. B95 keep high rates until the pulsation period has fallen below 50 days, whereas VW94 switch it off much earlier (when the model has moved off the TP-AGB by $\Delta \log_{10} T_{\rm eff} = 0.3$). As a consequence the starting post-AGB temperatures are much higher for the B95 models. Specifically the VW94 tracks begin with $T_{\rm eff}$ values between 3500 K and 5000 K, while the B95 starting temperature range is [6000 K, 7900 K].

Our post-AGB models get going earlier than the B95 ones because we do not wait until the period drop to 50 days. Instead we already stop the TP-AGB mass-loss at a period of 100 days; however we do not start as early as VW94. Accordingly our kickoff temperatures range from 3.58 to 3.73 (in logarithmic units), or $\approx$ 3800 K - 5400 K.

The models starting point will not be the only influencing factor on the transition times; the used mass-loss prescriptions also play an important role. Although both B95 and VW94 use the PN results compiled by Pauldrach et al. (1988) for radiation-driven winds in order to adopt an appropriate prescription, they derive distinct formulas and apply them differently. For example, contrarily to VW94, B95 does not include an effective temperature dependence. On the other hand, VW94 implement the radiation-driven wind relation for the PN regime as soon as the star has effectively left the AGB, whereas B95 uses a stronger Reimers rate until effective temperatures reach values that correspond more to the PN phase - around 20 000 K. Our approach is very similar to the B95 one (see Chapter 3), but we keep a higher Reimers mass-loss for the low-mass stars (η = 1.0 instead of B95's 0.5 value) until the radiation-driven wind values exceed it (this happens also around 20 000 K depending a stellar mass).

As a result, the transition times will behave differently in the various cases. The VW94 prescription leads to, an abrupt and steeper decrease of the mass-loss, lower average rates, and finally longer transition times. The B95 times (solar composition) strongly decrease with mass by almost two orders of magnitude (see figure 3 in Schonberner 1997). On the contrary the higher VW94 values stay constant and even slightly increase with core mass.

In Figure 8.4 we plot our results for the $t_{\rm tr}$ values as well as those of VW94. We only show our transition times that correspond to models that really do start at P = 100 days (those for which no asterisk is printed beside the t_{tr} values in the 8.1 and 8.2 Tables). Our core-mass range overlaps with the one from VW94 only over a few values below 0.6$M_\odot$. No particular dependence on metallicity or metal-scaling is discernible. We see that our transition times mainly decrease with increasing mass (except for the Z = 0.004 case) as did those of B95 for higher core masses between 0.524$M_\odot$ and 0.836$M_\odot$ (see figure 3 in Schonberner 1997). Most of our transition times gather around the 1000/2000 year marks, and only a few reach values above. In comparison, for a 0.524$M_\odot$ model, B95 gets ≈ 4000 days while his lowest transition times are obtained for 0.835$M_\odot$ with less than 10 days.

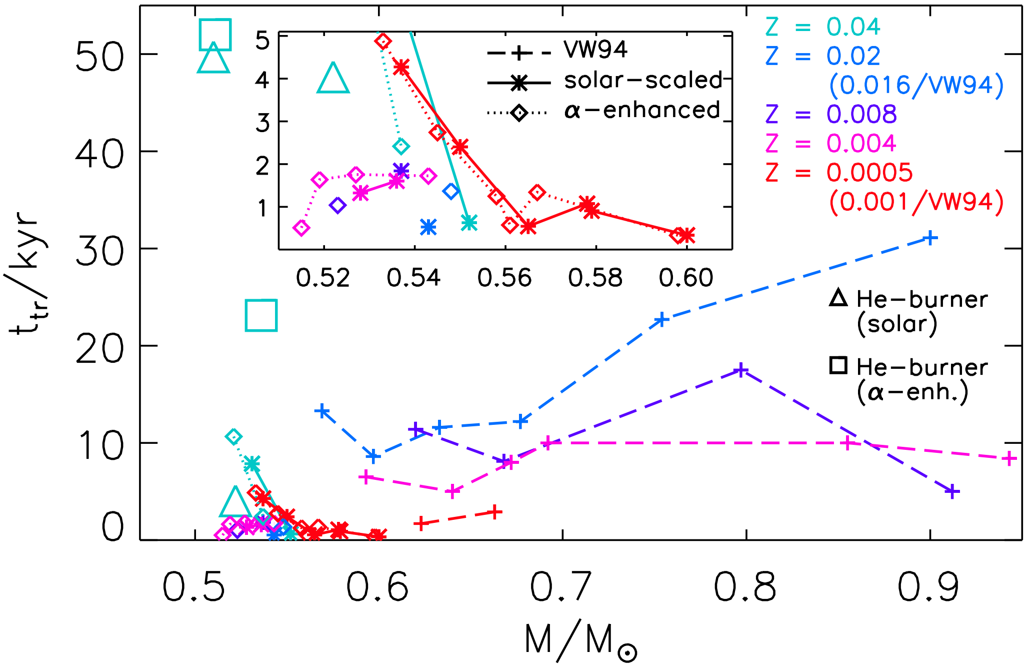

Figure 8.4.: Post-AGB transition times as defined in the text. Our results as well as those of (Vassiliadis & Wood 1994) [VW94] are given. All t_{tr} values correspond to H-burning post-AGB tracks, except for the large triangle and square symbols which are our 4 He-burning tracks.

Finally, it is to be noted that He-burning models have on average higher transition times than H-burning ones. This is of course expected because of the lower He-burning rates and thus the slower consumption of the envelope.

According to Schonberner & Blocker (1993) and Schonberner (1997) observations show that the coolest post-AGB stars have effective temperature around 5000K. The VW94 temperatures are therefore much too low. Instead the B95 ones seem to be better-suited. Our results cover a temperature range in between both and close to the 5000 K value. Furthermore, the constraints set by dynamical ages of the youngest PNe favor fast evolutionary timescales of about 1000 years. The VW94 tracks render too long transition times, whereas our and the B95 results are more in agreement with these lower timescales. Nevertheless, our transition times are on average still higher than 1000 years.

In the synthetic planetary nebulae luminosity function (PNLF) of Marigo et al. (2004), the transition time is taken as one of the adjustable parameter because of the great uncertainty associated with these quantities, but also because the AGB and post-AGB tracks used as input in the synthetic code, originate from unrelated grids. In the computed PNLF, values of 500 and 1000 years taken as a educated guess are simply assumed. Because the type of post-AGB evolution and the $t_{\rm tr}$ values have major consequences on the evolution of PNe, it would be more fitting, and is now possible, to use our transition times, since each value corresponds to a single H- or He-burning evolutionary track encompassing both the AGB and post-AGB phases.

8.3.3. Evolution Across the HR Diagram

In addition to the transition times mentioned earlier, we define two more temporal quantities, t_1 and $t_{\rm c}$. The second represents the *crossing time* in the HR diagram from the beginning of the post-AGB (the second zero-age at 10 000 K is considered) to the turn-around point (generally values above $\log_{10} T_{\rm eff} = 5$) when luminosity values start to decline towards the WD cooling track. With respect to the beginning of the post-AGB tracks, t_1 is the time necessary to reach the region where mass-loss is calculated according to the B95 relation based on the Pauldrach et al. (1988) results. We report the t_1 and $t_{\rm c}$ values in Table 8.3 for all our models.

During the PN phase, radiation pressure based mass-loss is relatively small compared with the rate at which the envelope is consumed through H-burning. Therefore, a crucial temporal quantity is the time between the departure form the TP-AGB and the beginning of the PN phase, namely t_1. We have used a similar prescriptions to the B95 models; we thus compare our values with his in the upper panel of Figure 8.5. Once again our mass range only covers the lower values and no overlap between the two sets is possible because of our initially lower AGB core-mass and the convergence issues.

Most of our values lie under the 3 000 years mark and only two models have t_1 values higher than 6 Kyr. The B95 ones range from 11 to 1 700 years for the most massive stars for an initial-mass range between $3M_\odot$ and $7M_\odot$. The increasing trend with decreasing mass obtained by B95 is thus well extended by our models to lower masses. The higher values that we obtain are also due to the fact that our post-AGB tracks begin earlier (100-day period) than the B95 (50-day period) ones. If our post-AGB tracks started as late as those of B95, t_1 values would be lower. This can be seen in one of the B95 models corresponding to the bigger sized blue cross symbol in Figure 8.5. The star is of identical mass than the one with a lower value of t_1 but has a post-AGB zero-age at the 100-day period point instead of the 50-day. It is not surprising that the t_1 increases for an earlier start to the post-AGB.

The second quantity tabulated in Table 8.3 is the crossing time. We plot our results together with those of VW94 in the lower panel of Figure 8.5. Crossing times values

Z = 0.04 / solar			Z = 0.02 / solar			Z = 0.008 / solar			Z = 0.004 / solar			Z = 0.0005 / solar		
M_{T4}	t_1	t_c	M_{T4}	t_1	t_c	M_{T4}	t_1	t_c	M_{T4}	t_1	t_c	M_{T4}	t_1	t_c
0.510	57.677	86.516	0.506	0.041*	26.417	0.531	1.730*	16.935	0.528	1.116*	16.348	0.537	5.365	14.464
0.522	31.515	48.850	0.523	0.038*	16.099	0.529	0.030*	14.369	0.531	1.386*	16.816	0.550	2.868	8.845
0.531	10.215	18.553	0.538	0.832*	7.388	0.537	2.178	6.995	0.536	0.681*	8.149	0.579	1.008	3.441
0.536	0.029*	6.926	0.541	0.021*	6.248	0.537	0.443*	5.595	0.536	1.909	6.330	0.578	1.213	4.129
0.536	1.805*	6.875	0.524	29.316*	47.833	0.526	0.025*	12.811	0.492	1.029*	2.810	0.565	0.860	3.917
0.552	1.131	4.523	0.543	0.868	3.614	0.528	0.014*	5.173	0.528	2.770	10.709	0.600	0.478	2.412

Z = 0.04 / α-enhanced			Z = 0.02 / α-enhanced			Z = 0.008 / α-enhanced			Z = 0.004 / α-enhanced			Z = 0.0005 / α-enhanced		
M_{T4}	t_1	t_c	M_{T4}	t_1	t_c	M_{T4}	t_1	t_c	M_{T4}	t_1	t_c	M_{T4}	t_1	t_c
0.511	58.338	35.345	0.508	2.798*	16.572	0.524	3.599*	1.141	0.530	4.600*	17.434	0.533	6.219	16.959
0.521	14.043	25.677	0.519	0.027*	14.592	0.531	0.732*	13.983	0.538	2.690*	11.122	0.545	3.431	10.276
0.536	24.661	16.080	0.537	1.833*	7.137	0.537	0.016*	0.859	0.543	2.062	6.962	0.567	1.585	5.490
0.535	0.021*	7.894	0.548	1.594	2.903	0.536	0.014*	6.688	0.519	1.969	3.728	0.558	1.438	4.958
0.537	5.980	16.977	0.540	0.973*	0.844	0.523	2.062	8.281	0.527	4.160	13.545	0.561	1.008	4.649
0.552	0.885*	0.387	0.537	0.403*	3.827	0.498	0.013*	6.163	0.515	1.014	0.016	0.598	0.510	3.621

Table 8.3.: The two t_1 and t_c timescales (in thousands of years) for all our tracks, For the t_1 values asterisks indicate that the zero-age post-AGB is taken after the critical 100-day period moment (similar to Tables 8.1 and 8.2) because of convergence problems; in those cases t_1 times are shorter than expected. The t_c correspond to intervals starting from our second zero-age point at 10 000K, for which data is available for all tracks. See text for more details.

range between a few hundreds of years and 20 000 years. The VW94 models show a trend of increasing value with decreasing mass but our results in the overlapping region are much lower. This is due once more to our different description of mass-loss.

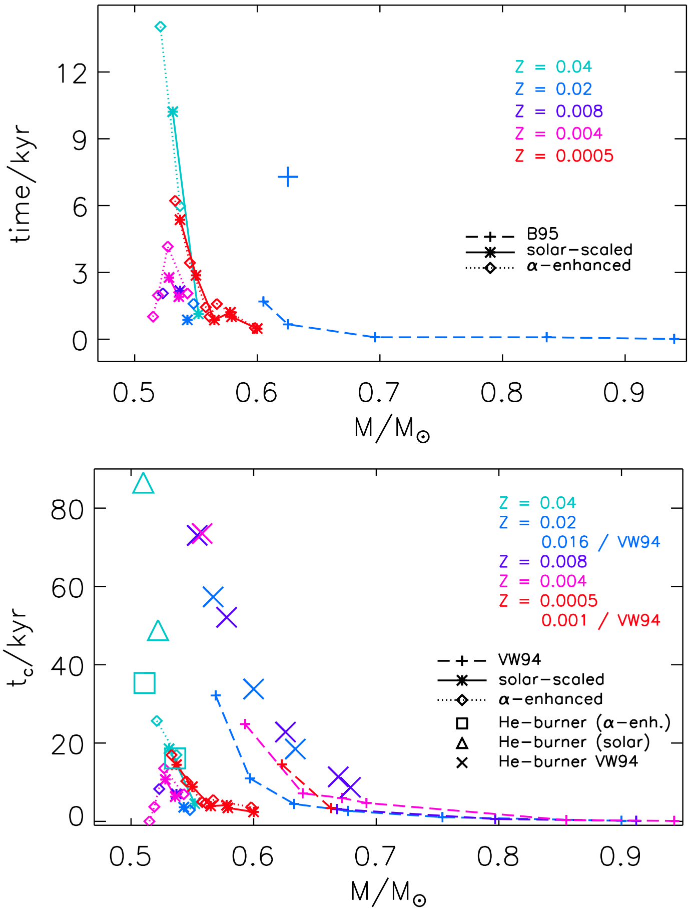

Figure 8.5.: *Top panel* - t_1 times as defined in the text vs stellar mass. *Bottom panel* - Post-AGB crossing times vs stellar mass. In addition to ours, the results from Blöcker (1995a) [B95] and Vassiliadis & Wood (1994) [VW94] are also plotted. Large symbols correspond to He-burning models.

The rates based on the radiation-driven wind theory are similar for both the VW94 and our results during the PN phase. But the earlier post-AGB is different. While VW94 have already started using their radiation-driven wind rate at the 10 000 K mark, we use a strong Reimers ($\eta = 1$) mass-loss rates until they drop below the radiation-driven prescription of B95; this usually happens for $\log_{10} T_{\rm eff} \approx 4.3$. In both cases, from the moment the PN rates are taken into account, these are used until the blue-most edge of the HR diagram track is reached. All our crossing times are shifted towards lower values because of our faster earlier evolution with respect to VW94. Once more, for our models as for the VW94 ones, He-burning tracks evolve much slower and crossing times reach values up to 80 kyr.

8.3.4. Born Again Times during the VLTP Scenario

During a VLTP evolution a TP takes place. At variance with the situation on the AGB, when the shell-flash occurs the above H-burning shell is already extinguished/ing; the star is on the WD cooling track. The pulse-driven convective zone grows in mass and extends until it reaches the H-rich envelope. In conventional TP cases, the H-burning shells high entropy barrier would prevent this from happening. But now, strong proton-burning will gradually begin as the upper part of the convective region engulfs increasingly more and more hydrogen. H-burning luminosity reaches a high peak that can go up to $10^{11}\mathrm{L}_{\odot}$. After the He-shell flash and the violent proton-burning are over the star grows in radius and moves back to the giant region as a born-again AGB star.

Among the observational examples of stars thought to experience an extra TP during their post-AGB evolution, the V4334 Sgr one (aka Sakurai's object) is believed to specifically be undergoing a VLTP (Duerbeck & Benetti 1996). In only a few years, different studies have shown that it has a rapid evolution in the HR diagram (Duerbeck et al. 1997, Asplund 1999, Hajduk et al. 2005). From the observational results, V4334 Sgr has evolved form the pre-WD stage to its current position in the HR diagram, which is one of a giant, in about 2 years.

Theoretical predictions do however not agree. Some studies find born again times of a few tens of years (Iben & MacDonald 1995, Lawlor & MacDonald 2002, Miller Bertolami et al. 2006) while others get values in the order of hundreds of years (Herwig et al. 1999, Herwig 2001b). More specifically, Iben & MacDonald (1995) present a VLTP sequence with t_{ba} = 17 yr, and Miller Bertolami et al. (2006) find born again times of 5-10 years. On the contrary the VLTP model presented by Herwig et al. (1999) needs a 350 year evolution to return on the AGB.

Herwig (2001b) proposed a reduction, with respect to the value predicted by MLT theory, of the mixing efficiency by a factor of 100 (for a $0.604\mathrm{M}_{\odot}$ model) during violent proton burning in order to match the observed born again time of V4334 Sgr. To the contrary, Miller Bertolami et al. (2006) and Miller Bertolami & Althaus (2007b) obtain t_{ba} values very close to the observed ones without reducing the mixing efficiency.

In a similar way to previous works, we define t_{ba} to be the interval between the maximum H-burning after a VLTP has occurred and the moment the star, as it is returning on the AGB, reaches $\log_{10} T_{\mathrm{eff}} = 3.8$. We present the results for our 10 VTLP models in Table 8.4.

Put aside the two $1.6\mathrm{M}_{\odot}$ models (Z = 0.008/solar and Z = 0.0005/α-enhanced) that give relatively low values, 56 and 11 years respectively, all other born again times range between values of approximatively 200 and 300. These are therefore similar to what is found by Herwig et al. (1999) and much higher than both the observed value for V4334 Sgr and the model values of Miller Bertolami & Althaus (2007b).

It has been shown though (Miller Bertolami et al. 2006, Miller Bertolami & Althaus

2007b), that born again times are dependent on time resolution. During the VLTP, evolution is characterized by extremely fast structural changes especially during the H-burning flash that occurs when the protons present in the envelope are mixed in the He-burning shell. The minimum time step during this phase must remain larger than the hydrodynamical time scale and the convective turnover time (Herwig 2001b) . Furthermore, Miller Bertolami et al. (2006) show that different time steps affect how well the H-burning peak luminosity can be resolve. In their calculations, while a minimum time step of 10^{-5} yr gives a 3% error estimation on the expected proton-burning luminosity, 3×10^{-6} and 10^{-3} year time steps render respectively errors of 10 and 100%!

$M_{\rm ZAMS}$ ($M_\odot$)	Composition	$M_{\rm T4}$ ($M_\odot$)	$t_{\rm ba}$ (yr)	$max \log_{10}(L_{\rm H}/L_\odot)$	Δt (yr)
1.5	Z = 0.004 / solar	0.536	200	10.34	10^{-4}
1.0	Z = 0.008 / solar	0.531	240	10.05	$10^{-7/-2}$
1.6	Z = 0.008 / solar	0.537	56	9.959	$10^{-7/-2}$
1.6	Z = 0.02 / solar	0.541	189	9.386	$10^{-7/-2}$
1.6	Z = 0.0005 / α-enhanced	0.558	11	11.39	10^{-6}
1.2	Z = 0.004 / α-enhanced	0.538	254	6.559	$10^{-4/-1}$
1.6	Z = 0.004 / α-enhanced	0.519	305	6.961	$10^{-6/-2}$
1.2	Z = 0.008 / α-enhanced	0.531	292	6.079	$10^{-5/-2}$
1.5	Z = 0.008 / α-enhanced	0.537	302	6.674	$10^{-5/-2}$
1.6	Z = 0.008 / α-enhanced	0.536	307	7.006	$10^{-5/-2}$

Table 8.4.: Born again times, $t_{\rm ba}$ for our models experiencing a VLTP. $t_{\rm ba}$ is the time between the maximum H-burning from after the occurrence of the VLTP until the moment the tracks reach $\log_{10} T_{\rm eff}$ = 3.8 on its AGB return. $M_{\rm T4}$ is identical as in Tables 8.1 and 8.2. Δt is the minimum time step used during the computations. When two values are present, this indicates that the minimum times step was changed during the evolution because of convergence problems.

In the last two columns of Table 8.4 we also plot the maximum H-burning luminosity of the models as well as the minimum time step used during the evolution. In most cases, the value of the minimum time step was modified during the evolution, often because of convergence difficulties. We notice that while all models lie in the same mass range, only the 1.6M$_\odot$ / Z = 0.02 (solar) one reaches a high maximum luminosity at 11.39. In all other cases the peak of proton-burning is not well resolved and the highest values reached can be as low as $\approx$ 6. Our model with the short 11 year born again time (0.558M$_\odot$) has a minimum time step that is almost identical to the one used by (Miller Bertolami et al. 2006), 5×10^{-5} yr, for which $t_{\rm ba}$ = 5 - 10 yr values are obtained. Moreover, Miller Bertolami & Althaus (2007b), with a minimum time step of 10^{-5} years, get $t_{\rm ba}$ = 7.5 and 10.8 respectively for 0.561M$_\odot$ and 0.565M$_\odot$ models with a solar type composition.

It is most likely that, if all our VLTP models were re-computed with a different time resolution (i.e. a minimum time step of 10^{-6} for example), they would, provided that convergence problems could be overcome, render lower born again times.

The two main outcomes of our results are thus: a) time resolution does indeed plays a role for born again times, b) low values of t_{ba} can be obtained without having to reduce the mixing efficiency during strong proton-burning.

8.4. Summary

The evolutionary timescales, the burning regime (hydrogen or helium) and the stellar masses of the post-AGB section of our tracks have been presented in this chapter. In addition, the difficult convergence problems occurring at the end of the AGB are mentioned since these are the essential reason why relatively few post-AGB models are available.

The AGB mass-loss prescription, because it directly influences the post-AGB evolution, and of course the mass-loss rates used specifically on the post-AGB, remain the greatest uncertainty of the models. A better theory of mass-loss is needed in the future. Few recent studies have dealt with this topic. For example, one problem is how one models the transition from the AGB to the post-AGB in term of mass-loss strength. According to the latest work from Schonberner & Steffen (2007), the strong AGB mass-loss must continue until temperatures of 5000 to 6000 K are reached before switching to post-AGB lower mass-loss rates. If not, as the bulk of the expelled material will be too far away from the central star, no double-peak spectral energy distribution of the post-AGB object will be observed and the formation of PNe will be impossible. This should therefore be taken into account in studies to come.

In the absence of a more recent one, we have adopted a similar mass-loss prescription as in Blöcker (1995a), and started the post-AGB a little earlier, at temperatures between 3 800 and 5 400K. Our timescale results are therefore more in agreement with Blöcker (1995a) and much shorter than the values of Vassiliadis & Wood (1994). For example, our transition times are of the order of a few thousand years. These values are more compatible with the dynamical ages of the PNe obtained from observations (Schonberner & Blocker 1993, Schonberner 1997) than the results of Vassiliadis & Wood (1994). Our mass-loss prescription favors moreover post-AGB tracks with high cycle phases. This translates into few (we get 4 our of 60) He-burning post-AGB tracks and H-burning ones which are relatively more subject to experience a LTP or a VLTP.

We also show how our computations, depending on time resolution, produce both long and short born again times for evolutions undergoing a VLTP. With the appropriate minimum time step, born again times almost as short as the observed values of Sakurai's object are possible. Our results are in agreement with the work of Miller Bertolami & Althaus (2007b).

Furthermore, as a substitute to the three separate grids for the evolution prior to the PN phase (Marigo et al. 1999, Girardi et al. 2000, Marigo 2001) and the older post-AGB tracks of Vassiliadis & Wood (1994), our models can be included in the Marigo et al. (2004) synthetic code (seen in Chapter 7) as a consistent and continuous evolutionary set, from the MS to the WD phase, for the PNLF calculations. In addition to the homogeneity of our tracks, our large metallicity range is another advantage. Furthermore, transition times - of the order of a few thousand years on average and ranging from 50 kyr (He-burning models) to as low as 300 years - specifically corresponding to each track, can be used in the PNLF code instead of the current arbitrarily set values at 500 and 1000 years. Finally, the major drawback is of course the limited ($1\mathrm{M}_\odot \leqq M_\mathrm{ZAMS} \leqq 2\mathrm{M}_\odot$) initial mass-range of the post-AGB part of the tracks, especially because stars with $M_\mathrm{ZAMS} \approx 2.5\mathrm{M}_\odot$ seem to be responsible for the cut-off luminosity.

In the future, the computational difficulties encountered should be more seriously addressed in order to be able to follow the entire evolution for all moderate-mass stars. This is even more essential, as additional numerical constraints like higher time resolution can often be crucial (e.g. VLTP). With the appropriate computer facilities, producing extended grids of detailed models is nowadays not an issue anymore. But the mission of such a task is limited if calculations are not easily feasible. Indeed, in the cases where multiple human interventions during the difficult phases are needed to overcome the convergence problems for intermediate-mass stars ($\gtrsim 2\mathrm{M}_\odot$), these are so time-consuming that only a few tracks can be obtained (e.g. Miller Bertolami & Althaus 2007a), and full grids are not possible. As a result, synthetic studies have been compelled to use the older post-AGB grid of Vassiliadis & Wood (1994), which was up to now the only available one computed for different masses and metallicities.

9. Conclusion

Moderate-mass theoretical stellar models from the main sequence to the white dwarf phase were computed with the most up-to-date version of the Garching stellar evolution code. The results are presented in this thesis. We concentrate our attention on the AGB (Asymptotic Giant Branch) and post-AGB phases of evolution. For this reason, improvements specifically relevant for these two phases have been implemented.

The main ameliorations brought with our set of models are four: a) new chemistry dependent low-temperature opacities (Chapter 4) b) new chemistry dependent mass-loss prescriptions (Chapter 3, section 3.1) c) treatment of convective boundaries by including overshooting (Chapter 3, section 3.2) d) extended initial mass-metallicity grid (Chapter 5).

We have constructed 12 sets of 126 two-dimensional (temperature and density) opacity tables for different compositions. The opacity data is a combination of the nowadays customarily used Iglesias & Rogers (1996) results for high temperatures and the new tables of Ferguson (2006) for the low temperatures. The opacity data provided to us by J. Ferguson take into account molecular opacities which become very important at low temperatures. With these new sets, appropriate opacities for different compositions can be calculated by three-dimensional interpolations. In particular for any given value of total metal content, we consider two different metal distributions, a solar-scaled and an α-enhanced one. More importantly, opacities are calculated for different carbon and oxygen contents, linked together and quantified by the C/O ratio, for both metal scalings.

Mass-loss loss has been taken into consideration during the entire evolution through different analytical relations, each appropriate for specific phases. In particular for the TP-AGB phase we have included two different mass-loss equations; one for oxygen-rich surface compositions (van Loon et al. 2005), and a second for carbon-rich ones (Wachter et al. 2002). The transition mass-loss rate from the TP-AGB to the post-AGB has been calculated in a smooth way and an approach similar to the one of Blöcker (1995a) is used for the post-AGB evolution.

In order to get efficient third dredge-up on the TP-AGB, we have included convective overshooting at all convective boundaries by implementing the prescription proposed by Herwig et al. (1997).

The initial stellar mass and metallicity intervals of our grid are: $1\mathrm{M}_{\odot} \leqq M \leqq 6\mathrm{M}_{\odot}$ and $0.0005 \leqq \mathrm{Z} \leqq 0.04$. Specifically models were computed for masses of 1, 1.2, 1.5, 1.6, 1.8, 2.0, 2.6, 3.0, 4.0, 5.0, 6.0 $\mathrm{M}_{\odot}$ and metallicities of Z = 0.0005, 0.004, 0.008, 0.02 and 0.04 (× 2 - for two different metal distributions). Because of computational difficulties some models were not computed in a satisfactory enough way. Therefore, from the initial $11 \times (2 \times 5) = 110$ combinations, 100 TP-AGB models are available and 60 of them evolve to the post-AGB.

The most recent grids of models, originating from detailed stellar evolution codes, were until now those of Vassiliadis & Wood (1993), Blöcker (1995b) and Karakas (2003) for the TP-AGB phase, and those of Vassiliadis & Wood (1994) and Blöcker (1995a) for the post-AGB phase. Our work aims to replace all these older models by providing a single homogeneous set that both covers a larger initial mass-metallicity parameter space, and features (none of the previous sets do) the improvements earlier mentioned. Moreover, because the TP-AGB and post-AGB models of Blöcker are merely available for one composition ($Z = 0.021$) and five different mass models, we target the substitution of the Vassiliadis & Wood and Karakas models.

The outcome of our work can be resumed by the following.

- *Before the TP-AGB (Chapter 6 and 7)* - For intermediate-mass stars ($2\mathrm{M}_\odot \leqq M \leqq 6\mathrm{M}_\odot$), our core masses agree well with the results from the previous grids when stars reach the TP-AGB. For low-mass stars ($1\mathrm{M}_\odot \leqq M \leqq 2\mathrm{M}_\odot$), because of stronger mass-loss rates and the inclusion of convective overshooting, our envelope and core masses at the 1^{st} TP are lower than the Karakas (2003) ones; they however agree well with studies in which convective overshooting is also used (Miller Bertolami 2006). In addition, because of core convective overshooting, the mass boundary between models that do experience a He-flash at the tip of the red giant branch and models that do not, is shifted to lower masses (from $\approx 2.25\mathrm{M}_\odot$ to $2\mathrm{M}_\odot$) with respect to the Karakas (2003) grid. A metallicity dependence - with lower Z values corresponding to lower masses - of this transition point is also shown through our wide composition range.

- *On the TP-AGB (Chapter 7)* - The higher mass-loss rates, the variable-C/O low-temperature molecular opacities and the convective overshooting, globally render, by comparison to the two previously available grids, more efficient dredge-up, less core growth, higher surface luminosities, lower interpulse periods, less thermal pulses, lower effective temperatures for C-rich models, lower final C/O ratios, and shorter evolutions for most stars, but longer ones for the longest lived models at the He-flash transition mass ($\approx 2\mathrm{M}_\odot$).

  The inclusion of the variable-C/O opacities do produce a cooling of the tracks after the C/O = 1 transition as previously shown by the synthetic models of P. Marigo. The consequence is an increased mass-loss rate and a shorter evolution. Moreover, we show how a warming up of the models can also occur when these opacities are considered and thus a prolongation of the TP-AGB evolution. Since such opacities can influence the temperature in both opposite direction, this work further confirms the necessity of including them in TP-AGB models.

  We present initial-final mass relations for five different metallicities that show increasing final masses for decreasing metallicity values. These are similar to the latest synthetic TP-AGB grids (Marigo & Girardi 2007).

  Results are compared to two sets of observational data. On one hand, for the intermediate-mass stars, our core masses are in good agreement with the empirical Weidemann (2000) relation and observed white dwarf data from open clusters and binary systems. For the low-mass stars our masses are lower by a few hundredths of solar masses with respect to the Weidemann (2000) results. On the other hand, our C-star lifetimes agree very well with observational results for C-star counts from the Large and the Small Magellanic Clouds (Girardi & Marigo 2007).

- *On the post-AGB (Chapter 8)* - Our TP-AGB mass-loss prescription favors post-AGB tracks with high cycle phases which translates into few (15%) He-burning post-AGB tracks and H-burning ones more prone to experience an extra TP during the post-AGB evolution. The mass-loss prescriptions we have used produce transition times of the order of a few thousand years. These are much lower than the values obtained by Vassiliadis & Wood (1994). However they are compatible with observational data (Schonberner & Blocker 1993, Schonberner 1997).

  We also show how, in the case of a very late thermal pulse, time resolution plays a major role on the time necessary for a star to return to the giant phase. With the appropriate minimum time step, and without the necessity to invoke a reduction of the mixing efficiency (Herwig 2001b), born again times of 11 years, close to the ones obtained from observations (e.g. ≈ 2 years for Sakurai's object) are possible. This result is also in agreement with latest work from Miller Bertolami et al. (2006) and Miller Bertolami & Althaus (2007b).

We consider the two ensuing examples, to show a possible use of our stellar library.

The Bruzual & Charlot (2003) population synthesis code, currently adopts the effective temperatures, luminosities and lifetimes of TP-AGB stars from the the models of Vassiliadis & Wood (1993). With higher lifetime values for the longest lived stars ($\approx 2\mathrm{M}_\odot$) but shorter ones at other masses, lower effective temperatures for the C-rich models, higher luminosities and different distribution of M- and C-type stars, our tracks will certainly influence the galaxy models.

On the other hand, the Marigo et al. (2004) planetary nebula synthetic code, includes three separate grids for the evolution prior to the planetary nebula phase (Marigo et al. 1999, Girardi et al. 2000, Marigo 2001) and the older tracks of Vassiliadis & Wood (1994) for the post-AGB phase. Because the type (H- or He-burning) of post-AGB evolution and the associated transition time values have major consequences on the evolution of the planetary nebulae, our updated homogeneous models, each corresponding to a single evolutionary track and to a related transition time, but encompassing both AGB and post-AGB phases, are the perfect candidates to be directly included in this second synthetic code.

The major drawback of our work, without which our grid would be much more complete, is the restricted initial mass interval ($1\mathrm{M}_\odot \leqq M \leqq 2\mathrm{M}_\odot$) for our post-AGB tracks, which correspondingly leads to a small final mass coverage with masses only up to $0.6\mathrm{M}_\odot$. Furthermore, two additional handicaps are the lack of good theories for the physics of mass-loss and of mixing processes. These are true limitations to more realistic and useful models. The three preceding obstacles, lead us to propose some possible directions, relevant for all currently available codes, for future investigations.

The computational difficulties encountered at the end of the TP-AGB, during the transition to the post-AGB, and on the born-again AGB phases should be more seriously addressed in order to be able to follow the entire evolution of moderate-mass stars. Solving these convergence problems and consequently gaining precious time, often lost because of the multiple necessary human interventions during the calculations, would give an additional advantage to full detailed models over synthetic ones in producing extended grids and stellar libraries.

Put aside the mass-loss prescription, which is badly in need of improvement, the mixing occuring at the convective boundaries on the TP-AGB, modeled for the moment by the overshooting treatment is also an important issue because it influences the dredge-up efficiency. The crucial point is that dredge-up links the structural and chemical evolution of the star and therefore affects any attempt (chemistry dependent mass-loss and opacity) to treat both together. This more general question, also brings forward another possible amelioration in the specific case of our evolutionary calculations. These are currently based on a few atomic species that mainly influence the models structure because they are relevant to the dominant energy generating reactions. Coupling a post-processing nucleosynthesis code to the evolutionary part would add an important feature in order to also be able to explain more elaborate stellar abundance patterns in addition to structural and evolutionary characteristics.

In conclusion, this work has mainly shown the possibility to produce a coherent an extended grid of tracks with a detailed code and updated physics for both the AGB and post-AGB phases. The resulting stellar library should be a very useful input-tool in population synthesis studies.

Bibliography

Abia C., Domínguez I., Gallino R., Busso M., Straniero O., de Laverny P., Wallerstein G., 2003, Publications of the Astronomical Society of Australia, 20, 314

Abia C., Isern J., 2000, ApJ, 536, 438

Adelberger E. G., Austin S. M., Bahcall J. N., Balantekin A. B., et al. 1998, Reviews of Modern Physics, 70, 1265

Alexander D. R., Ferguson J. W., 1994, ApJ, 437, 879

Alexander D. R., Rypma R. L., Johnson H. R., 1983, ApJ, 272, 773

Althaus L. G., Serenelli A. M., Panei J. A., Córsico A. H., García-Berro E., Scóccola C. G., 2005, A&A, 435, 631

Anders E., Grevesse N., 1989, Geochim. Cosmochim. Acta, 53, 197

Aringer B., 2000, Ph.D. thesis. Univ. Vienna, Austria

Arlandini C., Käppeler F., Wisshak K., Gallino R., Lugaro M., Busso M., Straniero O., 1999, ApJ, 525, 886

Arndt T. U., Fleischer A. J., Sedlmayr E., 1997, A&A, 327, 614

Arp H. C., Baum W. A., Sandage A. R., 1953, ApJ, 58, 4

Asida S. M., Arnett D., 2000, ApJ, 545, 435

Asplund M., 1999, in Le Bertre T., Lebre A., Waelkens C., eds, Asymptotic Giant Branch Stars Vol. 191 of IAU Symposium, Sakurai's object – stellar evolution in real time. pp 481–+

Balser D. S., 2006, AJ, 132, 2326

Battinelli P., Demers S., 2004, A&A, 418, 33

Bergeat J., Chevallier L., 2005, A&A, 429, 235

Bernard-Salas J., 2003, Physics and Chemistry of Gas in Planetary Nebulae. Rijksuniversiteit Groningen, Netherlands

Bertelli G., Bressan A., Chiosi C., Angerer K., 1986, A&AS, 66, 191

Bessell M. S., Brett J. M., Scholz M., Wood P. R., 1991, A&AS, 87, 621

Bessell M. S., Brett J. M., Wood P. R., Scholz M., 1989, A&AS, 77, 1

Blöcker T., 1995a, A&A, 299, 755

Blöcker T., 1995b, A&A, 297, 727

Blöcker T., 1999, in Le Bertre T., Lebre A., Waelkens C., eds, IAU Symp. 191: Asymptotic Giant Branch Stars Structure and Evolution of AGB Stars. pp 21–+

Blöcker T., Holweger H., Freytag B., Herwig F., Ludwig H.-G., Steffen M., 1998, Space Science Reviews, 85, 105

Bohm K. H., Cassinelli J., 1971, A&A, 12, 21

Böhm K.-H., Stückl E., 1967, Zeitschrift fur Astrophysik, 66, 487

Böhm-Vitense E., 1958, Zeitschrift fur Astrophysik, 46, 108

Bono G., Caputo F., Cassisi S., Marconi M., Piersanti L., Tornambè A., 2000, ApJ, 543, 955

Boothroyd A. I., Sackmann I.-J., 1988a, ApJ, 328, 641

Boothroyd A. I., Sackmann I.-J., 1988b, ApJ, 328, 653

Boothroyd A. I., Sackmann I.-J., 1999, ApJ, 510, 232

Bowen G. H., 1988, ApJ, 329, 299

Bowen G. H., Willson L. A., 1991, ApJL, 375, L53

Bressan A., Fagotto F., Bertelli G., Chiosi C., 1993, A&A, 100, 647

Bruzual G., Charlot S., 2003, MNRAS, 344, 1000

Buonanno R., Corsi C. E., Buzzoni A., Cacciari C., Ferraro F. R., Fusi Pecci F., 1994, A&A, 290, 69

Busso M., Gallino R., Wasserburg G. J., 1999, ARA&A, 37, 239

Canuto V. M., Mazzitelli I., 1991, ApJ, 370, 295

Carroll B. W., Ostlie D. A., 1996, An Introduction to Modern Astrophysics. An Introduction to Modern Astrophysics, by B.W. Carroll and D.A. Ostlie. Benjamin Cummings, 1996. ISBN 0-201-54730-9.

Casagrande L., Flynn C., Portinari L., Girardi L., Jimenez R., 2007, ArXiv Astrophysics e-prints

Cassisi S., Salaris M., Irwin A. W., 2003, ApJ, 588, 862

Castellani V., Chieffi A., Tornambe A., Pulone L., 1985, ApJ, 296, 204

Caughlan G. R., Fowler W. A., 1988, Atomic Data and Nuclear Data Tables, 40, 283

Caughlan G. R., Fowler W. A., Harris M. J., Zimmerman B. A., 1985, Atomic Data and Nuclear Data Tables, 32, 197

Chandrasekhar S., 1931, ApJ, 74, 81

Chapman J. M., Habing H. J., Killeen N. E. B., 1995, in Stobie R. S., Whitelock P. A., eds, ASP Conf. Ser. 83: IAU Colloq. 155: Astrophysical Applications of Stellar Pulsation RadioObservations of Mira Variables; OH/IR Stars and M-Supergiants. pp 113–+

Charbonnel C., Brown J. A., Wallerstein G., 1998, A&A, 332, 204

Charbonnel C., Zahn J.-P., 2007, A&A, 467, L15

Ciardullo R., 2003, in Alloin D., Gieren W., eds, LNP Vol. 635: Stellar Candles for the Extragalactic Distance Scale Extragalactic Distances from Planetary Nebulae. pp 243–263

Cioni M.-R. L., van der Marel R. P., Loup C., Habing H. J., 2000, A&A, 359, 601

Claver C. F., Liebert J., Bergeron P., Koester D., 2001, ApJ, 563, 987

Clayton D. D., 1968, Principles of stellar evolution and nucleosynthesis. The University of Chicago Press, Chicago

Coelho P., Bruzual G., Charlot S., Weiss A., Barbuy B., Ferguson J. W., 2007, MNRAS, 382, 498

Cox A. N., Stewart J. N., 1970a, ApJS, 19, 243

Cox A. N., Stewart J. N., 1970b, ApJS, 19, 261

Cristallo S., Straniero O., Lederer M. T., Aringer B., 2007, ApJ, 667, 489

De Marco O., Storey P. J., Barlow M. J., 1998, MNRAS, 297, 999

Deacon R. M., Chapman J. M., Green A. J., Sevenster M. N., 2007, ApJ, 658, 1096

Denissenkov P. A., Tout C. A., 2003, MNRAS, 340, 722

Dobbie P. D., Napiwotzki R., Burleigh M. R., Barstow M. A., Boyce D. D., Casewell S. L., Jameson R. F., Hubeny I., Fontaine G., 2006, MNRAS, 369, 383

Dominy J. F., 1985, PASP, 97, 1104

Dreizler S., Heber U., 1998, A&A, 334, 618

Duerbeck H. W., Benetti S., 1996, ApJL, 468, L111+

Duerbeck H. W., Benetti S., Gautschy A., van Genderen A. M., Kemper C., Liller W., Thomas T., 1997, AJ, 114, 1657

Eggleton P. P., 1971, MNRAS, 151, 351

Eggleton P. P., Dearborn D. S. P., Lattanzio J. C., 2006, Science, 314, 1580

Eggleton P. P., Dearborn D. S. P., Lattanzio J. C., 2007, ArXiv e-prints, 706

Eggleton P. P., Faulkner J., Flannery B. P., 1973, A&A, 23, 325

Ferguson J. W., 2006, private communication

Ferguson J. W., Alexander D. R., Allard F., Barman T., Bodnarik J. G., Hauschildt P. H., Heffner-Wong A., Tamanai A., 2005, ApJ, 623, 585

Ferrario L., Wickramasinghe D., Liebert J., Williams K. A., 2005, MNRAS, 361, 1131

Fleischer A. J., 1994, Hydrodynamics and Dust Formation in the Circumstellar Shells of Miras and Long-Period Variables. Technischen Universität Berlin

Fleischer A. J., Gauger A., Sedlmayr E., 1992, A&A, 266, 321

Formicola A., Imbriani G., Costantini H., et al. 2004, Physics Letters B, 591, 61

Fowler W. A., Caughlan G. R., Zimmerman B. A., 1975, ARA&A, 13, 69

Freytag B., Ludwig H.-G., Steffen M., 1996, A&A, 313, 497

Frost C. A., Lattanzio J. C., 1996, ApJ, 473, 383

Fujimoto M. Y., 1977, PASJ, 29, 331

Fukugita M., Kawasaki M., 2006, ApJ, 646, 691

Fynbo H. O. U., Diget C. A., Bergmann U. C., et al. 2005, Nature, 433, 136

Girardi L., Bressan A., Bertelli G., Chiosi C., 2000, A&A, 141, 371

Girardi L., Marigo P., 2007, A&A, 462, 237

Grevesse N., Noels A., 1993, Phys. Scr. T, 47, 133

Groenewegen M. A. T., de Jong T., 1993, A&A, 267, 410

Groenewegen M. A. T., de Jong T., 1994, A&A, 283, 463

Groenewegen M. A. T., Whitelock P. A., 1996, MNRAS, 281, 1347

Gurzadyan G. A., 1997, The Physics and Dynamics of Planetary Nebulae. Springer-Verlag Berlin Heidelberg

Habing H. J., 1996, A&ARv, 7, 97

Habing H. J., Olofsson H., 2004, Asymptotic Giant Branch Stars. Springer-Verlag New York

Hajduk M., Zijlstra A. A., Herwig F., van Hoof P. A. M., Kerber F., Kimeswenger S., Pollacco D. L., Evans A., Lopéz J. A., Bryce M., Eyres S. P. S., Matsuura M., 2005, Science, 308, 231

Harris M. J., Fowler W. A., Caughlan G. R., Zimmerman B. A., 1983, ARA&A, 21, 165

Herwig F., 2000, A&A, 360, 952

Herwig F., 2001a, Astrophys. Space Sci., 275, 15

Herwig F., 2001b, ApJL, 554, L71

Herwig F., 2004a, ApJ, 605, 425

Herwig F., 2004b, ApJS, 155, 651

Herwig F., 2005a, ARA&A, 43, 435

Herwig F., 2005b, private communication

Herwig F., Blöcker T., Driebe T., 2000, Memorie della Societa Astronomica Italiana, 71, 745

Herwig F., Blöcker T., Langer N., Driebe T., 1999, A&A, 349, L5

Herwig F., Bloecker T., Schoenberner D., El Eid M., 1997, A&A, 324, L81

Herwig F., Schoenberner D., Bloecker T., 1998, A&A, 340, L43

Hoefner S., Dorfi E. A., 1997, A&A, 319, 648

Huebner W. F., Merts A. L., Magee N. H. J., Argo M. F., 1977, Astrophysical Opacity Library (Los Alamos Scientific Laboratory, LA-6760-M)

Iben Jr. I., 1977, ApJ, 217, 788

Iben Jr. I., MacDonald J., 1995, in Koester D., Werner K., eds, White Dwarfs, Proceedings of the 9th European Workshop on White Dwarfs Held at Kiel, Germany, 29 August - 1 September 1994. Lecture Notes in Physics, Vol. 443, edited by Detlev Koester and Klaus Werner. Springer-Verlag, Berlin Heidelberg New York, 1995., p.48 The Born Again AGB Phenomenon. pp 48–+

Iben Jr. I., Renzini A., 1982a, ApJL, 263, L23

Iben Jr. I., Renzini A., 1982b, ApJL, 259, L79

Iben Jr. I., Renzini A., 1983, ARA&A, 21, 271

Iglesias C. A., Rogers F. J., 1996, ApJ, 464, 943

Itoh N., Mitake S., Iyetomi H., Ichimaru S., 1983, ApJ, 273, 774

Ivezic Z., Elitzur M., 1995, ApJ, 445, 415

Izzard R. G., Tout C. A., Karakas A. I., Pols O. R., 2004, MNRAS, 350, 407

Jascheck C., Jascheck M., 1987, The Classification of Stars. Cambridge University Press, Cambridge

Kahn F. D., 1989, in Planetary Nebulae Models of planetary nebulae : generalisation of the multiple winds model.

Kalirai J. S., Richer H. B., Reitzel D., Hansen B. M. S., Rich R. M., Fahlman G. G., Gibson B. K., von Hippel T., 2005, ApJL, 618, L123

Karakas A. I., 2003, Asymptotic Giant Branch Stars: their influence on binary systems and the interstellar medium. Monash University, Australia

Karakas A. I., Lattanzio J. C., 2007, ArXiv e-prints, 708

Karakas A. I., Lattanzio J. C., Pols O. R., 2002, Publications of the Astronomical Society of Australia, 19, 515

Keenan P. C., Boeshaar P. C., 1980, ApJS, 43, 379

Kholopov P. N., 1987, General Catalogue of Variable Stars, 5th Edition. Nakua Publishing House, Moscow

Kippenhahn R., Weigert A., 1990, Stellar Structure and Evolution. Springer-Verlag Berlin Heidelberg

Kippenhahn R., Weigert A., Hofmeister E., 1967, Methods for Calculating Stellar Evolution, Vol. 7 of Methods in Computational Physics, 129. New York: Academic Press

Kitsikis A., Weiss A., 2007, AGB and post-AGB Stellar Evolution: Theoretical Models for Synthetic Population Studies. Why Galaxies Care About AGB stars, Vienna. ASP Conference series

Knapp G., Pourbaix D., Jorissen A., 2001, A&A, 371, 222

Kneller J. P., Steigman G., 2004, New Journal of Physics, 6, 117

Koesterke L., Hamann W.-R., 1997, A&A, 320, 91

Kunz R., Fey M., Jaeger M., Mayer A., Hammer J. W., Staudt G., Harissopulos S., Paradellis T., 2002, ApJ, 567, 643

Kwok S., 1982, ApJ, 258, 280

Kwok S., Purton C. R., Fitzgerald P. M., 1978, ApJL, 219, L125

Lançon A., Mouhcine M., Fioc M., Silva D., 1999, A&A, 344, L21

Lançon A., Wood P. R., 2000, A&AS, 146, 217

Langer N., Heger A., Wellstein S., Herwig F., 1999, A&A, 346, L37

Lattanzio J. C., Boothroyd A. I., 1997, in Bernatowicz T. J., Zinner E., eds, American Institute of Physics Conference Series Nucleosynthesis of Elements in Low to Intermediate Mass Stars Through the AGB Phase. pp 85–+

Lawlor T. M., MacDonald J., 2002, ApSS, 279, 123

Little-Marenin I. R., Little S. J., 1979, AJ, 84, 1374

Lucy I. B., Robertson J. A., Sharp C. M., 1986, A&A, 154, 267

Ludwig H.-G., Freytag B., Steffen M., 1999, A&A, 346, 111

Lugaro M., Herwig F., Lattanzio J. C., Gallino R., Straniero O., 2003, ApJ, 586, 1305

Maciel W. J., 2001, Astrophysics and Space Science, 277, 545

Marigo P., 2001, A&A, 370, 194

Marigo P., 2002, A&A, 387, 507

Marigo P., 2007, A&A, 467, 1139

Marigo P., Bressan A., Chiosi C., 1996, A&A, 313, 545

Marigo P., Girardi L., 2007, A&A, 469, 239

Marigo P., Girardi L., Bressan A., 1999, A&A, 344, 123

Marigo P., Girardi L., Weiss A., Groenewegen M. A. T., 1999, A&A, 351, 161

Marigo P., Girardi L., Weiss A., Groenewegen M. A. T., Chiosi C., 2004, A&A, 423, 995

Mazzitelli I., 1979, A&A, 79, 251

Mazzitelli I., D'Antona F., Ventura P., 1999, A&A, 348, 846

McClure R. D., 1997, PASP, 109, 536

Meissner F., Weiss A., 2006, A&A, 456, 1085

Miller Bertolami M. M., 2006, private communication

Miller Bertolami M. M., Althaus L. G., 2006, A&A, 454, 845

Miller Bertolami M. M., Althaus L. G., 2007a, A&A, 470, 675

Miller Bertolami M. M., Althaus L. G., 2007b, MNRAS, 380, 763

Miller Bertolami M. M., Althaus L. G., Serenelli A. M., Panei J. A., 2006, A&A, 449, 313

Mouhcine M., Lançon A., 2002, A&A, 393, 149

Nowotny W., Kerschbaum F., Schwarz H. E., Olofsson H., 2001, A&A, 367, 557

Ohnaka K., Tsuji T., 1996, A&A, 310, 933

Ostlie D. A., Cox A. N., 1986, ApJ, 311, 864

Oudmaijer R. D., Waters L. B. F. M., van der Veen W. E. C. J., Geballe T. R., 1995, A&A, 299, 69

Paczyński B., 1970, Acta Astronomica, 20, 47

Pagel B. E. J., Portinari L., 1998, MNRAS, 298, 747

Pauldrach A., Puls J., Kudritzki R. P., Mendez R. H., Heap S. R., 1988, A&A, 207, 123

Peimbert A., Peimbert M., Luridiana V., 2002, ApJ, 565, 668

Peimbert M., 1978, in Terzian Y., ed., IAU Symp. 76: Planetary Nebulae Chemical abundances in planetary nebulae. pp 215–223

Pilachowski C., Sneden C., Freeland E., Casperson J., 2003, AJ, 125, 794

Reimers D., 1975, Circumstellar envelopes and mass loss of red giant stars. Problems in stellar atmospheres and envelopes., pp 229–256

Renzini A., 1981, in Chiosi C., Stalio R., eds, ASSL Vol. 89: IAU Colloq. 59: Effects of Mass Loss on Stellar Evolution Evolutionary effects of mass loss in low-mass stars. pp 319–336

Renzini A., 1989, in Torres-Peimbert S., ed., Planetary Nebulae Vol. 131 of IAU Symposium, Thermal pulses and the formation of planetary nebula shells.. pp 391–400

Renzini A., Voli M., 1981, A&A, 94, 175

Robinson F. J., Demarque P., Li L. H., Sofia S., Kim Y.-C., Chan K. L., Guenther D. B., 2004, MNRAS, 347, 1208

Rogers F. J., Swenson F. J., Iglesias C. A., 1996, ApJ, 456, 902

Russell H. N., 1934, ApJ, 79, 317

Sackmann I.-J., 1980, ApJL, 241, L37

Saviane I., Held E. V., Bertelli G., 2000, A&A, 355, 56

Scalo J. M., 1976, ApJ, 206, 474

Scalo J. M., Ulrich R. K., 1975, ApJ, 200, 682

Schaller G., Schaerer D., Meynet G., Maeder A., 1992, A&A, 96, 269

Schlattl H., Weiss A., 1999, A&A, 347, 272

Schoenberner D., 1983, ApJ, 272, 708

Schoenberner D., 1990, in Mennessier M. O., Omont A., eds, From Miras to Planetary Nebulae: Which Path for Stellar Evolution? Mass loss and evolution of planetary nebulae. pp 355–367

Schonberner D., 1997, in Habing H. J., Lamers H. J. G. L. M., eds, Planetary Nebulae Vol. 180 of IAU Symposium, Structure and evolution of central stars of Planetary Nebulae (Invited Review). pp 379–+

Schonberner D., Blocker T., 1993, in Sasselov D. D., ed., Luminous High-Latitude Stars Vol. 45 of Astronomical Society of the Pacific Conference Series, Evolution on the AGB and Beyond. pp 337–+

Schönberner D., Jacob R., Steffen M., Sandin C., 2007, A&A, 473, 467

Schonberner D., Steffen M., 2007, in Kerschbaum F., Charbonnel C., Wing R. F., eds, Why Galaxies care about AGB Stars: their importance as actors and probes Vol. 378 of Astronomical Society of the Pacific Conference Series, On the Mass-Loss History at the Tip of the AGB. pp 343–+

Schröder K.-P., Winters J. M., Sedlmayr E., 1999, A&A, 349, 898

Schwarzschild M., Härm R., 1965, ApJ, 142, 855

Seaton M. J., Zeippen C. J., Tully J. A., Pradhan A. K., Mendoza C., Hibbert A., Berrington K. A., 1992, Revista Mexicana de Astronomia y Astrofisica, vol. 23, 23, 19

Sedlmayr E., 1994, in IAU Colloq. 146: Molecules in the Stellar Environment From Molecules to Grains

Sedlmayr E., Winters J. M., 1997, in Stellar Atmospheres: Theory and Observations Cool Star Winds and Mass Loss: Theory

Shaviv G., Salpeter E. E., 1973, ApJ, 184, 191

Smith V. V., Lambert D. L., 1986, ApJ, 311, 843

Smith V. V., Lambert D. L., 1990, ApJS, 72, 387

Smith V. V., Terndrup D. M., Suntzeff N. B., 2002, ApJ, 579, 832

Spaeth H., 1973, Spline-Algorithmen zur Konstruktion glatter Kurven und Flächen. München: Oldenburg-Verlag

Spergel D. N., Bean R., Doré O., Nolta M. R., Bennett C. L., Dunkley J., Hinshaw G., Jarosik N., Komatsu E., Page L., Peiris H. V., Verde L., Halpern M., Hill R. S., Kogut A., Limon M., et. al 2007, ApJS, 170, 377

Stancliffe R. J., Tout C. A., Pols O. R., 2004, MNRAS, 352, 984

Straniero O., Chieffi A., Limongi M., Busso M., Gallino R., Arlandini C., 1997, ApJ, 478, 332

Tsuji T., 1966, PASJ, 18, 127

van den Hoek L. B., Groenewegen M. A. T., 1997, A&A, 123, 305

van Loon J. T., Cioni M.-R. L., Zijlstra A. A., Loup C., 2005, A&A, 438, 273

Vassiliadis E., Wood P. R., 1993, ApJ, 413, 641

Vassiliadis E., Wood P. R., 1994, ApJS, 92, 125

Ventura P., Zeppieri A., Mazzitelli I., D'Antona F., 1998, A&A, 334, 953

Wachter A., Schröder K.-P., Winters J. M., Arndt T. U., Sedlmayr E., 2002, A&A, 384, 452

Wagenhuber J., 1996, Entwicklung von Sternen vershiedener Massen und Metallizitäten auf dem asymptotischen Riesenast und danach. Technischen Universität München

Wagenhuber J., Groenewegen M. A. T., 1998, A&A, 340, 183

Wagenhuber J., Weiss A., 1994, A&A, 286, 121

Wallerstein G., Knapp G. R., 1998, ARA&A, 36, 369

Weidemann V., 2000, A&A, 363, 647

Weigert A., 1966, Zeitschrift fur Astrophysik, 64, 395

Weiss A., 1987, A&A, 185, 165

Weiss A., 1989, ApJ, 339, 365

Weiss A., Porcherot Q., 2007, private communication

Weiss A., Salaris M., Ferguson J. W., Alexander D. R., 2006, ArXiv Astrophysics e-prints

Weiss A., Schlattl H., 2000, A&AS, 144, 487

Weiss A., Schlattl H., 2007, ApSS, pp 341–+

Weiss A., Serenelli A., Kitsikis A., Schlattl H., Christensen-Dalsgaard J., 2005, A&A, 441, 1129

Werner K., Dreizler S., Rauch T., Koesterke L., Heber U., 1999, in Le Bertre T., Lebre A., Waelkens C., eds, Asymptotic Giant Branch Stars Vol. 191 of IAU Symposium, Born-again AGB stars: Starting point of the H-deficient post-AGB evolutionary sequence?. pp 493–+

Westerlund B. E., 1997, The Observatory, 117, 317

Williams K. A., Bolte M., Koester D., 2004, ApJL, 615, L49

Willson L. A., 2000, ARA&A, 38, 573

Winters J. M., Fleischer A. J., Le Bertre T., Sedlmayr E., 1997, A&A, 326, 305

Wood P. R., Faulkner D. J., 1986, ApJ, 307, 659

Wood P. R., Zarro D. M., 1981, ApJ, 247, 247

Zahn J.-P., 1991, A&A, 252, 179